

Development of a Compact High Resolution Gamma Camera

António Jorge Soares
Department of Physics and Astronomy
University College London

Submitted for the degree of
Doctor of Philosophy
2001



Abstract

The subject of this thesis is the development of new gamma ray imagers for nuclear medicine, in particular for scintimammography. The need for new compact detectors with high spatial resolution led to the design of the wavelength-shifting fibre (WSF) gamma camera, where the position of interaction of gamma rays inside an inorganic scintillator is read out by WSFs.

The feasibility of the concept of a WSF gamma camera was assessed by simple analytical calculations and Monte Carlo simulations, based on the known characteristics of the individual components: the wavelength-shifting fibres, the scintillation crystal and the photodetectors.

Studies were carried out of the light trapped inside WSFs coupled to CsI(Na) scintillation crystals irradiated by 122 keV gamma rays. The results confirm the feasibility of a WSF gamma camera despite the low light levels trapped in the fibres.

Experimental tests of several position sensitive photomultiplier tubes (PSPMT) of the Hamamatsu R5900 series were performed to assess their suitability for the readout of scintillation crystals and of optical fibres in photon counting mode. The latter application is important for the readout of the WSFs signals in a WSF gamma camera.

A WSF gamma camera prototype was built and tested. The R5900-M16 PSPMT was used to read out the signals from WSFs. The results confirm earlier predictions about its performance. In particular, the spatial resolution achieved is comparable to that of modern Anger cameras. It is expected that the inherently flexible design of the camera should allow better positioning around the object than conventional Anger cameras, which is important to optimise the spatial resolution of the system. Monte Carlo simulations show that the use of photodetectors with higher quantum efficiency than PSPMTs would significantly improve the intrinsic spatial resolution. A discussion on the most promising candidates for this application is presented.

Acknowledgements

This PhD project is the result of a collaboration between the Dept. of Physics and Astronomy, the Dept. Medical Physics and Bioengineering and, to a less official extent, the Institute of Nuclear Medicine of the Middlesex Hospital. There are therefore many people to whom, in different ways, I feel indebted.

I would like to express my gratitude to my supervisor, David Miller, for all the guidance, support and invaluable dedication throughout the PhD.

Likewise, I would like to thank my co-supervisor, Robert Speller, for his support and for making me feel welcome in the group.

I owe a great deal to Ian Cullum for his continuous advice and for many useful discussions, which led to many of the ideas pursued throughout this work. Thank you also for all the help with the electronics.

I wish to thank Jenny Thomas for all the help and advice in the evaluation of PSPMTs. Thanks to Brian Anderson for answering many of my questions about scintillators and PMTs and to Gordon Crone for all the help with computing issues. Thanks also to Derek Attree and Dominic Hayes for their technical support. Many thanks to Derek Thomas for aluminising the WSFs. Thanks to Gary Royle for many discussions and support during the project.

I would like to thank the detector group of the Thomas Jefferson National Accelerator Facility for the warm reception during my stay. In particular Stan Majewski for all the help and advice during our short collaboration. Special thanks also to Drew Weisenberger for his help with Kmax programming.

Thank you to all other friends and colleagues: Antonis, Angelo, Giulia, Beata, Ghirmay, Mike, Kenny, Emma, Dimitra, Tiago, Tavora and Kevin.

The Fundação para a Ciência e a Tecnologia, Portugal, is gratefully acknowledged for the financial support during the PhD.

Finally I would like to dedicate this work to my parents for all their love and support throughout the years. Equally I thank my sister Raquel and my brothers Tó and Tiago for all their encouragement. Very special thanks also to João, Belinha, Henrique, António José and Isabel. Obrigado.

To my wife Maria, for all the love and continuous encouragement that made this work possible.

António

Contents

1	Introduction	18
2	Gamma Ray Imaging in Nuclear Medicine	20
2.1	Introduction	20
2.1.1	Principles of nuclear medicine	21
2.1.2	Gamma ray imagers in nuclear medicine	21
2.1.3	Breast cancer detection	22
2.2	Radiopharmaceuticals	22
2.2.1	Radiopharmaceuticals for single photon emission	23
2.2.2	Radiopharmaceuticals for positron emission imaging	24
2.3	Gamma ray imaging detectors	25
2.3.1	The Anger camera	26
2.3.2	Performance of the Anger camera	33
2.3.3	Single Photon Emission Computed Tomography	37
2.3.4	Positron Emission Tomography	38
2.4	Scintimammography	40
2.4.1	Breast cancer screening	40
2.4.2	Scintimammography trials	40
2.4.3	Problems in scintimammography imaging	41
2.4.4	The need for new imagers for scintimammography	41
2.5	Requirements for a compact gamma camera for scintimammography	43
2.5.1	Spatial resolution of the scintillation imager	43
2.5.2	Energy resolution	43
2.5.3	Detection efficiency	43
2.5.4	Size, shape and dead regions of the camera	44
3	Survey of small gamma ray imagers	45
3.1	Inorganic scintillator crystals	45
3.1.1	Requirements for an ideal scintillator	46
3.1.2	Description of some common scintillators	47

3.1.3	Energy resolution	49
3.2	Properties of Position Sensitive Photomultipliers	52
3.2.1	Fine Mesh dynodes and Micro-channel Plates	52
3.2.2	Metal Channel Dynodes	56
3.2.3	Position sensitive anode configurations	59
3.2.4	Currently available PSPMTs	60
3.3	PSPMT gamma cameras for Single Photon Imaging	62
3.3.1	Single tube cameras	62
3.3.2	Arrays of PSPMT	67
3.4	PSPMT high resolution PET detectors	67
3.5	PSPMT readout methods	68
3.5.1	Resistor network	68
3.5.2	Individual anode readout	70
3.6	Gamma cameras with Hybrid Photodetectors (HPD)	72
3.7	Scintillation imagers with semiconductor photodiodes	73
3.7.1	Silicon pixel arrays	74
3.7.2	Mercuric Iodide pixel arrays	77
3.8	CdZnTe pixel arrays	78
4	The Wavelength-Shifting Fibre Gamma Camera	79
4.1	Principle of operation	79
4.2	Wavelength-shifting fibres	81
4.2.1	Light absorption and re-emission in WSFs	81
4.2.2	Light trapping in WSFs	83
4.2.3	Bicron BCF-91A WSFs	84
4.3	Expected performance of a WSF gamma camera	86
4.3.1	Spatial resolution	87
4.3.2	Efficiency	92
4.3.3	Energy resolution	93
4.3.4	Dead area at the edges	94
4.4	Light sensors for low light level readout of WSFs	94
4.4.1	Position sensitive PMTs (PSPMT)	95
4.4.2	Hybrid photodetectors (HPD)	96
4.4.3	Avalanche photodiodes	96
4.4.4	Visible light photon counters	97
4.5	Discussion and conclusions	98
5	Demonstration of light collection by WSFs coupled to CsI(Na) crystals	100
5.1	Introduction	100
5.2	Methods	101

5.2.1	Wavelength-shifting fibres	101
5.2.2	Scintillation crystals	101
5.2.3	Experimental set-up	101
5.2.4	Data analysis	103
5.3	Calibration of the photon counting system	105
5.4	Light collected by the WSFs with the PC-PMT	106
5.4.1	Tests with 1 mm diameter WSFs	106
5.4.2	Tests with square WSFs	110
5.4.3	Aluminium coating of the ends of the WSFs	111
5.5	Discussion and conclusions	112
6	Monte Carlo simulation studies	115
6.1	Simulation of a WSF gamma camera	116
6.1.1	The simulation packages	116
6.1.2	Light trapped in optical fibres	119
6.1.3	One WSF coupled to a CsI(Na) crystal	120
6.1.4	An idealised WSF gamma camera	125
6.2	Simulation of spatial resolution	128
6.2.1	The simulation algorithm	129
6.2.2	Results	130
6.3	Discussion and conclusions	134
7	Evaluation of PSPMTs	136
7.1	Introduction	136
7.2	Evaluation of the R5900-C8 PSPMT	137
7.2.1	Methods	138
7.2.2	Results from PSPMT scans	145
7.2.3	Discussion	159
7.3	Evaluation of the R5900-M16 PSPMT for use with WSFs . . .	160
7.3.1	Light source	160
7.3.2	Voltage divider circuit	161
7.3.3	Readout electronics and data acquisition	162
7.3.4	Data analysis for low light level measurements	162
7.3.5	Optimisation of PSPMT response	164
7.3.6	Results from scans	165
7.3.7	Discussion	175
7.4	Preliminary investigation of an R5900-M64 PSPMT	175
8	WSF gamma camera prototype	179
8.1	Description of the prototype	179
8.1.1	Scintillation crystals	179

8.1.2	Wavelength-shifting fibres	180
8.1.3	Photo-detectors for WSF readout	180
8.1.4	Photo-detectors for the energy signal readout	181
8.1.5	Readout electronics and data acquisition software	181
8.1.6	The prototype	184
8.2	Evaluation of the scintillation crystals	185
8.3	Light collected by the WSFs and M16s	187
8.3.1	Experimental procedure	187
8.3.2	Results	189
8.4	Imaging performance	193
8.4.1	Spatial resolution	193
8.4.2	Position linearity	196
8.4.3	Imaging efficiency	196
8.4.4	Image of two points	197
8.5	Energy response	197
8.5.1	Energy resolution	197
8.5.2	Energy uniformity	198
8.6	Monte Carlo simulations for a high quantum efficiency device .	198
8.7	Preliminary investigation of a NaI(Tl) WSF prototype	200
8.8	Discussion and conclusions	200
9	Conclusions and Future Work	202
9.1	Conclusions	202
9.2	Future Work	203
A	Energy resolution of inorganic scintillators coupled to PMTs	204
A.1	PMT resolution	204
A.2	Transfer resolution	205
A.3	Scintillator intrinsic resolution	206
B	Energy resolution and total light output	211
B.1	Light output and energy resolution	211
B.2	Components of the energy resolution	212
C	Operation settings of the R5900-M16s	216
C.1	Tube A	216
C.2	Tube B	216
C.3	Tube C	218

D	Development of techniques for the WSF camera	221
D.1	Photos of the scintillators	221
D.2	Photo of the E-PMTs	221
D.3	Electronics readout	221
D.3.1	Readout channels and timing	221
D.3.2	The effect of the sample-and-hold circuit	225
D.3.3	Comparison between the <i>hardware sum</i> and the <i>soft-</i> <i>ware sum</i>	226
D.4	Energy signal from the scintillators	226
E	A NaI(Tl) WSF prototype	228

List of Figures

2.1	Diagram of an Anger camera.	27
2.2	Cross-sectional views of the four basic types of Anger camera collimators	27
2.3	Schematic of a photomultiplier tube.	30
2.4	Arrangements of close-packed PMT matrices with circular and hexagonal PMTs.	32
2.5	Simplified example of a resistor network readout of 7 PMTs. .	33
2.6	Diagram showing the need to reject gamma rays scattered in the body.	36
2.7	Effective area of an Anger camera	37
2.8	SPECT system with three Anger cameras in a rotating gantry.	38
2.9	Principles of positron emission tomography imaging.	39
2.10	Diagram showing the importance of small dead areas at the edges to enable the detection of tumours deep inside the breast in scintimammography.	42
3.1	Combined plot showing the spectra of emission of some scintillators and the quantum efficiency curve for a bialkali photocathode.	48
3.2	A typical scintillation counter based on an inorganic scintillator coupled to a PMT.	50
3.3	Schematic detail of a fine mesh dynode.	53
3.4	PMT with a fine mesh dynode.	53
3.5	Schematic of a Micro-Channel Plate.	55
3.6	Example of an electron multiplier based on multi stage metal channel tubes.	56
3.7	Multi stage drilled metal sheets.	56
3.8	Multi stage etched metal masks electron multiplier.	56
3.9	Improved design for a metal channel dynode multiplier based on etched metal masks.	58
3.10	Hamamatsu metal channel dynode multiplier.	58
3.11	Segmented anode array.	60

3.12	Crossed wire anode with a reflective last dynode.	60
3.13	Diagram of a PSPMT based gamma camera.	63
3.14	Crossed-wire anode with resistor chain readout.	68
3.15	Illustration of a resistor chain.	69
3.16	Two simultaneous events which cannot be correctly identified with a resistor chain readout.	70
3.17	Individual anode readout of a crossed-wire anode PSPMT. . .	71
3.18	Individual anode readout of a segmented anode PSPMT. . . .	71
4.1	Diagram of the WSF gamma camera with a single continuous crystal.	80
4.2	Diagram of a WSF gamma camera with segmented crystals. .	81
4.3	Diagram of a double clad wavelength-shifting fibre.	82
4.4	Optical path for photons hitting round and square fibres. . .	82
4.5	Emission spectrum of CsI(Na) and mean free path in BICRON BCF-91A WSFs.	83
4.6	The absorption and emission spectra for the Bicron BCF-91A blue-to-green WSFs.	84
4.7	Trapping efficiency inside WSFs.	85
4.8	Definition of angles for the calculation of the numerical aper- ture of a double cladded optical fibre.	85
4.9	Definition of angles in Snell's law.	86
4.10	Solid angle subtended by the elemental area between $(x, x +$ $dx)$ and $(y, y + dy)$, and the point of emission of photons. . .	88
4.11	Graphical representation of the parameters used in the solid angle calculation.	90
5.1	Setup used for the measurement of the WSF signals.	102
5.2	Pulse-height distribution for one WSF coupled to the PC- PMT with pulses of very low intensity, showing the single photo-electron peak and the electronic pedestal.	104
5.3	LED pulser circuit.	105
5.4	Pulse-height distribution showing the single photo-electron peak for the PC-PMT.	106
5.5	Pulse-height distribution for two cases a) fibre 5 and b) all 9 fibres.	107
5.6	Output of groups of 1 mm diameter fibres.	108
5.7	Output of individual 1 mm diameter fibres.	109
5.8	Output of 1 mm diameter individual fibres coupled to both sides of the crystals with gel.	110
5.9	Output of individual $1 \times 1 \text{ mm}^2$ square fibres.	111

5.10	Output of individual $2 \times 2 \text{ mm}^2$ square fibres.	112
5.11	Output of individual 1 mm diameter fibres with one end aluminised to improve light output.	113
6.1	Definition of angles in Fresnel's reflection formula and Snell's law.	118
6.2	Geometry used for the simulation of light trapped inside WSFs. All dimensions in mm.	119
6.3	A 1 mm diameter WSF coupled to a 3 mm thick, $125 \times 125 \text{ mm}^2$ slab of CsI(Na).	121
6.4	Number of wavelength-shifting events as a function of the radial position of the absorption point within the WSFs.	122
6.5	Mean number of scintillation photons created at a radial distance $\sqrt{x^2 + y^2}$ from the gamma ray beam due to Compton interactions.	124
6.6	Geometry used to simulate a WSF gamma camera. The dimensions are in mm.	126
6.7	Simulation results for the number of photons in each WSF and the number of photoelectrons expected to be produced in a PMT.	127
6.8	Flow diagram of the simulation program (SR-SIM) developed to simulate the spatial resolution of a WSF camera.	131
6.9	Results from SR-SIM for the pulse-height distributions obtained from a PMT.	132
6.10	Spatial resolution results from SR-SIM.	133
7.1	Schematic outline of the Hamamatsu R5900-C8.	137
7.2	Schematic outline of the Hamamatsu E678-32B socket connected to the R5900-C8.	138
7.3	The CsI(Tl) with a black tape mask.	139
7.4	Set-up for the measurement of the light distribution created by the optical fibre on a CCD camera at a distance d from the fibre.	140
7.5	Results of the measurement of the light distribution created by the optical fibre on a CCD camera at a distance d from the fibre.	141
7.6	Readout circuit used to test the R5900-C8 PSPMT.	142
7.7	ADC sampling of the X anodes. The timing is shown in μs units.	143
7.8	Illustration of a two dimensional histogram of the x and y centroids.	145

7.9	Average x position \bar{x} as a function of fibre position x_j^f for three y lines y_6^f , y_{12}^f and y_{18}^f	146
7.10	Distributions of x centroids for the 24 x_j^f points along the Y_{12}^f line.	148
7.11	Average y position \bar{y} as a function of fibre position y_j^f for the x line x_{12}^f	149
7.12	Average x and y positions \bar{x} and \bar{y} as a function of fibre position x_j^f and y_k^f for the y and x lines y_{12}^f and x_{12}^f	149
7.13	SR_{x_j} as a function of x_j^f for y_{12}^f and for fibre-to-PSPMT distances of d=1, 7 and 15 mm.	151
7.14	SR_{y_j} as a function of y_j^f for x_{12}^f and for fibre-to-PSPMT distances of d=1, 7 and 15 mm.	151
7.15	Average x position \bar{x} for the gamma-ray scan as a function of collimator position x_j^f for three y lines y_6^f , y_{12}^f and y_{18}^f	152
7.16	Distributions of x centroids for the 24 x_j^f points along the y_{12}^f line, for the gamma-ray scan.	153
7.17	SR_{x_j} as a function of x_j^f for y_{12}^f and SR_{y_j} as a function of y_j^f for x_{12}^f , for the gamma-ray scan.	153
7.18	Schematic representation of a 5×5 CsI(Tl) crystal array and its position with respect to the PSPMT X anodes.	154
7.19	Images of the segmented crystal array coupled to the R5900-C8 and irradiated by 122 keV gamma-rays.	155
7.20	Superposition of the images of the segmented crystal array shown in figure 7.19.	155
7.21	Pulse-height distributions for the energy signal for the LED scans and for the gamma-ray scan.	157
7.22	Mean energy \bar{E} as a function of the position of the fibre or the gamma-ray collimator (x_k^f, y_k^f)	158
7.23	Schematic representation of an array of 4×4 C8s.	159
7.24	Schematic outline of the Hamamatsu linear voltage divider connected to the M16.	161
7.25	Typical charge distributions for 4 anodes of tube A with the same pulse from the fibre.	166
7.26	Typical charge distributions for 4 anodes of tube B.	167
7.27	Typical charge distributions for 4 anodes of tube C.	168
7.28	Mean values, in ADC channels, of the charge distributions for 4 adjacent anodes in tube B.	169
7.29	Number of photo-electrons for 4 adjacent anodes in a) tube A, b) tube B and c) tube C.	170
7.30	Matrix of 3×3 mm ² scan regions centered at each M16 anode.	171

7.31	Mean number of photo-electrons per anode for the three M16s using the same input pulse.	172
7.32	Gain \overline{G} per anode for the three M16s calculated from equation 7.6.	173
7.33	Illustration of the cross-talk between nearest neighbours for line x_{18}^f across tube C.	174
7.34	Charge distributions for anode P5 of the M64 at low light levels.	176
7.35	Charge distributions for the adjacent anodes P4, P5 and P6 of the M64.	177
8.1	Diagram of the electronic readout system.	182
8.2	Diagram of the WSF camera prototype.	184
8.3	Photograph of the WSFs coupled to an M16.	185
8.4	Diagram of the top view of the set-up showing the relative position of the E-PMTs, the scintillator and the WSFs.	186
8.5	Diagram showing the relative position of the E-PMTs, the scintillator and the beam of gamma rays.	187
8.6	Pulse-height distribution of the energy signal, for the 3 and the 5 mm thick crystals.	188
8.7	Mean number of photoelectrons μ for the X WSFs and the Y WSFs coupled to the 3 mm thick CsI(Na) crystal.	190
8.8	Mean number of photoelectrons μ for each pair of WSFs coupled to an M16 anode for the 3 mm thick CsI(Na) crystal. . .	191
8.9	Mean number of photoelectrons μ for the X WSFs and the Y WSFs coupled to the 5 m thick CsI(Na) crystals.	191
8.10	Mean number of photoelectrons μ for each pair of WSFs coupled to an M16 anode for the 5 mm thick CsI(Na) crystal. . .	192
8.11	Point source images for each of the 4 configurations studied. Note the different scales in the images on the left (1-16 mm) compared to the images on the right (1-32 mm).	194
8.12	Profiles across the highest intensity pixels in figure 8.11. Note the different scales in the plots on the left (1-16 mm) compared to the plots on the right (1-32 mm).	195
8.13	Measured position along two lines of scan across the imaging area of the 3 mm thick CsI(Na) prototype with one WSF per M16 anode.	196
8.14	Image of two points separated by 4 mm, using the 3 mm thick CsI(Na) and with 1 WSF coupled to each M16 anode.	197
8.15	Energy response for some selected points on the 3 mm CsI(Na) crystal.	198

8.16	Results of the Monte Carlo simulations for case A - using the experimental results for the WSF output; case B - twice the output per WSF; case C - four times the output per WSF and case D - six times the output per WSF	199
A.1	Schematic curves for the energy resolution R obtained with a scintillator coupled to a PMT compared to the resolution R_{PMT} obtained with a light flasher directly coupled to the PMT.	205
A.2	Gamma ray response functions for some common scintillators.	207
A.3	Electron response functions for some common scintillators. . .	210
B.1	Composed plot showing both the number of photoelectrons \bar{n}_{phe} and the peak resolution (in % FWHM) as a function of the ADC mean for the LED measurements.	213
C.1	Charge distributions for the anode P3 of tube A with different high voltages applied and for the same 10 ns wide input pulse.	217
C.2	Charge distributions for the EMI 9124 and for the anode P3 of tube A for the same pulser settings.	217
C.3	Charge distributions for the anode P3 of tube B with different high voltages applied and for an 8 ns wide input pulse.	218
C.4	Charge distributions for the anode P5 of tube C for different high voltages applied. The Hamamatsu voltage divider is used.	219
C.5	Charge distributions for the anode P5 of tube C. The M16 signals are amplified with a LeCroy 612A amplifier and the Hamamatsu voltage divider is used.	219
C.6	Charge distributions for the anode P5 of tube C with different high voltages applied. The modified voltage divider is used to optimise the single photo-electron response.	220
D.1	Photograph of the 4 scintillation crystals used in the experiments described in chapter 8.	222
D.2	Photograph of the 4 E-PMTs assembled in a 2×2 matrix for the experiments described in chapter 8.	222
D.3	Diagram of the two types of readout channels used in the experiments described in chapter 8: for the M16 channels and for the E-PMT channels.	223
D.4	Timing diagram for the readout system described in chapter 8.	224
D.5	Pulse-height distributions for anode 16 of M16-A.	225
D.6	Pulse-height distributions for the <i>hardware sum</i> and for the <i>software sum</i> for the setup described in section 8.2.	226

D.7	Pulse-height distributions for the the 3 mm thick CsI(Na) crystal from Hilger Crystals (section 8.2): a) no coupling between the crystal and the E-PMT light-guide and b) crystal coupled to the light-guide with silicon gel.	227
E.1	Two different configurations depending on the relative position of the WSFs and the NaI(Tl) crystal.	229
E.2	Distribution of centroids and mean number of photoelectrons per WSF using the NaI(Tl) crystal and configuration A. . . .	229
E.3	Distribution of centroids for 4 different positions of the gamma ray collimator, using configuration B.	230

List of Tables

3.1	Characteristics of some inorganic scintillators.	47
3.2	Characteristics of some PSPMTs commercially available. . . .	61
4.1	Physical and optical properties of the BCF-91A Bicron wave-length shifting fibres.	87
4.2	Results of the evaluation of the integral in equation 4.12 for consecutive 1 mm thick square WSFs.	92
5.1	Probability of obtaining zero photoelectrons, $P(0, \mu)$, for different mean numbers of photoelectrons, μ , calculated with equation 5.1.	105
5.2	Results of experiments to measure the average number of photoelectrons detected using bialkali PMTs to readout the WSFs.	113
6.1	Trapping efficiency values for photons generated isotropically at different radial positions inside the fibre.	120
6.2	Results from the EGS4 simulation of 140 keV gamma ray interactions in the 3 mm thick CsI(Na) crystal depicted in figure 6.3.	123
6.3	Mean fraction of photons created above a given radius.	123
6.4	Summary of the results obtained for the geometry depicted in figure 6.3.	125
6.5	Estimate of the total number of photons on a WSF in the geometry shown in figure 6.3 and the number of photoelectrons produced in a PMT photocathode.	125
6.6	Comparison between the results obtained with the Monte Carlo simulations and the calculations in section 4.3 for the case of gel coupling.	127
6.7	SR-SIM results for spatial resolution, as FWHM of the centroid distribution, and imaging efficiency.	132

7.1	Width of light distribution for different distances from the optical fibre to the CCD.	139
7.2	Voltage distribution ratios between the photocathode K and the anodes P for the standard linear voltage divider from Hamamatsu and for the modified voltage divider used with Tube C.	162
7.3	Voltage distribution ratio for the Hamamatsu M64.	176
8.1	Number of photoelectrons μ in the WSFs directly below the gamma ray beam and sum of the μ values in all WSFs along a given direction, for the four configurations of the system. . .	189
B.1	Results of the evaluation of the scintillation crystals without WSFs coupled to their surfaces.	212
B.2	Estimate of the contributions to the energy resolution other than the PMT resolution ($\sqrt{R_T^2 + R_i^2}$) using equation 3.5. . .	214

Chapter 1

Introduction

Nuclear medicine imaging has provided very important diagnostic information over the past 50 years. Despite continuous improvement in the imaging technology, the primary imaging tool in single photon emission imaging is the Anger camera, a device introduced over 40 years ago. The search for an optimization of the imaging techniques for specific diagnosis has led to considerable research into application-specific gamma ray imagers.

An area which can clearly benefit from such research is the detection of breast cancer through radioisotope imaging, also called scintimammography. A compact high resolution gamma camera is likely to enhance early tumour diagnosis by providing better images of small tumours (< 1 cm diameter). This may be achieved by better spatial resolution and by better positioning of the camera around the breast, in order to obtain the optimum projection.

This thesis describes the work carried out at UCL for the development of a small gamma camera prototype. It is based on wavelength-shifting fibre (WSF) readout of position of interaction of gamma rays in a scintillation crystal. The individual components of the prototype have been tested and optimised to design the final system. A simple imager was built and tested and its performance is compared with currently available imagers.

In **Chapter 2** a brief review of gamma ray imaging in nuclear medicine is presented. It focuses particularly on the description of the Anger camera and its performance characteristics. Some of the major shortcomings of this imager for scintimammography imaging are presented, leading to a set of requirements for an optimum gamma ray imager for this application.

Chapter 3 reviews the work carried out, particularly in the past 10 years, aimed at designing small gamma cameras with high spatial resolution. The most relevant work is based on Position Sensitive Photomultiplier Tubes (PSPMT) coupled to segmented crystal arrays. Other small prototypes based on semiconductor light sensors, hybrid photodetectors and CdZnTe arrays are

also presented.

The concept of the WSF gamma camera is presented in **Chapter 4**. Some simple analytical calculations are performed which allow an estimate of the performance of the imager. It is established that the light levels at the WSFs are expected to be of the order of a few photons (≤ 10) and that, therefore, single photon counting photodetectors are needed for the WSF readout. A review of single photon counting photodetectors is presented, describing currently available devices as well as promising devices which are still in a developing stage.

In **Chapter 5** we present a study of the light collection by WSF coupled to scintillation crystals. This study confirms the low light levels at the WSFs.

Based on the previous results, we have developed a Monte Carlo simulation to predict the spatial resolution of an ideal system, which is presented in **Chapter 6**. The results are used later to compare to experimental results of a WSF gamma camera prototype. This chapter also includes a Monte Carlo simulation of the light transport in an idealised WSF gamma camera.

Due to their promising characteristics as light sensors for high spatial resolution imagers, we tested several Multi-Anode PMTs from the R5900 Hamamatsu series. The experimental procedure, results and conclusions are presented in **Chapter 7**. We first consider the C8 as a candidate for the light sensor in a Anger-like configuration with high spatial resolution. Secondly, we test three M16s and an M64 as candidates to read-out the signals from the WSFs in the WSF gamma camera described in Chapter 5.

A WSF gamma camera prototype was developed and is presented in **Chapter 8**. The components used to build the prototype were chosen according to the studies presented in the previous chapters. A complete data acquisition system was developed with custom built amplifier boards and PC-ADC boards. PC-based data acquisition software for real time acquisition, analysis and display was also developed. The prototype was tested with gamma ray point sources to assess its main performance characteristics.

Chapter 9 presents the main conclusions of the work as well as suggestions for future work to improve the characteristics of the WSF gamma camera.

Chapter 2

Gamma Ray Imaging in Nuclear Medicine

2.1 Introduction

The use of ionising radiation for clinical diagnosis was prompted by two major scientific discoveries in the final decade of the nineteenth century. The first was the discovery of x-rays in 1895 by Wilhem Röntgen. Radiological x-ray images of the human body were promptly obtained and their clinical relevance as a means of diagnosing injuries was quickly realised. These events led to the development of radiology as a powerful non-invasive medical diagnostic discipline.

In most cases, x-ray imaging is used to obtain very detailed anatomic information on the structure of the objects under study. It is therefore known as structural imaging. Nevertheless, in some cases the use of contrasting agents injected into the body may also provide functional information.

The second major discovery occurred in 1896, with Becquerel's finding of natural radioactivity, which was followed by the discovery of several natural radioisotopes. The first controlled production of radioisotopes occurred during the 1930s leading to the wide availability of several types of radiation emitters. Of particular relevance for medical diagnosis was the development of radioisotope-labeled compounds (radiopharmaceuticals) selected for their ability to search out specific organs or to be involved in metabolic processes after injection in the human body. The radioisotopes of interest for clinical diagnostics are those that lead to the emission of gamma rays with energies above 80 keV, which can penetrate through several cm of human tissue. In this case, a significant percentage of gamma rays leaves the body and can be detected with a suitable gamma ray detector, to obtain the required

information.

The detector counts and possibly images the gamma radiation distribution providing physiological functional information about the specific organ or metabolic process under study. For this reason radioisotope imaging is also known as functional imaging, as opposed to the predominantly structural x-ray imaging.

2.1.1 Principles of nuclear medicine

In simple terms, nuclear medicine can be defined as a non-invasive medical diagnostic speciality where radiopharmaceuticals are injected into a patient and the resulting radiation emanating from the body is detected to provide the desired clinical information.

A wide range of nuclear medicine examinations is used today which may be divided into two main categories. The first is the determination of the amount of radioactivity in certain organs, which involves mainly a gamma ray counting detector with no particular requirement on position sensitivity. The second is to count and also to image the gamma rays to provide a two or three dimensional map of the distribution of the radiopharmaceutical inside the patient's body. A more sophisticated gamma ray detector with imaging capability is required in this case.

Radioisotope imaging is used for a variety of clinical assessments. Oncology is today one of the most important areas where radioisotope imaging examinations are performed. Carefully selected radiopharmaceuticals search out specific types of tumours producing higher uptake, and therefore higher activity, in the tumour region. The drugs usually take advantage of the very high metabolic activity of malignant tumours compared to normal tissues. For a case where such tumours are present, an image produced by a gamma ray imager should have spots of higher intensity (hot spots) compared to the surrounding background. These spots are associated with the malignant tumours, and the image should provide accurate information about their position and about their size.

2.1.2 Gamma ray imagers in nuclear medicine

Radioisotope imaging in nuclear medicine has traditionally been performed with two very distinct types of gamma ray imagers: the Anger camera and the PET scanner. These are very large and bulky devices which are designed for general purpose application, from whole-body imaging to imaging of small organs.

Recent studies have shown that the use of compact dedicated imagers for specific applications in small organ imaging may improve the image quality by allowing better positioning of the camera around the object [1, 2]. This is particularly important to avoid background emission from organs located nearby, which can overshadow the specific detail of interest.

Moreover, developments in detector technology in recent years allowed the improvement of spatial resolution of gamma ray imagers, which is particularly relevant in cancer detection. It enables the detection of smaller tumours which is of crucial importance since cancer survival rates are strongly correlated to early tumour detection.

2.1.3 Breast cancer detection

An application which could clearly benefit from the development of a compact gamma ray imager with good spatial resolution is breast cancer detection. Radioisotope imaging of the breast, often called scintimammography, can be used as an accurate diagnosis tool, leading to the reduction of unnecessary biopsies following false-positive findings in x-ray mammograms.

Together with lung cancer, breast cancer is the most common type of cancer in women in the UK, and also in Western Europe and North America. In these regions it has also the highest cancer-related death rate, which justifies the ongoing research effort in nuclear medicine to improve early detection. Research is focused on three separate areas: a) clinical trials using existing radiopharmaceuticals and Anger cameras, b) development of new radiopharmaceuticals and c) development of new application-specific gamma ray imagers.

2.2 Radiopharmaceuticals

The radiopharmaceuticals used in nuclear medicine are radio-labeled chemical compounds which are injected into the body to trace specific functions.

The decay process of the radioisotope should lead to the emission of gamma ray photons with energy above 80 keV, which have a high probability of escaping the human body. In this case, and using suitable imaging techniques, it is possible to trace back the point of emission of the gamma rays.

There are limits to how high the gamma ray energy should be. High energy gamma rays (e.g. above 300 keV) require collimation techniques with worse inherent spatial resolution (see section 2.3.1), and also pose handling problems to staff due to the difficulty of shielding.

The gamma ray emission should be monochromatic since, as described below (section 2.3.2), the rejection of scattered events based on energy discrimination is a very important technique that allows the suppression of random background events in the final image.

The half-life of the radioisotope should match the duration of the study, to avoid unnecessary dose to the patient afterwards. Other practical considerations like the preparation of the radiopharmaceutical usually introduce a lower limit to the radioisotope half-life.

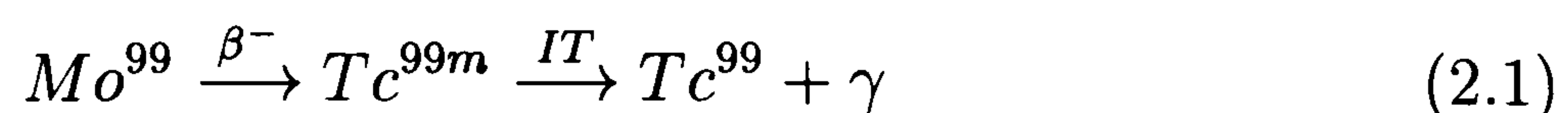
The chemical compound to which the radioisotope is to be linked should have a high specificity to trace the object of interest preferably without accumulating in nearby regions which may obscure the image of the object. It should have low toxicity and a suitable biological wash-out period (usually expressed as the biological half-life).

There are two basic types of radioisotopes used in nuclear medicine based on their emission characteristics, which lead to two distinct imaging techniques: single photon emission imaging and positron emission imaging.

2.2.1 Radiopharmaceuticals for single photon emission

Radiopharmaceuticals for single photon emission use radioisotopes whose decay is directly followed by the isotropic emission of gamma rays. The majority of these gamma ray emitters originate from radioisotopes which decay through beta emission and electron capture. These processes often leave the nucleus of the daughter isotope in an excited state, leading to a subsequent decay into the ground state with the emission of characteristic gamma rays. In many cases the excited state half-life of the daughter isotope is very short (e.g. pico-seconds) and the half-life of interest for clinical purposes is that of the parent decay process. In other cases, the daughter is left in a metastable excited state which may have a half-life of several hours and therefore be useful for nuclear medicine.

Technetium-99m (Tc^{99m}) is by far the most widely used radioisotope in nuclear medicine, where it is used in the vast majority of single photon imaging scans. It is linked to a wide variety of chemical tracers allowing specific imaging of a large number of different organs and metabolic processes in the human body. It has a half-life of 6.02 h and decays to (Tc^{99}) by isomeric transition (IT) emitting 140 keV gamma rays (98%). Its parent radioisotope is Mo^{99} , which decays via β^- emission to Tc^{99m} (85%) and to Tc^{99} (15%) with a half-life of 66 h:



Mo^{99} is commercially produced in nuclear reactors either by neutron activation of Mo^{98} or by uranium fission and it can be adsorbed into an alumina (Al_2O_3) column where it is kept for later use. Usually, a Mo^{99} supply lasts for a week during which Tc^{99m} can be eluted off the alumina column once a day using a saline solution. The separation of Tc from Mo^{99} is very efficient, with less than 0.1% of Mo^{99} breaking through [3].

The 140 keV gamma rays of Tc^{99m} allow for 50% penetration through 5 cm of tissue, and at the same time provide high detection efficiency with good spatial resolution with conventional Anger cameras (see section 2.3.1). Depending on the particular study, the injected activity of Tc^{99m} can vary typically between a few tens and several hundreds of MBq.

Since the beginning of the 1990s, several clinical studies demonstrated that the radiopharmaceutical Tc^{99m} sestamibi (Tc^{99m} methoxyisobutylisonitrile or simply Tc^{99m} -MIBI) have an increased uptake in malignant tumours [4]. This has led to many clinical studies on breast cancer detection via Tc^{99m} -MIBI imaging which demonstrated the high sensitivity and high specificity of this drug to trace malignant tumours in the breast. A review of the most relevant results of Tc^{99m} radioisotope imaging of the breast is presented below in section 2.4.

2.2.2 Radiopharmaceuticals for positron emission imaging

Other clinically useful radiopharmaceuticals are positron emitters. Following the decay, the positron travels until it combines with a free or loosely bound electron causing positron-electron annihilation, with the subsequent emission of two approximately antiparallel 511 keV gamma rays. Most of the positron emitters used in nuclear medicine (e.g. F^{18} , C^{11} , N^{13} , O^{15}) have a low atomic number, similar to the main components of the human body. These isotopes can therefore be integrated into some of the metabolic pathways inside the body more easily than the heavier isotopes for single photon imaging (e.g. Tc^{99m}).

These radioisotopes are usually produced by bombardment of stable nuclei with fast particles (protons, deuterons, etc) in a cyclotron. Due to the relatively short half-lives of the useful radioisotopes the clinical center must either have an on-site cyclotron or must be near a cyclotron site. While the former greatly adds to the cost of positron emission imaging, the latter limits this technique to only a few clinical sites.

A very important positron emission radiopharmaceutical is FDG or F^{18} -fluoro-2-deoxy-D-glucose. The F^{18} radioisotope has 110 minutes half-life

which requires close proximity between the clinical center and the radionuclide production site. This glucose analogue has been widely used for brain and heart studies as well as for tumour detection, taking advantage of the very high uptake of glucose by malignant tumours. Some preliminary clinical studies indicate that FDG positron emission tomography (PET) imaging is a useful technique for breast cancer detection [5].

2.3 Gamma ray imaging detectors

Radioisotope imaging is used to obtain a spatial mapping of the distribution of gamma rays emerging from a patient. The detector must therefore have high conversion efficiency for gamma rays and have imaging capability. It should also provide good energy discrimination in order to reject gamma rays undergoing Compton scatter in the body, which changes their initial direction with a subsequent loss of information about the original point of emission. Traditionally, inorganic scintillation crystals have been used coupled to light sensors, in particular to photomultiplier tubes (PMT). Sodium Iodide doped with thallium (NaI(Tl)) was the first choice of scintillator. It has a high conversion efficiency for gamma rays with over 90% of 140 keV gamma rays incident on a 9 mm thick NaI(Tl) crystal being converted into light pulses. It has high light yield, giving a higher signal than any other scintillator when coupled to PMTs. This provides good signal statistics which is essential to achieve good energy discrimination and good spatial resolution.

The first gamma ray imager for clinical use was the rectilinear scanner developed in the 1950s. It consists of a non-imaging scintillation counter - a single NaI(Tl) scintillation crystal viewed by a photomultiplier. A gamma ray collimator is attached to the scintillation counter and an electro-mechanical scanning system allows accurate scanning of the detector across a region of interest, where gamma ray interactions are recorded, and a two dimensional image is obtained. Despite a reasonable intrinsic spatial resolution of about 5 mm, these imagers have the disadvantage of low sensitivity due to the short time spent at each point, requiring a higher dose to the patient compared to a large device with intrinsic two-dimensional imaging capability. For the same reason, the acquisition times are long (≈ 30 min) which increases the chance for image blurring and other artifacts caused by patient motion.

The major developments in radionuclide imaging instrumentation have been the Anger camera and the PET scanner. They are today the primary imaging tools used in nuclear medicine. Below is a description of these imagers and of some of the associated techniques where they are used.

2.3.1 The Anger camera

The gamma camera was introduced in the late 1950s by Hal O. Anger and it became also known as the Anger camera¹. In its basic components it remains very similar today to the original concept proposed more than 40 years ago. Its excellent characteristics as a gamma ray imaging device has kept it the imager of choice until the present day, despite many attempts to produce other imagers with better characteristics.

The major components of an Anger camera are depicted in figure 2.1. One side of a large slab of NaI(Tl) is coupled to an array of close-packed PMTs. When a gamma ray interacts in the crystal, it produces a light signal which is distributed over many PMTs. The relative signals of the PMTs provide the information necessary to calculate the centroid of the light distribution, and therefore give an estimate of the position of interaction of the gamma ray in the crystal. The sum of all the PMT signals gives the energy signal, which is proportional to the energy of the incident gamma rays. The other side of the scintillator is coupled to a gamma ray collimator, typically made of lead. The collimator defines the angle of incidence of gamma rays on the crystal, providing a projection of the object onto the crystal along a given direction. The characteristics of the collimator contribute very significantly to the overall performance of the camera, in particular to the spatial resolution, to the gamma ray counting efficiency and to the size of the field-of-view. The whole system is surrounded by a lead shield to minimise background from radiation sources outside the field-of-view of the camera.

Gamma ray collimators

The four basic types of Anger camera collimators are the *parallel-hole collimator*, the *pin-hole collimator*, the *diverging collimator* and the *converging collimator* (figure 2.2). Since the collimation is done by absorption of gamma rays, the collimator should be made of a high Z and high density material. Lead is the usual choice although in some cases other materials like tungsten are also used.

The *parallel-hole collimator* is the most widely used, and in the discussions throughout this thesis, a parallel-hole collimator is assumed, except where otherwise stated. The holes, usually circular, hexagonal or square, are drilled or cast in lead or shaped from lead foils which are then stacked

¹In the context of this thesis, gamma camera is used to describe any single photon emission gamma ray imager while Anger camera is used for the original design by Hal O. Anger, which is still the imager of choice in the overwhelming majority of nuclear medicine imaging examinations.

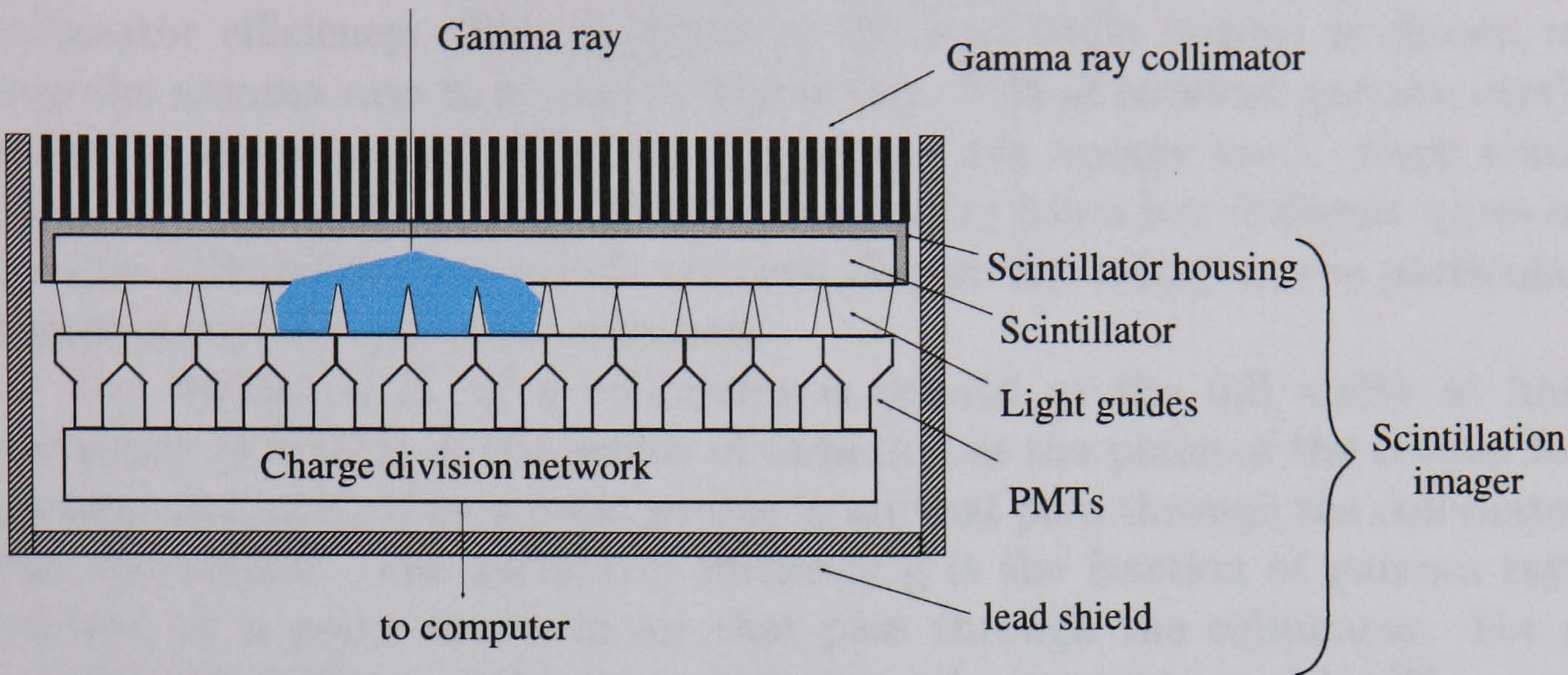


Figure 2.1: Diagram of an Anger camera.

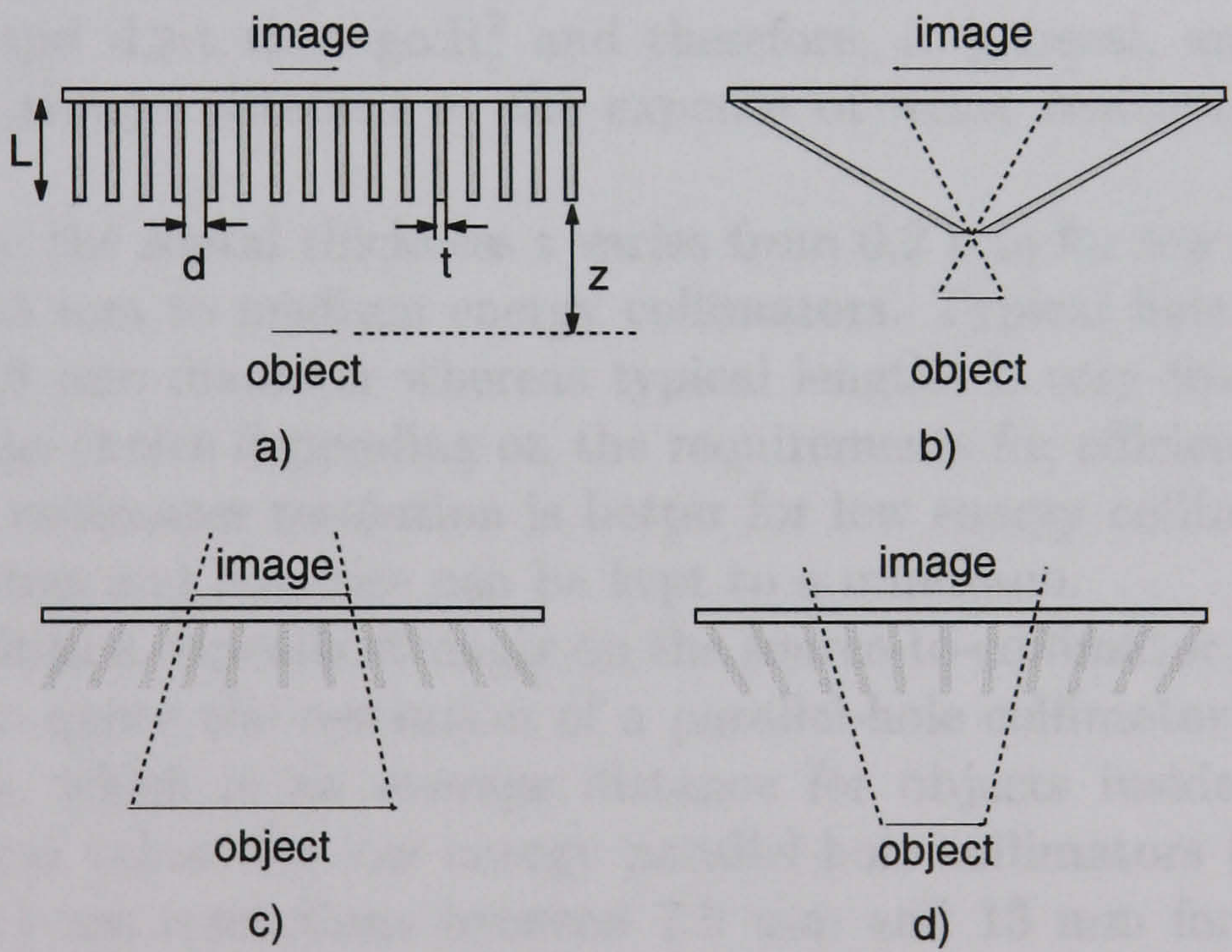


Figure 2.2: Cross-sectional views of the four basic types of Anger camera collimators : a) parallel-hole, b) pin-hole, c) diverging and d) converging.

together. The dimensions of the holes determine the two most important characteristics of the collimator: the collimator spatial resolution and the collimator efficiency. The thickness of the lead walls (septa) is chosen to stop the gamma rays to a certain degree (e.g. 95% of incident gamma rays), and it is therefore dependent on the gamma ray energy used. Each clinical site performing radioisotope imaging usually has a few different types of parallel-hole collimators, which are then chosen depending on the particular requirements of a given examination.

The resolution R_c of a collimator is defined as the full width at half maximum (FWHM) of the profile of radiation at the plane of the crystal for gamma rays emitted by a point source in air that pass through the collimator into the crystal. The geometric efficiency g is the fraction of gamma rays emitted by a point source in air that pass through the collimator. For a parallel-hole collimator these parameters can be approximated by [6]:

$$R_c \simeq \frac{d(L+z)}{L} \quad ; \quad g \simeq \left[\frac{Kd^2}{L(d+t)} \right]^2 \quad (2.2)$$

where d , L , t and z are defined in figure 2.2 and K is a constant depending upon the shape and configuration of the holes (e.g. ~ 0.26 for hexagonal holes in a hexagonal array).

If $z \gg L$ and $d \gg t$ then $g \propto R_c^2$ and therefore, in general, an increase in efficiency is always obtained at the expense of worse resolution and vice-versa.

Typically, the septal thickness t varies from 0.2 mm for low energy collimators to 1.5 mm to medium energy collimators. Typical hole sizes d vary from 2 to 3.5 mm diameter whereas typical lengths L vary from 1.5 cm to over 3 cm, the choice depending on the requirements for efficiency and resolution. The collimator resolution is better for low energy collimators where septal thickness and hole size can be kept to a minimum.

The resolution depends strongly on the source-to-collimator distance and it is usual to quote the resolution of a parallel-hole collimator for a source 10 cm away, which is an average distance for objects inside the human body. Typical values for low energy parallel-hole collimators (energies below 150 keV) are resolutions between 7.5 mm and 13 mm for a source at 10 cm and efficiency between 0.02% and 0.06% [3].

Clearly, to take full advantage of the imager, the source-to-collimator distance should be minimized. For distances of less than 3 cm, for example, a collimator resolution of less than 3.5 mm is achievable, using high resolution parallel-hole collimators, with a resolution of approximately the hole diameter (1.5-2 mm) for sources at the face of the collimator.

A different type of parallel-hole collimators is the slant-hole collimator in which the holes are slanted with respect to the crystal plane. These collimators are usually chosen for convenience of positioning close to the object or to obtain more favorable views.

The *pin-hole collimator* consists of a small aperture in lead. It produces an inverted image of the object with a variable magnification (or minification) depending on the source-to-collimator distance. Therefore, for three dimensional objects some distortions are introduced due to the variable depth of the points of radiation emission. These collimators are mainly used to obtain magnified images of small organs (e.g. thyroid), with the collimator very close to the object. They provide excellent spatial resolution but lower efficiency than the other types of collimators.

Diverging collimators are useful to obtain minified images of objects larger than the size of the useful camera area and are mainly used with small area cameras. The holes usually converge at a distance of 40-50 cm behind the collimator. As with the pin-hole collimator, the level of minification varies with the source-to-collimator distance, which introduces some image artifacts. They have worse resolution and lower efficiency than parallel-hole collimators.

Converging collimators produce magnified non-inverted images if the object is between the collimator and the convergence point (see figure 2.2), which is usually 40-50 cm in front of the collimator. It is unusual to image objects at greater distances, where inversion and even minification may occur. Again, they have magnification dependency on source-to-collimator distance. They are mainly used to image small objects with large cameras, providing higher efficiency and better resolution than parallel-hole collimators.

A particular type of converging collimator which is often used is the *fan beam* collimator. It is particularly used in single photon emission computed tomography (SPECT) where an Anger camera rotates around the patient. The holes are aligned as in a converging collimator along the transaxial direction and as in a parallel hole collimator along the axis of rotation.

Scintillation crystals

Since their invention and up to the present day, Anger cameras use NaI(Tl) scintillators in large slabs (e.g. 40 cm diameter). NaI(Tl) is highly hygroscopic and it must be encapsulated to prevent damage from moisture. It is usually encapsulated in an aluminium can with a transparent (glass) window on one side. The inner surface of the protective can is usually coated with a diffuse reflector to re-direct some of the isotropically generated photons out of the crystal and into the PMT array.

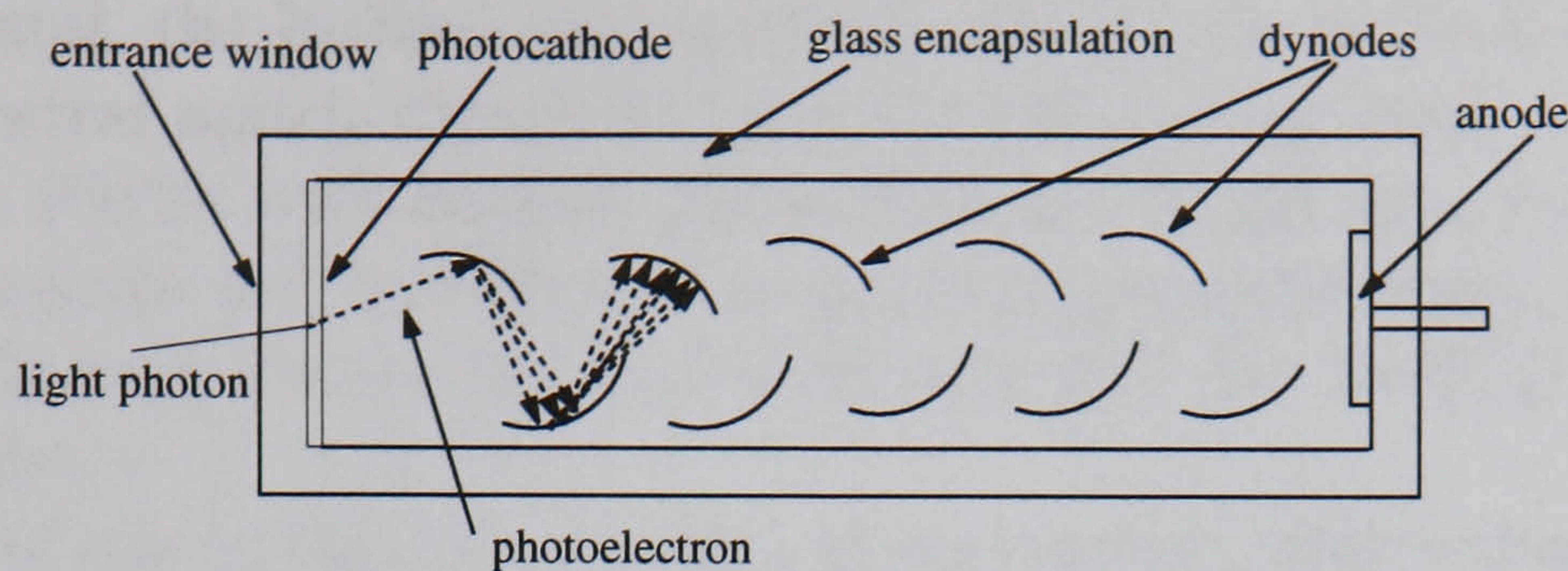


Figure 2.3: Schematic of a photomultiplier tube.

The thickness of the crystal has a direct impact on the detection efficiency and on the intrinsic spatial resolution R_i of the scintillation imager shown in figure 2.1 (R_i is defined in section 2.3.2). The thickness of the crystal in most cameras takes into account the fact that most studies are performed with Tc^{99m} which emit 140 keV gamma rays. Therefore, a thickness between 9 and 13 mm is common, which absorbs over 90% of 140 keV gamma rays. In some cases, and to improve intrinsic spatial resolution, 6 mm thick crystals are used, which is still considered adequate with an 80% efficiency for 140 keV gamma rays [6].

NaI(Tl) has a high light yield and its emission spectrum matches well the spectral response of PMT photocathodes. As shown in figure 2.1, the crystal may be coupled to the active areas of the PMTs using light guides to optimize the light collection. Optionally or additionally, a simple continuous light spreader may be used to spread the light over a minimum number of PMTs in order to obtain the desired signal sharing which provides the spatial information. Also, to optimise the light collection, all components are coupled together with silicone grease or oil.

Photomultiplier tubes

Photomultiplier Tubes (PMT) are photosensitive devices with a charge multiplication stage, which provides detection of light photons with a high signal-to-noise ratio. The principle of operation of the PMT is illustrated in figure 2.3.

It consists of a vacuum-sealed tube usually made of glass. A photosensitive material, the *photocathode*, is deposited on the inner surface of the *light entrance window*. The photocathode is usually a compound semiconductor with a low work function. Its properties determine the spectral sensitivity of the PMT, which should match the emission spectrum of the light source (e.g. scintillation light from an inorganic scintillator). When coupled to a

NaI(Tl) crystal, the bialkali photocathode (Sb-Rb-Cs or Sb-K-Cs) provides the best spectral match (figure 3.1) and for this reason most modern Anger cameras use PMTs with bialkali photocathodes. Light photons incident on the photocathode are converted into primary photoelectrons, with typical quantum efficiency values between 15% and 25% for NaI(Tl) and bialkali photocathodes.

A series of electrodes, the *dynodes*, at successively high voltage potentials make up the charge multiplying stage. The primary photoelectrons are accelerated towards the first dynode where they deposit their kinetic energy. The dynodes are covered by a layer of a secondary emissive material, which releases a number of secondary electrons depending on the kinetic energy of the incident electrons. This process is repeated in a number of stages until the desired charge amplification is achieved. Typical numbers of dynodes are between 6 and 14, with gains between 10^4 and 10^7 . The voltage differences between the photocathode and the first dynode, and between each dynode, is about 100 V. The large signal collected by the anode, even for single photoelectrons, provides a high signal-to-noise ratio using relatively simple readout electronics.

Although during the last decade a wide range of position sensitive photomultiplier tubes have become available (see section 3.2), Anger cameras use single anode PMTs, with no intrinsic position sensitivity. The position information is obtained by close-packing a matrix of PMTs, which is coupled to a single large slab of scintillator. The scintillation light spreads over the PMTs and the relative amount of charge collected at each PMT anode provides the information needed to estimate the position of interaction of the gamma rays on the crystal.

Photomultiplier tubes are available in a variety of sizes and shapes. The most widely used in Anger cameras have circular or hexagonal shaped entrance windows, allowing close packing in a hexagonal pattern as shown in figure 2.4. The size of the PMT is usually a compromise between factors involving performance and cost. Using a large number of small tubes provides the best spatial resolution, but at a significant cost - the cost of PMTs is lowest for “medium sized” tubes, with a diameter of 3-7 cm.

Typical figures in modern cameras are 61 to 91 tubes with 3 to 5 cm diameter (or 3 to 5 cm between opposite sides in hexagonal tubes), in Anger cameras of about $40 \times 40 \text{ cm}^2$.

Readout electronics and image reconstruction

The signals from the PMT matrix are connected to a charge division network of resistors or capacitors, as shown for the simple case of 7 tubes with a

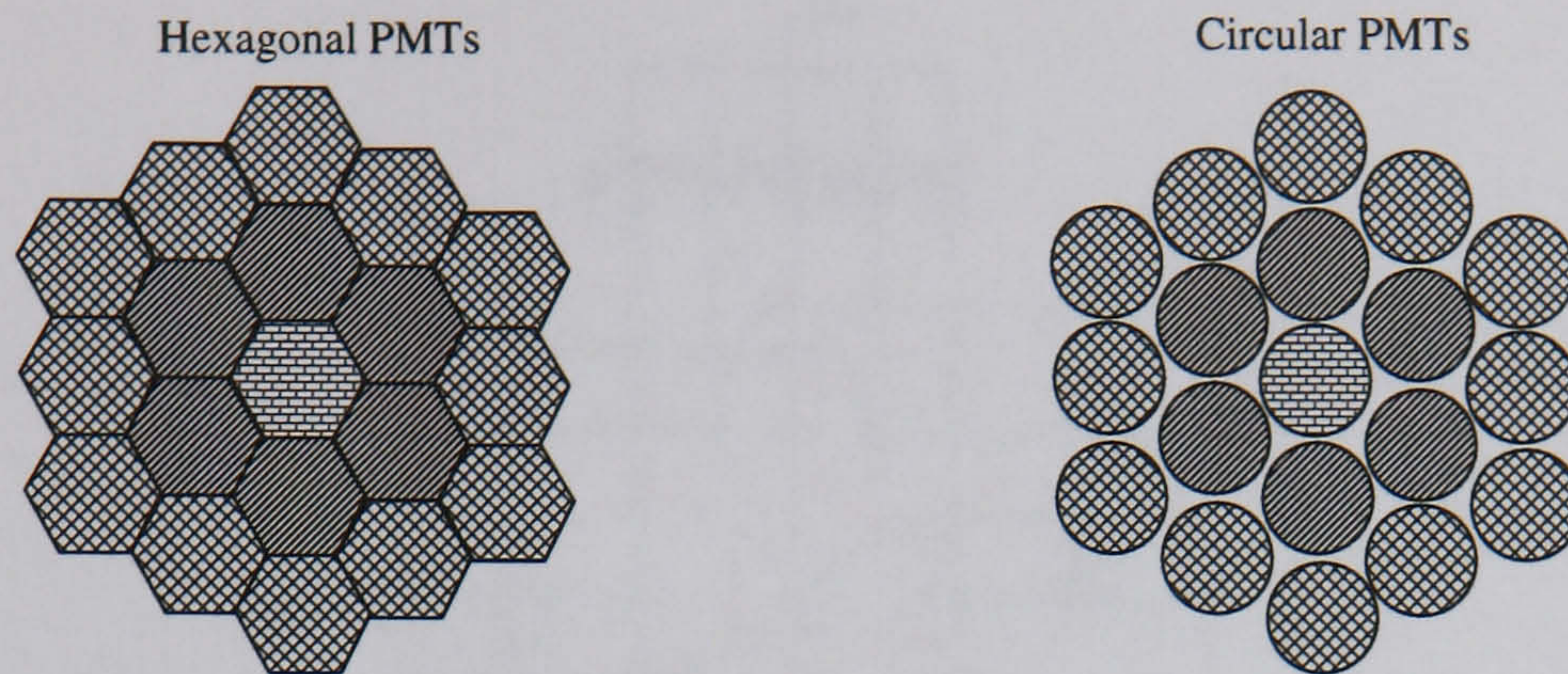


Figure 2.4: Arrangements of close-packed PMT matrices with circular and hexagonal PMTs.

resistor network in figure 2.5. The network has 4 output values, X^- , X^+ , Y^- , Y^+ , corresponding to the two directions, x and y , of interest. For each direction (e.g. x), the difference between the two signals (e.g. $X^- - X^+$) is proportional to the position of the centroid of the distribution of charge on the PMTs, which in turn, reflects the distribution of light created by the gamma ray interaction. Therefore, in its simplest form, the position readout requires two basic subtractions to provide an estimate of the position of interaction of the gamma ray in the crystal:

$$x = k(X^- - X^+) \quad ; \quad y = k(Y^- - Y^+). \quad (2.3)$$

Essentially, this centroid calculation is a weighted sum of the signals of the PMTs in each direction. This centroid estimator assumes a uniform response of all PMTs which in practice is not achievable, leading to position distortions in the reconstructed image. Several correction methods are introduced. The gains of the PMTs may be adjusted after a calibration with LED flashes. Another technique is the generation *a priori* of high-statistics uniformity correction maps, which can be used as look-up-tables to correct the clinical images.

The sum of all 4 signals provides the energy signal E :

$$E = X^+ + X^- + Y^+ + Y^- \quad (2.4)$$

During the data acquisition, a window is selected around the pre-calibrated position of the peak corresponding to the original energy of the gamma rays. Only for events falling inside this energy window are the positions x and y recorded in the image. This avoids random noise from gamma rays inelastically scattered inside the body that reach the scintillator (figure 2.6).

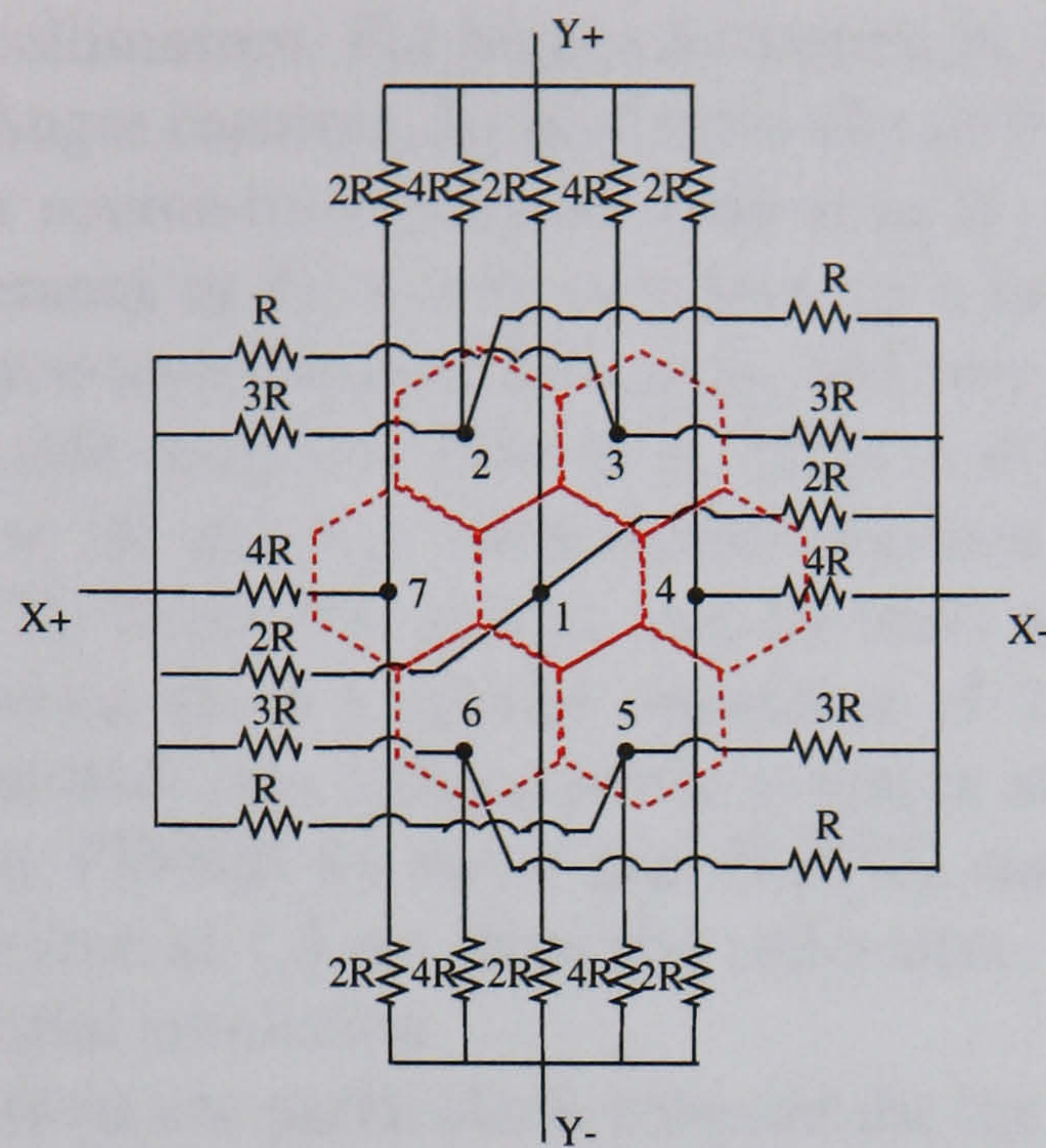


Figure 2.5: Simplified example of a resistor network readout of 7 PMTs.

2.3.2 Performance of the Anger camera

The performance of an Anger camera is determined by the characteristics of its two major components: the collimator and the *scintillation imager*. As depicted in figure 2.1, the scintillation imager is the camera without the collimator, i.e., the scintillator, the PMTs, the electronics, etc.

Spatial resolution

The spatial resolution R of an Anger camera is defined as the FWHM of the distribution of centroids² for a point source of gamma rays in air at a given distance from the collimator³.

The overall resolution of the Anger camera is a convolution of two independent contributions: the collimator resolution R_c and the intrinsic resolution R_i of the scintillation imager:

$$R^2 = R_c^2 + R_i^2. \quad (2.5)$$

It was mentioned above that R_c depends strongly on the source-to-collimator distance, and that for distances of less than 3 cm, R_c is less than 3.5 mm FWHM

²The centroids are calculated using equations 2.3

³Note that the *lower* the value of R the *better* the resolution, which is sometimes referred to a *higher* resolution. This ambiguity is avoided whenever possible.

for high resolution collimators. For bigger distances, R_c increases very significantly. In modern Anger cameras, R_i is of the order of 3 mm FWHM [7, 8, 9]. Therefore, for large source-to-collimator distances, R_c is the dominant factor and an improvement in R_i would only lead to a marginal improvement in R . For short source-to-collimator distances, however, improvements in R_i may lead to noticeable improvements in R . This is illustrated in the work by H.D. Royal *et al* [9] where a comparison between two Anger cameras with different NaI(Tl) thickness (6 mm and 13 mm) was carried out. The 13 mm NaI(Tl) camera gives a spatial resolution of 3.2 mm FWHM with a high-resolution parallel-hole collimator for a source at the collimator face, compared to 2.5 mm FWHM for the 6 mm NaI(Tl) camera under the same conditions. For a source at 7.5 cm from the collimator, both cameras gave a 4.8 mm FWHM spatial resolution.

These considerations are particularly relevant for the development of compact, application-specific gamma ray imagers, which is the main subject of this thesis. A dedicated breast imaging camera, for example, may be positioned very close to the object, perhaps even using moderate breast compression to minimize the object-to-collimator distance. In this case, an improvement in the intrinsic resolution R_i may provide a better overall resolution R .

The intrinsic resolution R_i of a scintillation imager at a given gamma ray energy is usually defined as the FWHM of the distribution of centroids for a pencil beam of gamma rays impinging on the scintillator.

Barrett and Swindell [10] have shown that, for a scintillation imager using a centroid estimator, the width of the distribution of centroids along a given direction, has two main dependencies:

Light distribution. The spatial resolution R_i is proportional to the width of the light distribution over the PMTs. This is mainly dependent on the thickness of the scintillator and of the light spreader. The thickness of the scintillator has a minimum acceptable value which is determined by the detection efficiency. For 140 keV gamma rays, a minimum thickness of 6 mm of NaI(Tl) is used. The thickness of the light spreader is such that the width of the light distribution is enough to encompass 3-5 PMTs in each direction, to allow an accurate centroid calculation.

Number of photoelectrons generated. The spatial resolution R_i is inversely proportional to the square root of the number of photoelectrons generated in the PMTs. This depends mainly on the gamma ray energy, on the scintillator light yield and on the spectral match between the emission of the scintillator and the photocathode sensitivity.

J.W. Scrimger *et al* [11] measured the light distribution from a 13 mm thick NaI(Tl) crystal coupled to a 2 cm thick light spreader by coupling a photographic film to the other side of the light spreader. A collimated beam of 70 keV x-rays impinging on the crystal produced a light distribution of about 6 cm FWHM at the sheet of film.

High resolution cameras use small PMTs (3 cm diameter or less) and thin scintillator-spreader combinations (6-9 mm thick NaI(Tl) and 1-2 cm thick spreader).

The use of NaI(Tl) coupled to PMTs with alkali photocathodes is the standard choice in Anger cameras to obtain a high number of photoelectrons. For 140 keV, for example, a mean number of 4,200 photons are generated for a full gamma ray deposition event. These photons either directly hit the PMTs or are reflected inside the scintillator capsule and re-directed out through the light window. With efficient reflectors and assuming a 25% photocathode quantum efficiency, a total of the order of 1,000 photoelectrons is usually generated in a full gamma ray absorption.

The intrinsic resolution of the scintillation imagers in modern high resolution Anger cameras is about 3-4 mm FWHM, for 140 keV gamma rays. For higher gamma ray energies, the scintillator must be thicker, for detection efficiency reasons. This however is compensated for by the higher number of photoelectrons generated. Nevertheless, the overall spatial resolution of the Anger camera is much worse for higher energies due to the worse collimator resolution.

Energy resolution

The energy resolution of an Anger camera determines its ability to reject gamma rays which undergo Compton scattering in the body before hitting the scintillator. These events (figure 2.6) lose the information about the original position of gamma ray emission and therefore would add random noise to the image.

The energy resolution of a scintillator-PMT module depends on the number of photoelectrons generated at the photocathode as well as on the intrinsic resolution of light emission process in the scintillator. The factors affecting the energy resolution in these types of detectors are described in detail in appendix A. The energy resolution of modern Anger cameras is about 9-10% FWHM for 140 keV gamma rays.

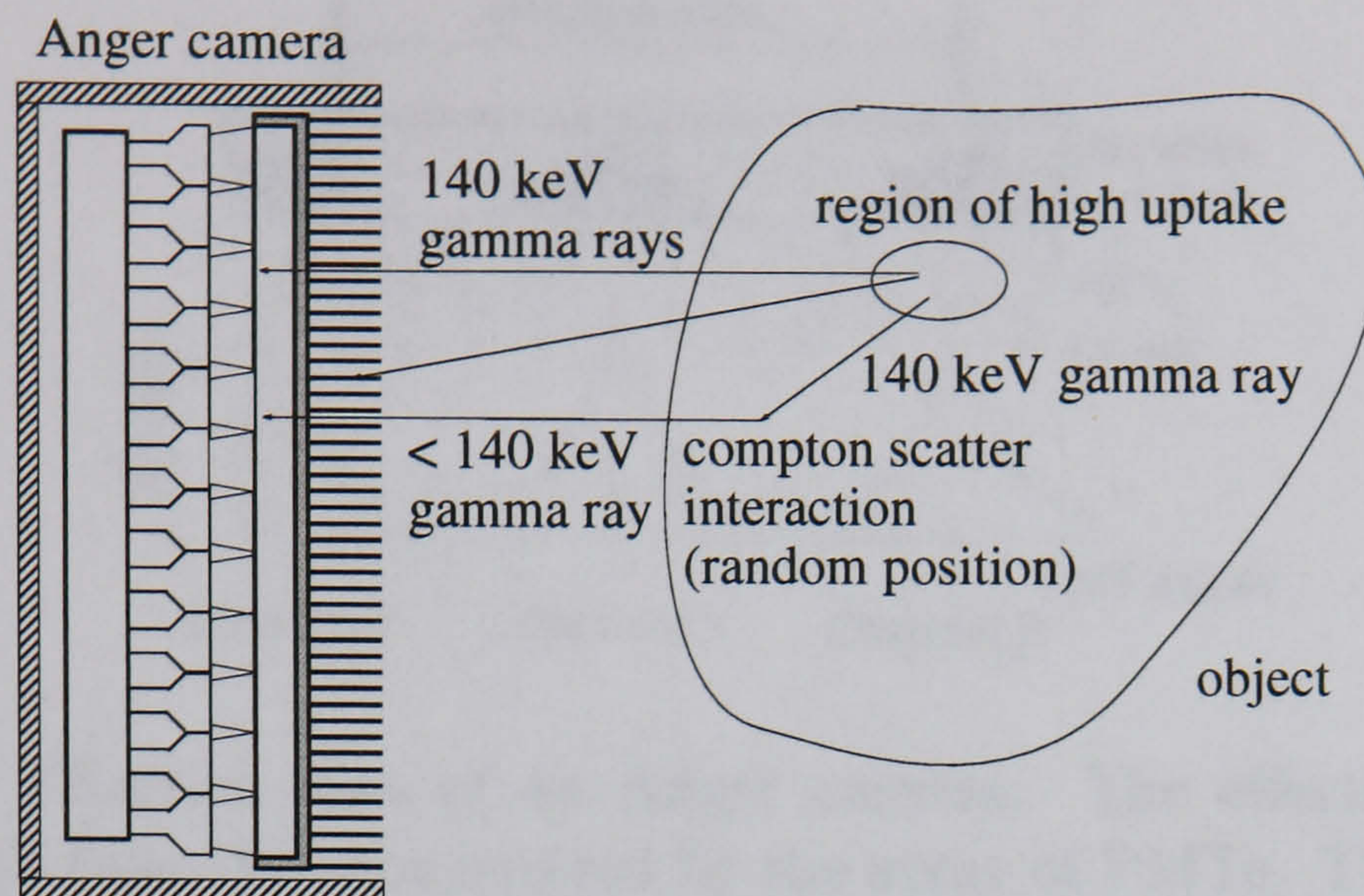


Figure 2.6: Diagram showing the need to reject gamma rays scattered in the body.

Detection efficiency

The overall efficiency of an Anger camera is mainly determined by the collimator efficiency, which is in the order of 0.02% to 0.06%. The efficiency of the scintillation imager is determined by the thickness of the scintillator and the energy of the gamma rays. A value of 80% or greater is usually acceptable [3].

In each clinical situation, a compromise between spatial resolution and efficiency has to be made, which is reflected in the choice of collimator. Higher efficiency gives more counts in the image in less acquisition time. The better image statistics may result in higher quality images compared to the ones obtained with a collimator with better spatial resolution but lower efficiency [12].

Camera size and field of view

The physical size of an Anger camera is determined by the size of the NaI(Tl) crystal and of the array of PMTs. Most cameras are about 40 cm diameter. The effective area of the camera is the area which is used for imaging. This is usually considerably smaller than the physical size. The reason for this is the presence of an outer ring of PMTs outside the usable imaging area. These PMTs are used to sample the light distribution for events occurring in inner parts of the camera only.

The centroid estimator assumes a symmetric charge distribution over the

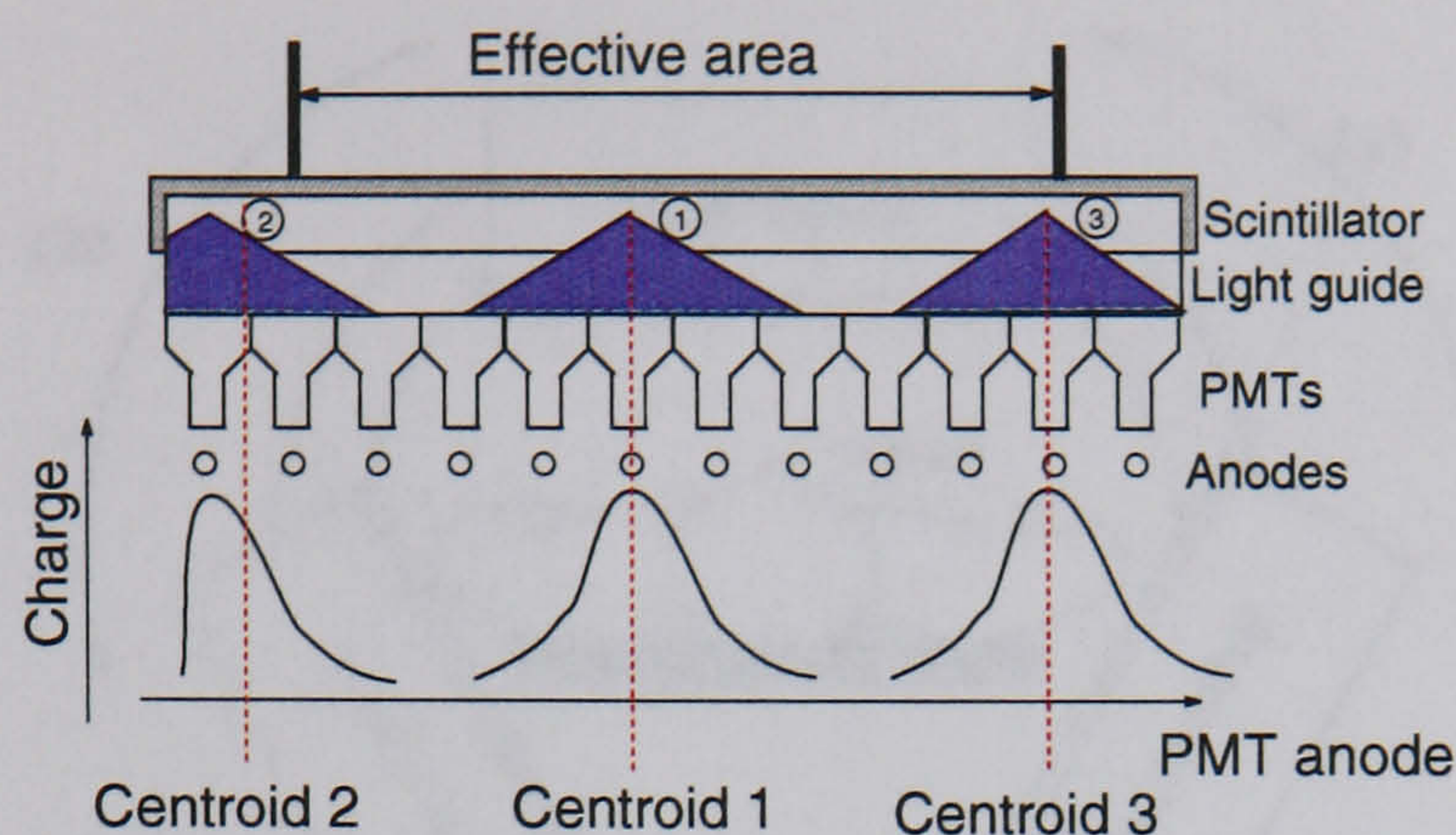


Figure 2.7: Effective area of an Anger camera. The effective area of the camera is less than the area covered by the array of PMTs. The outer ring of tubes is used only to centroid events occurring above the penultimate ring or further inside (events 1 and 3 in the picture). For events over the outer ring, a pronounced non-symmetric charge distribution would lead to a distortion in the centroid calculation and the position would be shifted towards the central region of the camera (event 2).

PMTs as illustrated in figure 2.7. For events occurring near the edges, the light distribution, and the corresponding charge distribution, are truncated and the centroid calculation shifts the reconstructed position towards the center of the camera (event 2 in the figure). This causes an outer ring of high intensity dots in the image, an effect sometimes referred to as *edge-packing* [13, 14]. The dead area around the edges is about the size of one PMT side-to-side, which is normally between 3 and 5 cm.

The field-of-view of the camera is the size of the imaged area on the object plane. It is determined by the type of collimator used. For parallel-hole collimators, there is a one-to-one relationship between the camera effective area and the field-of-view, whereas other types of collimators may provide a field-of-view larger than the camera effective size, through image minification, or smaller through magnification.

2.3.3 Single Photon Emission Computed Tomography

Single photon emission computed tomography, SPECT, is a nuclear medicine imaging technique that uses the Anger camera to obtain three dimensional images. The camera rotates around the object recording a set of two dimensional planar images. The images are combined in tomographic reconstruction algorithms to produce a three dimensional map of the radioisotope distribution.

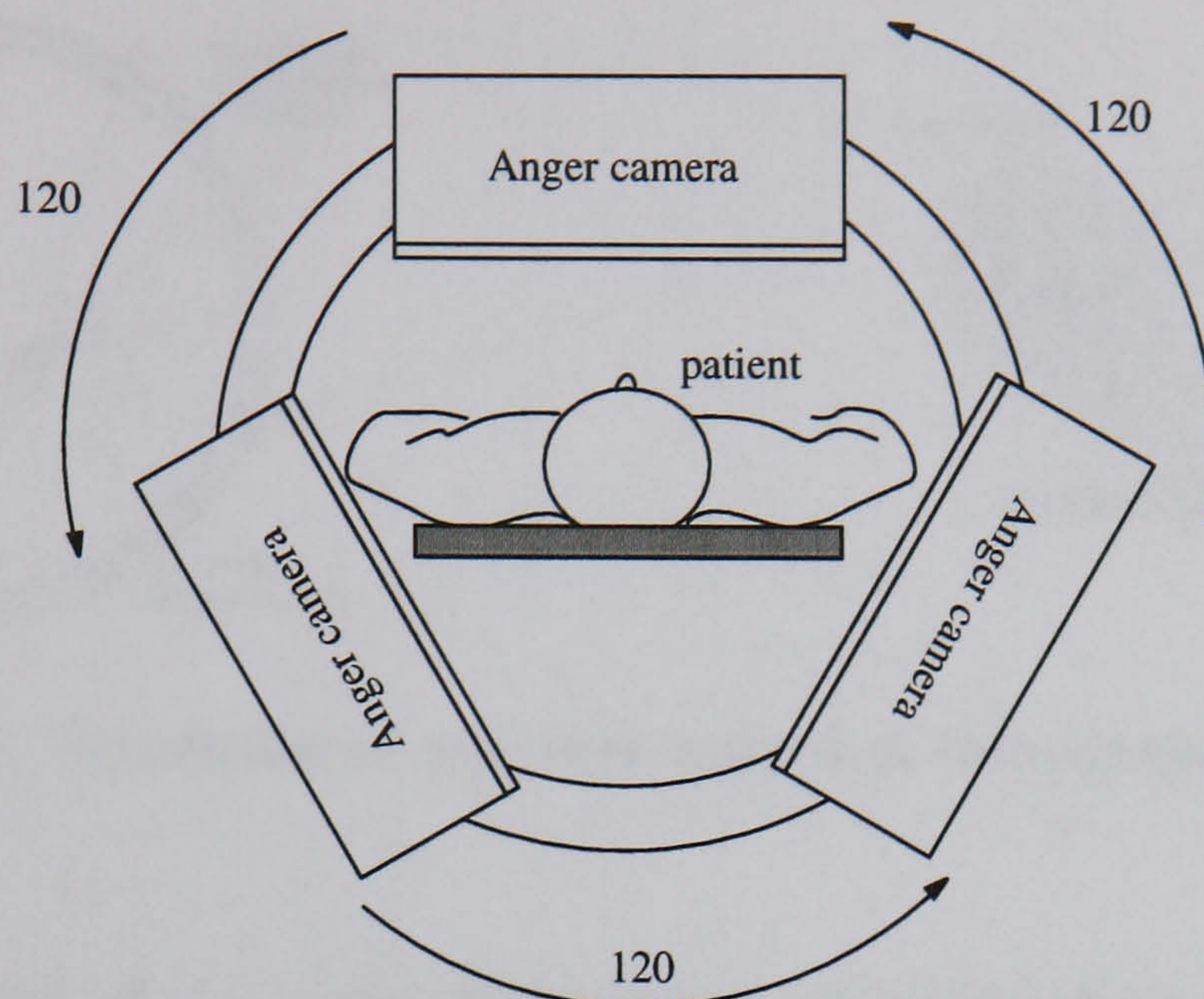


Figure 2.8: SPECT system with three Anger cameras in a rotating gantry.

Usually 60 to 120 projections are acquired, each taking about 30 seconds. The poor sensitivity of the Anger camera often introduces problems due to low statistics in the image. The acquisition times are determined by the maximum dose given to the patient and to the maximum time expected for patient comfort and immobility. To increase the sensitivity, modern SPECT systems are equipped with 2 or 3 Anger cameras (figure 2.8).

SPECT employs well established techniques associated with planar imaging with Anger cameras, such as the same radiopharmaceuticals and the same detectors. It has therefore found widespread use in nuclear medicine imaging centers.

2.3.4 Positron Emission Tomography

The principles of positron emission tomography imaging are illustrated in figure 2.9.

The positrons emitted inside the patient travel a short distance, usually less than 2 mm, before annihilating with an electron in the surrounding matter, generating a pair of back-to-back 511 keV gamma rays. The coincident detection of these gamma rays defines a line along which the annihilation occurred. The emission of gamma rays is isotropic, and therefore, a ring of several detector modules detects annihilations along several lines the intersection of which defines the original point of positron emission. As in SPECT, a tomographic reconstruction algorithm generates a three-dimensional map

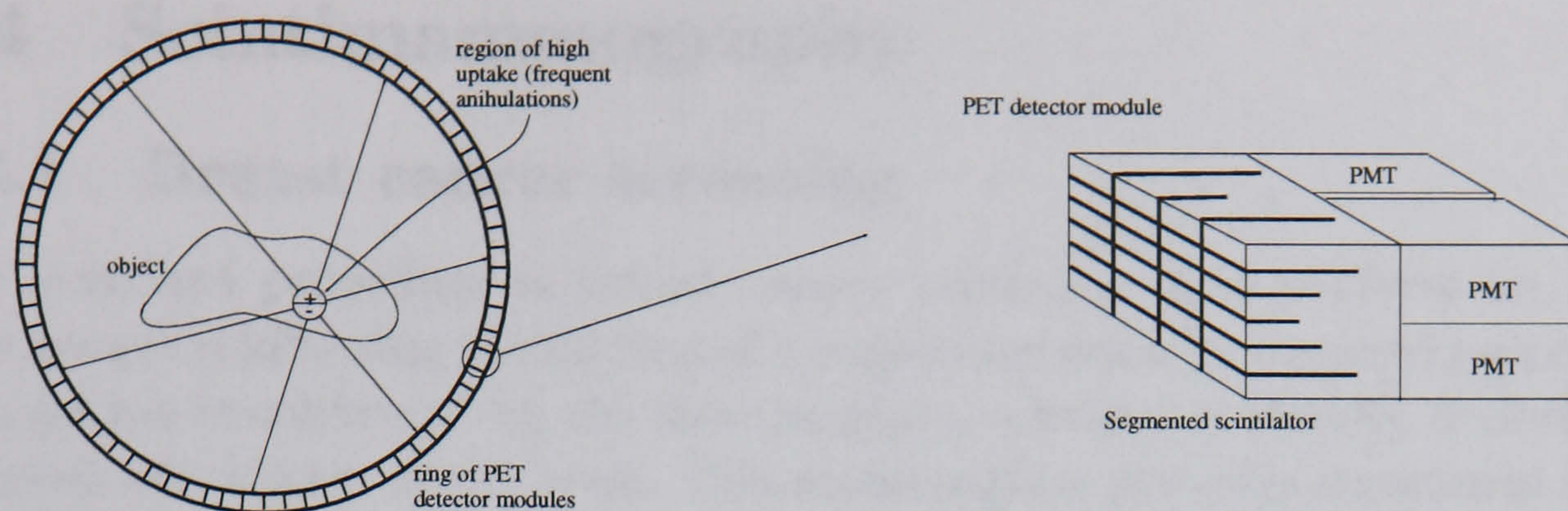


Figure 2.9: Principles of positron emission tomography imaging.

of the distribution of the radiopharmaceutical inside the body.

PET rings are traditionally made of modules of segmented BGO scintillators coupled to PMTs. BGO has higher density and higher effective atomic number than NaI(Tl), providing higher conversion efficiency for 511 keV gamma rays. A typical PET module is shown in figure 2.9. The crystal segmentation is done with variable depth slits which provide a light-sharing scheme between the PMTs. A charge division centroid calculation determines the segment where the gamma ray interaction occurred. The segment widths along the transaxial orientation are usually of 2-3 mm.

The coincidence technique determines the original point of emission of the positrons without the need for the collimators used in single photon emission imaging.

Compared to single photon emission imaging, PET has a better performance. It provides a higher overall counting efficiency and a spatial resolution of about 2-3 mm FWHM.

The major disadvantage of PET is its high cost. The detector system and the production of the positron emitters are very expensive and therefore only a few clinical centers can afford this technique. Another advantage of single photon emission imaging compared to PET is the wider variety of radiopharmaceuticals available for the former, which is a result of the long term use of this technique.

In some cases, dual-head gamma cameras are used as PET detectors. The cameras are aligned facing each other, with the collimators removed, and a coincidence technique is employed as described above, providing a relatively low cost option for PET imaging.

2.4 Scintimammography

2.4.1 Breast cancer screening

The standard procedure in breast cancer screening is to perform an x-ray mammogram following the finding of a suspicious mass by physical palpation. If suspicion is confirmed by the mammogram, a biopsy is usually undertaken to assess the nature of the mass. The mammogram provides structural information on the size, location and shape of the lump with an excellent accuracy within a few tens of a micron. It provides a high ($\geq 80\%$) sensitivity to breast cancer, defined as the number of true positive findings divided by the total number of non-malignant cases.

However, x-ray mammography does not provide much information about the nature of the object found. For this reason, the majority ($\sim 80\%$) of the biopsies performed after a suspicious x-ray mammogram reveal a non-malignant structure [15, 16]. This is also expressed as a low specificity to malignancy, defined as the number of true negative findings divided by the total number of non-malignant cases. This large number of “unnecessary” biopsies causes significant physical and psychological distress to the patients.

Moreover, some women have radiodense breasts, which means that their breast tissue is “opaque” to the usual x-ray energies used in mammography. In these cases, x-ray mammography does not provide useful information even at a structural level.

In view of these considerations, there is clearly a need for a non-invasive diagnostic technique with high sensitivity and high specificity for detection of breast cancer.

2.4.2 Scintimammography trials

Tc^{99m} -MIBI has been shown to have a high specificity for detection of breast cancer, which has lead to several scintimammography trials [15, 17, 16]. These studies have been performed with standard Anger cameras and have shown that scintimammography has a sensitivity similar to x-ray mammography, for tumours larger than 1 cm diameter, and a much better specificity of over 85%. There is however a strong dependency of sensitivity on tumour size. For non-palpable tumours of less than 1 cm diameter, the sensitivity is poor, which can be attributed to a poor uptake of Tc^{99m} -MIBI and to a poor imaging technique. Other radiopharmaceuticals have been investigated [18] promising further improvements in the specific uptake of malignant breast tumours in the near future.

The possibility of detecting axillary lymph node metastases with the same

technique has also been studied in several trials [5, 19]. Again, the results are found to be dependent on the size of the metastatic masses.

Contrary to x-ray mammography, the results of scintimammography have not been found to be affected by breast density [20] which gives a useful diagnosis option in those cases.

The detection of small masses is very important to improve survival rates, which are strongly linked to successful diagnosis at the early stages of the disease. It is therefore important to improve the spatial resolution and the detectability of small tumours, either by improving the imaging technique or by developing new, highly specific radiopharmaceuticals. The former is the basis for the investigation described in this work.

2.4.3 Problems in scintimammography imaging

One of the major problems of scintimammography with standard Anger cameras is the difficulty in obtaining the optimum projection. This is due to the size of the Anger camera which makes it difficult and sometimes impossible to position the camera close to the breast. Furthermore, the large dead regions around the edges of the camera (see figure 2.7) also makes certain projections impossible. This is illustrated in figure 2.10 where the edge of the camera is positioned against the chest wall. In this case, the dead region of about 5 cm impairs the detection of tumours deep inside the breast.

The correct positioning of the camera has two main advantages:

Proximity to object As discussed above, the source-to-collimator distance significantly affects the spatial resolution of the Anger camera, and therefore its ability to detect small tumours.

Avoiding background emission In typical clinical examinations there is a very high uptake of Tc^{99m} -MIBI by the liver ($\sim 20\%$), heart ($\sim 1.2\%$) and lungs ($\sim 1.5\%$) [2], compared to breast tumour uptake which may be 1,000-10,000 times lower than in the liver. It is therefore very important to avoid projections that include emission from those organs, which can overshadow the much fainter emission from the tumours.

2.4.4 The need for new imagers for scintimammography

A compact gamma camera, with small dead areas around the edges would clearly be beneficial. This has been suggested by researchers [18, 21] involved in scintimammography trials with Anger cameras after facing some of the

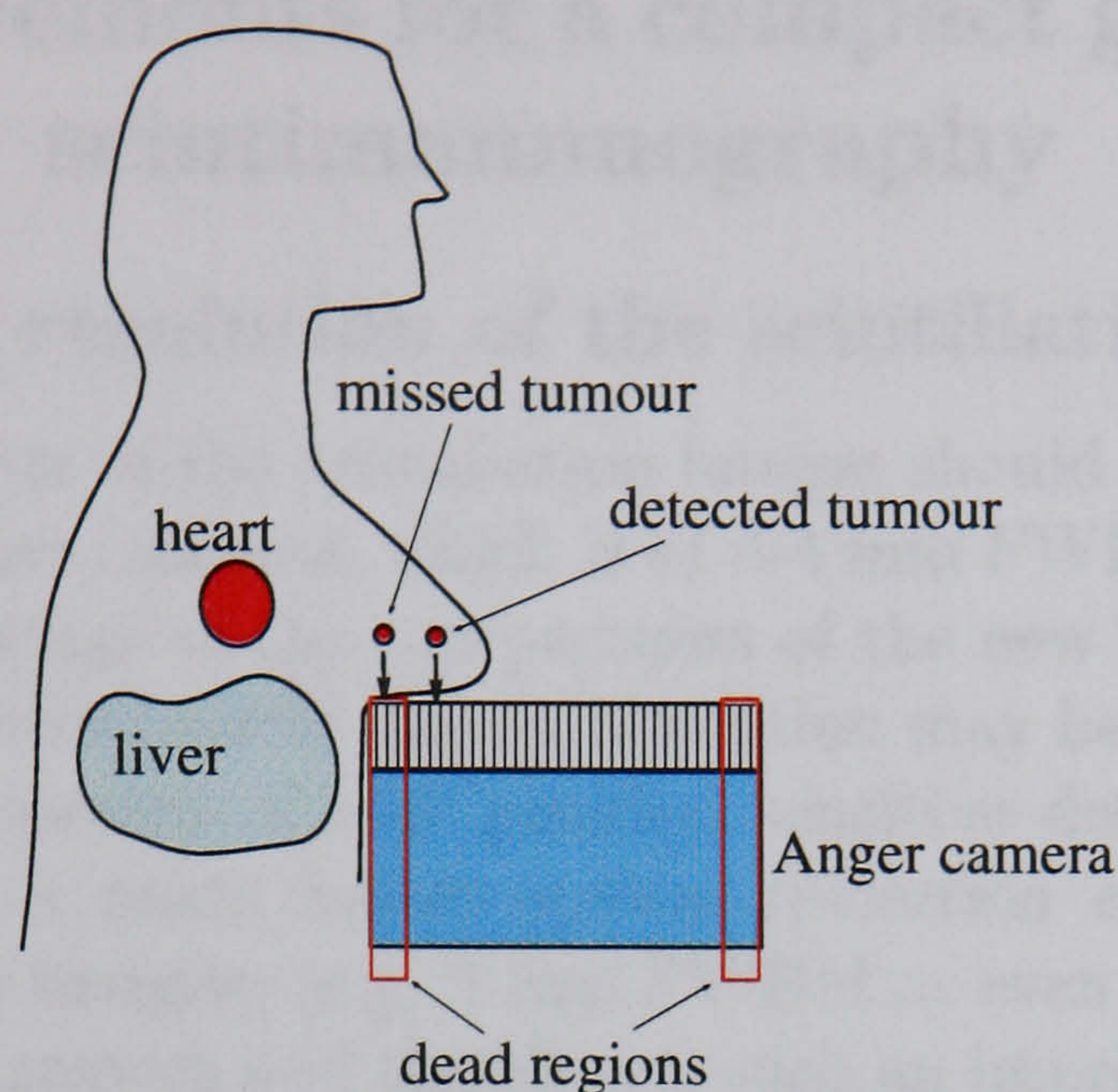


Figure 2.10: Diagram showing the importance of small dead areas at the edges to enable the detection of tumours deep inside the breast in scintimammography.

above mentioned problems in detecting small (≤ 1 cm diameter) tumours. Furthermore, if closer proximity to the object is achieved together with an improvement in the intrinsic spatial resolution of the scintillation imager, it is likely that the overall spatial resolution obtained in scintimammography can be improved even further.

There are many ongoing research efforts dedicated to the development of compact gamma cameras with better spatial resolution than the Anger camera, as described in the next chapter. Some preliminary clinical trials and phantom studies have demonstrated the usefulness of these new detectors to detect small tumours [2, 1]. In particular, Scopinaro *et al* [1] compared images obtained with an Anger camera and with a compact, high resolution application-specific gamma camera for tumours of less than 1 cm diameter. Taking advantage of the compactness of the application-specific camera, the positioning around the object was optimized which, together with the better spatial resolution of this imager, gave a better sensitivity (81%) compared with the conventional Anger camera (50%).

2.5 Requirements for a compact gamma camera for scintimammography

2.5.1 Spatial resolution of the scintillation imager

The spatial resolution of the scintillation imager should be at least equal to that of modern Anger cameras, which is of 3-4 mm FWHM. In this case, by simply taking advantage of the compactness of the new imager to get closer to the objects, a better overall spatial resolution may be obtained.

With the development of new position sensitive detectors, it has been demonstrated that a much better spatial resolution can be achieved for 140 keV gamma ray imaging (e.g. 1 mm FWHM or even less). For short distances between the camera and the object, such an improvement would have a significant impact in the overall spatial resolution. It is therefore desirable to achieve a better spatial resolution than with the scintillation imagers in Anger cameras, the usual goal being between 1-2 mm FWHM.

2.5.2 Energy resolution

Modern Anger cameras have an energy resolution of 9-10% FWHM for 140 keV gamma rays. Using a compact imager with the same energy resolution, and by simply taking advantage of a better positioning of the camera, it should be possible to avoid background emission from the heart and liver more efficiently and therefore reject scattered radiation better than with Anger cameras.

The importance of energy resolution for scintimammography has been recently estimated experimentally by R. Pani *et al* [22]. This study indicated that an energy resolution between 10% and 20% clearly enhances tumour detection, when compared to a 30% energy resolution. However, it is still not clear whether an improvement in energy resolution to much less than 10% would result in a significant image improvement. Recent Monte Carlo simulations [23] have shown that for an optimized positioning of a compact gamma camera for scintimammography, no significant improvement is observed within the range of 5-15% FWHM energy resolution. However, there is, as yet, no experimental data to substantiate this hypothesis.

2.5.3 Detection efficiency

The number of gamma rays detected should be maximised in order to reduce the statistical fluctuations in the images. The sensitivity of a gamma camera is mainly determined by the collimator efficiency, which is usually of the order

of 0.02%, for a high resolution collimator. Due to this low efficiency it is important that nearly all the gamma rays reaching the scintillator are detected. For a given gamma ray energy, this depends on the type of scintillator and its thickness. In high spatial resolution gamma cameras for 140 keV gamma ray imaging, a 6 mm thick NaI(Tl) crystal is acceptable, corresponding to an efficiency of about 80% [9].

2.5.4 Size, shape and dead regions of the camera

The size of an application-specific scintimammography camera should be large enough to encompass the whole breast. Areas of about $12 \times 12 \text{ cm}^2$ are usually accepted as ideal.

It may be convenient for the shape of the camera to match particular anatomic features like the curvature in the chest wall (see figure 2.10). The camera design should therefore ideally allow for a flexible choice of shape, which may be optimised and changed after clinical trials.

Finally, it is important to reduce dead areas at the edges to a minimum, ideally to less than 5 mm.

Chapter 3

Survey of small gamma ray imagers

This chapter is a review of research dedicated to the development of small gamma cameras based on scintillator-photodetector combinations. A brief description of the properties of the scintillator materials is followed by a survey of position sensitive photomultiplier tubes (PSPMT) and their application for small gamma ray imagers. Alternative techniques based on hybrid photodetectors (HPD) and on semiconductor photodetectors are discussed. Finally, there is a brief discussion on CdZnTe cameras, where gamma rays are directly converted.

3.1 Inorganic scintillator crystals

Inorganic crystal scintillators have particularly suitable characteristics for gamma ray detection in the energy range of interest in Nuclear Medicine (80 keV to 511 keV), and have been widely used for the last 50 years in scintillator-photodetector combinations. They provide a high conversion efficiency for gamma rays due to their high density and the high atomic number of their elements. They can be grown into large ingots which can easily be cut into different shapes and sizes to provide large area imagers at a relatively low cost compared to semiconductor-based gamma ray detectors.

The scintillation properties of inorganic scintillators can be described as a function of the energy states of the crystalline lattice. In the majority of cases pure crystals do not have adequate scintillation properties due to several factors. The scintillation efficiency (ratio of total energy deposited converted into photons) is low, the wavelength of emission is often inadequate to match standard photodetectors (e.g. PMTs), or the scintillation

characteristic decay time is too slow for the application.

Very efficient scintillators can be made by adding a small concentration of a carefully chosen impurity (activator) during the crystal growth which creates particularly efficient scintillation sites. The scintillation properties are then dictated by the energy states of the activator in the crystal lattice [24]. Typical examples are the addition of Tl atoms to NaI and CsI to create the widely used NaI(Tl) and CsI(Tl) scintillators and the addition of Ce to many inorganic crystals which has led to an extensive development of new scintillators in the past 10 years, some of which are described below.

3.1.1 Requirements for an ideal scintillator

Light output depends on the efficiency of conversion of the deposited gamma ray energy into optical photons. A high output is important to obtain a good energy resolution and spatial resolution (see sections 2.3.1 and 2.3.2) through the minimization of statistical fluctuations. Furthermore, the light output should be proportional to the energy deposited in a gamma ray interaction.

Wavelength of emission The emission spectrum of the scintillator must match the spectral sensitivity of the photodetector. The scintillator should also be transparent to its own emission.

Refractive Index The optical coupling between the scintillator and the photodetector is crucial to determine the light collection efficiency (LCE), defined as the fraction of light created in the scintillator that reaches the sensitive area of the photodetector. A large mismatch of the refractive indices of these two components will impair a good LCE due to total internal reflection occurring at the interface. Conventional photomultiplier tubes have glass entrance windows with refractive index of about 1.5, and for the most common scintillators the refractive index is greater than 1.8 (see table 3.1).

Density and Atomic Number (Z) directly determine the conversion efficiency for gamma rays. In medical applications this is crucial to reduce as much as possible the radiation dose given to the patient. Conversion efficiency of over 80% is usually a requirement for gamma ray medical imaging.

Scintillation decay time should be short to avoid pulse pile-up (which degrades energy resolution) specially in high count-rate conditions. A

short decay time is also necessary in applications where coincidence timing is important, e.g. PET.

3.1.2 Description of some common scintillators

Table 3.1 shows a summary of the main characteristics of some scintillator materials of potential interest in nuclear imaging applications.

Scintillator	Light yield (ph/keV)	Density (g/cm ³)	Effective Z	Wavelength of maximum emission, λ_{max} (nm)	Refractive index at λ_{max}	Principal decay constant (ns)	ref
NaI(Tl)	38-45	3.67	51	415	1.85	230	[25, 26, 27]
CsI(Na)	37-43	4.51	54.1	420	1.84	630	[26, 27]
CsI(Tl)	52-61	4.51	54.1	540	1.80	1000	[26, 27, 28]
YAP(Ce)	13-23	5.4	36	370	1.95	25	[29, 30, 31, 28]
YSO(Ce)	44	4.5	34	420	1.8	70	[32, 33]
GSO(Ce)	8/1	6.7	59	440	1.85	60/600	[34, 35, 28]
BGO	8-10	7.13	75	480	2.15	300	[27, 26]
LSO(Ce)	25-27	7.4	66	420	1.82	40	[36, 35, 37, 28]
LuAP(Ce)	8-20	8.34	65	365	1.94	18	[38, 39, 40, 41]
BaF ₂	11/1	4.89	—	325/220	1.5/1.58	630/0.6	[27]

Table 3.1: Characteristics of some inorganic scintillators.

NaI(Tl) was the first inorganic crystal to be used as a scintillator for radiation detection. It is still the material of choice in Anger cameras for single photon imaging due to its high light yield and high conversion efficiency for gamma rays of ≤ 300 keV. NaI(Tl) is hygroscopic and has to be encapsulated in an air-sealed can to protect it against moisture. **CsI(Na)** has very similar characteristics to NaI(Tl) but is much less hygroscopic so it may be used without encapsulation. It has higher conversion efficiency for gamma rays, due to its higher density and higher effective atomic number, and comparable light yield and light emission spectrum. In spite of these very attractive features, CsI(Na) has not been used to replace NaI(Tl) in many applications. It has a slower decay constant and, most importantly, it usually shows poorer energy resolution, as discussed below. **CsI(Tl)** has a very high light yield but its emission spectrum does not match well the spectral sensitivity of PMT photocathodes (see figure 3.1). It has been predominantly used with silicon photodetectors which have a high quantum efficiency at

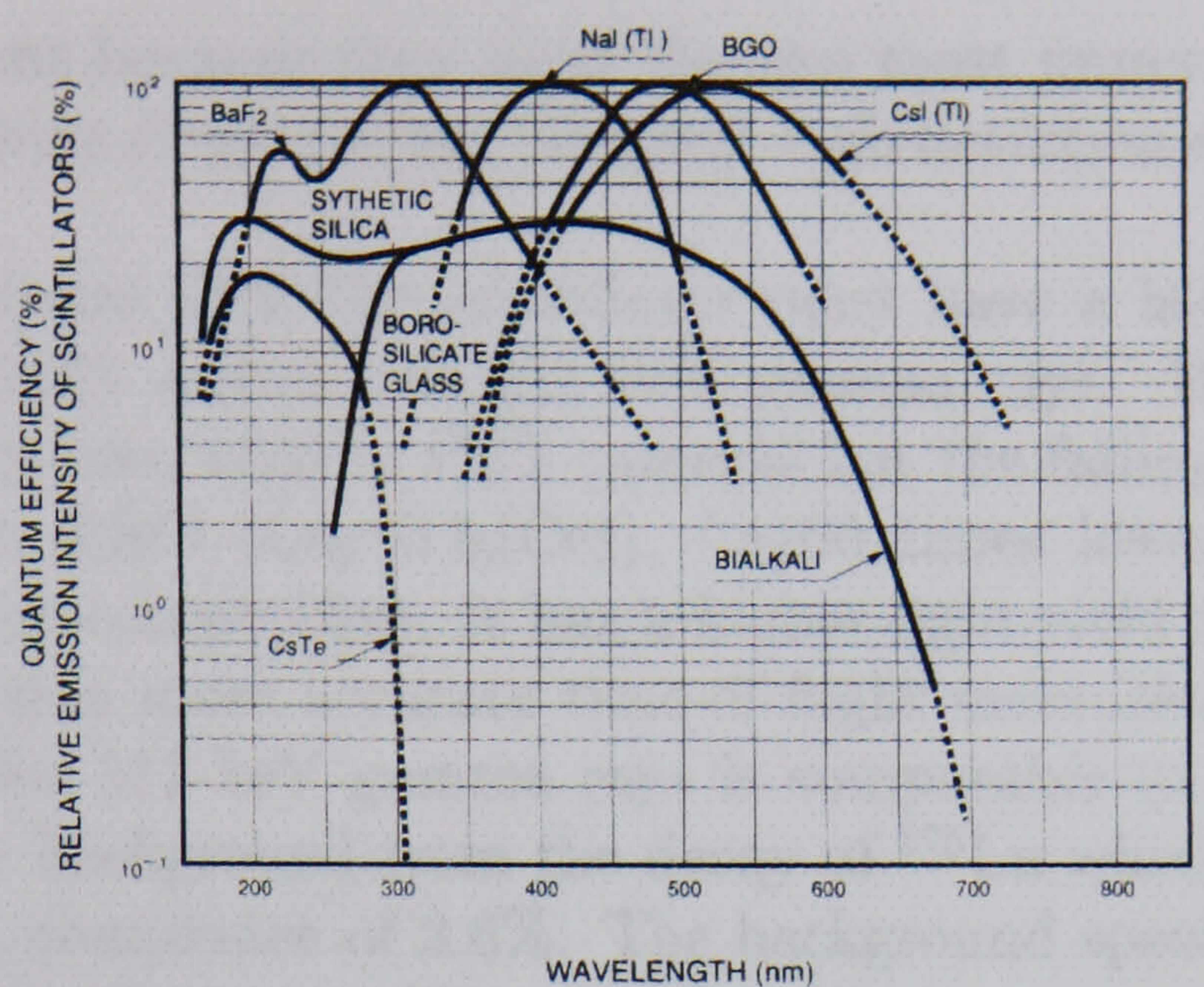


Figure 9-16: Scintillator emission spectra and photocathode spectral response of photomultiplier tubes

Figure 3.1: Combined plot showing the spectra of emission of some scintillators and the quantum efficiency curve for a bialkali photocathode.

the wavelength of maximum emission of this scintillator (540 nm). NaI(Tl), CsI(Tl) and CsI(Na) have been used for single photon gamma ray imaging for the last 40 to 50 years.

In the past decade, a range of new scintillator materials have been developed which show promising features for some applications.

YAP¹ ($\text{YAlO}_3(\text{Ce})$) is a fast scintillator and can easily be machined to produce very thin arrays of small crystals, allowing sub-millimetre pixels. Despite its lower light yield and lower conversion efficiency compared to NaI(Tl), it has been tried in high resolution gamma ray imaging [42], and also in small animal PET studies [43] where the conversion efficiency is not such an important requirement.

GSO ($\text{Gd}_2\text{SiO}_5(\text{Ce})$) has the advantage of a higher conversion efficiency than NaI(Tl) with a relative light yield of 25%. It has been suggested for both single photon [44] and PET applications [45].

YSO ($\text{Y}_2\text{SiO}_5(\text{Ce})$) has been reported to have a light yield similar to that of NaI(Tl) but has lower conversion efficiency due to its lower effective atomic number.

Despite the recent appearance of these newer scintillator materials, the classical scintillators (NaI(Tl), CsI(Tl) and CsI(Na)) are still the choice for

¹Yttrium aluminium perovskite

most applications because they meet the two most important requirements in nuclear medicine single photon imaging: high detection efficiency and high light yield.

For conventional PET the scintillator must have a high conversion efficiency to efficiently absorb the 511 keV gamma rays. **BGO** ($\text{Bi}_4\text{Ge}_3\text{O}_{12}$) has traditionally been used in PET cameras but the falling price of lutetium oxyorthosilicate, **LSO** ($\text{Lu}_2\text{SiO}_5(\text{Ce})$), (≈ 100 times lower since 1991 [40]) has made it more competitive. It has a higher light yield and a faster decay time, which enable more accurate time-of-flight measurements. Its conversion efficiency for 511 keV gamma rays is comparable to BGO. LSO has a natural activity background from the decay of ^{176}Lu which is present in the crystal with an abundance of 2.6%. The background spectrum is present in the energy range of interest (80 to 1000 keV) due to gamma emission (89, 202 and 307 keV) and continuous beta emissions. The typical background of 300 counts/s/cm³ in LSO samples impairs its use in single photon imaging, where typical count rates are about 10,000 counts per second (cps). LSO based PET cameras have been developed [46] and an excellent performance has been demonstrated.

LuAP ($\text{LuAlO}_3(\text{Ce})$) is similar to YAP except that the yttrium atoms are replaced by lutetium. The result is a scintillator with similar characteristics of fast decay, reasonable light yield and with a similar emission spectrum but with a much higher density and higher effective atomic number, which makes it ideal for PET. There are still some problems to overcome in the growth of reliable and uniform crystal samples [41], which is reflected in the wide range of light output values measured for different samples (see table 3.1). However, these preliminary results show that LuAP is a very promising scintillator for PET.

An example of the use of **BaF₂** in nuclear medicine is the so-called PET-TRA camera [47]. The crystal is coupled to a multi wire proportional chamber (MWPC) which is filled with a photo-sensitive vapour (TMAE) particularly sensitive to the fast UV emission component (at 220 nm) of BaF_2 . The UV light produced after a gamma ray interaction in the crystal creates photo-electrons within the MWPC by photo-ionisation, and the ionisation charge is amplified and read out in the MWPC, providing the position signal.

3.1.3 Energy resolution

The principle of operation of a typical scintillation counter based on an inorganic scintillation crystal coupled to a PMT is depicted in figure 3.2. Consider the full absorption of gamma rays in the crystal with the subsequent creation of a mean number of photons N_{ph} . Each photon has a probability



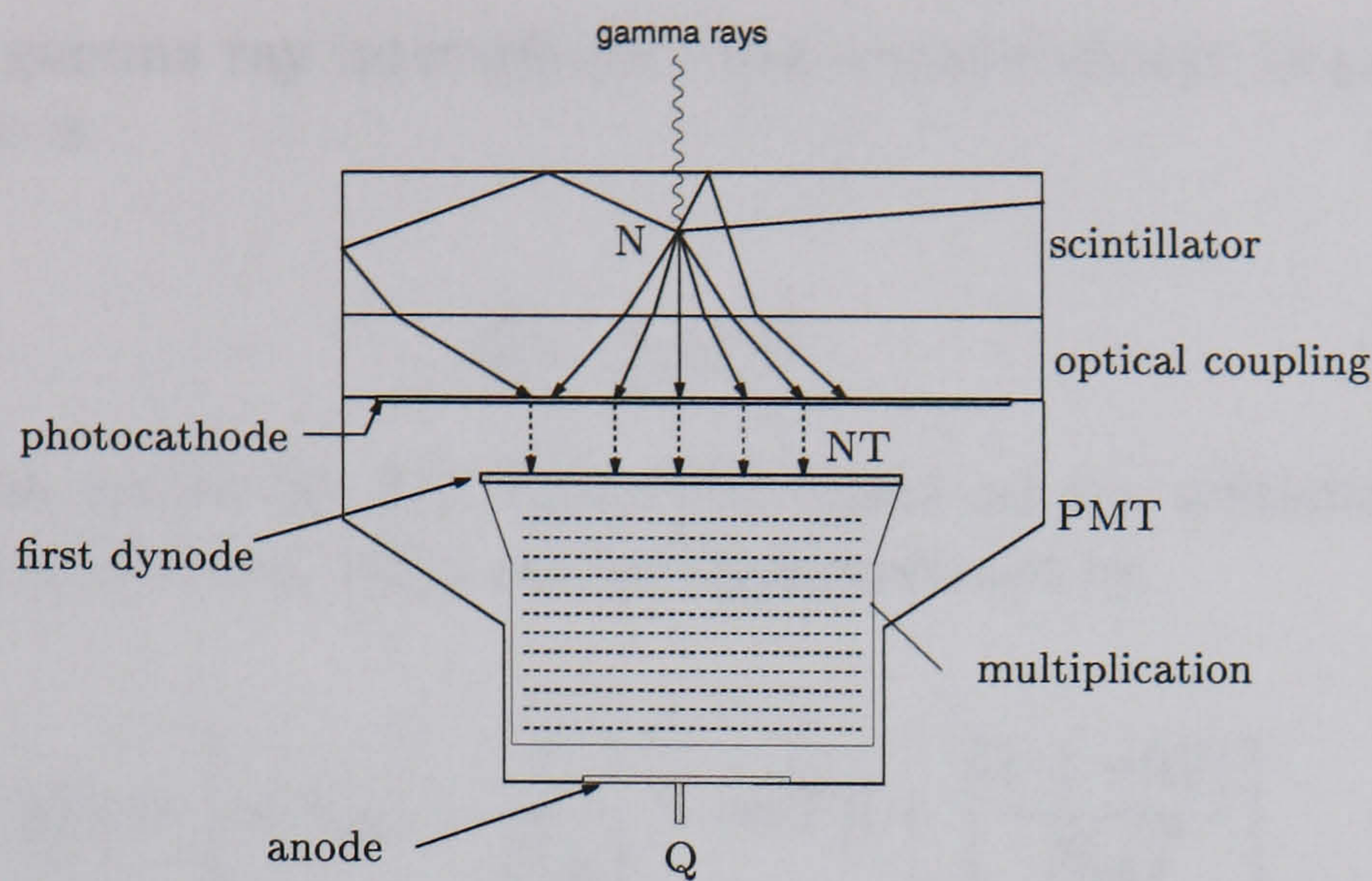


Figure 3.2: A typical scintillation counter based on an inorganic scintillator coupled to a PMT.

f_1 of reaching the photocathode of the PMT depending on the direction of emission, on the reflectivity of the crystal coating and on the optical coupling between the crystal and the PMT window. Those that reach the photocathode may generate photoelectrons according to the quantum efficiency QE at the wavelength of the incident photons, defining a probability f_2 . The PMT collection efficiency defines the fraction f_3 of photoelectrons released from the photocathode that reach the first dynode initiating a multiplication cascade. A combination of the processes determined by f_1 , f_2 and f_3 is called the transfer efficiency $T = f_1 f_2 f_3$ and is the probability that a photon generated in the scintillator creates a photoelectron collected by the first dynode. After the charge amplification of all the photoelectrons in the dynode stages with gain G , the total charge Q created at the PMT anode is $Q = N_{ph} \times T \times G$.

The measured value of Q is proportional to the gamma ray energy E_γ and for large \bar{N}_{ph} it is found to be well described by a Gaussian distribution with an rms σ_Q . The energy resolution R is then usually defined as

$$R = 2.35 \frac{\sigma_{E_\gamma}}{E_\gamma} = 2.35 \frac{\sigma_Q}{\bar{Q}} = 2.35 \sqrt{v(Q)} \quad (3.1)$$

where 2.35σ is the full width at half maximum (FWHM) for a Gaussian distribution with a σ rms and $v(Q)$ is the relative variance of Q ($v(Q) = \sigma_Q^2 / \bar{Q}^2$). The resolution can therefore be obtained analysing the pulse height distribution of charge.

Fluctuations in Q arise from individual fluctuations in N_{ph} , in T and in

G for different gamma ray interactions. The average charge \bar{Q} generated at the PMT anode is

$$\bar{Q} = \bar{N}_{ph} \bar{T} \bar{G} \quad (3.2)$$

Following the review by J.B. Birks [48] based on the statistical fluctuations in cascade processes, $v(Q)$ can be approximated by

$$v(Q) \approx \left[v(N_{ph}) - \frac{1}{\bar{N}_{ph}} \right] + [v(T)] + \left[\frac{1 + v(G)}{\bar{N}_{ph} \bar{T}} \right] \quad (3.3)$$

where the approximations are $v(N_{ph}) \ll 1$ and $v(T) \ll 1$. The relative variances $v(N_{ph})$, $v(T)$ and $v(G)$ are defined similarly to $v(Q)$.

The first term in square brackets in equation 3.3 can be seen as the variance in the number of photons due to contributions other than Poisson statistics and is called the intrinsic resolution of the scintillator. The middle term in equation 3.3 is the variance of the transfer efficiency. Assuming that the generation of photons in the crystal follows a Poisson distribution ($v(N_{ph}) = 1/\bar{N}_{ph}$) with $\bar{N}_{ph} \gg 1$, and that the transfer T is constant, then the charge variance is simply

$$v(Q) = \frac{1 + v(G)}{\bar{N}_{ph} \bar{T}} \quad (3.4)$$

which represents the PMT response variance under the above simplistic assumptions.

Therefore, the energy resolution R can be expressed as

$$R^2 = R_i^2 + R_T^2 + R_{PMT}^2 \quad (3.5)$$

where R_i represents the intrinsic resolution of the scintillator, R_T is the transfer resolution and R_{PMT} is the resolution associated with the photomultiplier tube. Each of these terms corresponds to the terms in square brackets in equation 3.3.

A detailed discussion of each component of R is presented in appendix A. The major conclusion of studies on the energy resolution of scintillators coupled to PMTs indicates that the two most important components are R_{PMT} and R_i . The former is mainly dependent on the number of photoelectrons created at the PMT photocathode. This is determined by the light output

of the scintillator and the match between its emission spectrum and the photocathode sensitivity spectrum. The latter term is due to a non-uniform distribution of the activator sites in the crystal volume as well as to a non-proportional response of the scintillator to electrons with different energies (refer to appendix A for a complete explanation). This non-proportionality is the major component of R_i and its contribution to R is found to be of the same order of that of R_{PMT} .

3.2 Properties of Position Sensitive Photomultipliers

Over the last ten years, there has been a considerable effort dedicated to the development of small high resolution gamma cameras which is closely linked to the advent and development of Position Sensitive Photomultiplier Tubes (PSPMT). The sub-millimetre intrinsic spatial resolution of the PSPMT suggests that good spatial resolution can be achieved with single tube gamma cameras, coupling scintillation crystals to PSPMTs. Moreover, the similarity of behavior (e.g., gain, quantum efficiency) to single anode PMTs indicates that the most important performance parameters of the Anger Camera, such as energy resolution and counting efficiency, should be matched with an adequate scintillation crystal.

The development of PSPMTs has been led by two manufacturers, Hamamatsu Photonics and Photonis (previously Philips). Position sensitivity is obtained with the introduction of two distinct and novel features in photomultiplier tubes: a new type of dynode structure and a set of multiple anodes in each PMT, instead of the usual single anode configuration.

3.2.1 Fine Mesh dynodes and Micro-channel Plates

In conventional non-imaging PMTs, the dynode structures are designed to provide high gain, high collection efficiency, fast and accurate timing properties and compactness. There are several designs that optimize some parameters, usually at the expense of others. Among the most commonly used are the *Venetian Blind*, *Linear Focused*, *Box-and-Grid* and *Circular Cage* [49, 50] types. The electric fields inside the PMT define complex electronic trajectories in vacuum, first from the photocathode to the first dynode and then within the dynode structure. This makes them very sensitive to even low intensity external magnetic fields that deviate the electrons from their optimum paths, resulting in a loss of gain. In conventional PMTs a 50% drop of the overall gain occurs at a few Gauss (0.1 mT) [49].

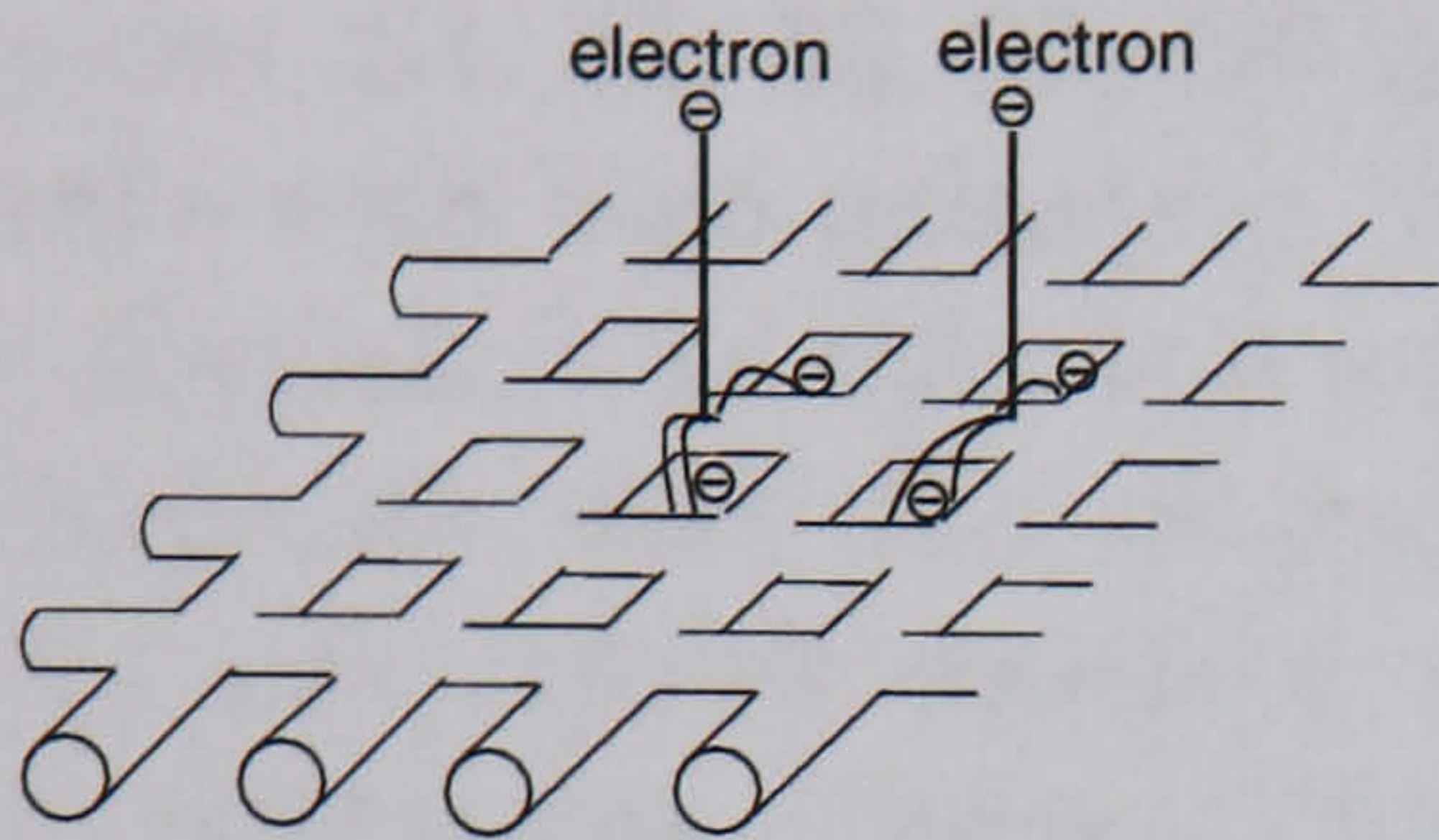


Figure 3.3: Schematic detail of a fine mesh dynode.

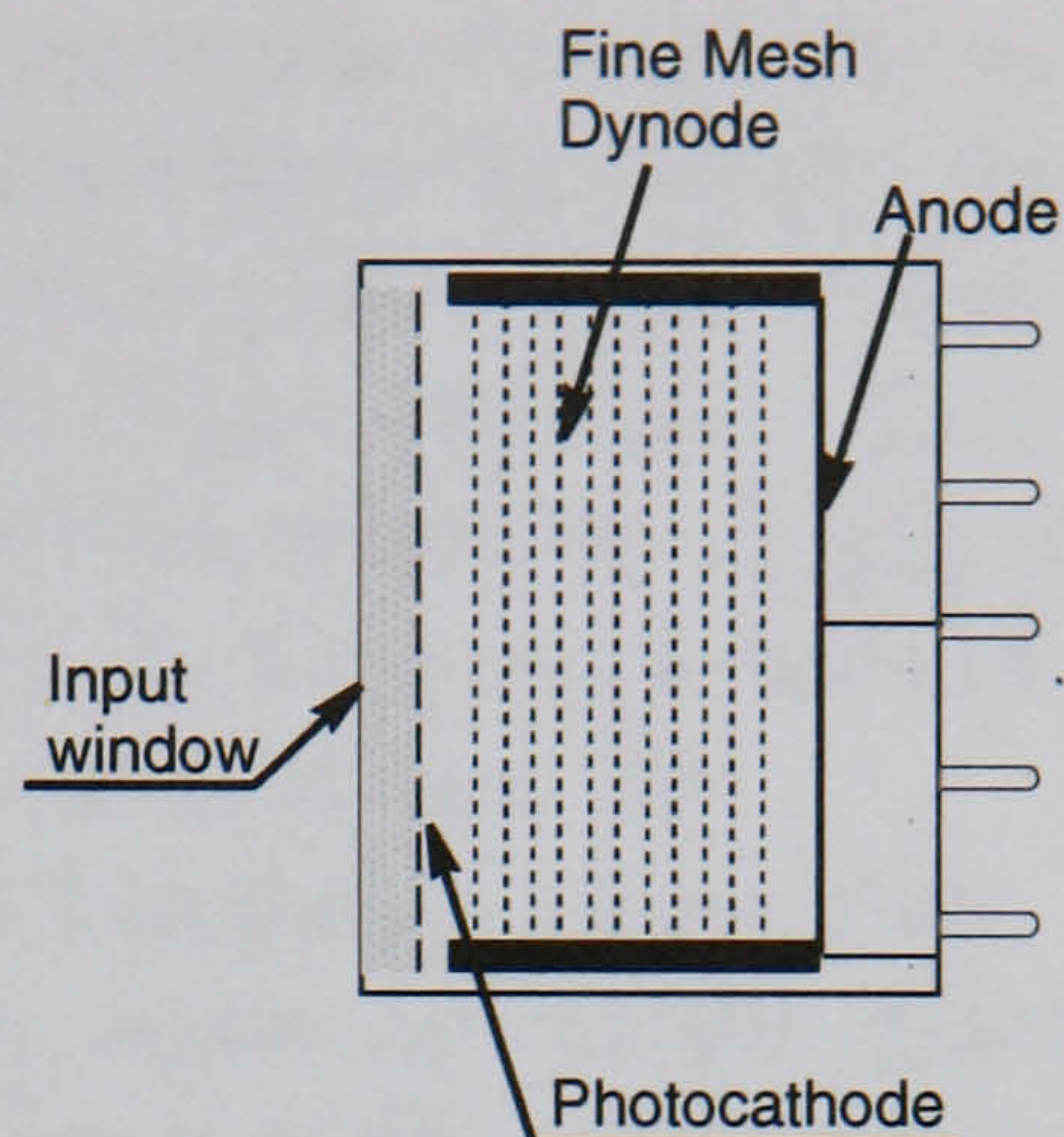


Figure 3.4: PMT with a fine mesh dynode.

In nuclear and high energy physics experiments, where high magnetic fields are often present, this effect must be overcome by proper magnetic shielding or by the use of long light-guides to bring the PMT away from the high magnetic field regions. Shielding is expensive and sometimes difficult, whereas the light-guides usually result in a significant loss of signal.

The demand for PMTs with greater immunity to magnetic fields, improved timing performance and with position sensitivity led to the development of PMTs using special electron multiplier structures, namely *Mesh dynodes* [51] and *Micro-channel Plates* [52]. Both structures meet the main requirements to improve magnetic field immunity, which are: to minimize the electron transit distance and to create an electric field along the tube axis, so that the electrons follow short and straight paths from the photocathode to the anode. Under these conditions it is possible to obtain excellent immunity to magnetic fields aligned with the tube axis. These characteristics are also important to provide fast response (short *Transit Time*) and short *Transit Time Spread* (T.T.S.) [53]. Furthermore, both structures are inherently position sensitive in the sense that they preserve the information about the localisation of the light pool at the photocathode.

The **Mesh Dynode Structure** (figure 3.3) consists of closely packed sets of parallel mesh planes of thin wire. The distance between the first dynode and the photocathode is small, as is the separation between each dynode stage. The electric fields produced are parallel to the tube axis and therefore the electron trajectories are straight and along this axis. A high magnetic field immunity can be achieved if the PMT is oriented with its symmetry axis along the direction of the existing magnetic field. Photomultiplier tubes using mesh dynodes (figure 3.4) became available during the 1980s [53, 51, 54].

Several designs have been studied for different levels of immunity to magnetic fields. A coarse mesh [51] with 7 mm distance from the photocathode to the first dynode and dynodes with an inter-stage separation of 1.3 mm could be operated in axial magnetic fields up to 200 Gauss (20 mT). Fine Mesh Dynodes [54, 55, 56, 57, 58] have provided the best immunity, being able to operate with high gains (e.g. $10^4 - 10^5$) at 1 to 2 T . Fine mesh dynodes have wire diameters as thin as 5 μm with a wire pitch of 13 μm [59].

Together with the desired magnetic field immunity, these Fine Mesh PMTs also exhibit excellent timing properties, again due to the short electron trajectories. Transit Time values of 2 ns are typical, compared to 30 to 50 ns in other dynode structures. Transit time spread values of 200 - 300 ps are usual, which make the fine mesh dynode structure an excellent option for experiments that require fast and accurate timing [57].

Position sensitivity is a result of the low transverse diffusion of the electronic cloud during the amplification process so that the final charge cloud produced has a spatial distribution which retains the position information about the light pool at the photocathode. The charge cloud is spread over a two dimensional set of anodes and a centroid algorithm is used to estimate the center of the light pool at the photocathode. The intrinsic spatial resolution of the PSPMT is defined as the width of the peak of the pulse-height distribution of centroids for a beam of photons incident at a given point in the photocathode (which can be measured with a small diameter optical fibre). It depends on the spread of the electronic charge and on the mean number of photoelectrons released from the photocathode. Intrinsic charge spreads of 4 to 5 mm have been reported for coarse mesh dynodes [49]. This leads to sub-millimeter values for spatial resolution for light levels of a few thousand photons per event [60, 61, 53]. The electron charge spread is usually minimised in mesh dynode PMTs by “proximity focusing”: the photocathode is placed at a short distance from the first dynode, the space between dynodes is reduced as much as possible and the distance between the last dynode stage and the anode section is minimised.

In addition to the performance aspects just described, mesh dynode PMTs have been found to behave in a similar way to conventional tubes, as far as overall gain, quantum efficiency, stability and linearity of response are concerned.

Hence, immediate use for these PMTs was found in a variety of fields, such as Medical Imaging [61, 62, 63, 64, 65, 66, 67], High Energy Physics [68, 69, 70]) and Astrophysics [71, 72, 73, 74, 75, 76].

Micro-channel Plate Photomultiplier Tubes (MCP-PMT) are PMTs with a micro-channel plate (MCP) charge multiplier. MCPs were developed in the 1970s for defense applications, in particular as lightweight

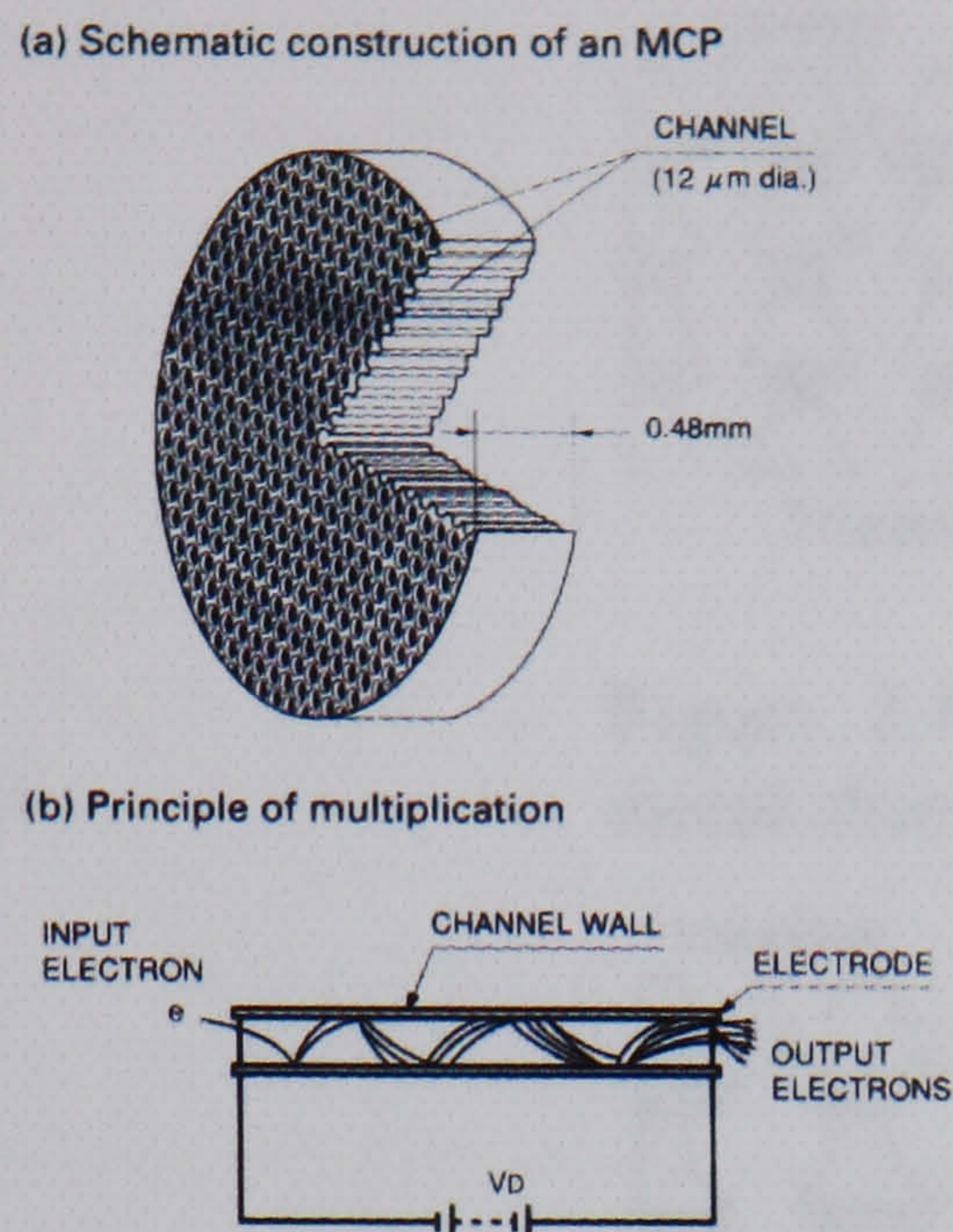


Figure 3.5: Schematic of a Micro-Channel Plate[49].

image intensifiers for night vision and later declassified for general scientific use. MCPs (figure 3.5) consist of very thin glass capillaries bundled together to form a two-dimensional array of electron multiplying channels. The inner wall of each channel is processed to have optimum electrical resistance and secondary electronic emission [52].

A voltage difference is applied between the input and output surfaces to accelerate the electrons inside the channels. The electrons collide with the channel walls releasing more secondary electrons, creating a multi-stage amplification process analogous to that of a PMT dynode structure. The overall gain is proportional to the length-to-diameter ratio of the channel and gains of the order of 10^6 are currently achieved [57], for channel diameters of a few micron and length of half a millimetre.

In an MCP-PMT, the electrons follow short paths and, therefore, the tube shows excellent immunity to magnetic fields oriented along its symmetry axis, in much the same way of the fine mesh dynodes, making it a very attractive detector for high energy physics applications [77, 78]. Moreover, the timing performance of these tubes is excellent, with transit times of typically less than 1 ns and time spread of the order of 200 ps [49, 79, 80].

Because channel electron multipliers were primarily developed as image intensifiers [81], one can say that the MCP-PMT is intrinsically a position sensitive device. It uses proximity focusing to optimize spatial resolution, which also depends on the MCP dimensions and the anode and electronics

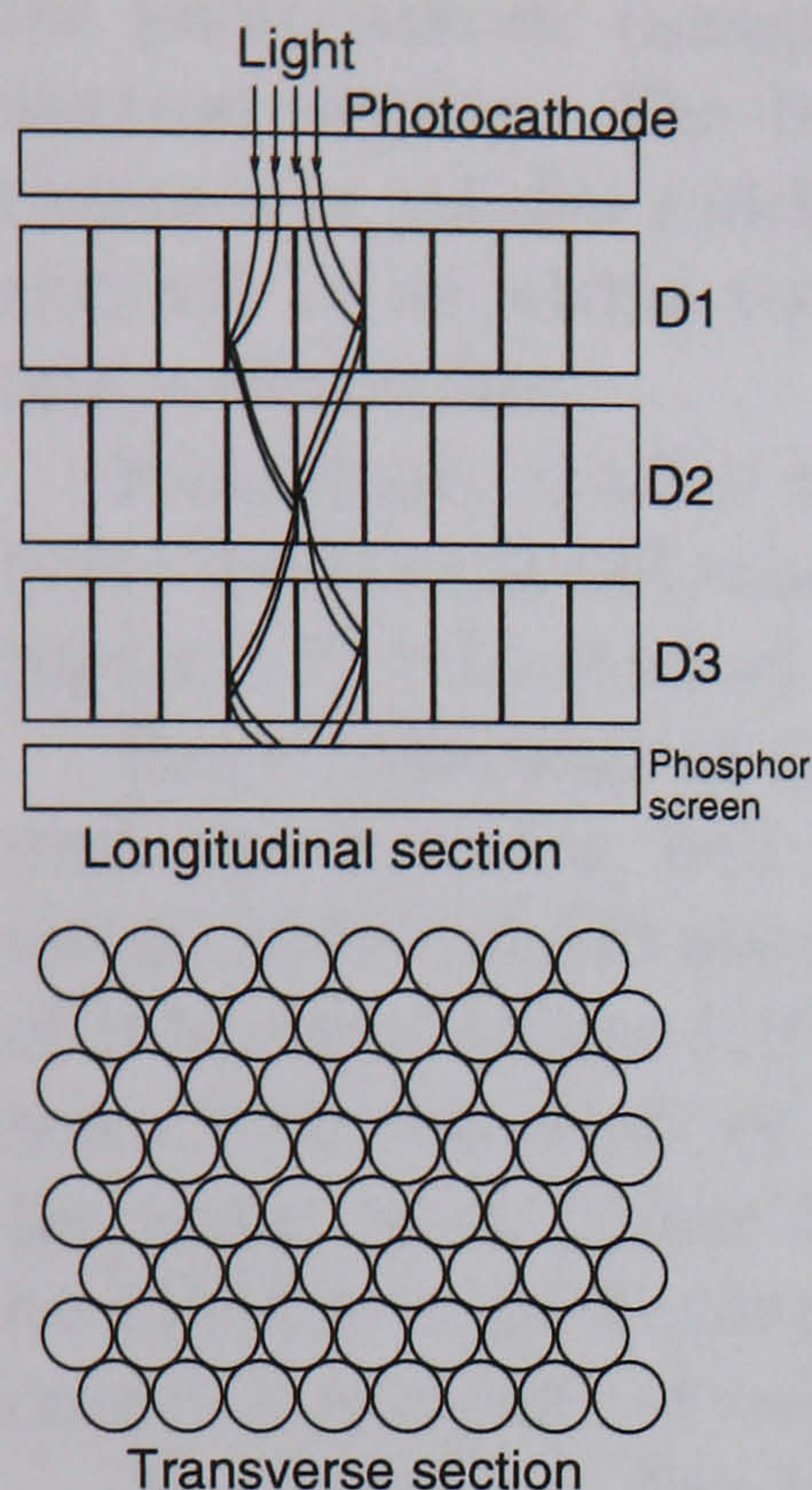


Figure 3.6: Example of an electron multiplier based on multi stage metal channel tubes[84].

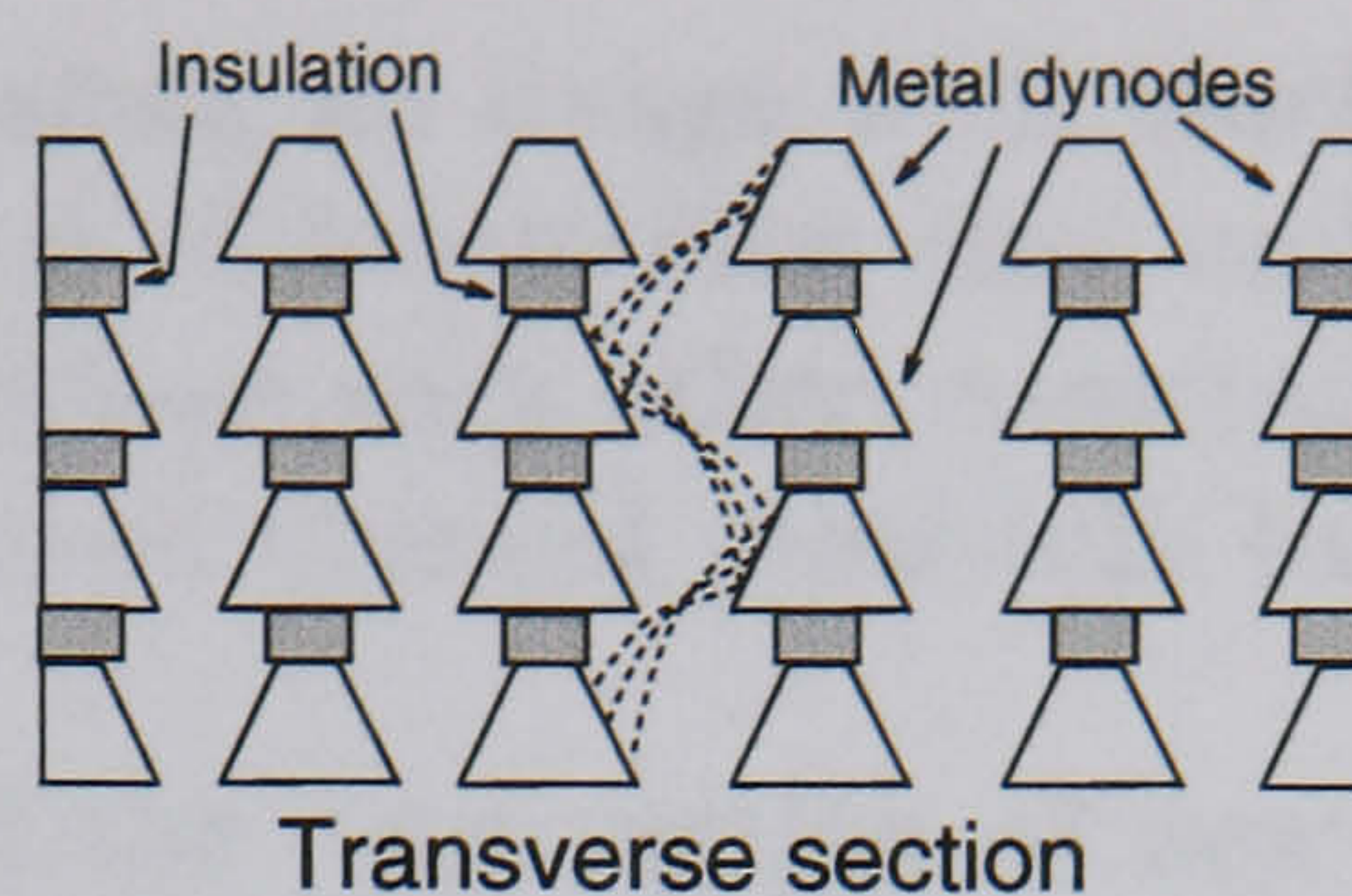


Figure 3.7: Multi stage drilled metal sheets [85]

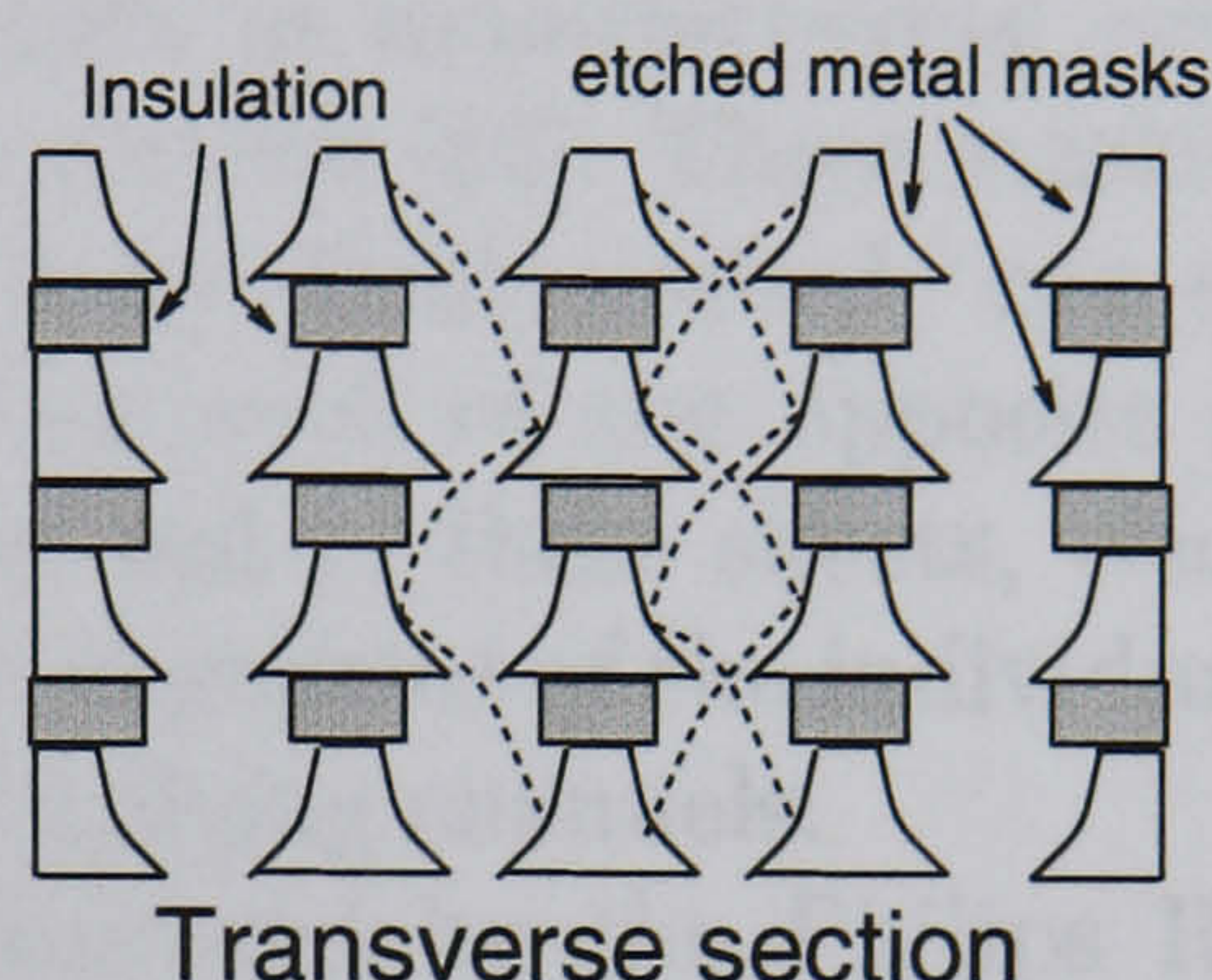


Figure 3.8: Multi stage etched metal masks electron multiplier[86].

readout installed. With a careful design, a spatial resolution dominated by the size and spacing of the MCP pores can be achieved, and values of $20\text{ }\mu\text{m}$ FWHM have been reported [82, 83].

In spite of the excellent characteristics mentioned, MCP-PMTs have some disadvantages such as their limited count rate capability due to long recovery times, shorter lifetime at high count rates due to positive ion bombardment of the photocathode, and also the very expensive manufacturing process which is reflected in the price of the final product.

3.2.2 Metal Channel Dynodes

Another kind of position sensitive electron multiplier is the metal channel dynode structure. The underlying concept is similar to the glass micro-channel plate, and it was developed primarily as an image intensifier. Photomultiplier tubes have been well established as very efficient electron multipliers for more than 50 years, with gains of 10^7 or more. This suggested the idea of constructing a tube with similar gain characteristics and with the capability of retaining the spatial information of an image formed on

the photocathode (image intensifier), creating an image with much higher electron density. The basic idea consisted of assembling tiny multiplying channels in parallel which must be isolated from each other, constraining the electron cloud within its boundaries to avoid channel cross-talk leading to image distortions.

Preliminary studies in 1960 suggested the construction of new dynode types based on small tubes [84] (figure 3.6) and on perforated metal foils [85] (figure 3.7) to be stacked in separate stages as in conventional PMT dynodes.

Some technological difficulties in micro-machining these structures were overcome by using well developed techniques in manufacturing perforated metal shadow masks used in colour television tubes [86]. These masks consist of thin metal sheets ($150\text{ }\mu\text{m}$ thick) with individually etched “cup shaped” holes with diameters of 400 and $250\text{ }\mu\text{m}$ on each of the opposite sides of the metal sheet (figure 3.8). Arranging several of these sheets, electrically insulated from each other, with an accurate alignment of the individual holes, creates a structure of individual small multiplying channels.

The technique has been taken and improved by the Philips Research Laboratories. Studies of electron trajectories using ray-tracing simulation techniques helped in reaching a satisfactory design based on the metal sheets shown in figure 3.8. The new arrangement is shown in figure 3.9 where, except for the first, each dynode is made by placing two sheets face to face. This design has improved performance with respect to focusing the electron trajectories, hence providing a more uniform multiplication and a better pulse height resolution.

Using this structure, an imager was demonstrated [87] with a spatial resolution limited by channel separation (0.77 mm in that particular case). Applying this dynode structure to a PMT configuration, a 64 channel photomultiplier was developed [88]. It consisted of 10 stages of metal channel dynodes (figure 3.9) achieving a typical gain of 10^6 , a bialkali photocathode and 64 separate anodes. The low cross-talk between channels makes this tube effectively equivalent to an array of several miniature PMTs. More detailed specifications of these tubes are given in section 3.2.4. Etching techniques have also been described to produce metal channel dynodes [89]. Thin silicon wafers ($200\text{ }\mu\text{m}$) are chemically etched to create a hole pattern and are subsequently coated with a secondary electron emitter material (AgMg(O)).

Hamamatsu has also developed a PMT based on a Metal Channel Dynode [90] with similar characteristics of high gain and low inter-channel cross-talk (see section 3.2.4) using fine machining and etching techniques. This structure is similar to arrays of many small venetian blind dynodes, as depicted in figure 3.10.

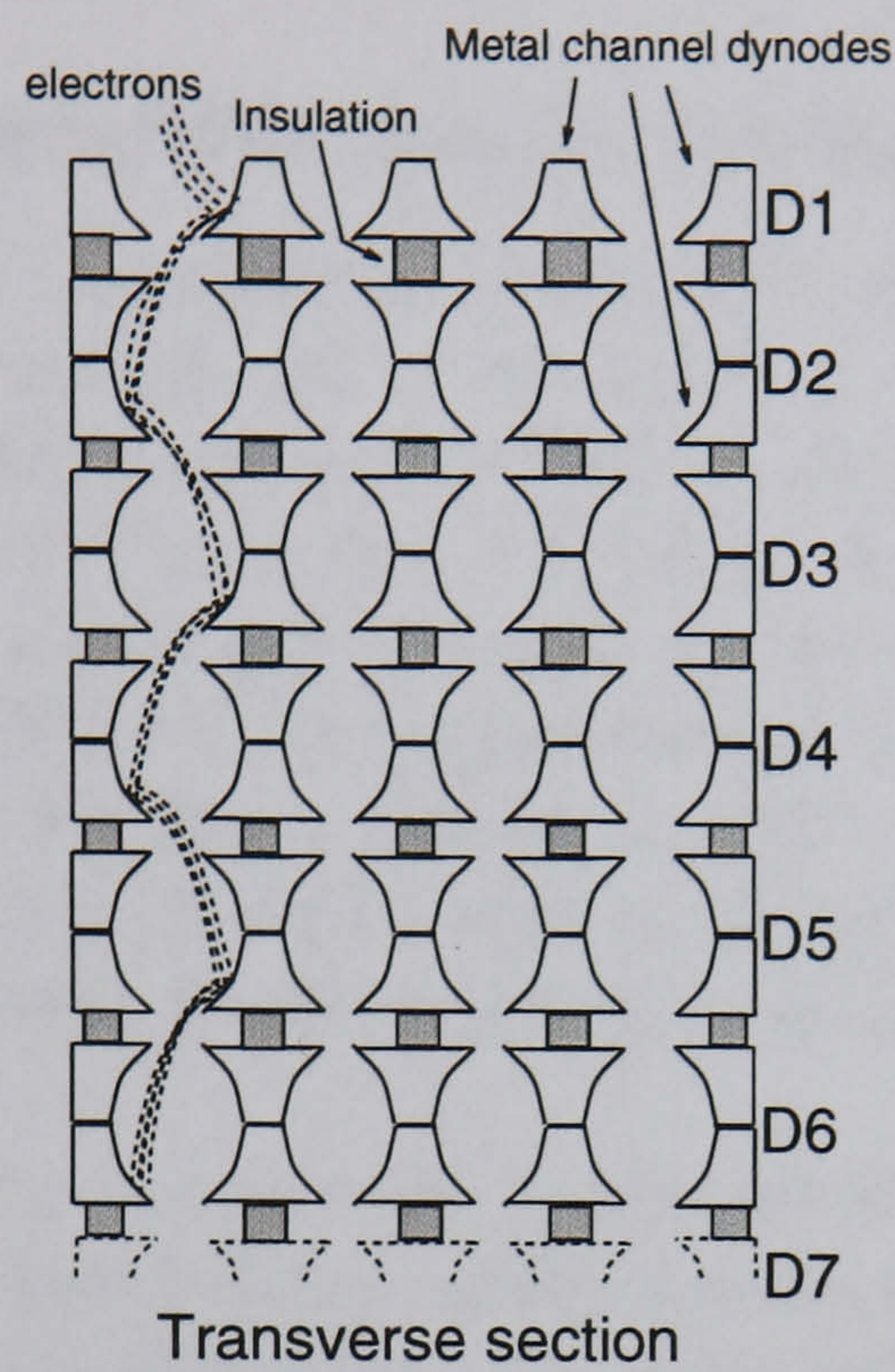


Figure 3.9: Improved design for a metal channel dynode multiplier based on etched metal masks[87].

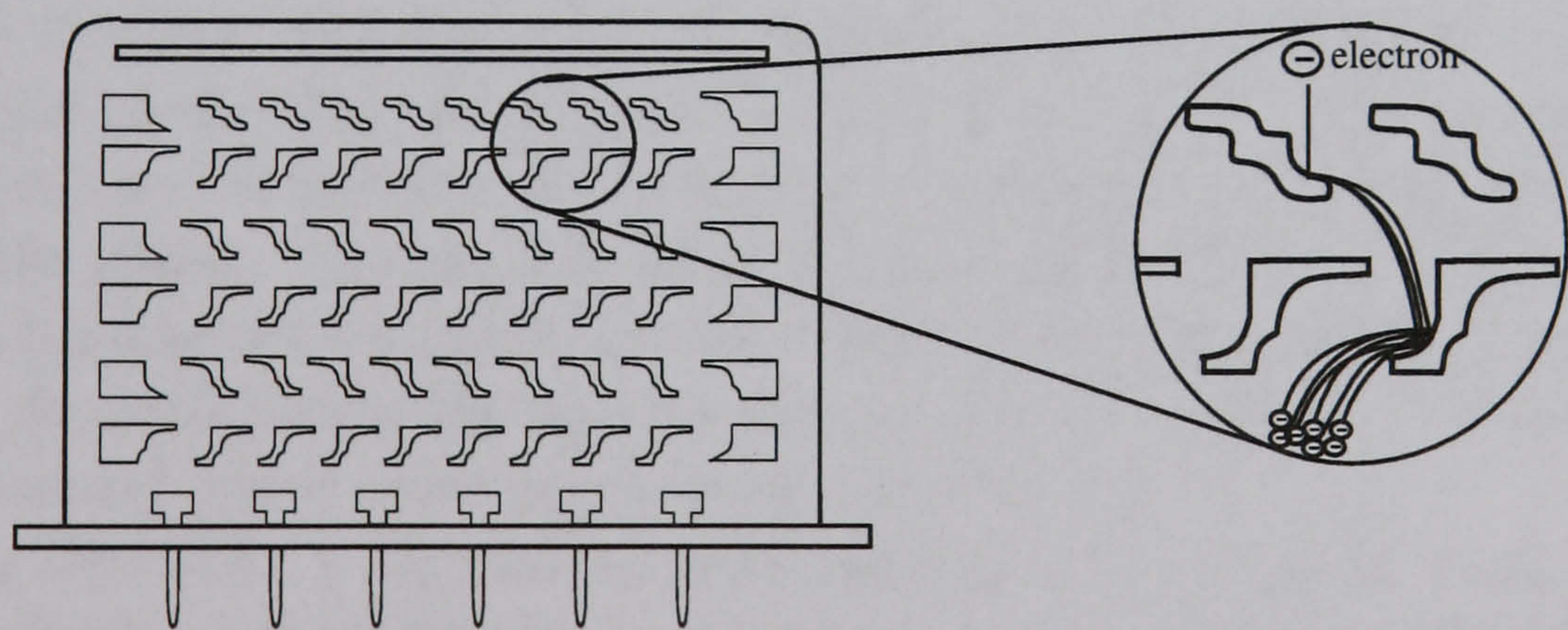


Figure 3.10: Hamamatsu metal channel dynode multiplier.

The design of these electron multipliers provides good timing characteristics as well as immunity to moderate magnetic fields [90, 88].

3.2.3 Position sensitive anode configurations

The spatial information contained in the electron cloud following the multiplication process must be read-out by means of an appropriate set of anodes (PSPMTs are often called multi-anode PMTs). Several configurations have been developed for MCP-PMTs and PSPMTs, depending on the requirements for spatial resolution, spatial linearity, count rate and simplicity (number of channels). In MCP-PMTs a spatial resolution of the order of $40\ \mu\text{m}$ is possible using Resistive Anodes or Wedge and Strip Anodes [83, 91, 82, 92].

Commercially available PSPMTs with mesh dynodes and metal channel dynodes use either discrete anode pixels [88], crossed-wire [61] or crossed-plate anodes [93].

The first consists of separate solid anodes usually read out individually (figure 3.11). These are particularly useful in cases where the charge cloud is narrower than the pixel cross-section (e.g. with metal channel dynodes). In these cases, a high count rate is achievable, since only one pixel is used per event and the others are available to detect simultaneous events. There is also an unequivocal determination of the position. However, it requires more expensive readout electronics, due to the large number of channels.

Less expensive and simpler read-out is achieved with crossed-wire (figure 3.12) or crossed-plate anodes. They consist of two perpendicular sets of parallel wires, or thin ($\approx 0.5\ \text{mm}$ thick) plates, which are located between the two last dynodes. Charge from the next-to-last dynode passes through the anode wires, or plates, and is multiplied in the last dynode, which is a reflective type dynode. The electronic transparency in the crossed-wire anodes is determined by the size of the mesh (usually $4\ \text{mm}$ pitch with less than $1\ \text{mm}$ thick wires) and in the crossed-plate type it is adjusted by drilling small holes in the thin plates. The anodes define a region of high potential between the two last dynodes which optimizes the collection of charge released by the last dynode. By positioning the anodes close to the last dynode a strong electric field is created which reduces space charge effects.

Some PSPMTs with crossed-wire anodes are optionally supplied with resistor chains connecting the anode wires in each direction to simplify the readout by a charge division scheme (e.g. Hamamatsu R2486/7, R3292 - table 3.2).

With crossed-wire (plate) anodes there is position ambiguity for multiple simultaneous events at different positions across the photocathode. For two simultaneous charge distributions centered in (x_1, y_1) and (x_2, y_2) it is not

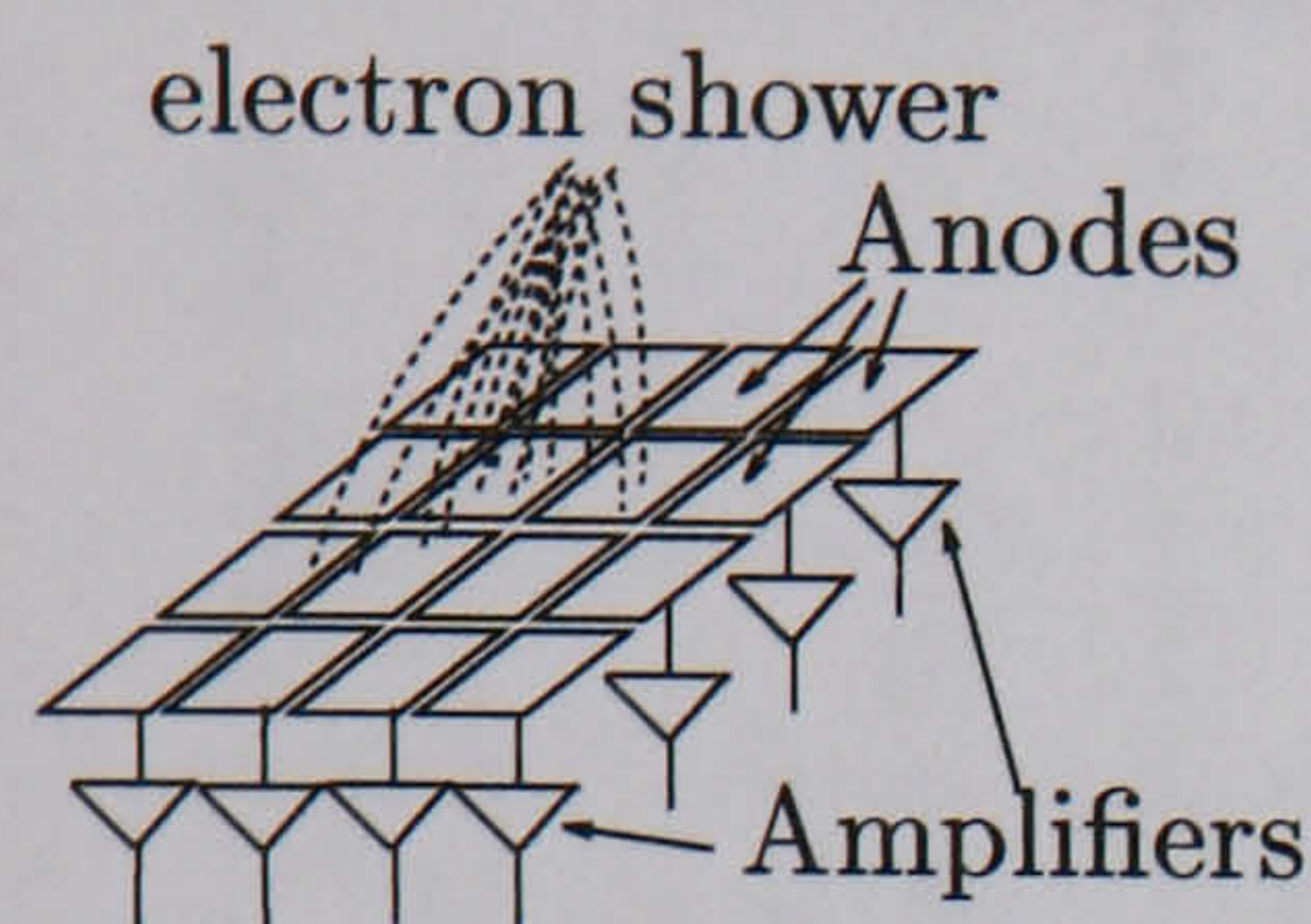


Figure 3.11: Segmented anode array.

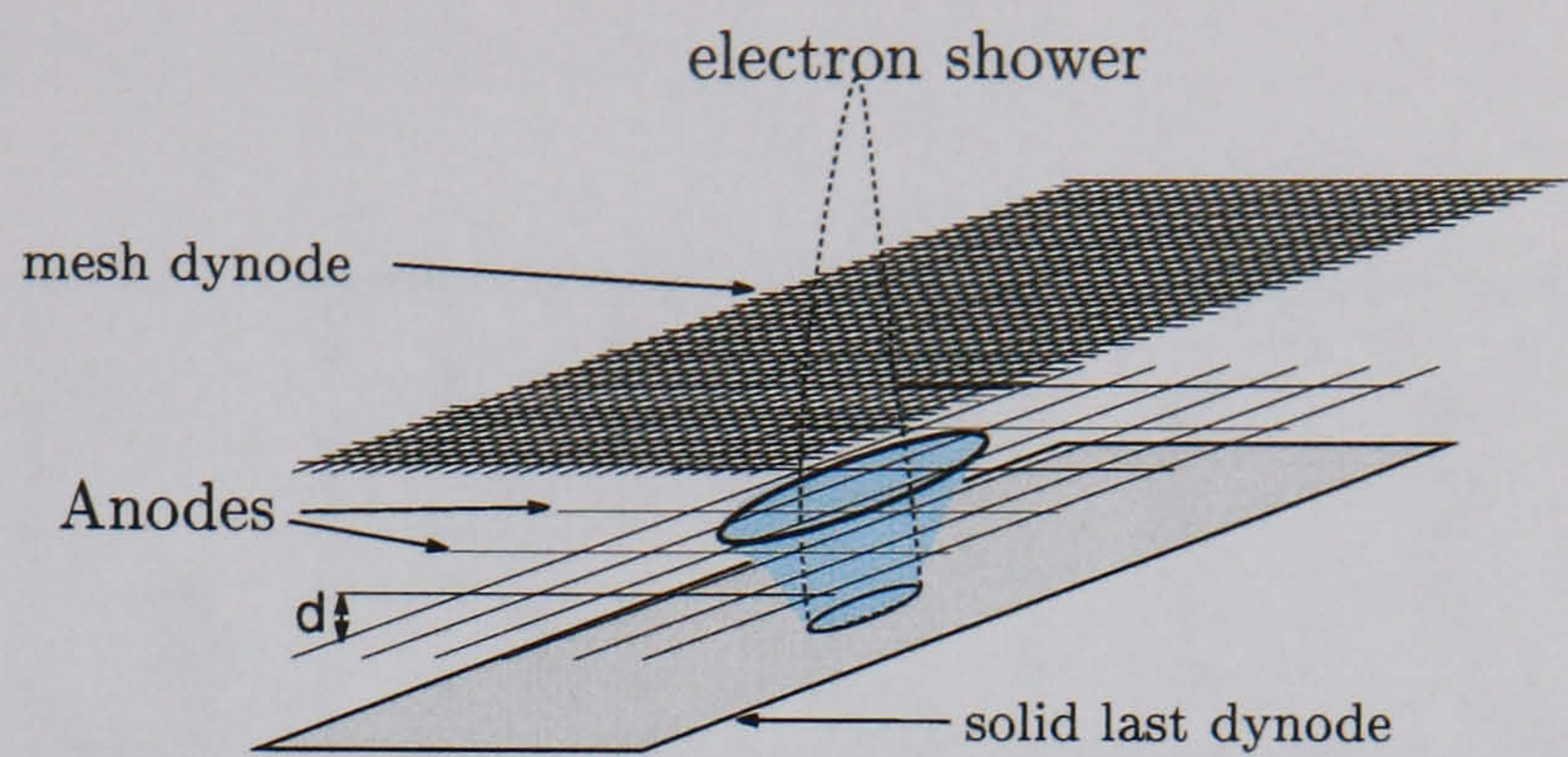


Figure 3.12: Crossed wire anode with a reflective last dynode.

possible to establish the correct (x, y) combinations with the information contained in the anode wires, thus reducing the count rate capability.

3.2.4 Currently available PSPMTs

There are several types of PSPMTs commercially available, with entrance window sizes ranging from $28 \times 28 \text{ mm}^2$ to 5 inch diameter. The dynode structures used are coarse mesh and metal channel, the latter being used only for small size tubes ($28 \times 28 \text{ mm}^2$). A choice of segmented anode arrays or crossed wire anodes is also available. A compilation of the basic characteristics of the most relevant PSPMTs is presented in table 3.2. Due to their relatively large areas, the Hamamatsu R2486/7 and R3292 have been proposed for single PMT small gamma cameras. Smaller PSPMTs are particularly suited for optical fibre readout and for very small gamma ray imaging probes.

PSPMT	Entrance window	Anode Layout	Dynode structure	Gain	Electron cloud spread	Photon counting	Cross talk
Hamamatsu coarse mesh dynode PSPMTs							
R2486/7	3" round/square	16 + 16 crossed wires	coarse mesh	$10^5 - 10^6$	$\sim 4\text{ mm}$ [49]	not appropriate (low gain)	N/A
R3292	5" round	28 + 28 crossed wires	coarse mesh	$10^5 - 10^6$	$\sim 4\text{ mm}$ [49]	not appropriate (low gain)	N/A
Hamamatsu R5900 series - metal channel dynodes							
C8(12)	$1 \times 1\text{ in}^2$	4(6) + 4(6) crossed wires	metal channel	10^6	$\leq 1\text{ mm}$ (section 7.2)	see section 7.2	N/A
M16	$1 \times 1\text{ in}^2$	4×4 multi-anode	metal channel	$10^6 - 10^7$	$\leq 1\text{ mm}$ (section 7.3)	excellent (section 7.3)	$\leq 1\%$ (section 7.3)
M64	$1 \times 1\text{ in}^2$	8×8 multi-anode	metal channel	$10^6 - 10^7$	$\leq 1\text{ mm}$ (section 7.4)	excellent (section 7.4)	$\leq 1\%$ (section 7.4)
Photonis XP1700 series - metal channel dynode PSPMTs							
1702/4 Glass window	1 inch diameter	64/96 pixels multi-anode	metal channel	$10^6 - 10^7$	$\leq 1\text{ mm}$	adequate	$\leq 20\%$ [94]
1722/4 Fibre-optic window	1 inch diameter	64/96 pixels multi-anode	metal channel	$10^6 - 10^7$	$\leq 1\text{ mm}$	adequate	$\leq 10\%$ [94]

Table 3.2: Characteristics of some PSPMTs commercially available. The cross-talk figures correspond to average cross-talk between nearest neighbours.

3.3 PSPMT gamma cameras for Single Photon Imaging

3.3.1 Single tube cameras

Continuous crystal cameras

The concept of a compact gamma camera based on a single PSPMT is similar to that of the Anger camera. A planar scintillation crystal is coupled to the PSPMT and, for a given gamma ray interaction, the light pool created at the PSPMT photocathode creates a charge pulse in the PSPMT. The charge is collected by an array of anodes (or crossed-wires), and, as discussed above, its spatial distribution preserves the information about the position of the gamma ray interaction (figure 3.13). Following the commercial introduction of the 3" PSPMT from Hamamatsu, several groups have proposed small gamma ray imagers for applications in small organ imaging in nuclear medicine [65, 66, 95], for gamma ray telescopes and spectrometers in astronomy [74, 75], for nuclear survey instruments [96] and for radionuclide mapping [97].

The diagram in figure 3.13 shows a scintillator coupled to a PSPMT. If the scintillator is hygroscopic, like NaI(Tl), it requires a moisture proof encapsulation, otherwise it may be directly coupled to the PSPMT window with an optical gel or cement to optimize the light collection. The internal surfaces of the encapsulation are usually coated with a highly reflective material.

The spatial resolution of such imagers is primarily dependent on three factors:

1. The width of light distribution created at the photocathode. The light that reaches the photocathode can be divided into direct and indirect light. The former is the fraction of light that exits the scintillator directly through the window without any reflections inside the scintillator. It depends mainly on the differences in refractive indices of the scintillator, scintillator window, optical gel and PSPMT window, which define the exit cone of acceptance according to the critical angle for total internal reflection. Indirect light is reflected inside the scintillator and eventually reaches the PSPMT. This component does not usually contribute reliable spatial information but degrades the spatial resolution. It is however unavoidable, and helps to improve the energy resolution.

The dimensions of the light pool at the photocathode depend strongly

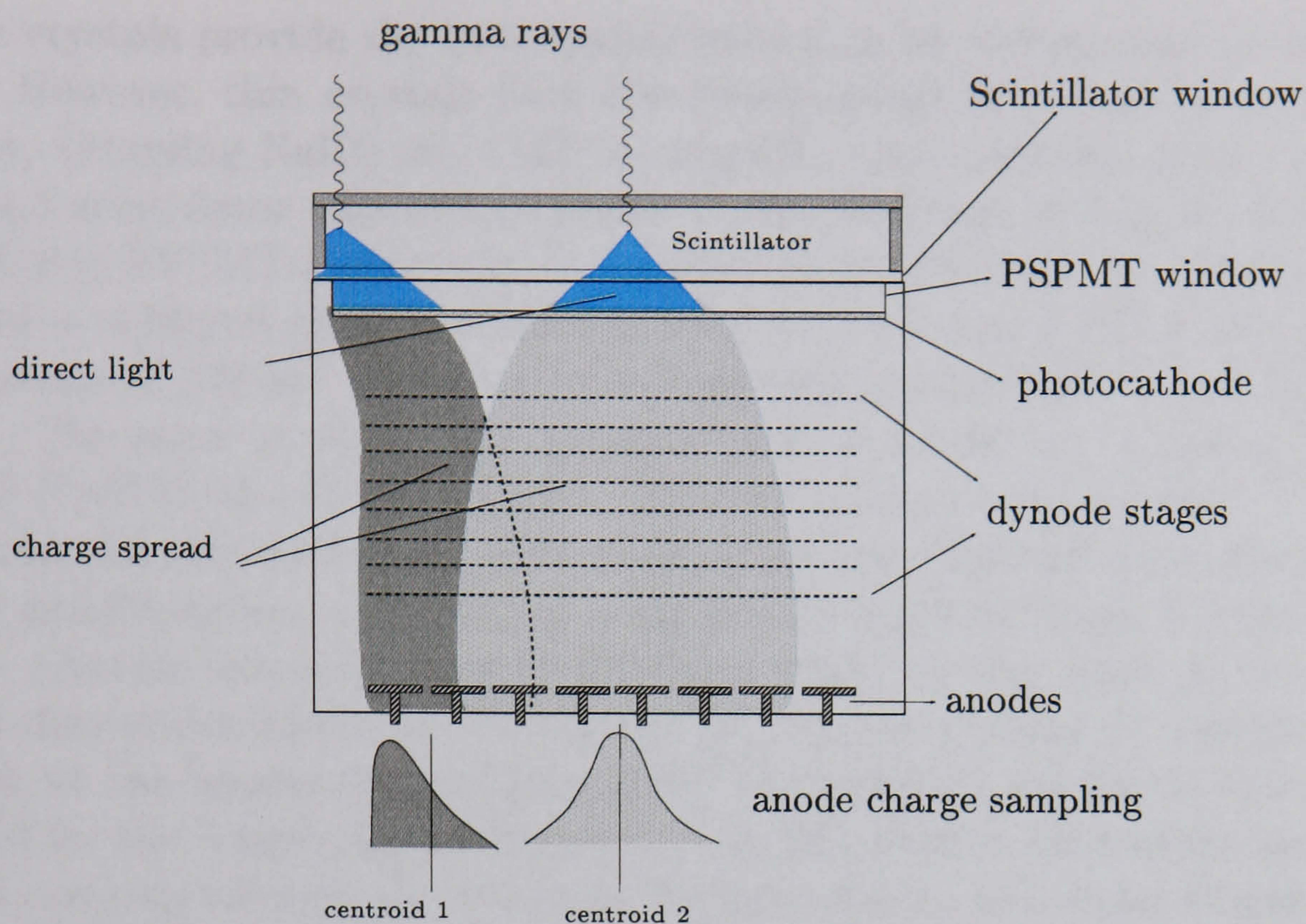


Figure 3.13: Diagram of a PSPMT based gamma camera.

on the distance between the region where the optical photons are created and the photocathode plane. This distance is determined by the thickness of the scintillator, the thickness of the tube window and the properties of any other optical components.

2. The electronic cloud spread through the multiplication process in the dynode stages before reaching the anodes. It depends on the specific characteristics of the dynode structure. For the Hamamatsu coarse mesh dynodes (3" and 5" tubes) this spread has been measured to be of the order of 4 mm FWHM [61].
3. The number of photoelectrons created at the photocathode.

Items 2 and 3 above can be expressed as the intrinsic resolution of the PSPMT for a given number of photoelectrons. An intrinsic sub-millimetre resolution has been reported by H. Kume *et al* [60, 61] and by K. Kuroda *et al* [53] for pulses of about 100 photoelectrons or more using fine-mesh dynode PSPMTs. This is the number of photoelectrons expected to be produced by gamma ray interactions with energy greater than 60 keV on the most common inorganic scintillators.

Therefore, of the three factors above, the first is usually dominant in determining the spatial resolution of the gamma ray imager.

Thin crystals provide the best spatial resolution by minimising the light spread. However, thin crystals have the disadvantage of a worse detection efficiency. Coupling NaI(l) and CsI(Na) crystals, with thickness from 1.6 to 3 mm and scintillator windows of about 2 mm thickness, to the 3" Hamamatsu R2846 PSPMT (table 3.2), C.J. Hailey *et al* [74] and J.M. Poulsen *et al* [75] have achieved spatial resolution from 1.7 to 2 mm FWHM for collimated beams of 122 keV gamma rays at the centre of the field of view of the camera. The same authors have found an energy resolution of about 10% and 12% FWHM, at 122 keV, for NaI(Tl) and CsI(Na) respectively.

Another feature which has been observed is the small effective imaging area (40 mm diameter) of the camera compared to its physical size (75 mm diameter). Outside this area, close to the edges of the camera, there are strong position distortions which are introduced by the non-symmetric charge distribution at the anode wires (figure 3.13) The effect is similar to the one described for the Anger camera (figure 2.7) and it causes a shift of the reconstructed position towards the center of the tube due to the center of gravity calculation with a non-symmetric charge distribution ("centroid 1" in figure 3.13). The distortions are even more significant with a resistive chain readout of crossed-wire anodes (as explained in section 3.5), the simpler and less expensive readout method.

The energy resolution is also worse near the edges as a result of poorer light collection. A.J. Bird *et al* [66] have reported an energy resolution of up to 16% FWHM at the edges, for a NaI(Tl) crystal coupled to a Hamamatsu R2487 PSPMT.

For even thinner (1 mm thick) YAP crystals, which do not require encapsulation, and an optimized individual anode readout (section 3.5) a spatial resolution of 1.2 mm FWHM for 122 keV gamma rays has been reported by A.G. Weisenberger *et al* [43].

For nuclear medicine the need for high conversion efficiency requires thicker NaI(Tl) crystals. These increase the distortions at the edges of the camera, reducing even more the field of view and worsen the spatial resolution. This was demonstrated using 5 and 8 mm thick NaI(Tl) with a 3" square Hamamatsu R2487, where spatial resolutions of 2.5 to 4 mm FWHM were obtained by A.J. Bird *et al* [66], by N.J. Yasillo *et al* [65] and by J.N. Aarsvold *et al* [98].

Due to its small effective area, the 3" PSPMT has found very few applications in nuclear medicine, despite the excellent performance demonstrated. Moreover, their small field of view compared to the physical size of the PSPMT means there is a dead area of about 2 cm from the edge of the field of view to the edge of the PSPMT, making it difficult to pack several of these PSPMTs into a large area array.

The 5" diameter circular R3292 (table 3.2) seems for this reason more attractive for a single tube camera. It is very similar to its 3" counterpart but, in order to withstand atmospheric pressure over a large area, its entrance window is 6 mm thick compared to 3 mm in the 3" PSPMT. According to the previous considerations the spatial resolution should be worse due to a greater light spread over the photocathode. For a 3 mm thick NaI(Tl) crystal, resolutions of 4 and of 15 mm FWHM have been reported by Z. He *et al* [99] at the center of the camera and near its edges respectively. There are also strong position distortions near the edges of the camera with the 5" PSPMT using a resistive chain readout scheme, where the effective imaging region is only about 75 mm diameter compared to 120 mm diameter of the 5" PSPMT.

In section 3.5 other electronic readout methods are described which decrease the size of the distorted region and improve the spatial resolution. Recently, for example, N. Schramm *et al* [100] coupled a 5" PSPMT to a 2 mm thick NaI(Tl) and with an optimized readout system obtained an intrinsic spatial resolution of 1.4 mm FWHM with an energy resolution of 8.5% FWHM for 140 keV gamma rays. The usable field of view had a diameter of 90 mm, which is still small compared to the 120 mm diameter of the PSPMT.

However, to obtain good spatial resolution the most powerful method is to concentrate the light in a small spot on the photocathode, and, with a single crystal, this can only be accomplished by reducing its thickness. This approach is not a practical solution in the case of nuclear medicine imaging due to the reduction in detection efficiency, which is dictated by the maximum reasonable dose given to the patient (for the 2 mm NaI(Tl) mentioned in the previous paragraph, the conversion efficiency for 140 keV is only about 40%).

Segmented crystal arrays

Localisation of the light can be achieved without loss of detection efficiency by the use of segmented crystal arrays. The crystals are cemented together with an epoxy loaded with a highly reflective component (e.g. titanium dioxide) that optimises the light collection and optically isolates each element from its neighbours. The width of the light distribution at the PSPMT is determined by the cross sectional area of the crystal segments. Most common scintillators can be cut into elements as small as $1 \times 1 \text{ mm}^2$, with enough height (thickness) to provide the adequate efficiency (e.g. 10 mm or more).

Several scintillators have been used with a variety of element sizes. As mentioned in section 3.3.1, the intrinsic resolution of the PSPMTs is less than 1 mm for pulses of 100 photoelectrons or more, which is the expected light output of common scintillators for 140 keV gamma rays. Therefore,

the spatial resolution of a gamma camera with segmented crystal arrays is usually dictated by the dimensions of the crystal elements (*pixel resolution*) as shown by K. Blazek *et al* [101]. Having a thinner window than the 5" tube, the 3" PSPMT has a better resolution. This is seen in its ability to differentiate crystals as small as $0.5 \times 0.5 \text{ mm}^2$ as reported by L.M. Barone *et al* [102] and by F. Vittori *et al* [103].

However, crystal elements with small cross-section and large thickness introduce a severe drawback. The light created inside an element undergoes multiple reflections at the boundaries of the crystal which increases the probability of absorption. This reduces the number of photoelectrons created, with a direct impact on the energy resolution of the imager.

Light reduction increases with the ratio between the crystal height and its cross-section area. As an example, R. Pani *et al* [104] have observed that the signal from a $0.6 \times 0.6 \times 7 \text{ mm}^3$ YAP crystal was 4 times smaller than from a large area 1 mm thick YAP crystal, giving an energy resolution degradation from 20% to 50%, for 140 keV gamma rays.

Several authors have measured the light yield of various scintillators with different areas and thickness and demonstrated that, for areas less than $1 \times 1 \text{ mm}^2$ and thickness of more than 10 mm a strong loss of light occurs with a corresponding degradation in energy resolution.

Small gamma cameras with multiple crystal elements of $2 \times 2 \text{ mm}^2$ and $3 \times 3 \text{ mm}^2$ and about 5 mm thickness have been built by several research groups [105, 106, 107, 42, 108] providing a spatial resolution of 2 or 3 mm FWHM (pixel resolution), when coupled to the 3" or to the 5" PSPMTs.

Another effect that has been studied is the finish of the surfaces of the crystals, whether it is polished or ground, if it is coated with a specular reflector, with a diffuse reflector or left uncoated. A. Wirrwar *et al* [109] have performed Monte Carlo ray tracing simulations, confirmed by experimental results, which have shown that a highly reflective diffuse coating such as titanium dioxide should be used to optimize the light output.

The best results obtained by other authors for 140 keV have shown an energy resolution of 18% FWHM for $2 \times 2 \times 6 \text{ NaI(Tl)}$ [108] and CsI(Na) [109] elements and 17% FWHM for $2 \times 2 \times 3 \text{ CsI(Tl)}$ elements [107]. These results are poor compared to 10% FWHM energy resolution of modern Anger cameras which is also obtained with single crystal PSPMT-based cameras [100].

In summary, the choice between single continuous crystals and segmented crystal arrays implies a trade-off between spatial resolution, conversion efficiency, energy resolution and effective field of view. With single crystals, good spatial resolution, large field of view and good energy resolution are obtained at the expense of conversion efficiency (thin crystals). With segmented arrays, good spatial resolution, large field of view and high conversion

efficiency are obtained at the expense of energy resolution.

3.3.2 Arrays of PSPMT

The design of small gamma cameras based on a single large PSPMT has the disadvantage of restricting the size and shape of the camera to the dimensions of the PSPMT itself. A more flexible design is achieved by using smaller area PSPMTs which may be assembled in arrays to provide the required shape and size of the imaging area.

Due to their compactness and square shape, the 1×1 in² Hamamatsu R5900 series PSPMTs are particularly suitable for this application. Chapter 7 presents our own results from the evaluation of the performance of some of these PSPMTs, including a discussion of the performance of small gamma cameras based on arrays of R5900 PSPMTs.

3.4 PSPMT high resolution PET detectors

Segmented scintillators are used with conventional single anode PMTs in commercially available high spatial resolution PET imagers [110, 111]. The crystal arrays are coupled to an array of PMTs (usually 2×2) and the crystal of interaction is identified through light sharing between the PMTs and using an Anger logic readout scheme (figure 2.9 shows an example of a PET detector module). Better spatial resolution could in principle be achieved using the PSPMTs described in the previous section. PET modules have been proposed where arrays of segmented crystals are coupled directly to the Hamamatsu 3" PSPMT [112, 64, 62, 113] able to distinguish individual crystal elements as small as 2×2 mm². Smaller modules have also been built with Hamamatsu 1" R5900-C8 PSPMTs which provide good spatial resolution in a very compact and close packing geometry, with the advantage of higher count rate compared to the 3" PSPMT design. This is due to the smaller size of each module allowing a higher number of simultaneous gamma ray events per unit area if each PSPMT module is read out independently. The reduction of light due to segmentation can be compensated by the use of LSO instead of BGO which is a much brighter scintillator and with the further advantage of a faster decay time.

Another technique aimed at optimizing the close packing of scintillator crystals in a PET ring is to couple individual crystals to the PSPMTs using optical fibres, as suggested by S.R. Cherry *et al* [114]. The metal channel PSPMTs from Philips and Hamamatsu (table 3.2) have very low cross-talk and are therefore very suitable for the readout of multiple optical fibres. An-

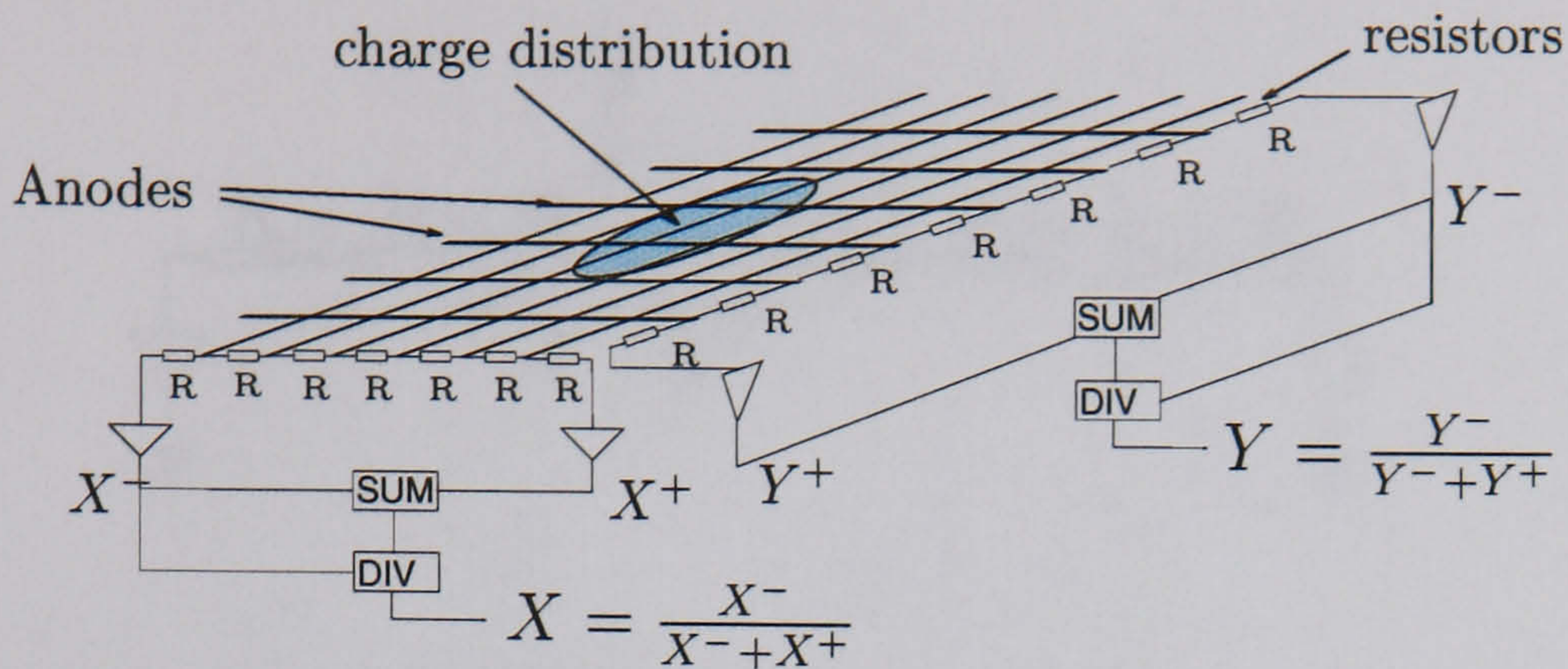


Figure 3.14: Crossed-wire anode with resistor chain readout.

other advantage of such a design is to be able to physically separate the scintillators from the PSPMTs, opening the possibility for a PET-NMR (Nuclear Magnetic Resonance) compatible system [115], with the PSPMTs outside the magnetic field.

3.5 PSPMT readout methods

The readout of PSPMTs may be performed by two distinct methods: resistor network readout or individual anode readout.

3.5.1 Resistor network

Resistor network readout is based on the Anger logic readout of gamma cameras (section 2.3.1). The PSPMT anodes are connected to a resistor network that divides the charge and allows a centroid calculation by a centre of gravity method. Its simplest design is often used with crossed-wire anodes where a resistor chain connects all the anodes (figure 3.14).

Only four signals need to be read out, X^- , X^+ , Y^- , Y^+ which greatly simplifies the electronics system and also reduces the cost. An illustration of the charge division is shown in figure 3.15, where 7 anode wires perpendicular to a given direction x are represented, all connected by a resistor chain.

When a charge Q^j is injected at a wire j ($j = 1, \dots, 7$), it is divided in two components Q^- and Q^+ according to the number of resistors between that anode and the extremities of the resistor chain. These charge signals may be read out using charge sensitive amplifiers producing voltage signals X^- and X^+ proportional to Q^- and Q^+ . A value X proportional to the position of charge injection along the x direction may be defined as

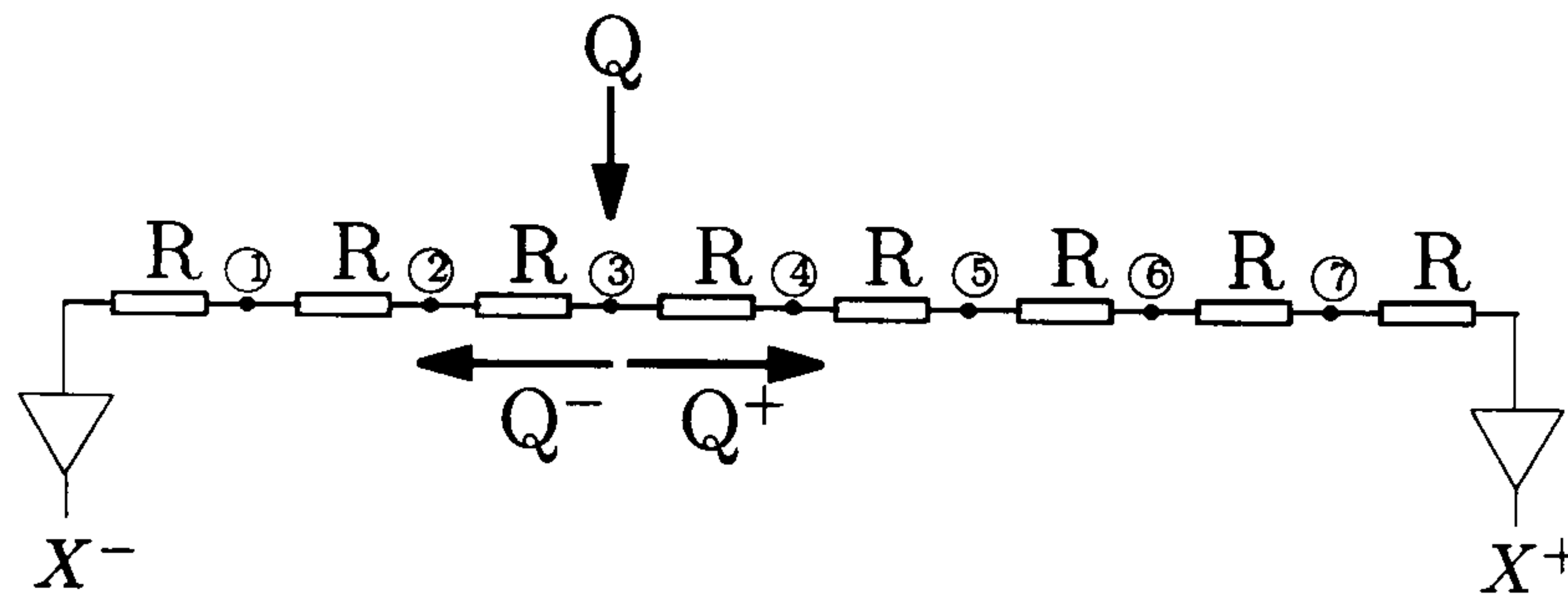


Figure 3.15: Illustration of a resistor chain.

$$X = \frac{X^-}{X^- + X^+} = \frac{j}{8} \quad (3.6)$$

where j is a number representing the wire anode where the charge is injected, and 8 is the total number of resistors. If charge is injected at more than one anode wire, which is the realistic case in a PSPMT, the value of X is

$$X = \frac{X^-}{X^- + X^+} = \frac{\sum_{j=1}^7 jQ^j}{8 \sum_{j=1}^7 Q^j} \quad (3.7)$$

which is the centre of gravity calculation (or centroid) for the total charge distributed across the anodes.

This method works well if the charge is symmetrically distributed around the position of gamma ray interaction, which is the case for interactions occurring in the central region of a PSPMT. Towards the edges, the charge distribution is truncated at the peripheral anode and the position calculation is distorted towards the center of the camera, decreasing the effective imaging area (figure 3.13). A way of reducing this effect has been suggested which consists of increasing the resistor values at the edges of the resistor chain to compensate for the truncated charge distribution. A 39% increase in the effective field of view was reported with this simple technique [116].

PSPMTs with discrete anode pixels (figure 3.11) can also be read out with resistor networks very similar to Anger cameras, where the PMT array is replaced by the PSPMT anode array [117].

In section 3.2.3 it is mentioned that the crossed-wire readout method reduces the count rate capability of the PSPMTs. If two narrow beams of

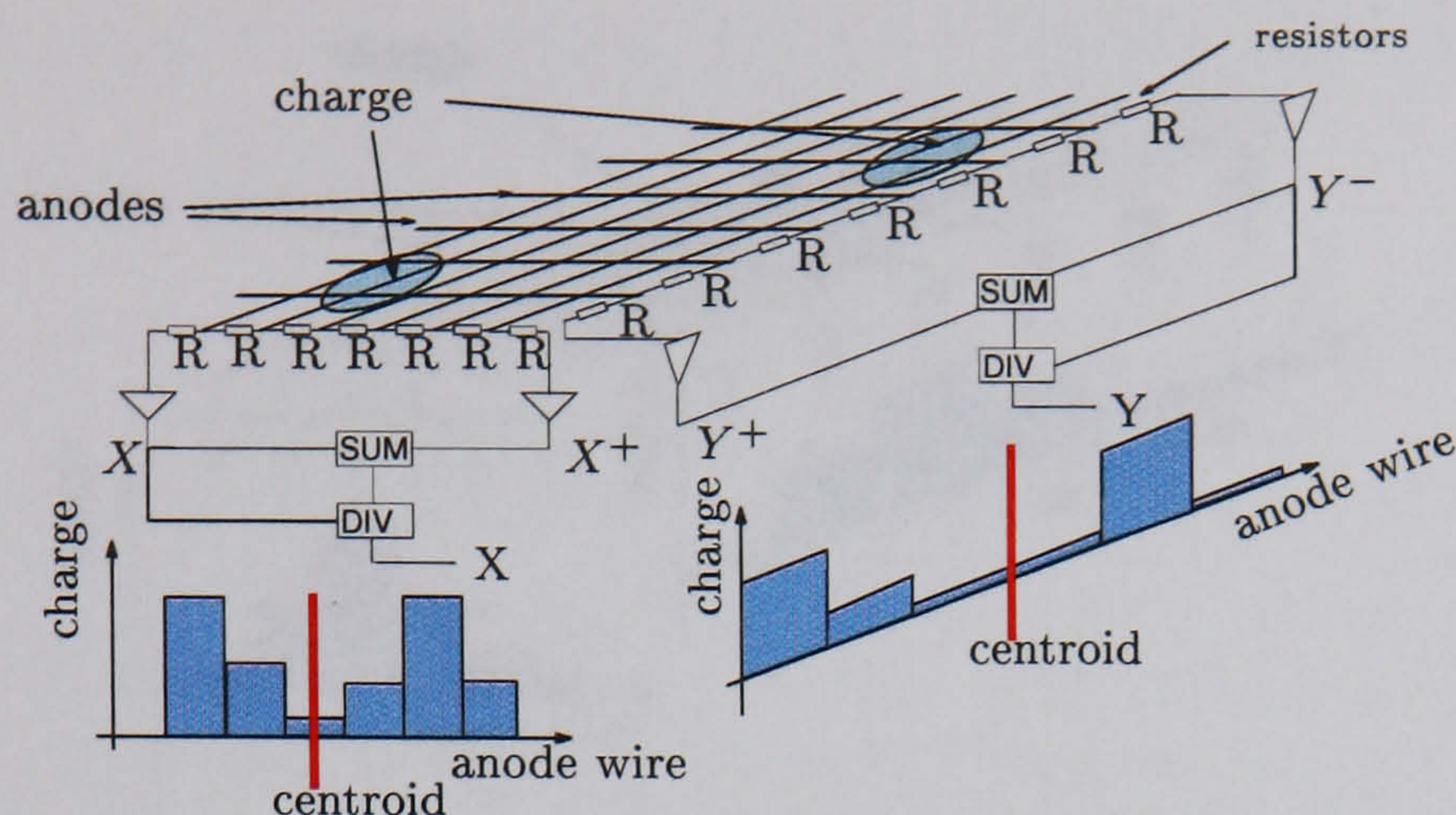


Figure 3.16: Two simultaneous events which cannot be correctly identified with a resistor chain readout.

light (e.g. from optical fibres or segmented crystal arrays), representing simultaneous uncorrelated events, impinge on the photocathode, the centroid calculation wrongly represents the middle point between the two light distributions (figure 3.16). For the case of crossed-wire anodes this cannot be corrected even reading out each anode individually. Discrete anode pixels can be read out separately to avoid this position ambiguity. However, if they are connected to a resistor network this effect occurs in a similar way to the crossed-wire anode. In some cases this effect is not very important. An example is gamma ray imaging with scintillation crystals in nuclear medicine in which the count rates are relatively low (e.g. < 25 kHz) and, therefore, it is very unlikely that two gamma rays interact in the crystal simultaneously. In this case, resistor networks may prove to be a useful choice if simplicity and cost are major requirements.

3.5.2 Individual anode readout

If each anode signal is read out and digitised independently it is possible to sample the charge distribution across the anodes and the position finding may be done in software with the most appropriate method. A simple centroid, for example, is equivalent to a resistor chain readout. However, in this case there is the possibility of setting thresholds in each individual anode, and prevent electronic noise from low signal anodes from distorting the centroid calculation [118, 119] and degrading the energy resolution.

The charge distribution across the anodes may also be fitted with an appropriate function and the position of the event determined by the parameterisation. Fitting a Gaussian [120] distribution to the charge profile

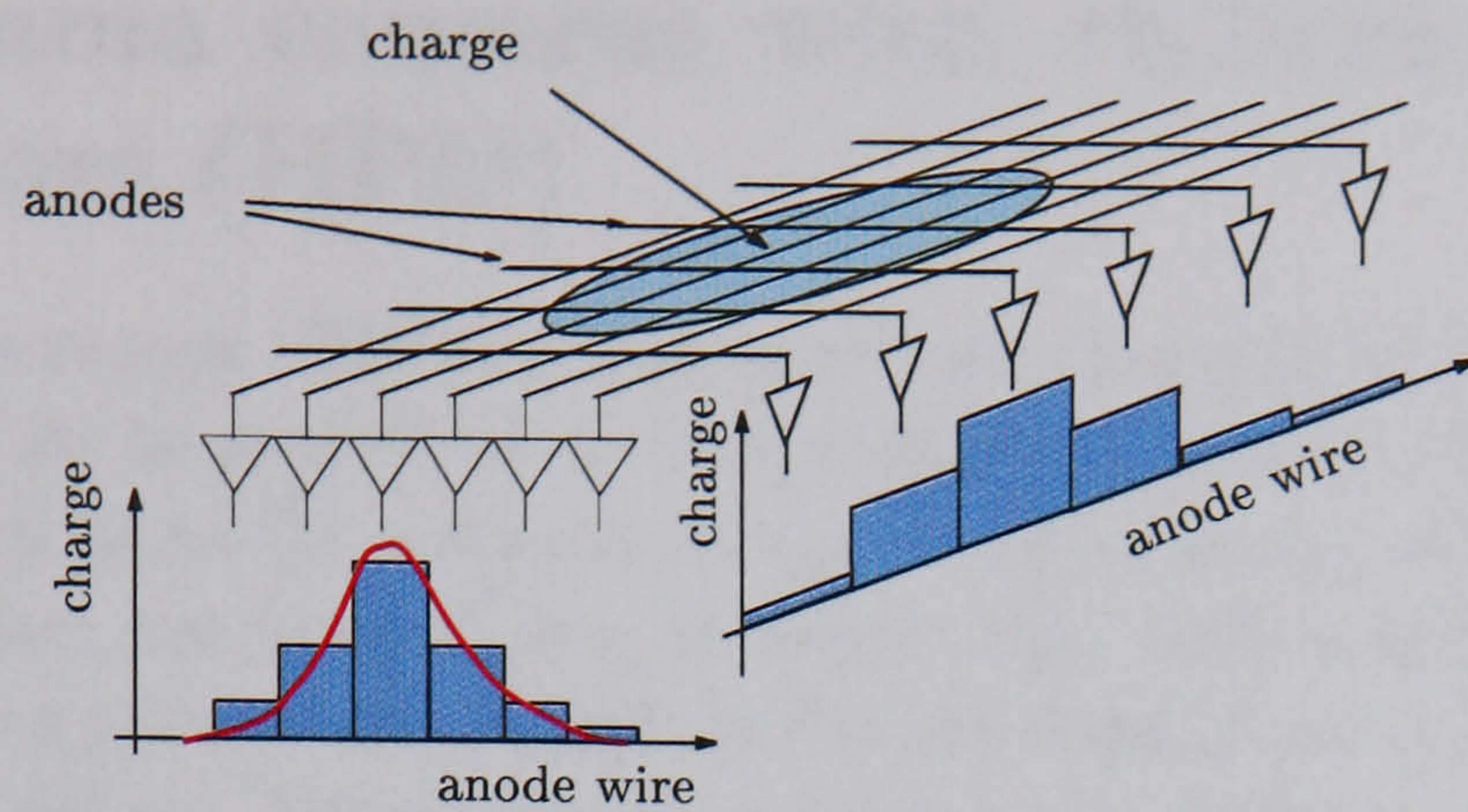


Figure 3.17: Individual anode readout of a crossed-wire anode PSPMT. The charge profile across the anode wires is sampled.

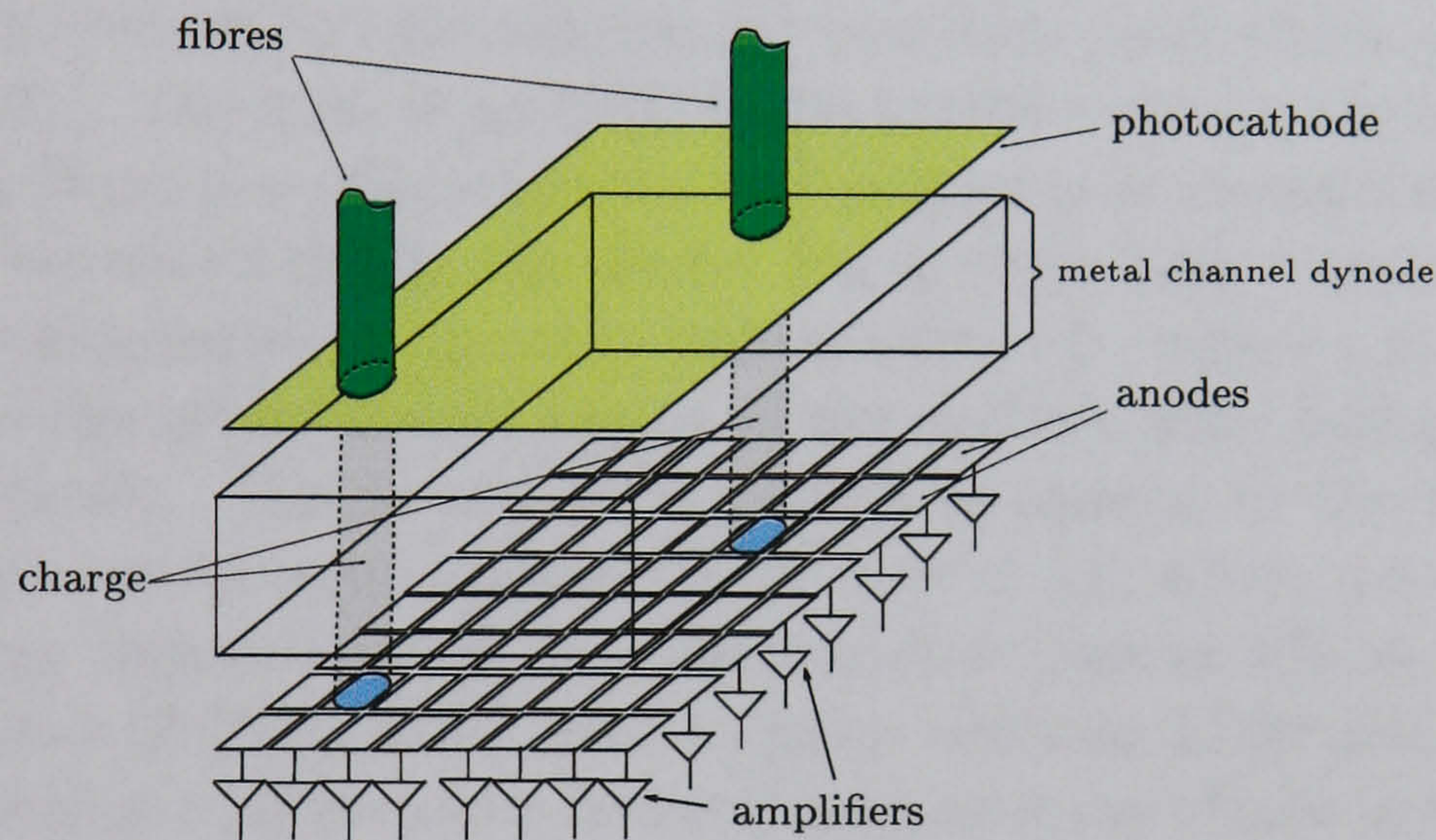


Figure 3.18: Individual anode readout of a segmented anode PSPMT.

across the anodes of a crossed-wire anode PSPMT as depicted in figure 3.17, a significant improvement in linearity (field of view) has been achieved, with improved spatial resolution [105] compared to a resistor chain readout.

In some cases it is important to be able to read out correctly simultaneous light distributions such as those shown in figure 3.16, which may be created, for example, by several optical fibres. For these cases it is adequate to use a PSPMT with low transverse diffusion of the electron charge (e.g. with metal channel dynodes) and discrete anode pixels which, if read out individually provide unambiguous position reconstruction even for simultaneous events at different anodes. The charge stimulated by each fibre is then collected by a single anode and the individual anode readout gives an unequivocal identification of each fibre (figure 3.18).

3.6 Gamma cameras with Hybrid Photodetectors (HPD)

Hybrid photodetectors (HPD), sometimes also called hybrid photodiodes or hybrid PMTs, can be described as image intensifiers where the output phosphor screen is replaced by a silicon diode, or by an array of several of them. Like a PMT, they are housed in a vacuum tube, with a light entrance window, which also serves as the substrate for the deposition of a photocathode. The anode is a silicon diode located opposite the entrance window. A high voltage difference (10 to 25 kV) is applied between the photocathode and the anode, to accelerate the photoelectrons created at the photocathode into the diode, by means of a carefully designed electrostatic focusing system. The diode is biased and fully depleted. When the high energy electrons hit the diode, they lose their energy by creating electron-hole pairs which produce a charge signal [121]. The gain of an HPD is the number of electron-hole pairs created in the silicon per photoelectron and is primarily dependent on the energy of the electron as it hits the diode. For a given high voltage, V , the energy of the impinging electron is the sum between eV , where e is the electron charge, and the initial kinetic energy of the electron after being released by the photocathode. The second is very small compared to the first, and therefore the gain can be approximated by $G = eV \div 3.6$, where 3.6 eV is the amount of energy required to create a electron-hole pair in silicon. Typical high voltage values of 10 to 25 kV lead to gains between 2,500 and 7,000.

A position sensitive HPD can be created using an array of silicon diodes [122]. Imagers with excellent spatial resolution have been built with pixel sizes ranging from $75 \times 500 \mu\text{m}^2$ to $2 \times 2 \text{ mm}^2$. They are very attractive for optical fibre readout [122], for ring imaging Cherenkov counters [123] and for gamma ray imaging when coupled to a suitable scintillation crystal [124]. Small HPD-based gamma cameras have been proposed to take advantage of the high intrinsic spatial resolution of the HPDs. With a thin (1 mm) single CsI(Tl) crystal a 0.7 mm FWHM intrinsic resolution was obtained [125]. With segmented YAP arrays of $0.3 \times 0.3 \text{ mm}^2$ and $0.6 \times 0.6 \text{ mm}^2$, 5 mm thick pixels, the spatial resolution was 0.5 mm FWHM, but with poor energy resolution of 40% due to the segmentation.

The number of readout channels increases with the size of imaging HPDs, requiring more complex and more expensive readout circuits. Recently there has been a considerable effort in developing low cost, integrated multi-channel readout systems for HPDs, mainly using technology from silicon strip detectors [123, 126]. Being still in a development stage, HPDs are considerably more expensive than PSPMTs.

3.7 Scintillation imagers with semiconductor photodiodes

Light sensitive semiconductor detectors are also very attractive for readout of light pulses from scintillation crystals. They are more compact than photomultipliers and cost much less. They have higher quantum efficiency across the visible spectrum, and good immunity to magnetic fields due their planar structure and to the short electrical carrier paths. Scintillation crystal arrays with small pixels can be individually matched to small photodiodes to produce high spatial resolution imaging detectors for gamma rays and high energy charged particles. Applications for these imagers are found in nuclear and high energy physics [127, 128, 129], astronomy [130], nuclear medicine [131, 132, 133, 134, 135, 136, 137] and explosives detection [138]. The typical disadvantage of photodiodes compared to photomultipliers is the fact that the former usually have no internal charge amplification, except for avalanche photo-diodes (APD) and visible light photon counters (VLPC), which will be described later. This imposes a lower limit on the energy of a particle which can be detected with a photodiode-scintillator combination (energy detection threshold). This is due to the presence of electronic noise, coming from two main sources:

- leakage currents. Bulk leakage arises primarily from thermal generation of electron-hole pairs. It depends therefore on the temperature, on the bandgap energy of the material (e.g. 1.12 eV for Si at 300 K) and on the volume on the diode. It can be reduced by cooling the photodiode. Surface leakage take place at the edges of the junction, where the electric fields are very high. It varies with type of encapsulation used, with humidity and with surface contamination. It can be reduced by the use of guard rings, by high quality encapsulation or by surface passivation techniques (e.g. creation of a SiO_2 insulation layer).
- noise in the pre-amplification stage of the external electronics. This, to a first approximation, depends on the noise of the input transistor and on the junction capacitance of the diode.

The electronic noise contributes significantly to the energy resolution of the detector, particularly for energies near the minimum energy threshold. Furthermore, the noise levels mean that there are no gain-free semiconductor detectors with single photon detection capability.

3.7.1 Silicon pixel arrays

Some of the first attempts at using silicon photodiodes with scintillation crystals were aimed at the detection of high energy charged particles in cosmic ray telescopes and nuclear particle detectors in the early 1960s [139, 140, 128, 129]. Silicon surface-barrier diodes with diameters from 1 mm to 2.5 cm were coupled to CsI(Tl) crystals, and the detector was irradiated with about 40 MeV protons and 5.5 MeV α particles. The advantages of CsI(Tl) over other scintillators (see table 3.1) are its high light yield, moderately high Z and density and the good match between its emission spectrum and the photo-sensitivity of silicon (which increases towards the infra-red region). The results confirmed the high photo-sensitivity of silicon ($\geq 70\%$) for the emission light of CsI(Tl). However, the high leakage current of the diode, together with the difficulty in preparing low noise pre-amplifiers to match its high capacitance, limited the use of these detectors to particles with energies ≥ 5 MeV. A similar geometry was used with p-n junction diodes and CsI(Tl) for gamma ray spectrometry [141] at around the same time. The lower leakage current of the diode and the use of low noise FET transistors at the input of the pre-amplifier, resulted in 180 keV energy threshold for gamma rays.

Silicon PIN Diodes

Silicon PIN photodiodes have an intrinsic region between a p and an n region which is usually created by the diffusion of donor (e.g. lithium) atoms to compensate the excess in acceptor impurities observed even in high purity silicon samples. Thus, low leakage current is obtained which, combined with small diode capacitance, produces an overall reduction in electronic noise even in large area ($\geq 10 \times 10$ mm²) devices. Silicon PIN diodes are widely available at very low cost (e.g. \$1 per pixel) and have a very reliable performance.

Arrays of small size photodiode pixels (1.5 mm to 3 mm) coupled one-to-one to segmented CsI(Tl) crystals can in principle provide simple, compact and inexpensive gamma imagers with a high intrinsic spatial resolution limited by pixel size. Two recent studies, using photodiode arrays with 2×2 mm² [142] and 3×3 mm² [143] pixels, have shown noise levels per pixel of 26 electrons rms (at -30°C) and 140 electrons rms (at room temperature) respectively. In the first study, this led to a very low energy detection threshold of 3.7 keV and an energy resolution of 7.5% FWHM for 122 keV gamma rays, when $2 \times 2 \times 4$ mm² CsI(Tl) pixels were individually coupled to the photodiodes. In the second, quantum efficiency values of 75% and 90% were measured for 415 nm and 480 nm respectively.

Integrated circuit amplifier arrays have been developed for silicon microstrip detectors, particularly for particle physics applications, which may be customised to read-out silicon photodiode arrays [144].

Following these results, a gamma camera prototype for breast imaging (140 keV gamma rays) has been built [132]. An 8×8 array of $1.5 \times 1.5 \text{ mm}^2$ photodiodes size-matched to a segmented CsI(Tl) crystal, with $1.5 \times 1.5 \times 6 \text{ mm}^3$ pixels, showed an energy resolution of 8.3% FWHM for 140 keV at room temperature, with an intrinsic spatial resolution of 1.5 mm FWHM, limited by pixel size. For the same application, another prototype has been built with 3×3 pixel photodiodes coupled to $3 \times 3 \times 5 \text{ mm}^3$ pixels [131]. Again an excellent energy resolution of 10.6% FWHM was obtained for 140 keV gamma rays at room temperature, with a spatial resolution given by the pixel size. Although the spatial resolution is worse in this design, it has the advantage of reducing by 4 the number of read-out channels in a full-size device. For a $12 \times 12 \text{ cm}$ camera, for example, there will be 6,400 channels in the first and 1,600 in the second design, which contrasts with the simpler PSPMT readout. However, the constant improvement in multi-channel integrated read-out chips, with corresponding price reductions, makes this design very promising for future developments.

PET is another nuclear medicine technique which may benefit from the use of scintillator-photodiode modules, in particular to improve spatial resolution by the use of thin segmented crystal arrays. The concept is similar to the one discussed above, except that, due to the higher energy involved (511 keV), the scintillators most commonly used are BGO [145] and, more recently, LSO [136], which are more efficient than CsI(Tl). Their lower light yield (table 3.1) is a disadvantage for energy resolution. However, the small size of the photodiodes allows more favorable geometries for light collection. It was suggested, for example, that thin photodiode strips ($< 250 \mu\text{m}$) could be coupled to the sides of crystal segments to improve light collection [136]. In that work, photodiode strips of $3 \times 30 \text{ mm}^2$ were coupled to one of the larger faces of a $2 \times 2 \times 20 \text{ mm}^3$ segment of BGO and an energy resolution of 30% FWHM was achieved for 511 keV. Using the brighter scintillator LSO in a similar measurement with $2.5 \times 2.5 \times 20 \text{ mm}^3$ crystals the energy resolution was 23% FWHM.

Another option which has been studied is cooling the photodiode to reduce its dark current [146, 133]. The energy resolution for 511 keV gamma rays of a $3 \times 3 \times 3 \text{ mm}^3$ BGO crystal coupled to a $3 \times 3 \text{ mm}^2$ photodiode was 30%, 8.2% and 7.2% FWHM at 20°C , -75°C and -150°C , compared to 12% FWHM for the same crystal measured at room temperature with a PMT with a bialkali photocathode [146].

Recently, a CsI(Tl)-photodiode gamma camera became commercially avail-

able [147] from Digirad² with a pixel size of $3 \times 3 \text{ mm}^2$ and a field of view of $20 \times 20 \text{ cm}^2$ at an approximate cost of \$250,000.

Drift Si Photodiodes

Silicon drift photodiodes have an anode configuration which creates a potential well parallel to the diode surface in which the majority carriers (electrons) are made to drift towards a small collection anode [148]. Because of the small size of the anode, the detector capacitance is much smaller than that of a conventional diode and is independent of the active area of the diode. This reduces the electronic noise, with potential benefits for energy resolution and energy detection threshold. Furthermore, the front-end pre-amplification can be integrated on the detector chip [149], minimizing stray capacitances of the connections, further optimising the noise reduction. A circular diode with 3 mm diameter and 0.1 pF capacitance coupled to a CsI(Tl) of the same diameter showed an energy resolution of 7.5 and 4.4% FWHM for 122 and 662 keV gamma rays, at room temperature [150] with an energy detection threshold of 10 keV. Very recently, a gamma camera prototype was built based on a linear array of 6 hexagonal diodes coupled to a $14 \times 1.4 \times 1.4 \text{ mm}^3$ CsI(Tl) slab [135]. The concept is similar to a conventional Anger camera in which the PMTs are replaced by drift diodes, in the sense that the position of interaction of a gamma ray is calculated on the basis of light sharing between many photodiodes. Since these diodes have a homogeneous and non-structured entrance window, it is possible to build arrays with close to 100% fill factor when coupled to single CsI(Tl) slabs, which optimises the light collection efficiency. An average spatial resolution of about 0.7 mm FWHM was obtained. This excellent result is due to the small size of the diodes, the small thickness of the crystal and the close packing of the scintillator onto the diode array. The average energy resolution, obtained by summing the signals of all individual diodes, was 16.3% FWHM for 122 keV gamma rays, with the system cooled to about -40°C to reduce the leakage current. The difference between this result and that of a single drift photodiode mentioned above, can be explained by a larger contribution of the electronic noise due to the sum of the noise of multiple photodiodes.

Avalanche Photodiodes

In simple terms, avalanche photodiodes (APD) are silicon diodes to which a high electric field is applied in order to create an internal charge multiplication process (avalanche). The electrons created are accelerated by the

²Digirad, San Diego, CA, USA, www.digirad.com

electric field acquiring sufficient kinetic energy to create new electron-pair holes by impact ionisation, which will initiate a cascade. This internal amplification increases the signal-to-noise ratio compared to conventional silicon diodes, and is therefore very promising to achieve better spectral resolution. Avalanche photodiodes are also very competitive compared to PMTs for light measurements, since they combine the internal gain with a much higher quantum efficiency across the visible spectrum.

Early reliability problems were associated with local resistivity variations in the silicon which gave rise to gain variations and premature breakdown at these regions. However, due to significant improvements in the manufacturing technology, very reliable APDs, with active areas from a few micron to over 15 mm diameter, are now commercially available and have been tested with success. Internal gains usually range from 50 to 500 with quantum efficiency of over 60% between 400 and 800 nm [151, 152, 153]. Large area APDs (over 2 mm diameter) were suggested for PET [154] for a high spatial resolution imager with one-to-one coupling to segmented scintillators. LSO-APD modules for PET provide an energy resolution of 10% FWHM for 662 keV [155, 156], whereas for 122 keV gamma rays, encouraging results show 8.5% FWHM energy resolution using NaI(Tl) and CsI(Tl) [155]. A thorough comparison between APDs and PMTs for scintillation readout by Moszyński *et al* [157] led to the conclusion that currently available APDs perform equally and sometimes better than PMTs for the most commonly used scintillator materials.

To compete with PMTs at very low light levels, a higher gain is necessary to provide single photon detection. This will be discussed in the next chapter as part of a review of single photon detectors.

3.7.2 Mercuric Iodide pixel arrays

HgI₂ is a room temperature semiconductor. Its energy band gap is 2.13 eV which, compared with 1.12 eV for the case of silicon, provides a significant noise reduction at room temperature. Moreover, its quantum efficiency of about 70% over the visible spectrum makes it particularly attractive for detection of light from most common inorganic scintillators. Scintillation counters based on this design have been proposed [158] with BGO and CsI(Tl). The HgI₂ detectors had an active area ranging from 16 to 100 mm². In 1983, energy resolutions of 10% FWHM and 25% FWHM for 511 and 140 keV gamma rays were obtained with CsI(Tl) [158].

HgI₂ photodiodes have been suggested for high resolution PET modules using BGO [159]. A 4×4 mm² HgI₂ pixel coupled to a 4×4×4 mm³ BGO crystal had an energy resolution of 25% FWHM. More recent work [137], has

shown that, with the improvement in the manufacturing techniques of the HgI₂ photodiodes, high quality scintillation counters can be built with energy resolution values approaching the best results obtained with any scintillator-photodetector combination. A high resolution gamma ray imager for scintimammography has been proposed using segmented CsI(Tl) crystals with segments coupled one-to-one to arrays of $1 \times 1 \text{ mm}^2$ and $2 \times 2 \text{ mm}^2$ HgI₂ pixels where the spatial resolution is determined by pixel size. An energy resolution of 10% and 9.4% FWHM was obtained for the smaller and larger pixels respectively.

Presently, the main disadvantage of HgI₂ is its complex manufacturing process compared to silicon photodiodes. The difficulty in producing large enough samples with consistent properties leads to much higher prices.

3.8 CdZnTe pixel arrays

Gamma ray detection can also be carried out directly by using semiconductor detectors. However, silicon does not provide the necessary conversion efficiency due to its low atomic number and low density, and, in spite of their excellent energy resolution and reasonable conversion efficiency, germanium detectors have to be cooled to liquid nitrogen temperature for noise reduction, which makes them impractical to use and expensive, especially for large area imaging devices.

Cadmium zinc telluride (CdZnTe) is a room temperature semiconductor which can be used for direct detection of gamma rays. It provides high detection efficiency, good spatial resolution limited by the pixel size, and perhaps most importantly, a better energy resolution than scintillator-photodetector combinations. However, there have been several problems in growing large volume crystals with reliable characteristics, making it expensive. Recent techniques have promised more reliable production of high quality samples. Energy resolution values of 1.5% [160] and 5.7% [161] FWHM for 662 and 122 keV have been obtained.

Chapter 4

The Wavelength-Shifting Fibre Gamma Camera

As discussed in the preceding chapters, the need for new application-specific gamma ray imagers, with good spatial resolution, good energy resolution, high detection efficiency and compactness has led to significant research involving new technologies and new designs. This chapter describes the concept of the wavelength-shifting fibre (WSF) gamma camera for nuclear medicine applications. Although the concept may be applied for a general purpose gamma ray imager, the present discussion is based on scintimammography imaging. Together with the general requirements mentioned above, this particular application also requires a flexible camera design and small dead regions at the edges of the camera. As explained below, the WSF gamma camera design is potentially suitable to fulfill these requirements.

The chapter also includes a discussion on the performance characteristics expected based on analytical calculations and a brief review of available technology that might be used in a WSF gamma camera.

4.1 Principle of operation

Figure 4.1 shows a conceptual diagram of the proposed gamma camera. Application of this design to nuclear medicine gamma imagers was first suggested by Worstell et al [162]. Its principle of operation is analogous to the Anger camera. The gamma ray converter is an inorganic scintillator which is coupled to two orthogonal layers of wavelength-shifting fibres laid on opposite sides of the crystal. A gamma ray interaction in the crystal is followed by the emission of scintillation photons which impinge on both layers of WSFs. The fibres sample the profile of light in two perpendicular directions which

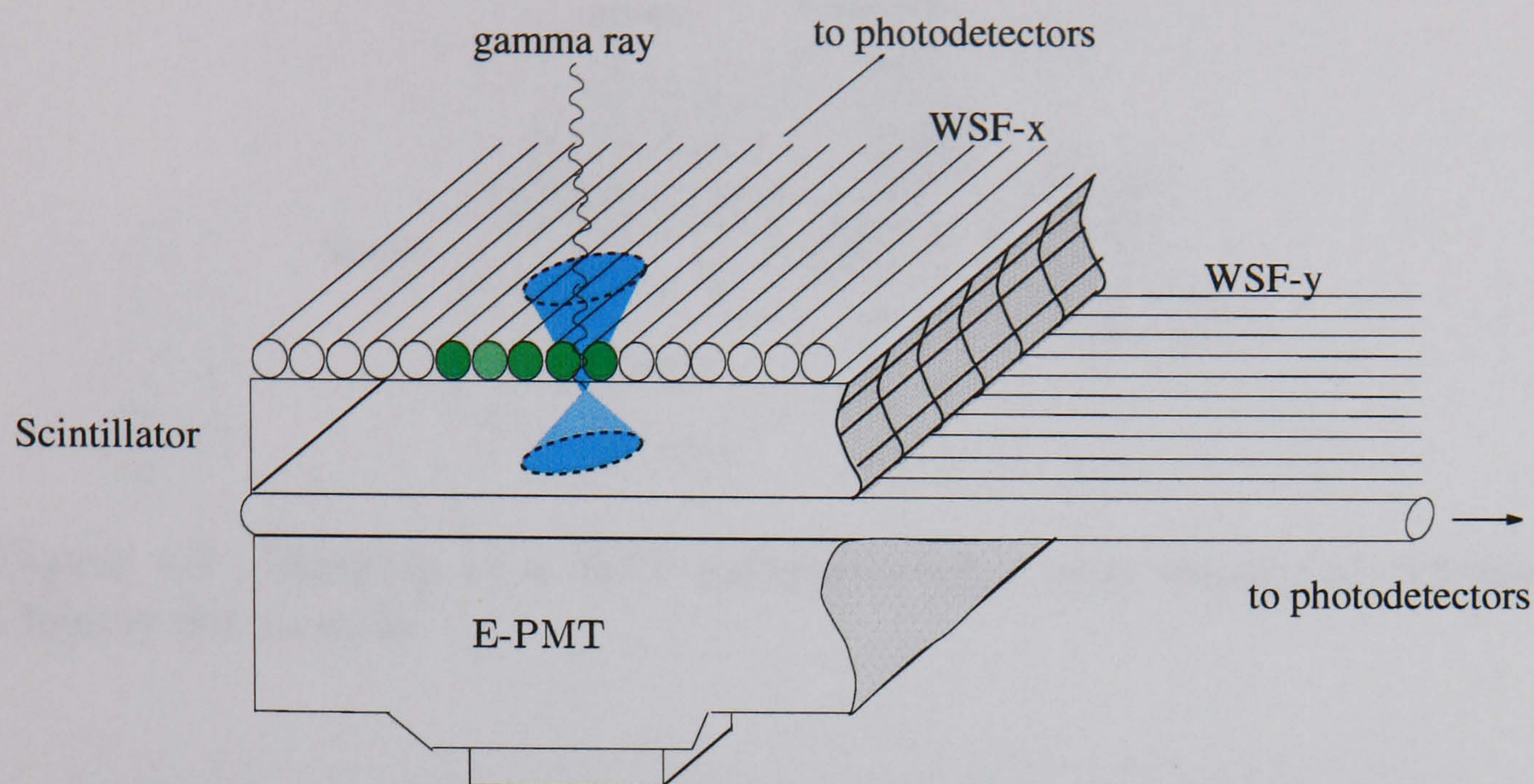


Figure 4.1: Diagram of the WSF gamma camera with a single continuous crystal. Objects not to scale.

provides the spatial information on the position of interaction of the gamma ray.

Figure 4.1 shows a single continuous crystal coupled to two layers of WSFs. Only the fraction of direct light hitting the fibres is depicted. Some of these photons are absorbed in the fibres and subsequently re-emitted at a longer wavelength. A fraction of them are trapped inside the fibres and piped to their ends where they may be detected with suitable photodetectors. The light profiles in the WSFs can be used to calculate the position of interaction of the gamma rays.

Using segmented crystals (figure 4.2) the light would be concentrated only on the fibres directly above and below the segment where the interaction occurred and the position of the event could be unambiguously encoded by the signals in these fibres. If the crystals are segmented in an $N \times N$ matrix, the WSFs may be used to encode the crystal of interaction using a simpler $N+N$ readout scheme.

The light passing through the lower layer of WSFs together with the wavelength-shifted light not trapped, may be collected by another photodetector (the E-PMT in the figure) to obtain the energy signal. This is important because, as will be seen, only a very small fraction of the total light emitted in the crystal is expected to be trapped in the WSFs, and these signals would not provide an acceptable energy resolution.

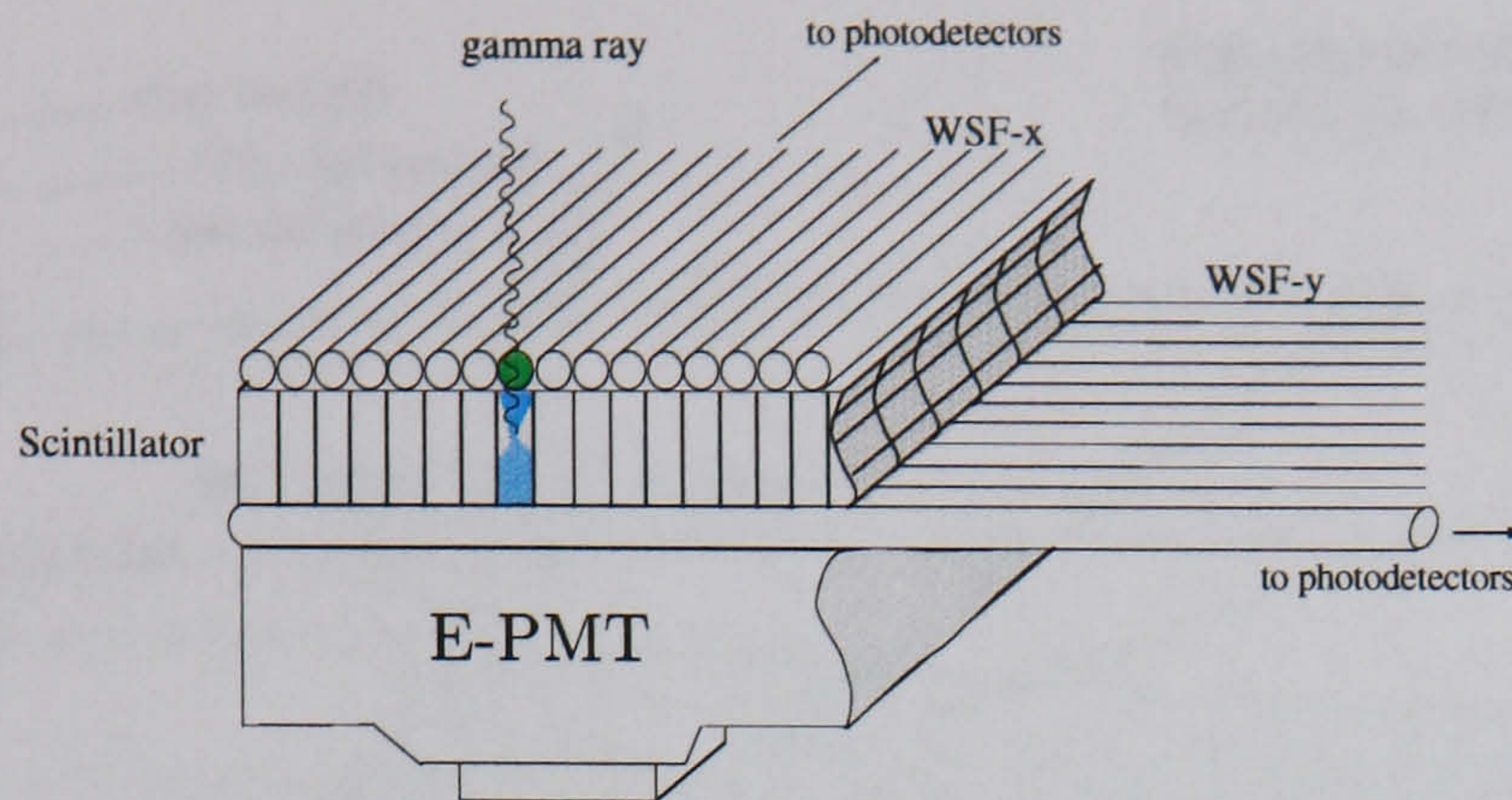


Figure 4.2: Diagram of a WSF gamma camera with segmented crystals. Objects not to scale.

This camera design is inherently very flexible. The dimensions of the camera head are mainly determined by the dimensions of the crystal. This is a clear advantage over gamma imagers based on large area PSPMTs (3", 5") where the shape and size of the camera head is restricted by the dimensions of the PSPMT.

4.2 Wavelength-shifting fibres

Optical fibres are used to pipe light signals and convey them to distant photodetectors. They usually consist of a core material which is transparent to the wavelength of light to be transported. The core is coated with a material with a lower refractive index. This difference in refractive indices defines an angle for total internal reflection, which, for a given direction of the photon with respect to the axis of the fibre, determines whether it is trapped inside the WSF or whether it escapes. Often a second cladding with a refractive index lower than the first cladding is introduced to increase the fraction of trapped light and to reduce the effects of surface damage on light transmission.

4.2.1 Light absorption and re-emission in WSFs

Wavelength-shifting fibres have a phosphor dopant embedded in the core material which absorbs light of a specific wavelength range and isotropically re-emits longer wavelength photons (figure 4.3).

According to the manufacturer [163], the dopant levels are set such that over 80% of the light is absorbed in a length of 1 diameter for incident pho-

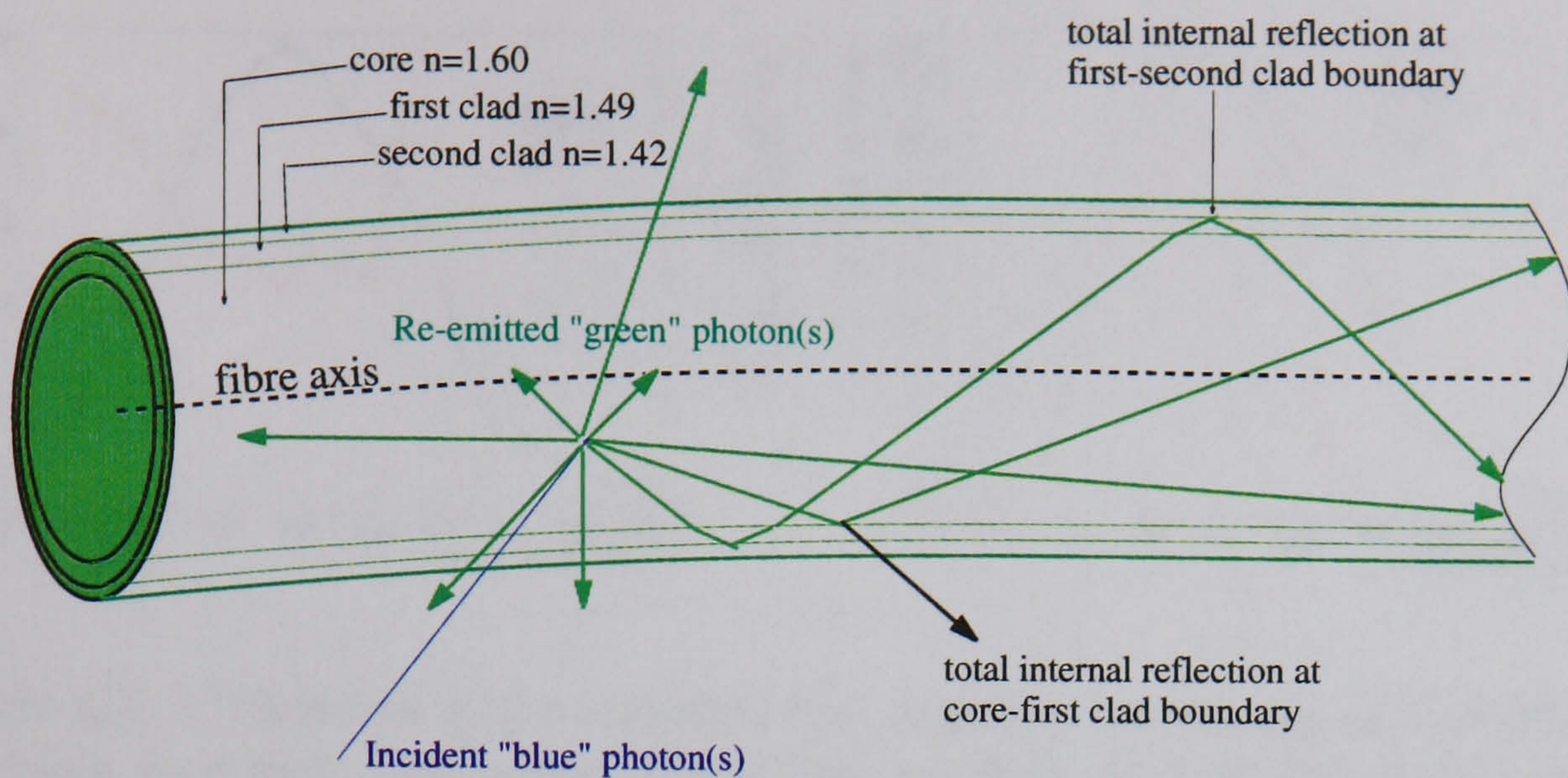


Figure 4.3: Diagram of a double clad wavelength-shifting fibre.

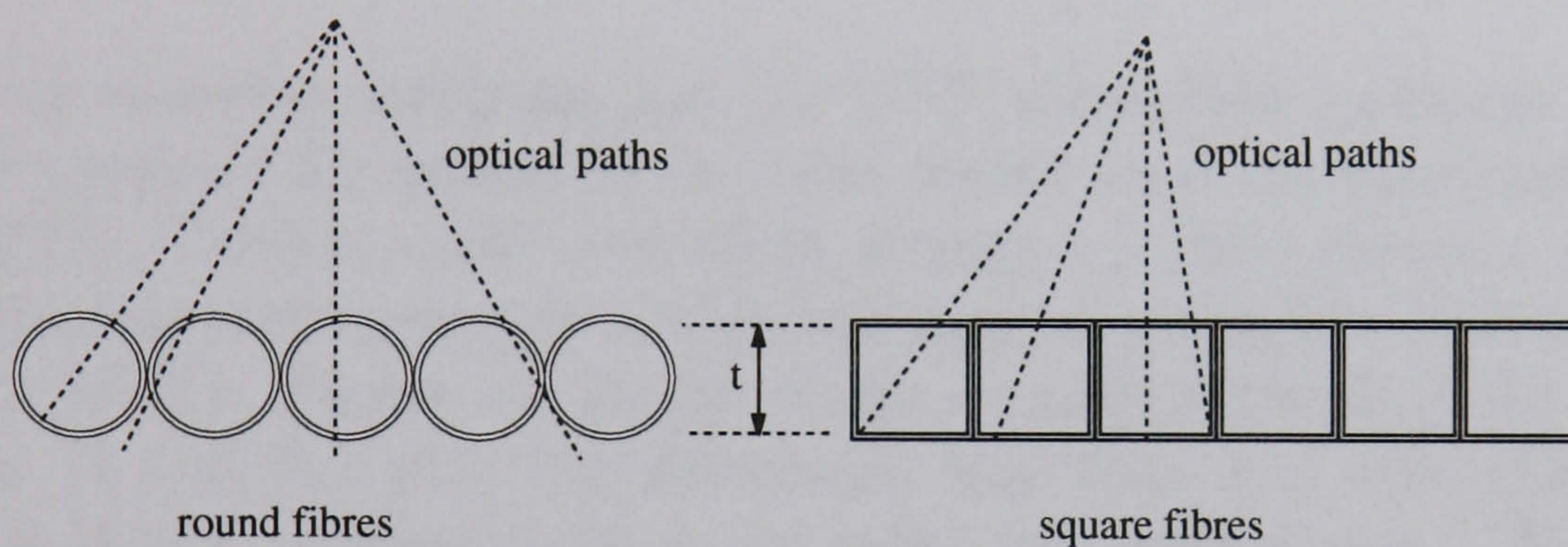


Figure 4.4: Optical path for photons hitting round and square fibres.

tons with wavelength equal to the wavelength of maximum absorption of the fibres. For a 1 mm thick Bicon BCF-91A WSFs, these levels correspond to a $\approx 250 \mu\text{m}$ mean free path [163] for the wavelength of maximum absorption.

For photons hitting fibres at random locations the absorption also depends on the relative position and direction of the photon with respect to the fibre. This is more significant for round fibres where some positions may lead to a very small optical path along the fibre core. This effect is demonstrated in figure 4.4. As shown, for square fibres the minimum path is 1 mm (ignoring photons passing through the middle of adjacent fibres) whereas for round fibres minimum paths of near 0 mm are possible. Therefore, square fibres should provide a more efficient coupling to flat surfaces.

In the case of inorganic scintillator readout with WSFs, the absorption of scintillation light from the WSFs is also determined by the match between the

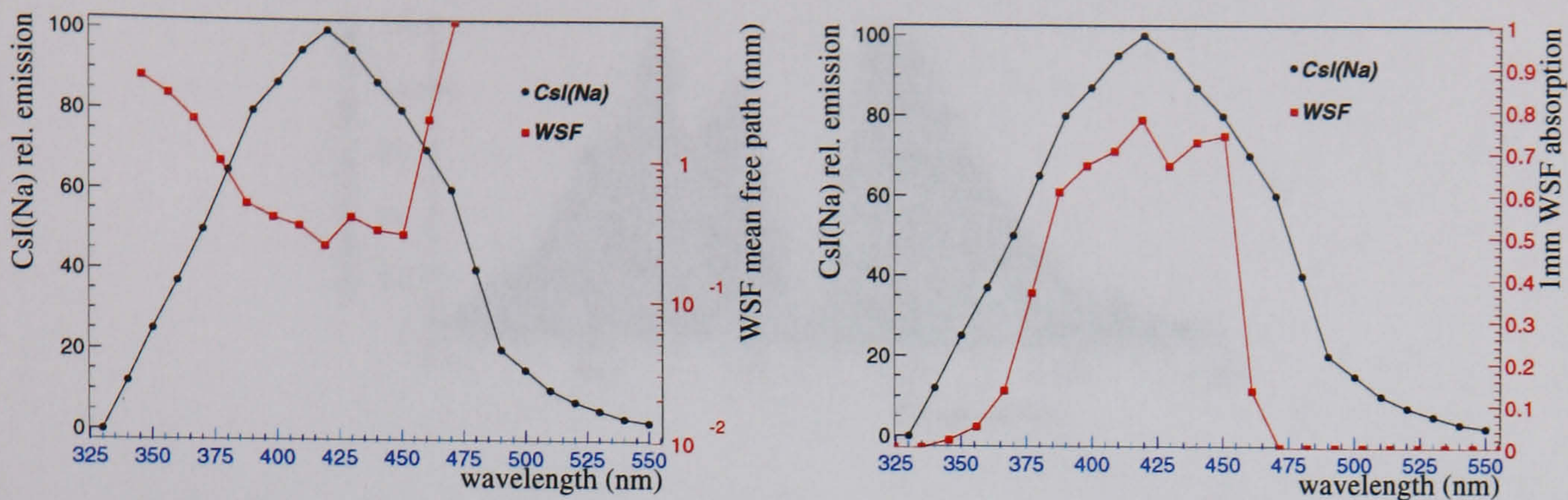


Figure 4.5: Combined plots showing the emission spectrum of CsI(Na) and the mean free path (log scale) of the Bicon BCF-91A WSFs (left); and the emission spectrum of CsI(Na) and the absorption in a WSF thickness of 1 mm (right).

scintillator emission spectrum and the WSF absorption spectrum. A good match is obtained for several of the most widely used inorganic scintillators like NaI(Tl), CsI(Na), LSO and GSO. Figure 4.5 (left) shows a combined plot of the emission spectrum of CsI(Na) and the mean free path for Bicon BCF-91A WSFs. Figure 4.5 (right) shows a combined plot of the emission spectrum of CsI(Na) with the absorption spectrum in 1 mm thick Bicon BCF-91A WSFs, calculated using the mean free path values. The spectral match is estimated to be 46%, defined as the percentage, ε_{spect} , of light emitted by CsI(Na) which is absorbed by 1 mm thick WSFs according to the mean free path values in figure 4.5. For $1 \times 1 \text{ mm}^2$ square fibres, this is a conservative estimate since the mean optical path inside the fibres is higher than 1 mm (figure 4.4).

The probability that an absorbed photon is re-emitted (wavelength-shifted) with a longer wavelength is defined as its conversion quantum efficiency QE_{WS} and it is an inherent property of the dopant used.

The absorption and emission spectra of the wavelength-shifting fibres should be well separated. Figure 4.6 shows typical spectra for blue-to-green WSFs, which are the most commonly used due to their suitability to absorb the blue light emitted from many common plastic scintillators.

4.2.2 Light trapping in WSFs

A fraction of the isotropically re-emitted photons is trapped inside the WSFs and piped to its ends. This fraction is the fibre trapping efficiency, which

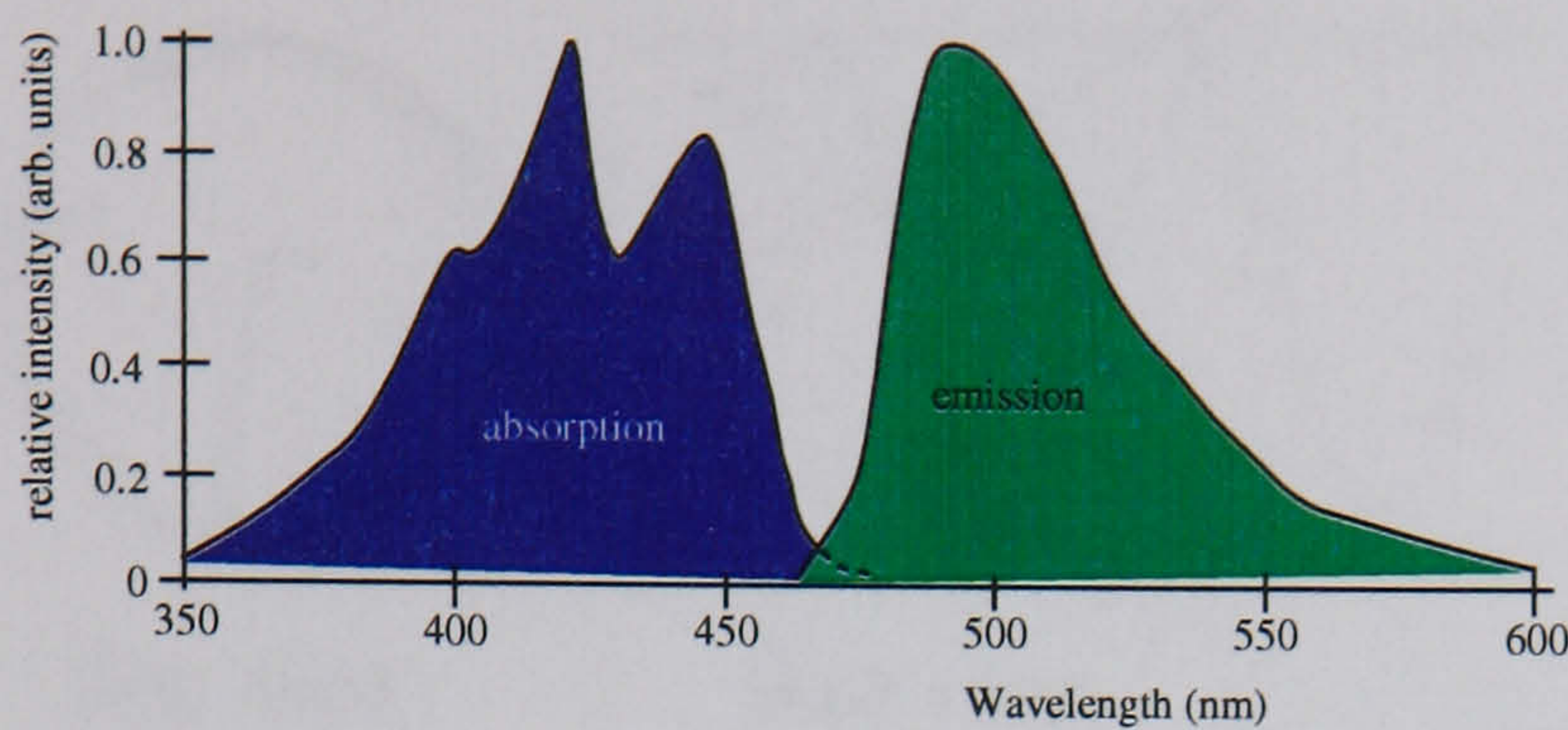


Figure 4.6: The absorption and emission spectra for the Bicron BCF-91A blue-to-green WSFs [164, 165].

is determined by the refractive indices of the core and cladding materials and also by the fibre geometry. For a round fibre, for example, it varies from point to point along the radius of the fibre, increasing from the axis to the cladding, whereas for a fibre with a square cross section the trapping efficiency is virtually independent of the point where the light is absorbed and re-emitted.

This effect on round fibres is illustrated in figure 4.7 where ray 2 is trapped in a spiral trajectory along the fibre axis. The trapping efficiency is higher for photons generated near the cladding. However, photons in these spiral trajectories undergo many more reflections per unit fibre length and have longer path lengths. This increases the probability of bulk absorption and/or scatter which may cause a loss of these photons when transmitting through very long fibres. For the WSFs used (Bicron BCF-91A) these losses have been estimated by other authors by measuring the output of WSFs with various lengths under the same illumination conditions [166]. It was found that a significant loss (40%) is observed for fibre lengths of up to 0.5 meters followed by a much smaller loss rate for longer lengths.

The refractive index of the material surrounding the fibres (e.g. air or an optical cement) is not taken into account in the usual calculation of the trapping efficiency. The outer surface of the fibre is to be handled frequently and therefore can be easily damaged. Thus it is assumed that it can not be used reliably as a perfect optical surface for total internal reflection.

4.2.3 Bicron BCF-91A WSFs

Wavelength-shifting fibres have been widely used in nuclear and high energy physics [167, 164, 168, 169] to read out large areas of plastic scintillators, enabling simple, compact and close packing geometry with a small number

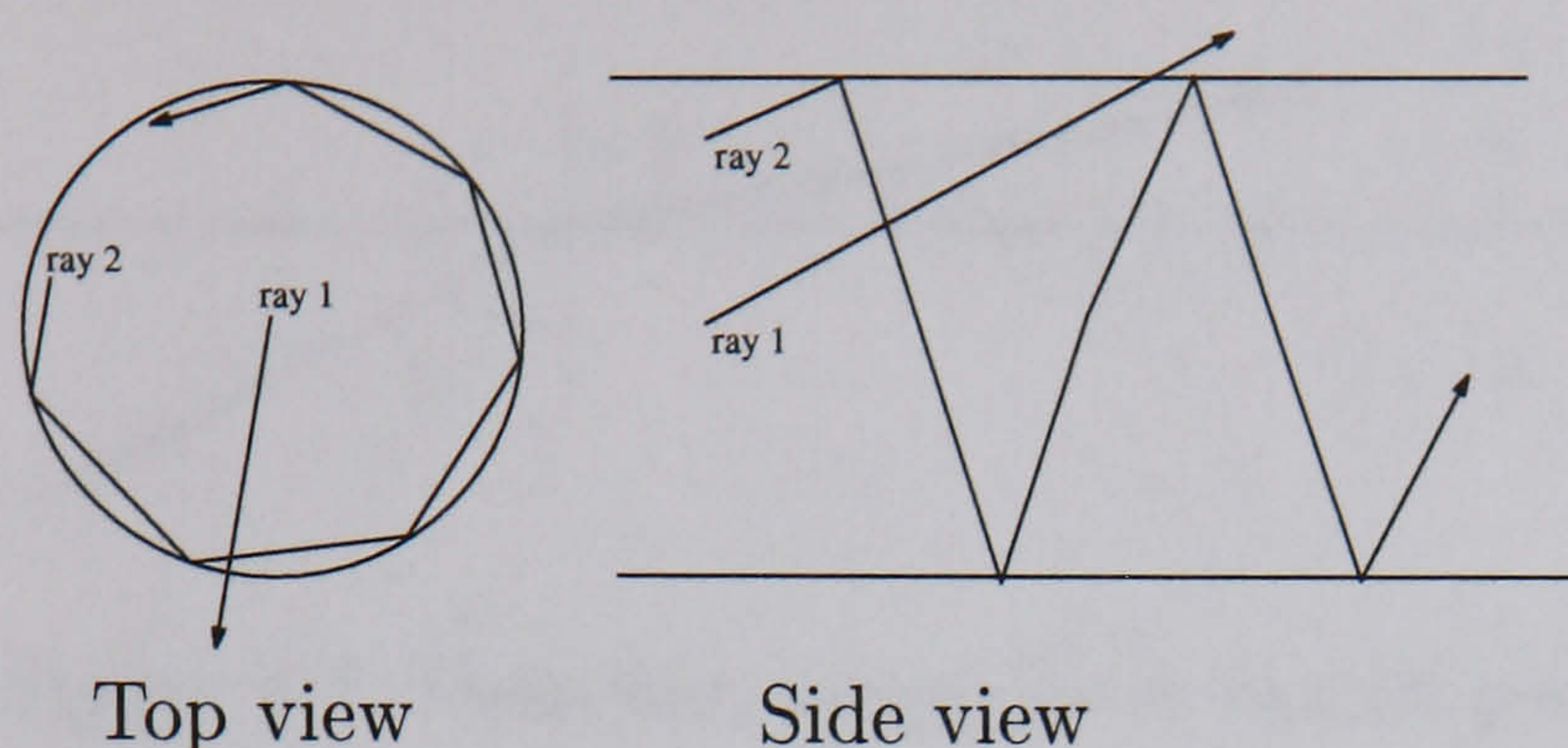


Figure 4.7: Illustration of the trapping efficiency inside fibres. Although the two rays shown have the same direction, ray 2 is trapped and ray 1 escapes the fibre. This is due to the photons being generated at different positions along the fibre radius. For the case of ray 2, the trapping occurs due to a spiral trajectory along the fibre axis.

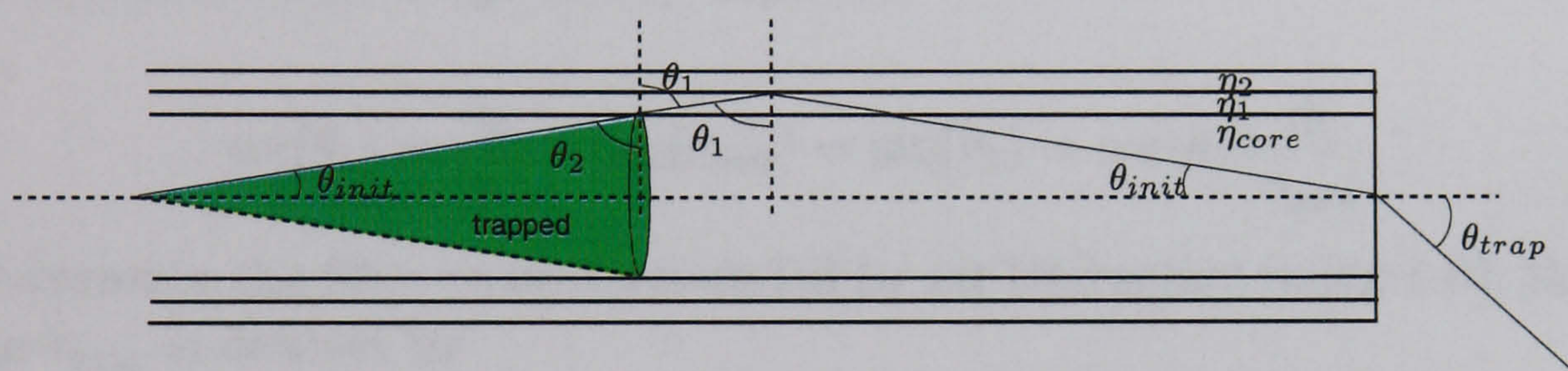


Figure 4.8: Definition of angles for the calculation of the numerical aperture of a double cladded optical fibre.

of readout fibres. There are several WSFs commercially available [165, 170], most of which have been purposely optimized for these applications.

Some general characteristics of the Bicon BCF-91A WSFs are described in table 4.1. The numerical aperture is defined as the sine of the maximum angle θ_{trap} in figure 4.8 between the fibre axis and the direction of a trapped photon exiting through the fibre end. This maximum value can be calculated using the angles defined in the picture together with the refractive indices of the fibre materials, where the case of a double clad fibre is shown. The maximum of θ_{trap} corresponds to the minimum angle θ_1 for which total internal reflection occurs at the boundary between the two claddings. According to Snell's law, the relation between the directions of photons incident and refracted at an optical interface is

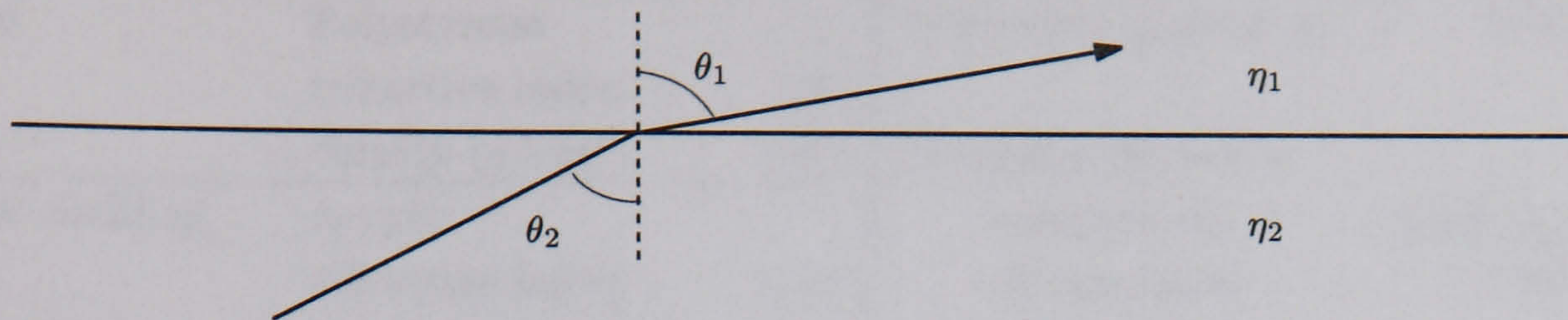


Figure 4.9: Definition of angles in Snell's law.

$$\eta_1 \sin(\theta_1) = \eta_2 \sin(\theta_2). \quad (4.1)$$

where the indices 1 and 2 refer to two different materials with refractive indices η_1 and η_2 as depicted in figure 4.9 for the case of $\eta_1 < \eta_2$

Therefore, from the geometry depicted,

$$\sin(\theta_1) = \frac{\eta_2}{\eta_1}; \quad \cos(\theta_{init}) = \sin(\theta_2) = \sin(\theta_1) \frac{\eta_1}{\eta_{core}}. \quad (4.2)$$

Assuming the fibre to be surrounded by air (refractive index 1.0), the exit angle θ_{trap} is defined by

$$\sin(\theta_{trap}) = \eta_{core} \sin(\theta_{init}), \quad (4.3)$$

which is the numerical aperture of the fibre. For this case a value of 0.74 is obtained.

The value of θ_{init} in this case is 27.4° and it can be used to calculate the trapping efficiency according to the geometry in figure 4.8. For the double clad WSFs under discussion this value is 5.6% per fibre end, for photons emitted isotropically from the fibre axis.

The wavelength shifting dopant used in these fibres ("G2") has a conversion quantum efficiency, QE_{WS} , of 75% [163] from blue-to-green.

Finally, it should be noted that square WSFs are approximately twice as expensive as round WSFs.

4.3 Expected performance of a WSF gamma camera

Based on the properties of WSFs presented above it is possible to make some predictions for the behaviour of a WSF gamma camera. Due to the impor-

Core	Polystyrene		Numerical Aperture	0.74
	refractive index	1.6		
	density (g/cm ³)	1.05	Trapping efficiency	
First cladding	Acrylic		round fibers	5.6% minimum
	refractive index	1.49	square fibers	7.3%
round	% of fibre diameter	3%	Operating Temperature	-20 to +50°C
square	% of fibre thickness	4%		
Second cladding	Fluoro-Acrylic		Vacuum compatible	Yes
	refractive index	1.42		
round	% of fibre diameter	1%	Phosphor dopant	G2
square	% of fibre thickness	1%		

Table 4.1: Physical and optical properties of the BCF-91A Bicon wavelength shifting fibres. *Source:* Bicon Multiclad Plastic Scintillating, Wavelength Shifting and Optical Fibers Preliminary, URL: <http://www.bicon.com>, Bicon, USA.

tance of energy resolution in single photon gamma ray imaging, the single crystal geometry in figure 4.1 is chosen. The most promising scintillators are CsI(Na) and NaI(Tl) due to their high light yield and emission spectrum peaked at about 420 nm.

4.3.1 Spatial resolution

As discussed in section 2.3.2 the two main factors determining the spatial resolution of the Anger camera are the light spread over the imaging detectors and the number of photoelectrons involved in the centroid calculation. The same argument applies to the spatial resolution of a WSF gamma camera. In Anger cameras it is necessary to spread the light over more than a single PMT to allow a centroid calculation based on the light sharing between adjacent PMTs (section 2.3.1). Typical light distributions in Anger cameras are between 10 and 20 cm FWHM wide.

In the case of the WSF camera, the imaging detectors are the WSFs, which are much smaller than the PMTs used in Anger cameras - 1 mm diameter compared to 3 to 7 cm side-to-side. Therefore, for crystals with a thickness of 3 mm to 5 mm for example, the light spread is expected to be sufficient to illuminate at least 3 fibres, and provide a light sharing scheme similar to the Anger cameras. In this case, the small light spread over the fibres forms the basis for a potentially good spatial resolution, by localising the light spot in a small region.

It is important at this stage to estimate the width of the light distribution

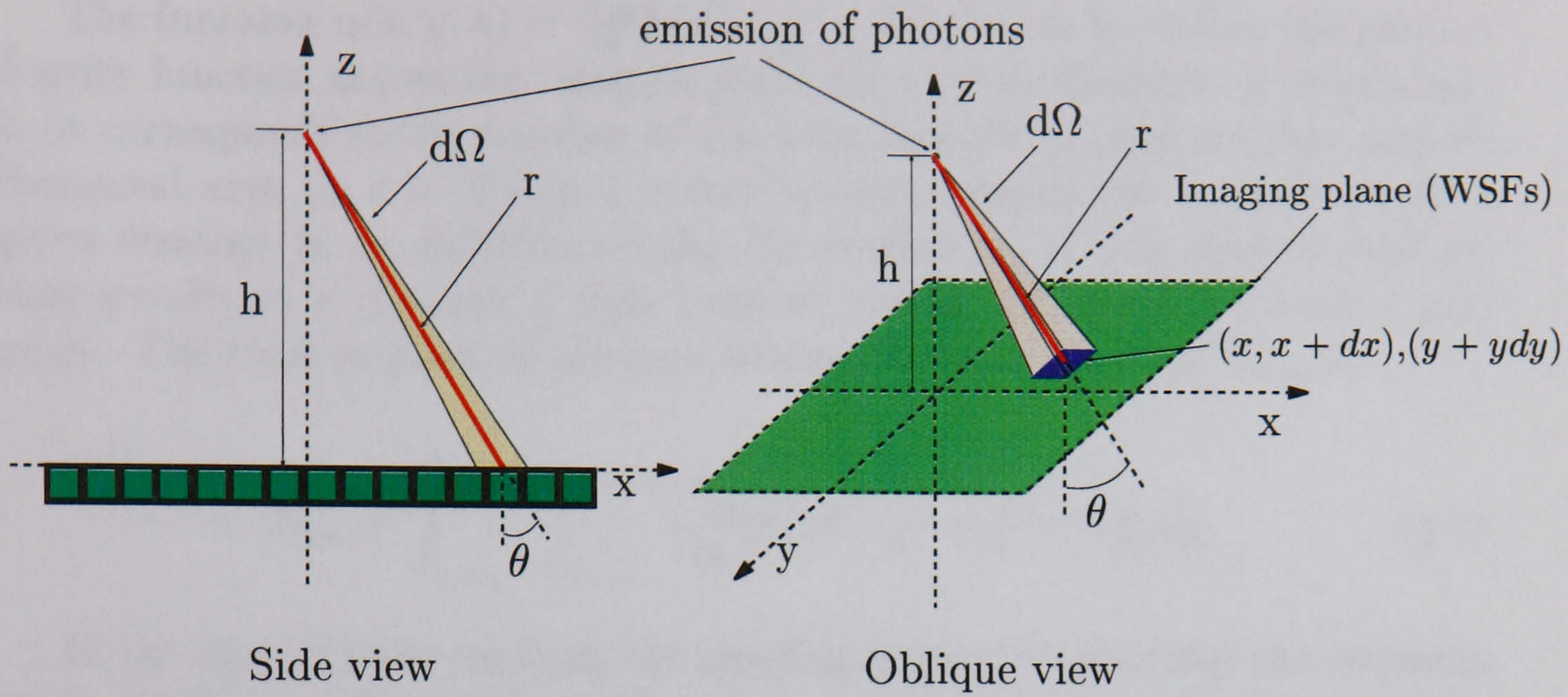


Figure 4.10: Solid angle subtended by the elemental area between $(x, x + dx)$ and $(y, y + dy)$, and the point of emission of photons.

over a ribbon of WSFs coupled to a thin (e.g. 3 mm) scintillator. For simplicity, let us consider only the direct light hitting the WSFs (figure 4.1). The width of the light distribution is determined by the thickness of the scintillator and also by the difference in refractive indices at the scintillator interfaces. In figure 4.10 a point of emission of photons is represented. Square WSFs are considered for geometric simplicity.

Assuming an isotropic emission of N_{ph} scintillation photons in the crystal, at a distance h above the WSF plane (the imaging plane), the number, n , of photons reaching the infinitesimal area $dxdy$ is defined by the solid angle $d\Omega$ as

$$n = N_{ph} \frac{d\Omega}{4\pi} \quad (4.4)$$

where

$$d\Omega = \frac{\cos \theta}{r^2} dxdy, \quad \cos \theta = \frac{h}{r}, \quad r^2 = x^2 + y^2 + h^2 \quad (4.5)$$

and therefore

$$n = \frac{N_{ph}}{4\pi} h (x^2 + y^2 + h^2)^{-\frac{3}{2}} dydx. \quad (4.6)$$

The function $n(x, y, h) = \frac{N_{ph}}{4\pi} h(x^2 + y^2 + h^2)^{-\frac{3}{2}}$ can be called the photon density function across the imaging plane for a given distance of interaction h . It corresponds to the fraction of the total number of photons that hits an elemental area $(x, x + dx), (y, y + dy)$ for each gamma ray interaction at a given distance h , or, in other words, the probability that a photon emitted isotropically at a distance h falls between x and $x+dx$ and between y and $y+dy$. The total number of photons hitting the imaging area, N_{im} is

$$N_{im} = \int_{y_{min}}^{y_{max}} \int_{x_{min}}^{x_{max}} \frac{N_{ph}}{4\pi} h(x^2 + y^2 + h^2)^{-\frac{3}{2}} dy dx. \quad (4.7)$$

In the case of light reaching the imaging plane directly from the emission point (without reflections), the limits in x and in y are given by the cone of acceptance defined by the difference in the refractive indices between the scintillator and the coupling material (e.g. optical grease or air).

The profile of light along the direction perpendicular to the fibre axis (e.g. x) is obtained by integrating $n(x, y, h)$ along the fibre axis direction (e.g. y), and is the Point Spread Function (PSF) of the light distribution:

$$PSF(x, h) = \int_{y_{min}}^{y_{max}} \frac{N_{ph}}{4\pi} h(x^2 + y^2 + h^2)^{-\frac{3}{2}} dy. \quad (4.8)$$

A similar concept, which is also more useful in this case, is the total number of photons incident on each WSF. It may be obtained carrying out an integration similar to equation 4.8 but integrating also in the x direction to account for the thickness d of the fibre. This function depends on the fibre, i , in question and may be called the *Fibre Point Spread Function* ($FPSF(i, h)$)

$$FPSF(i, h) = \int_{x_{min}^i}^{x_{max}^i} \int_{y_{min}}^{y_{max}} \frac{N_{ph}}{4\pi} h(x^2 + y^2 + h^2)^{-\frac{3}{2}} dy dx. \quad (4.9)$$

where the limits of integration x_{min}^i and x_{max}^i represent the boundaries of the fibre along the direction perpendicular to its symmetry axis.

Let us consider the fibres to be either embedded in an optical coupling material (e.g. silicon gel, clear epoxy) with a refractive index $\eta = 1.5$, or laid directly on the crystal, in which case $\eta = 1.0$ (air) is assumed outside the crystal. Light exiting the crystal at a given angle θ as defined in figures 4.10 and 4.11 finds a boundary where there is a drop in refractive index. It can undergo total internal reflection if θ exceeds the critical angle θ_c , defined as,

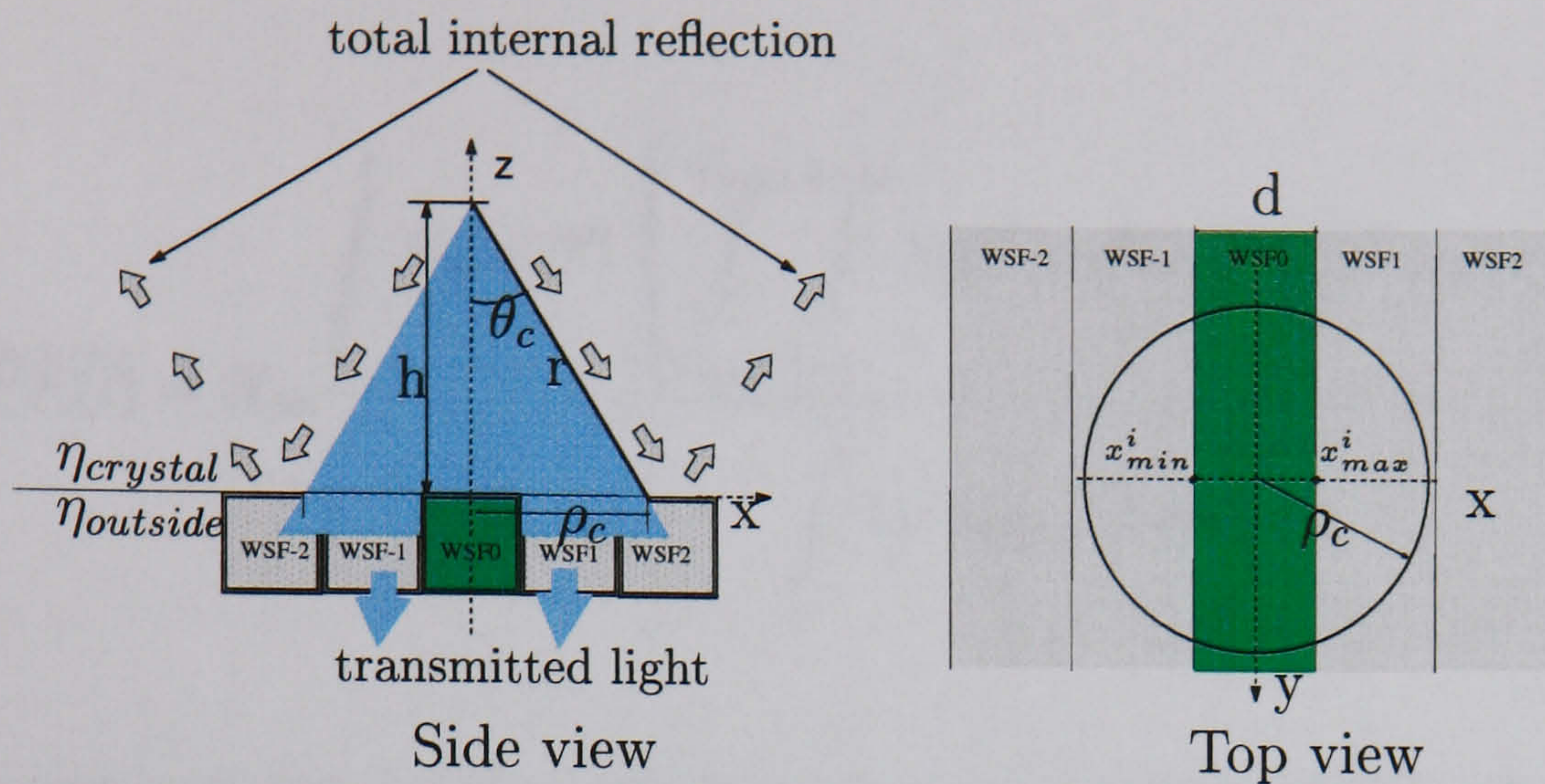


Figure 4.11: Graphical representation of the parameters used in the solid angle calculation.

$$\sin \theta_c = \frac{\eta_{outside}}{\eta_{crystal}}. \quad (4.10)$$

With the parameters described in figure 4.11, it is possible to define the limits of the integral 4.9. For the fibre directly under the gamma ray interaction point (WSF⁰) they are: $x_{min}^0 = -d/2$; $x_{max}^0 = +d/2$; $y_{min} = \sqrt{\rho_c^2 - x^2}$; $y_{max} = -\sqrt{\rho_c^2 - x^2}$, where $\rho_c = h \tan \theta_c$, and $i=0$ corresponds to the central fibre ($i = \dots, -3, -2, -1$ to one side and $i = +1, +2, +3, \dots$ to the other).

The FPSF defined in equation 4.9 depends on the distance h from the emission of photons to the WSFs. To find the average fraction of photons reaching a fibre it is necessary to take into account the probability distribution of gamma ray interactions along the z axis. For a given thickness, t , of scintillator (along the z axis), the number of gamma rays transmitted is given by:

$$N(t) = N_0 e^{-\mu t} \quad (4.11)$$

where μ is the linear attenuation coefficient of the scintillator for a specific gamma ray energy (140 keV in our case) and N_0 is the number of gamma rays impinging on the crystal.

For a crystal of thickness t , the average FPSF for gamma rays interacting at a range of h values, determined by equation 4.11, is:

$$\overline{FPSF}(i) = N_{ph} \frac{\int_0^t N_0 \mu e^{-\mu h} \left\{ \int_{x_{min}^i}^{x_{max}^i} \int_{y_{min}}^{y_{max}} h(x^2 + y^2 + h^2)^{-3/2} dy dx \right\} dh}{\int_0^t 4\pi N_0 \mu e^{-\mu h} dh} \quad (4.12)$$

which represents the number of photons reaching fibre WSF^i . Note that, according to this definition, the FPSF is assymmetric in the two directions for a given fibre.

Table 4.2 shows the results of evaluating equation 4.12 for 1 mm thick square ($d = 1$ mm) fibres. The results show the average fraction of solid angle, f^i , subtended by fibres WSF^0 , WSF^1 , WSF^2 and WSF^3 which is obtained by dividing the results of equation 4.12 by N_{ph} . The scintillator is chosen to be CsI(Na) which is among the brightest scintillators and is also a blue emitter, which makes it suitable to couple to blue-to-green WSFs. Hence a refractive index of 1.84 and a linear attenuation coefficient μ of 0.39 mm^{-1} for 140 keV gamma rays is assumed. The crystal is 3 mm thick, i.e., h varies from 0 to 3 mm. This thickness of CsI(Na) corresponds to about 70% of 140 keV gamma rays absorbed. Two separate cases are presented: a) no coupling material between the fibres and the crystal (air coupling) and b) coupling the fibres to the crystal with a 1.5 refractive index optical compound.

The table also shows the total number of photons incident on each fibre WSF^i , $\overline{FPSF}(i)$, assuming a scintillator light yield of 37 photons/keV. For an incident gamma ray energy of 140 keV (^{99m}Tc), this gives a value of $N_{ph} \approx 5200$ blue photons per full energy deposition of a gamma ray.

The table also shows the number of photoelectrons, n_{phe}^i , created by each WSF on a bialkali photocathode, which is calculated from:

$$n_{phe}^i = f^i \times N_{ph} \times \varepsilon_{spect} \times QE_{WS} \times \varepsilon_{trapp} \times QE_{PMT-500} \quad (4.13)$$

where:

1. the trapping efficiency, ε_{trapp} , of the WSFs is 6% per fibre end, and only one end is read out;
2. the spectral match between the scintillator and the WSFs, ε_{spect} , is 46% (figure 4.5);

		WSF ⁰	WSF ¹	WSF ²	WSF ³	sum
f^i	gel	0.12	0.032	0.008	0.002	0.21
(frac. of sol. angle)	air	0.062	0.0088	0.00024	–	0.08
$\overline{FPSF(i)}$	gel	647	168	45	11	1096
(no of photons/WSF)	air	324	46	1.23	–	419
n_{phe}^i	gel	2.0	0.52	0.14	0.03	3.4
(no of photoelect./WSF)	air	1.0	0.14	0.004	–	1.3

Table 4.2: Results of the evaluation of the integral in equation 4.12 for consecutive 1 mm thick square WSFs. The gamma rays are assumed to be generated above WSF⁰, in a 3 mm thick CsI(Na) crystal. The WSFs and the CsI(Na) are either optically coupled with a 1.5 refractive index medium (gel) or with no coupling medium (air). The last column correspond to the sum of the values in all WSFs (from WSF⁻ⁱ to WSF⁺ⁱ) in which it is assumed that the results shown for WSF⁺ⁱ are equal to the results for WSF⁻ⁱ, from symmetry. Note the small expected numbers of photoelectrons n_{phe}^i per fibre.

3. the wavelength shifting quantum efficiency, QE_{WS} , is 75%;
4. the quantum efficiency, $QE_{PMT-500}$, of the photocathode is 15% for 500 nm photons.

These results show that the profile of light is concentrated in a very small region encompassing at most 5 fibres. Due to the small number of photoelectrons involved in the centroid calculation, both for gel and air coupling, it is expected that the spatial resolution of the system will be limited to a value close to the width of the light distribution (refer to discussion in section 2.3.2). Therefore, a spatial resolution of about 3 mm FWHM might be expected from the profiles of light shown in table 4.2.

4.3.2 Efficiency

As in an Anger camera (section 2.3.1), the intrinsic sensitivity of a WSF gamma camera is the fraction of those gamma rays directed at the scintillation crystal that add a valid point in the two-dimensional histogram of centroids (image). In the Anger camera the sensitivity of the scintillation imager is determined primarily by the scintillator detection efficiency, defined as the probability that a photon interacts in the crystal and deposits

its full energy, creating an energy signal which falls inside the energy window. For these events, the centroid calculation is carried out and a point is added to the image. For a given gamma ray energy, the scintillator detection efficiency depends on the mass attenuation coefficient of the scintillator and on its thickness.

Thick crystals benefit the sensitivity but also increase the width of the light distribution, degrading the spatial resolution. Therefore, from this point of view CsI(Na) is preferable over NaI(Tl) due to its higher density and higher effective atomic number, allowing the use of thinner crystals.

The intrinsic sensitivity of the WSF imager proposed also depends on the scintillator detection efficiency in the same way described for the Anger camera. But there is another factor affecting the intrinsic sensitivity to be taken into account. If the light levels at the WSFs are very low, it is possible that, following a gamma ray interaction, none of the fibres on one face of the crystal will produce any photoelectron at the light sensors. For these cases, even if the energy signal falls inside the energy window, no valid point is added to the image. Since this efficiency loss is related to the imaging process, we call it the *imaging efficiency*. As shown in table 4.2, the mean number of photoelectrons expected in a layer of WSFs coupled with gel to CsI(Na) is of the order of 3.4, for 140 keV gamma rays. Assuming Poisson statistics, the probability of getting zero photoelectrons, $P(0)$, is less than 4% at these light levels, which corresponds to over 96% imaging efficiency. Therefore, for gel coupling, there is not a significant loss of efficiency.

However, for air coupling, the mean number of photoelectrons expected in a layer of WSFs is of 1.3, giving a $P(0)$ of 27% and a corresponding lower imaging efficiency of 73%.

4.3.3 Energy resolution

In a close packed set-up, with no gaps between the fibres, a large fraction of scintillation light is expected to be absorbed by the WSFs. However, since the trapping efficiency is small, most of the wavelength-shifted light (green light) escapes the fibres. A fraction of these escaping photons are measured by the E-PMTs as part of the energy signal. Compared to a direct couple of the crystal to the E-PMTs, there is an inevitable loss of light and, consequently, an energy resolution degradation.

An estimate of the energy signal obtained with a scintillator covered by WSFs can be obtained using the previously described properties of these fibres. The energy signal may be divided into two components: a) direct (or non-shifted) light from the scintillator and b) wavelength-shifted light that escapes the WSFs and is collected by the E-PMT.

Direct light passes through the WSF layer without being absorbed, mainly because of the spectral match between the crystal emission and the WSF absorption - ε_{spect} . The value of ε_{spect} was estimated above for square Bicron BCF-91A WSFs to be about 46%. Let the average quantum efficiency of the E-PMT for the wavelength of the direct light be QE_1 .

The remaining 54% photons are absorbed by the WSFs, 75% of which are wavelength-shifted (shifted = $54\% \times 0.75 = 40.5\%$). Assuming a trapping efficiency of 6% per fibre end (12% both ends), the total number of trapped photons is $40.5\% \times 0.12 = 4.9\%$. Therefore, $40.5\% - 4.9\% = 35.6\%$ photons exit the fibres in random directions. Let us assume that half of these are directed at the E-PMT. Then, of the initial number of photons passing through the WSF layer, a total of $35.6\% \times 0.5 \sim 18\%$ shifted photons reaches the E-PMT. The sensitivity of the E-PMT photocathode at the wavelength of the shifted photons is usually lower than at the original wavelength. Assuming an E-PMT quantum efficiency for the shifted light of $QE_2 = 70\%QE_1$, which is a typical relation for the quantum efficiency of alkali photocathodes at 500 and 420 nm respectively, then the energy signal corresponding to the 18% shifted photons is scaled to $18 \times 0.7 = 13\%$.

The total energy signal is therefore expected to be $46\% + 13\% = 59\%$ compared to direct coupling of the crystal to the E-PMT. The results of experimental measurements are presented in chapter 8. This prediction of a relatively small loss in energy signal is an encouraging result. Assuming that Poisson fluctuations on the number of photoelectrons n_{phe} are the dominant factor then $R = 1/\sqrt{n_{phe}}$ and a reduction to $0.58n_{phe}$ leads to a 30% increase in R.

4.3.4 Dead area at the edges

As discussed above, the profiles of light expected for thin (3 mm) scintillators are approximately 5 mm wide (~ 5 fibres). Therefore it should be possible to use the whole crystal area as the field-of-view of a WSF gamma camera, with a dead region of only ~ 2.5 millimeters near the edge.

4.4 Light sensors for low light level readout of WSFs

Since the light levels expected give only a few detected photons per fibre (table 4.2), the photodetector must have single photon detection capability. This requires the excellent signal-to-noise ratio which is usually achieved in

sensors with a high internal gain. The quantum efficiency of the photodetector should be as high as possible to maximize the imaging efficiency and to improve the spatial resolution, by maximising the number of photoelectrons generated. In the case of multi-channel photodetectors, the inter-channel cross talk should be as low as possible.

A description of the most promising devices follows, with particular emphasis on the important requirements - quantum efficiency at 500 nm, single photoelectron response and inter-channel cross-talk in the case of multi-channel devices.

4.4.1 Position sensitive PMTs (PSPMT)

PSPMTs are excellent candidates for the readout of optical fibres. They have high gain and provide single photon detection. Their position sensitivity allows simple and inexpensive readout of multiple fibres with a single tube. The metal-channel-dynode PSPMTs from Hamamatsu and from Photonis (table 3.2) have been used in a number of applications for fibre readout [171, 94, 172], with one-to-one coupling between the fibres and the PSPMT anodes.

Generally, the inter-channel cross-talk is due to two main contributions. The first is light cross-talk, light emitted from one fibre that hits the photocathode in a region above an adjacent anode, producing a signal in this anode. This light spread depends mainly on the thickness of the PSPMT window and on the size of the fibres and of the anodes. The second main source of cross-talk is charge cross-talk. It is usually generated by the spread of charge in the amplification process, leading to a charge cloud distributed over more than one anode.

The Hamamatsu R5900 series provides several models which differ mainly in the anode structure. The most appropriate for fibre readout are the individual anode pixel devices (table 3.2), due to the unambiguous readout, where the fibres are associated one-to-one with the individual anodes. The thin entrance window (1.5 mm thick) and the low transverse diffusion of charge given by the metal channel dynodes provide low cross-talk between channels. They have been shown to achieve a charge gain of 10^7 and excellent single electron resolution [173, 174, 172]. An evaluation of Hamamatsu R5900 PSPMTs is the subject of chapter 7, where details of the single photon counting performance characteristics are presented.

Similar characteristics have been found for the Photonis XP1700 PSPMT series for photon counting with optical fibres [88, 175, 171, 176, 177]. These devices can be supplied with a conventional glass window or with a fibre optic window which reduces the light spread, and therefore the cross-talk, at the expense of a $\approx 30\%$ reduction in light transmission above 400 nm.

The single electron resolution of PSPMTs is similar to that of PMTs, which, at best, are only able to separate the peaks corresponding to up to 3 or 4 photoelectrons. The single electron resolution is mainly determined by the amplification process at the first dynode which is characterised by its gain (usually up to 10) and its inherent statistical fluctuations.

The main disadvantage of the PSPMTs is their relatively low quantum efficiency for 500 nm photons. They have similar photocathode technology to conventional PMTs and the highest quantum efficiency at this wavelength is about 20%, obtained with bialkali photocathodes.

In all other aspects, PSPMTs are an excellent choice for single photon counting readout of optical fibres.

4.4.2 Hybrid photodetectors (HPD)

As discussed in section 3.6, imaging HPDs are attractive devices for fibre readout. Their performance is similar to PSPMTs in some aspects. The quantum efficiency is comparable since the same photocathode technology is used and sub-millimeter spatial resolution can be achieved, depending on the Si-anode segmentation and the light spread over the photocathode.

HPDs have inferior gain ($\approx 10^3$) compared to PSPMTs (up to 10^7). However, the charge amplification in HPDs is a one-stage process with a gain at least 100 times higher than the first stage gain in PSPMTs. This implies lower statistical fluctuations and a much better single electron resolution. It has been shown that the number of resolved photoelectron peaks can be as high as 15 [178, 179], as opposed to 3 or 4 with the best PMTs or PSPMTs.

Another advantage of HPDs over PSPMTs is that practically 100% of the photoelectrons released from the photocathode are collected and amplified in the silicon anode. In PSPMTs, only a fraction (usually 80 to 90%) of the total number of photoelectrons is collected by the first dynode (collection efficiency).

4.4.3 Avalanche photodiodes

Silicon avalanche photodiodes (APD) are very attractive for single photon counting due to the high quantum efficiency of silicon devices across the visible range (60% to 80%).

Compared to the APD readout of scintillators discussed in section 3.7.1, single photon counting requires higher internal gain, in order to create a signal above the electronic noise. These high gains however, are usually obtained in small area APDs (less than 150 μm diameter) [180, 181], due to the problems of electronic noise and breakdown described in section 3.7.1 for larger area

APDs. However, the improvement seen in the past few years indicates that larger areas may be achieved in the near future, with increased reliability at affordable prices.

Recently, a large area (e.g. over 1 mm diameter) APD has shown a high internal gain of the order of 10^5 . This is a special type of APD, the Metal Resistive layer-Semiconductor avalanche photodiode (MRS-APD). Although it has been reported to provide single photon detection [182, 183], there are still some problems with the poor quantum efficiency below 600 nm due to absorption of photons in the metal resistive layer, and, despite recent progress achieving 50% [184] quantum efficiency at 500 nm, the technology is in an preliminary R&D stage.

Also in a very preliminary R&D phase are the drift avalanche photodiodes (drift-APD) [185]. The concept is a combination between the silicon drift photodiodes described in section 3.7.1 and conventional APDs, to provide large devices with low capacitance and high amplification gain. The purpose of current research is to build relatively large area devices (e.g. 1 cm^2) but with a small anode capacitance which, combined with high gain, may provide photon counting capability at short shaping times (e.g. tens of ns). If such a device could be developed, with small dimensions (matched to single fibres), single photons sensitivity and 80% quantum efficiency, it could be the ideal detector for a WSF gamma camera.

4.4.4 Visible light photon counters

The visible light photon counter (VLPC) is another silicon device with internal charge amplification. The amplification takes place through impurity band conduction in a small region (a few μm thick) of the silicon diode (gain zone), where a high concentration ($\approx 10^{-7} \text{ cm}^{-3}$) of a donor impurity (arsenic) [186, 187] is present.

An electron-hole pair is created in the intrinsic zone of the diode. By the action of the electric field in the depletion region, the hole moves into the gain zone, where it collides with a neutral donor atom. An electron is released starting an electron avalanche by impact ionization with the donor impurities. Since the impurity band is only 50 mV below the silicon conduction band, a high gain of typically 10^4 is achieved, even at a low diode operating bias of 6 to 7 V. The avalanche process is self-limiting due to space charge effects created by the slowly drifting donor impurity band holes which are created by the avalanche. The small impurity band gap determines a low operation temperature of about 6 to 7 K.

VLPCs with 1 mm diameter pixels are being extensively used and tested in the DØ fibre tracker upgrade [188] at the Fermi National Accelerator

Laboratory (Fermilab), where nearly 100,000 such diodes are used. The tests show a high quantum efficiency of 60 to 80% across the visible spectrum and single photon detection with an excellent single electron resolution, due to a very well defined gain. The mass production of these devices shows reliable operation for use in large numbers at a cost of \$40 per pixel [189, 188], and they can be considered, therefore, to be readily available technology.

Despite their ideal performance for the requirements of a WSF gamma camera, VLPCs have the disadvantage of a very low temperature of operation. The required liquid helium cooling system is a drawback, in particular for small-scale systems, where cost, portability and convenience of use are important requirements. For this reason, some work has been dedicated to the development of compact cooling systems to be used in small-scale laboratory tests [190], with low liquid helium consumption (0.15 liters per hour), providing stable operation for periods of several weeks.

The use of a cryostat introduces a limit to the proximity of the photodetectors to the camera head. To avoid light losses in long WSFs via self-absorption, it is normal practice[167] to make a transfer of the WSFs signal to clear optical fibres with less attenuation, for cases where long fibres are required. The small light loss in the fibre connection compensates the light attenuation in the WSFs.

The VLPC is presently the only device that reliably combines high quantum efficiency with excellent single photon sensitivity. It is therefore an excellent candidate for the WSF gamma camera. The higher quantum efficiency compared to PSPMTs could significantly improve the spatial resolution of the camera.

To measure the impact of such an increase in quantum efficiency, Monte Carlo simulations of the spatial resolution of a WSF gamma camera were developed and are shown in chapters 6 and 8. The simulations with quantum efficiency of $\sim 80\%$ are intended mainly to predict the performance of a camera using VLPCs.

4.5 Discussion and conclusions

The design of the WSF gamma camera is very flexible, allowing its application to specific nuclear medicine imaging examinations where the positioning of the camera may be crucial in obtaining an optimum image.

Simple analytical calculations indicate that the light levels at the WSFs are high enough to be detected with currently available PSPMTs. Due to the narrow light distribution over the WSFs, it is expected that a spatial resolution comparable to that of Anger cameras may be achieved using PSPMTs

to read out the WSFs.

But the spatial resolution improves with the inverse of the square root of the number of photoelectrons in the centroid calculation (section 2.3.2). Hence, a device with higher quantum efficiency than the PSPMTs would clearly provide better spatial resolution. Such a device, the VLPC, exists and is currently used in high energy physics experiments for a similar readout of WSFs. Its potential is further discussed below (sections 6.2.2 and 8.6).

Chapter 5

Demonstration of light collection by WSFs coupled to CsI(Na) crystals

5.1 Introduction

This chapter describes experimental work to assess the practical feasibility of the wavelength-shifting fibre (WSF) gamma camera introduced in chapter 4. In particular, measurements are carried out on the amount of light trapped inside WSFs for different experimental conditions, as previously reported in ref. [191]. The results lead to the optimization of the scintillator characteristics and of the optical coupling between the fibres and the scintillator and are used for the subsequent construction of a WSF gamma camera prototype (described in chapter 8).

As discussed in chapter 4, the common inorganic scintillators NaI(Tl) and CsI(Na) are particularly suited to couple to commercially available blue-to-green WSFs [165, 170]. Both scintillators have high light output with a light emission spectrum matching the absorption spectrum of the WSFs. Compared to NaI(Tl), CsI(Na) has the advantage of a higher stopping power. Therefore, thinner CsI(Na) crystals may be used to reduce the light spread over the WSFs, hence improving the spatial resolution, for the same gamma ray detection efficiency. Furthermore, CsI(Na) is only slightly hygroscopic and can therefore be used without the encapsulation required by NaI(Tl).

For these reasons, the experiments described in this chapter are carried out using blue-to-green WSFs coupled to CsI(Na).

In these experiments, the signals from one or more WSFs are read out with a single channel photomultiplier tube. Among the photon counting

photodetectors described in section 4.4, PSPMTs and HPDs are the most widely available at a reasonable cost and with well established photon counting capabilities. Hence the use of a PMT in this study, since it has similar quantum efficiency to those of PSPMTs and HPDs, and therefore provides similar photo-electron statistics for the WSF readout.

5.2 Methods

5.2.1 Wavelength-shifting fibres

The Bicron BCF-91A double clad WSFs used in this study were described in detail in section 4.2. Fibres with different cross-sectional dimensions were tested: 1 mm diameter round, $1 \times 1 \text{ mm}^2$ square and $2 \times 2 \text{ mm}^2$ square. Both ends of the fibres were polished and only the signals from one end were read out for each fibre.

The readout of both ends would lead to a more complex geometry in the final design of a WSF gamma camera. One of the main disadvantages would be the introduction of regions on both sides of the crystal where the edge of the camera would be inaccessible, for instance, to be pressed against the chest wall, as shown in figure 2.10.

5.2.2 Scintillation crystals

Two CsI(Na) crystals manufactured by Hilger Crystals¹ were used with an area of $12.7 \times 12.7 \text{ cm}^2$, a suitable area for scintimammography. The crystals had different thickness of 3 mm and 5 mm which correspond to 69% and 86% absorption of 140 keV gamma rays. With respect to conversion efficiency this is roughly equivalent to 5 mm and 8 mm thick NaI(Tl) crystals, in the range of NaI(Tl) thickness used in high spatial resolution Anger cameras for 140 keV gamma rays (6 to 9 mm thickness).

The $12.7 \times 12.7 \text{ cm}^2$ surfaces were well polished and the smaller surfaces at the edges were left un-polished.

5.2.3 Experimental set-up

Figure 5.1 depicts the experimental conditions in this study. The CsI(Na) crystal was coupled with silicone gel to a 5" circular PMT (E-PMT), EMI 9530.

A set of WSFs was coupled to the other side of the crystal either with silicone gel (gel coupling) or without any coupling compound (air coupling).

¹Hilger Crystals, Westwood, Margate, Kent, CT9 4JL, UK.

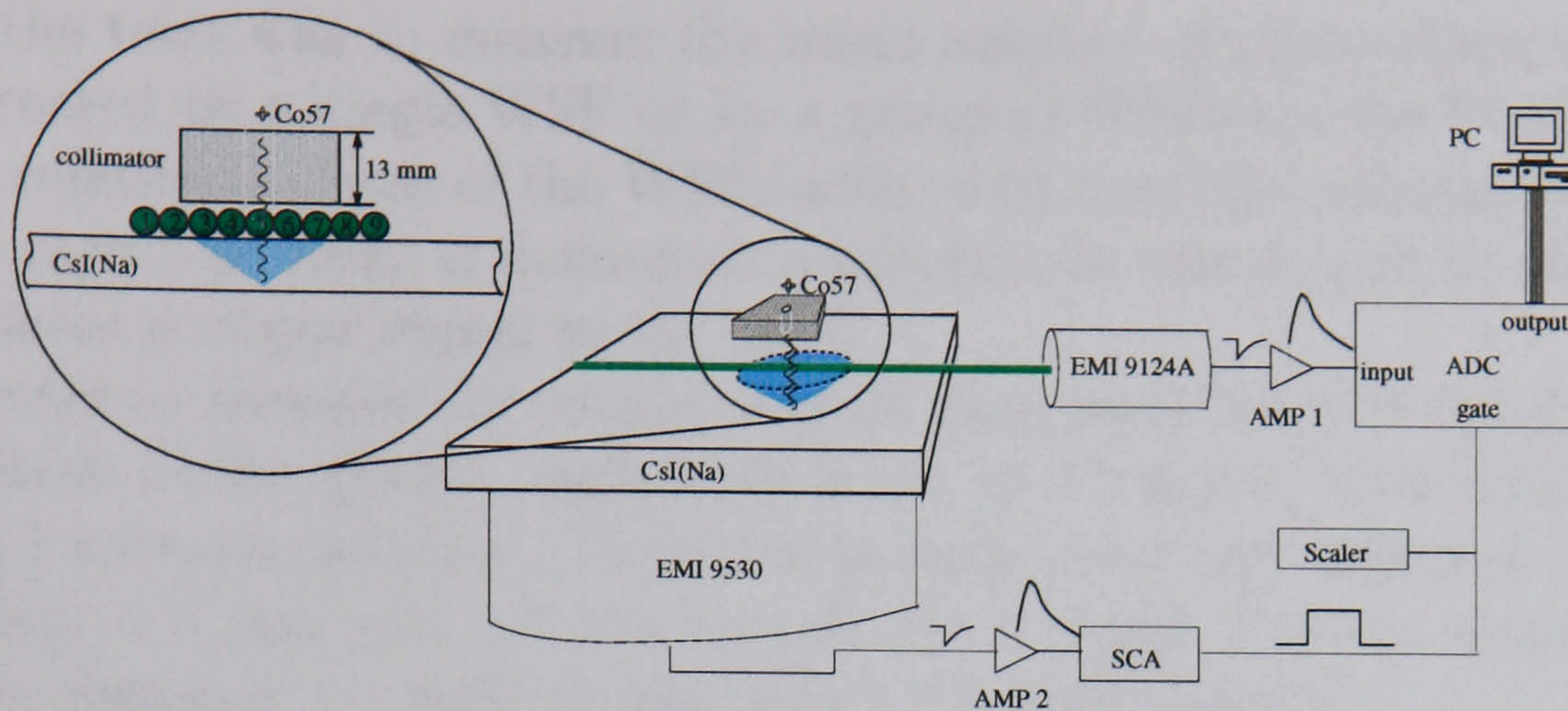


Figure 5.1: Setup used for the measurement of the WSF signals.

The signals from one or more fibres were read out with a 30 mm diameter photon counting PMT (PC-PMT), model 9124A from Electron Tubes Ltd². This tube has an 11 stage linear focused dynode structure which, according to the manufacturer's data sheets, achieves a gain of over 2×10^6 for a 900 V high voltage setting. It has a RbCs photocathode with 20% quantum efficiency at a wavelength of 500 nm, a good single electron resolution (peak-to-valley ratio of 2:1) and a dark emission of 284 counts per second for a 0.2 photo-electrons threshold.

A lead collimator with a 1 mm diameter hole and 13 mm thickness was used to irradiate the scintillator at known positions with Co^{57} gamma rays (predominantly 122 keV). Following a gamma ray interaction in the scintillator, part of the light was collected by the E-PMT, creating a total energy signal. This signal was amplified with a Canberra 2012 NIM amplifier (AMP 2) and the amplified signal was processed by a single channel analyser (Canberra SCA 2037AS, NIM) to produce a trigger pulse for the ADC gate. The number of trigger pulses was counted with a Canberra 2071A scaler.

Simultaneously, some light was absorbed, wavelength-shifted and trapped inside the WSFs. These signals were read out with the PC-PMT, amplified with a Canberra 2020 NIM amplifier (AMP 1) with an adjustable shaping time set to $1.5 \mu\text{s}$ and digitised with a Canberra 8075 NIM peak sensing ADC. The digitised values were then transferred to a PC to produce pulse-height distributions for the WSF signals.

Several tests were performed for both scintillators, changing the type of WSF and the optical coupling between the fibres and the scintillator. The

²Electron Tubes Ltd, Bury Street, Ruislip, Middlx HA4 7TA, UK, www.electron-tubes.co.uk.

aim of the tests was to measure the mean number of photo-electrons μ per event created by a single WSF or by a group of WSFs on the PC-PMT, for a given relative position of the WSFs with respect to the collimated beam of gamma rays. An event is defined as a gamma ray interaction in the crystal that creates a trigger signal in the SCA.

In order to measure the output of more than one fibre with the PC-PMT, three black Delrin covers, each with a set of 13 holes, were fitted to the PC-PMT entrance window. The holes in each cover had different diameters of 1.1 mm, 1.5 mm and 2.9 mm to suit the 3 types of fibres tested (1 mm diameter round, $1 \times 1 \text{ mm}^2$ square and $2 \times 2 \text{ mm}^2$ square).

Each hole defined a fixed position at the PC-PMT photocathode. It was found that the variation between the response at different positions was less than 5%. Measurements with single fibres were taken always at the same position at the PC-PMT photocathode and measurements with more than one fibre were made by fitting each fibre in an different hole.

5.2.4 Data analysis

For a given mean light intensity on the photocathode of the PC-PMT there is a mean number of photo-electrons μ that are released from the photocathode, captured by the first dynode and subsequently amplified in the dynode structure. Hence, for a given light intensity per event the probability of a particular event creating n photoelectrons collected by the first dynode is given by

$$P(n; \mu) = \frac{\mu^n e^{-\mu}}{n!}. \quad (5.1)$$

For very low light levels, the probability $P(0; \mu) = e^{-\mu}$ that, for a given event, zero photo-electrons are created, is significant. It can be calculated by measuring the number of pulses N_{th} in the PC-PMT above threshold and the total number of triggers N_T measured with the scaler in figure 5.1

$$P(0; \mu) = \frac{N_T - N_{th}}{N_T}. \quad (5.2)$$

The value of μ can then be calculated from equation 5.1

$$\mu = -\ln(P(0; \mu)) = -\ln\left(\frac{N_T - N_{th}}{N_T}\right). \quad (5.3)$$

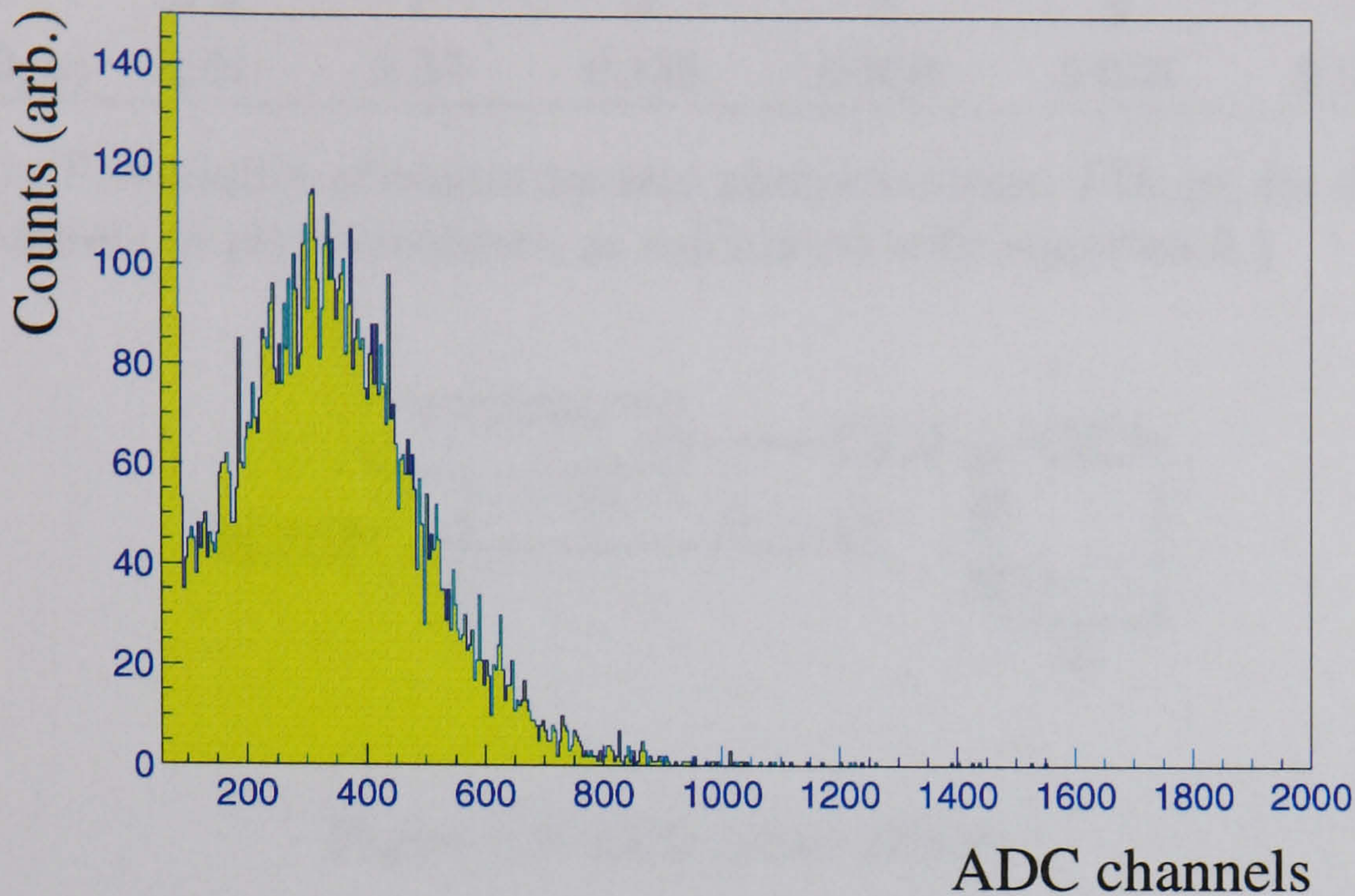


Figure 5.2: Pulse-height distribution for one WSF coupled to the PC-PMT with pulses of very low intensity, showing the single photo-electron peak and the electronic pedestal.

The numbers of background events, measured in a control experiment before each exposure to the source, were subtracted from N_T and from N_{th} . Typically, each acquisition took 120 s. For this period of time, the total number of background events counted by the scaler was $\sim 10\%$ of N_T . In the same period, the number of background events above threshold in a WSF was $\sim 2\%$ of N_{th} .

A typical pulse-height distribution at low light levels with the set-up described in the previous section is shown in figure 5.2. The noise pedestal is visible on the left followed by the single photoelectron peak. A good separation between the pedestal and the single photoelectron peak is observed allowing a threshold level to be set in the region between the two (in ADC channel 86), which is known as the valley. The single electron peak-to-valley ratio is 2:1 which agrees with the manufacturer's specifications.

Table 5.1 shows $P(0, \mu)$ for different values of μ . For $\mu \gtrsim 3$ the value of $P(0, \mu)$ becomes very small and the calculation of μ using equation 5.3 is less accurate. For these cases it is necessary to calibrate the pulse-height distribution from the fibres in terms of ADC channels per photo-electron. Therefore, in the data analysis, if $P(0, \mu) < 5\%$, then μ is found by the mean of the pulse-height distribution after this calibration.

μ	0.5	1	2	3	4	5
$P(0, \mu)$	0.61	0.37	0.135	0.050	0.018	0.007

Table 5.1: Probability of obtaining zero photoelectrons, $P(0, \mu)$, for different mean numbers of photoelectrons, μ , calculated with equation 5.1.

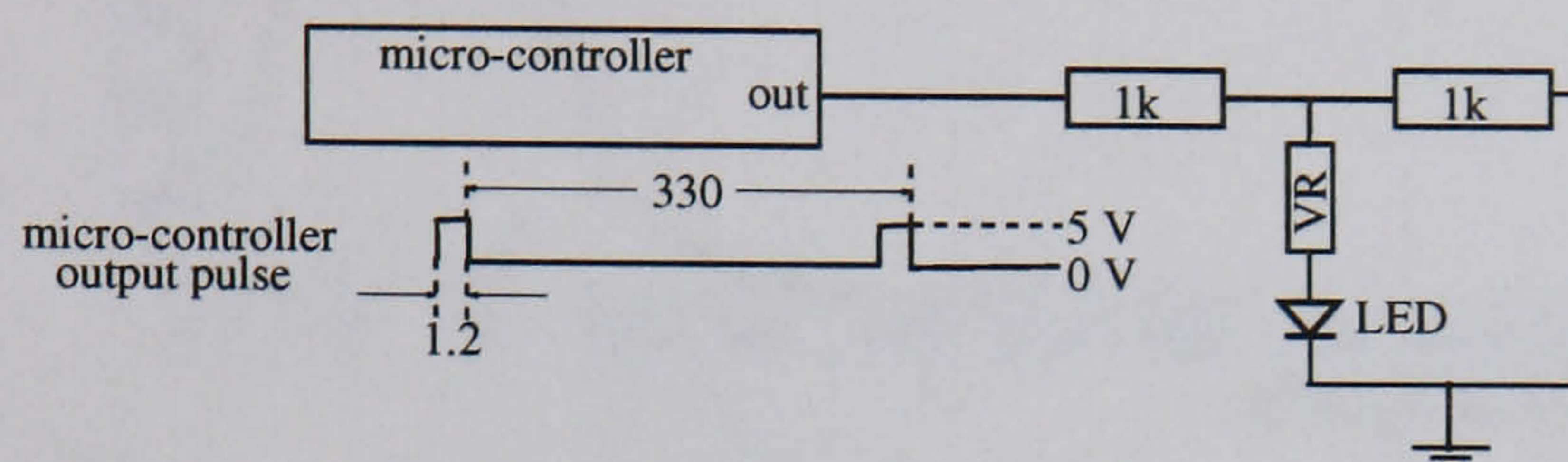


Figure 5.3: LED pulser circuit.

5.3 Calibration of the photon counting system

The PC-PMT was first illuminated by an LED-pulsed optical fibre. A red-emitting LED with maximum emission at 660 nm was optically coupled to one end of a 1 mm diameter quartz optical fibre. The other end of the fibre was used to illuminate the tube. The LED was pulsed by a programmable micro-controller with a $1.2 \mu\text{s}$ wide square pulse every $330 \mu\text{s}$. The LED light intensity was regulated with the circuit shown in figure 5.3, where the variable resistor VR was used to adjust the current intensity across the LED.

The electronics readout system was similar to the one shown in figure 5.1. The ADC gate signal was, in this case, provided by the micro-controller, simultaneously with the LED pulse, with no need for AMP 2 and the SCA.

The single photo-electron peak for the PC-PMT was obtained by adjusting the LED intensity to low light levels. From Poisson statistics, for a mean number of photoelectrons of less than 0.5 for example, the probability of creating more than one photoelectron is less than 10%. Therefore, the pulse-height distribution consists mainly of events with 0 or 1 photo-electrons which is ideal to obtain the single photo-electron peak. A typical pulse-height distribution is shown in figure 5.4. The noise pedestal is not visible since the ADC's lower level discriminator was set above its level. Comparing with the position of the single photoelectron peak, the discriminator threshold was at 0.15 photoelectrons.

The value of $P(0; \mu)$ was obtained by calculating the area under the peak

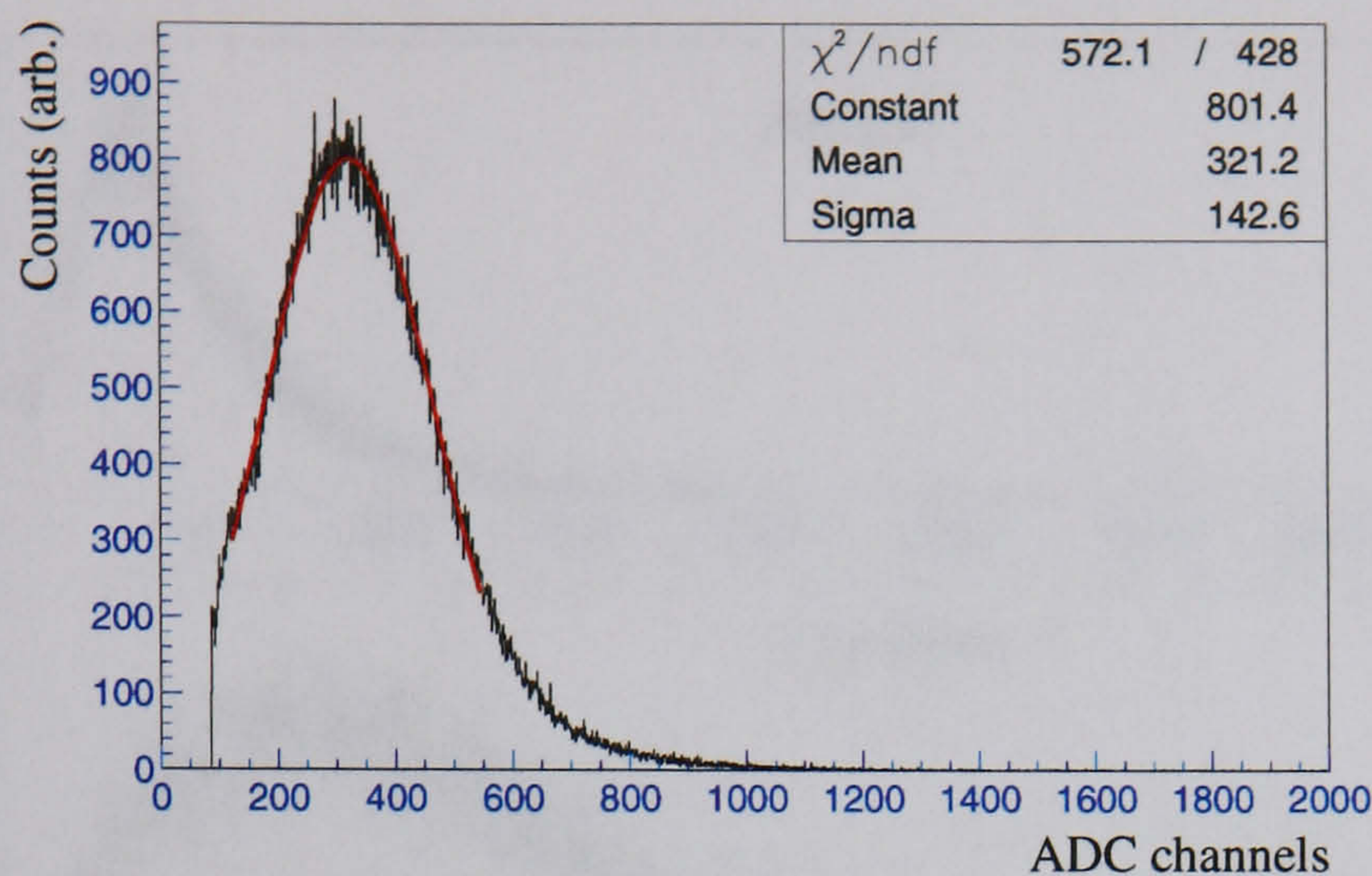


Figure 5.4: Pulse-height distribution showing the single photo-electron peak for the PC-PMT.

and comparing to the total number of ADC trigger pulses from the LED pulser during the acquisition time (equation 5.2). A value of 92% is obtained which gives a mean $\mu=0.08$ (equation 5.3). A Gaussian fit to the peak gives a mean of 278 ADC channels per photo-electron ($278=321-43$, where 321 is the mean of the fit and 43 is the electronic pedestal) with an rms of 143 ADC channels. This rms value is the single electron resolution of the PMT σ_{SER} which for this tube is found therefore to be 0.51 photo-electrons.

To measure the effect of the dark pulses from the PC-PMT, the tube was completely light sealed (with no fibre coupled to it) and the ADC was triggered as above. It was found that the number of pulses above threshold was about 0.1% of the total number of triggers.

5.4 Light collected by the WSFs with the PC-PMT

5.4.1 Tests with 1 mm diameter WSFs

For each CsI(Na) slab (3 and 5 mm thick) a set of 9 round WSFs (1 mm diameter) were laid packed closely together and in close contact with the crystal surface. The fibres were coupled to the crystal either with silicone gel with a measured relative refractive index of 1.46 (gel coupling) or with no optical compound (air coupling). The fibres were 40 cm long and only one end of each fibre was coupled to the PC-PMT. The lead collimator was positioned

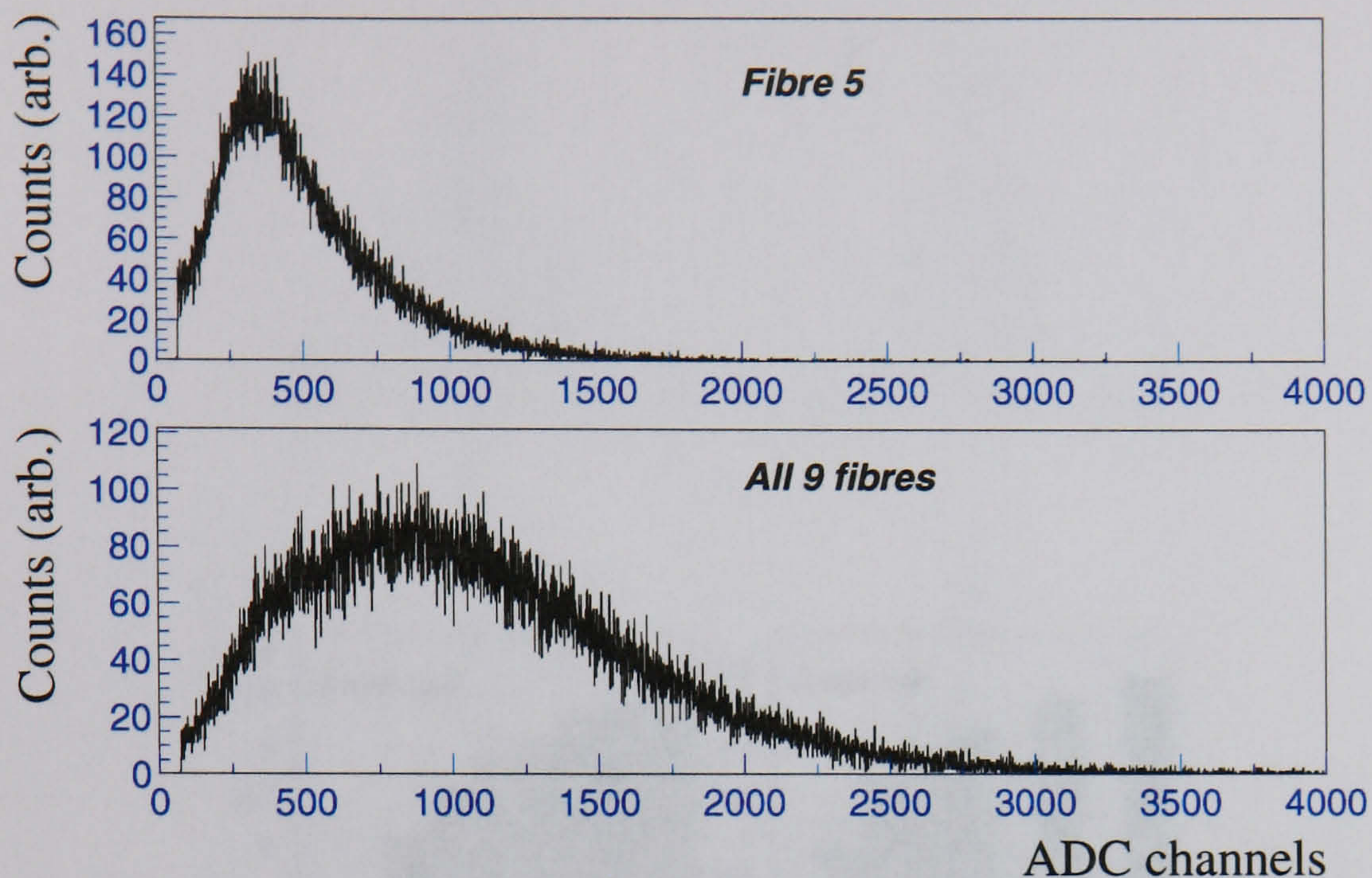


Figure 5.5: Pulse-height distribution for two cases a) fibre 5 and b) all 9 fibres. Results are shown for the 3 mm thick crystal with the fibres coupled to it with gel. See figure 5.1 for details of the setup.

above fibre 5 in figure 5.1 (with an estimated precision of ± 0.5 mm).

Figure 5.5 shows the pulse-height distributions obtained with the 3 mm thick crystal with gel coupling for the signals from fibre 5 and for the signals from all 9 fibres together.

Figure 5.6 shows the output of groups of fibres. In these plots, 1 fibre corresponds to fibre 5 only, 2 fibres to fibre 5 plus one of its immediate neighbours, and so on, each time adding a fibre further away from the collimated gamma ray beam.

The number of photoelectrons μ obtained from the 9 WSFs is higher with gel coupling, being almost double compared to air coupling for both crystals. This is explained by the greater amount of light reaching the WSFs with gel coupling, as shown in table 4.2.

The output of each fibre is shown in figure 5.7 which correspond to the $FPSF(i)$ defined in equation 4.12. The light distributions are narrower for air coupling as expected, since total internal reflection inside the crystal prevents more light from reaching the WSFs in the case of air coupling (see figure 4.11). Again, the fibre output is higher for gel coupling in agreement with the results of figure 5.6.

Comparing these results with the predictions presented previously in ta-

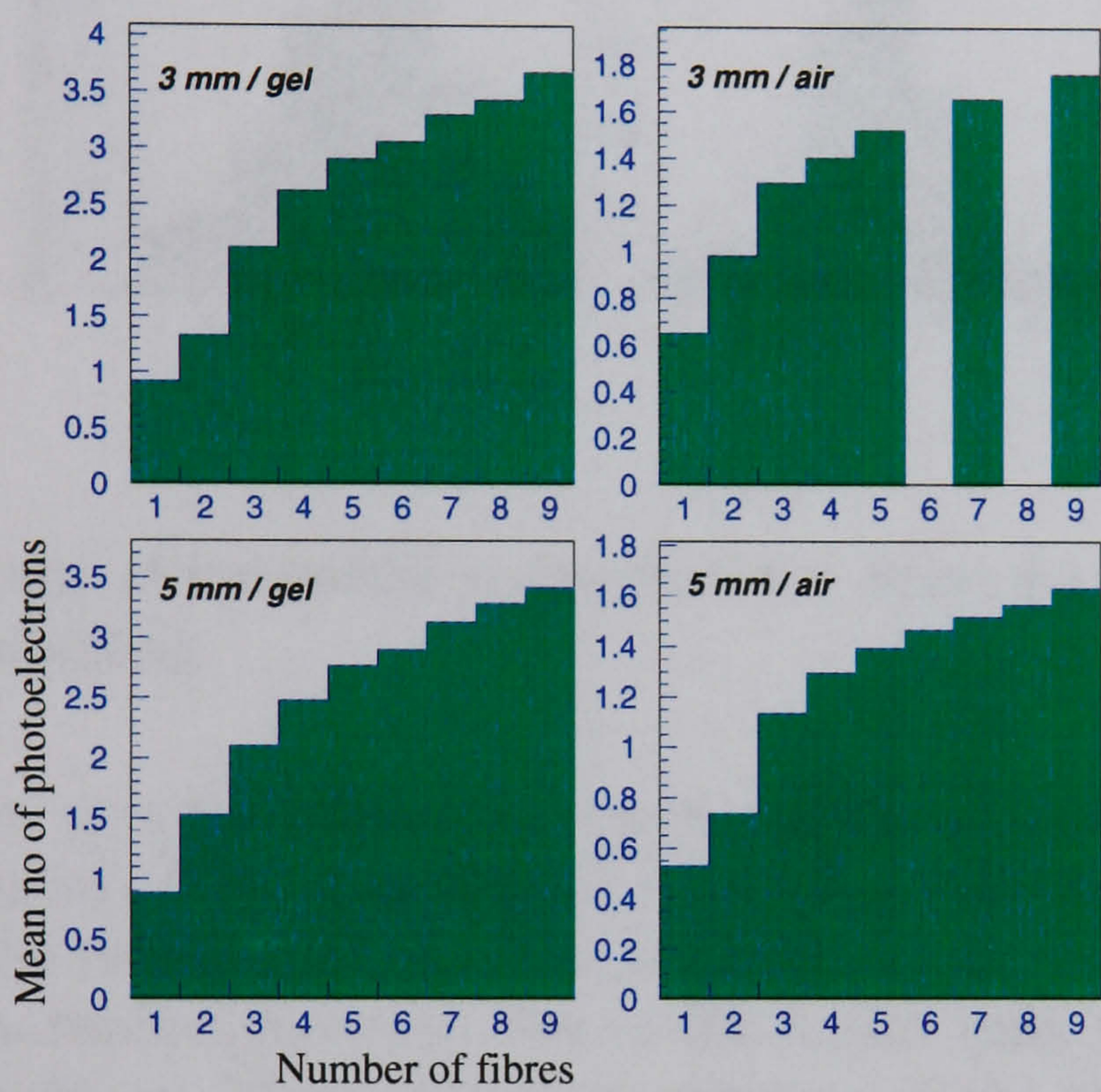


Figure 5.6: Output of groups of 1 mm diameter fibres obtained with the 3 mm and the 5 mm thick CsI(Na) crystals with gel or air coupling. See text for a more detailed explanation.

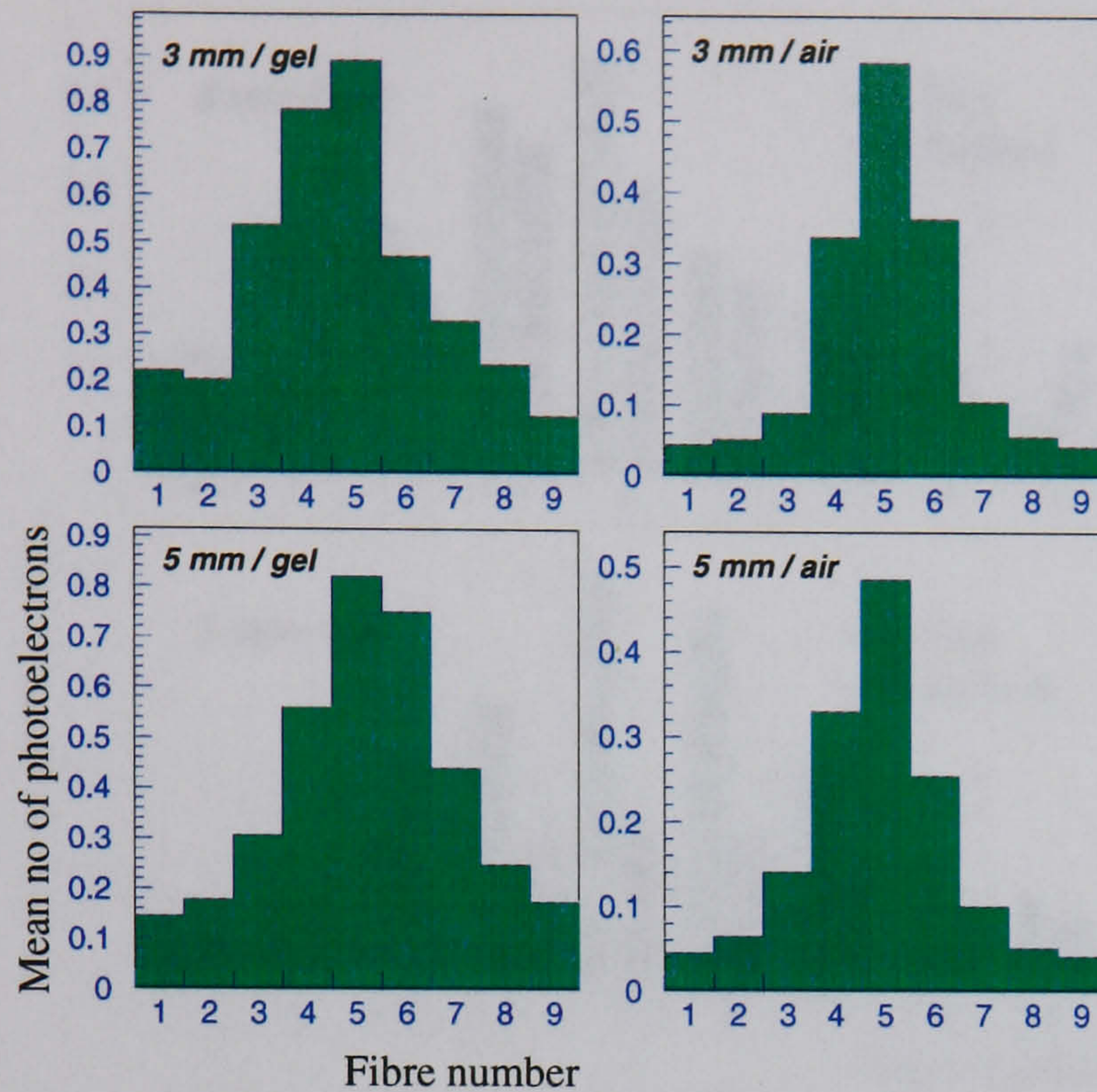


Figure 5.7: Output of individual 1 mm diameter fibres for the two crystals with gel or air coupling.

ble 4.2, it is seen that the output for a group of fibres agrees well, both for gel and air coupling. The experimental results for individual fibres show a lower signal in the central fibre than the predicted value. The sum in a group of fibres remains similar, however, due to the higher than predicted signals in the peripheral fibres. These differences observed in the signal distribution over the fibres between the experiments and the calculations are due to the simplistic assumptions in the analysis of section 4.3. As an example, the refraction of scintillation photons exiting the crystal into the gel layer and subsequently into the WSFs, was not taken into account.

No significant difference is observed between the results obtained with the two crystals. This might be due to the fact that the gamma rays enter the crystal through the same surface where the WSFs are coupled (top surface). From the gamma ray attenuation coefficients for 122 keV gamma rays in CsI(Na) it is found that 81% and 94% of the gamma rays are absorbed in 3 mm and 5 mm respectively. Therefore only a small fraction of interactions occur at different depths in the crystals and the output of the WSFs is expected to be similar for both crystals.

The main difference in performance between the two crystals should be in the light profiles over WSFs located between the crystal and the E-PMT

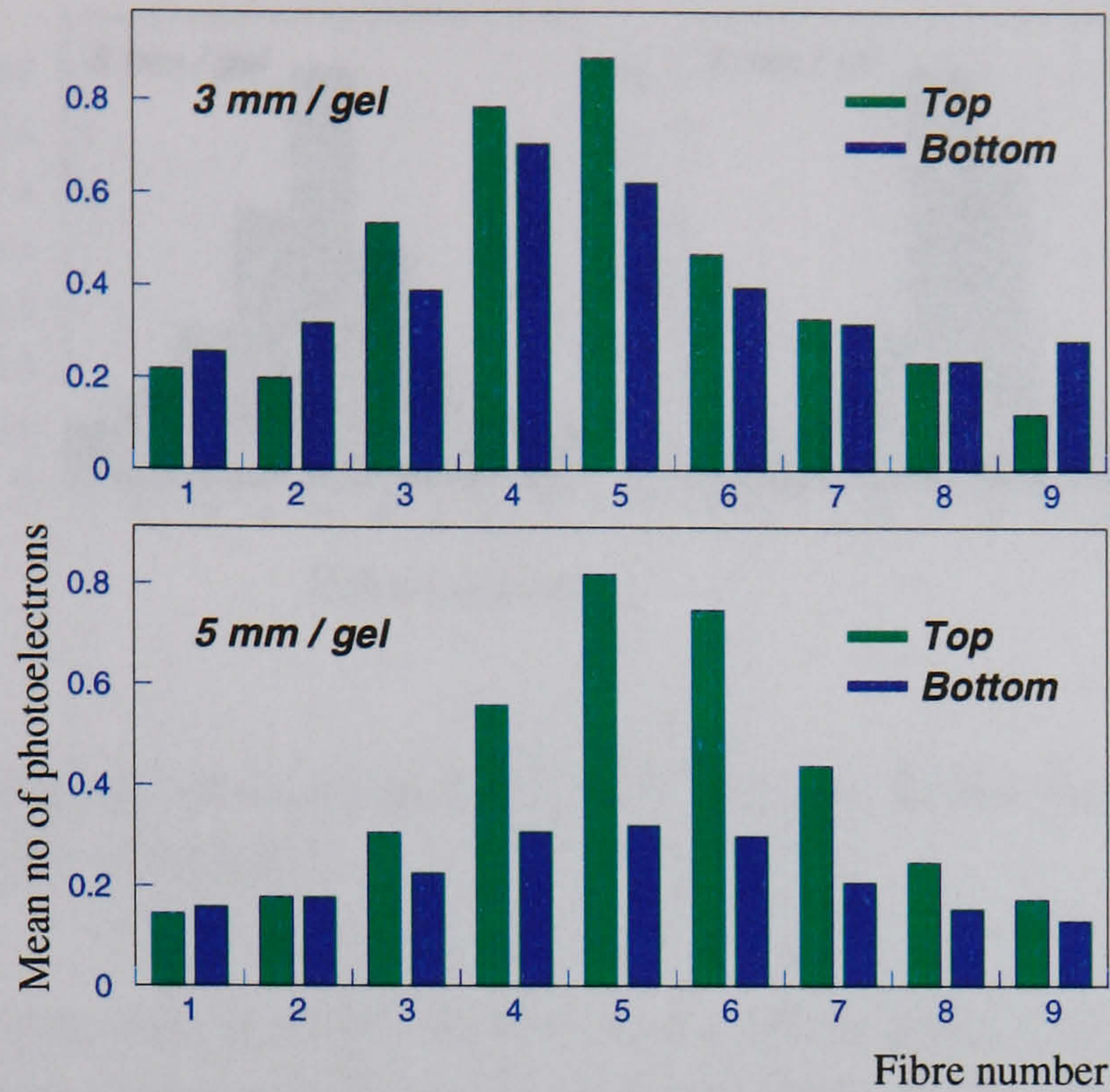


Figure 5.8: Output of 1 mm diameter individual fibres coupled to both sides of the crystals with gel.

(bottom WSFs). For 122 keV gamma rays incident perpendicularly on the 5 mm thick CsI(Na) crystal, $\sim 80\%$ of the interactions occur at a depth of less than half of the crystal thickness. Therefore, the light profile over the bottom fibres is wider than over the top fibres. This effect should be less important for the thinner crystal.

To confirm this hypothesis, the experimental setup in figure 5.1 was modified and the WSFs were positioned between the CsI(Na) and the E-PMT, coupled to both with gel. The output of each fibre when the gamma ray collimator is above fibre 5 is shown in figure 5.8, together with the results from figure 5.7 for comparison.

A broader profile is indeed observed for the 5 mm thick crystal for the bottom fibres compared to the top fibres. For the 3 mm thick this effect is much less noticeable.

5.4.2 Tests with square WSFs

The same procedure was followed to test WSFs with square cross-sections. These fibres have similar properties to the 1 mm round fibres as seen in table 4.1. Square fibres provide a more efficient coupling to the flat surface

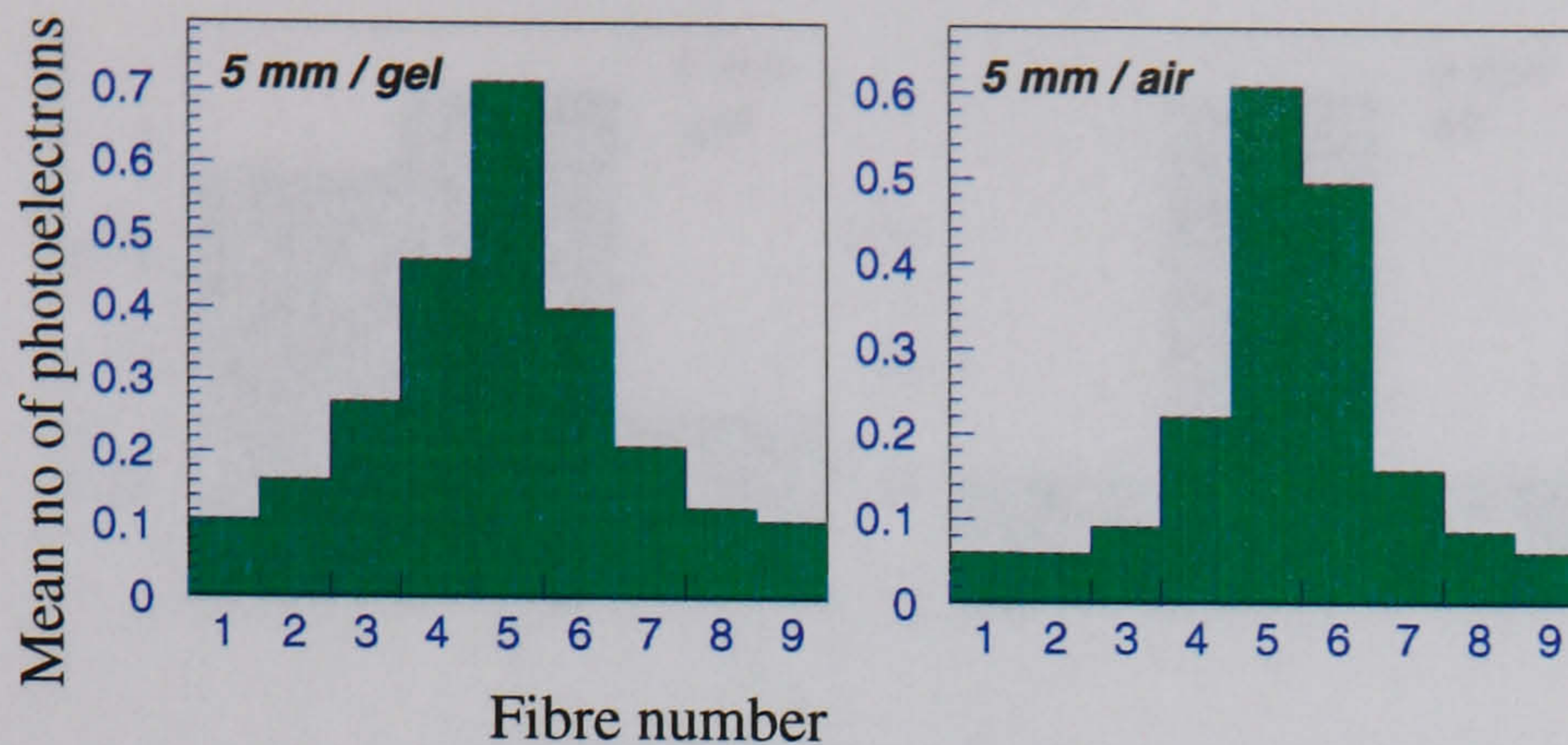


Figure 5.9: Output of individual $1 \times 1 \text{ mm}^2$ square fibres for the two crystals and with gel or air coupling.

of the scintillators, which may result in an enhanced light collection. The trapping efficiency of square fibres is independent of the position inside the fibre where the green photons are generated. It is slightly higher than the trapping efficiency for photons generated on the axis of round fibres (see section 4.2.2).

A set of 9 square WSFs with $1 \times 1 \text{ mm}^2$ cross-section, 40 cm length and with both ends polished was coupled to the 5 mm thick CsI(Na) crystal on its top surface (see figure 5.1) with and without silicone gel.

The output of individual fibres is shown in figure 5.9 and it is in good agreement with the results in figure 5.7 for the 1 mm diameter round fibres. No significant difference between square and round fibres was apparent from these results.

Similar measurements were performed with a set of 3 WSFs with $2 \times 2 \text{ mm}^2$ cross-section and 40 cm long. The results for the individual fibres are shown in figure 5.10. Comparing with the results for the same area covered by 6 fibres of 1 mm diameter or $1 \times 1 \text{ mm}^2$ cross-section there is a similar total number of photoelectrons (≈ 3).

Round fibres have the advantage of being less expensive than square ones which makes them preferable for this application, since no significant difference in performance is observed.

5.4.3 Aluminium coating of the ends of the WSFs

As discussed in section 5.2.1 only one end of the fibres is read out. An increase in the light levels detected from the fibres could be achieved simply by reading out both fibre ends, but this has the disadvantage of creating dead

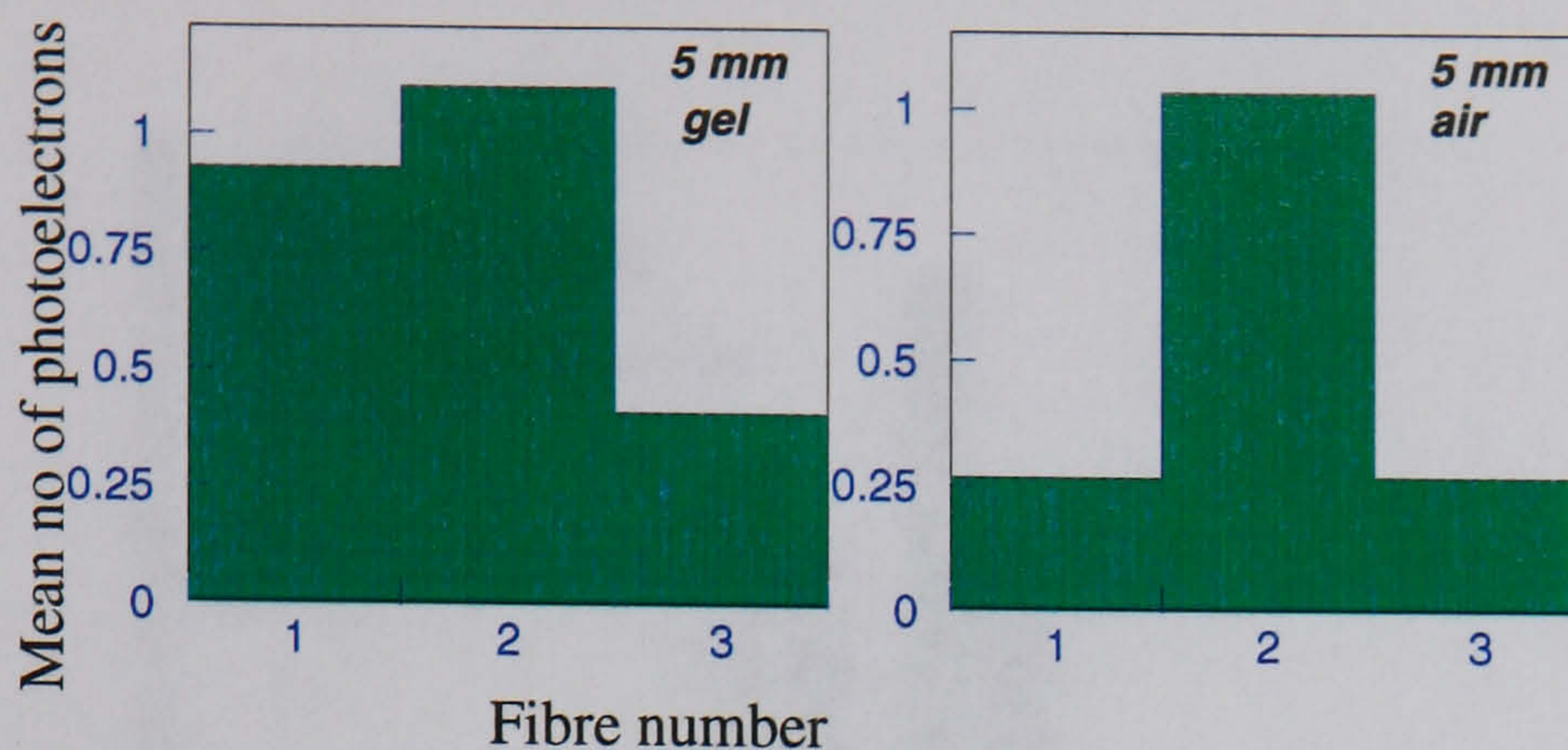


Figure 5.10: Output of individual $2 \times 2 \text{ mm}^2$ square fibres for the two crystals and with gel or air coupling.

regions at the edges of the camera. Alternatively, the unused fibre end may be coated with a specular reflector so that some photons might be reflected and transmitted to the other fibre end. After carefully polishing both ends of 1 mm round WSFs, several layers of aluminium were evaporated onto one end until it shows total opacity under microscope inspection ³.

A set of 6 aluminised WSFs was coupled to the top surface of the 5 mm thick crystal with gel. The results are shown in figure 5.11, together with the results shown in figure 5.7 for the case of the 5 mm thick CsI(Na) and gel coupling. Although difficult to measure accurately with this experimental technique, these results indicate a slight improvement.

5.5 Discussion and conclusions

In preliminary work by Worstell et al [162, 192, 193] and Williams et al [194], the output of bundles of WSFs coupled to several scintillators was also measured with PMTs. They used thin (2~5 mm thick) single crystals with the larger faces covered by WSFs, and measured the average number of photoelectrons per gamma ray interaction using photomultipliers with standard bialkali photocathodes. The results obtained are shown in table 5.2 together with those from the present work with the 3 mm thick crystal.

The number of photoelectrons obtained even with the very bright CsI(Na) crystal is very small. This is mainly due to a) a spectral mismatch between the emission of the scintillator and the absorption of the WSFs; b) the low

³Thanks are due to Mr. Derek Thomas, Department of Physics and Astronomy, UCL, for aluminising the fibres.

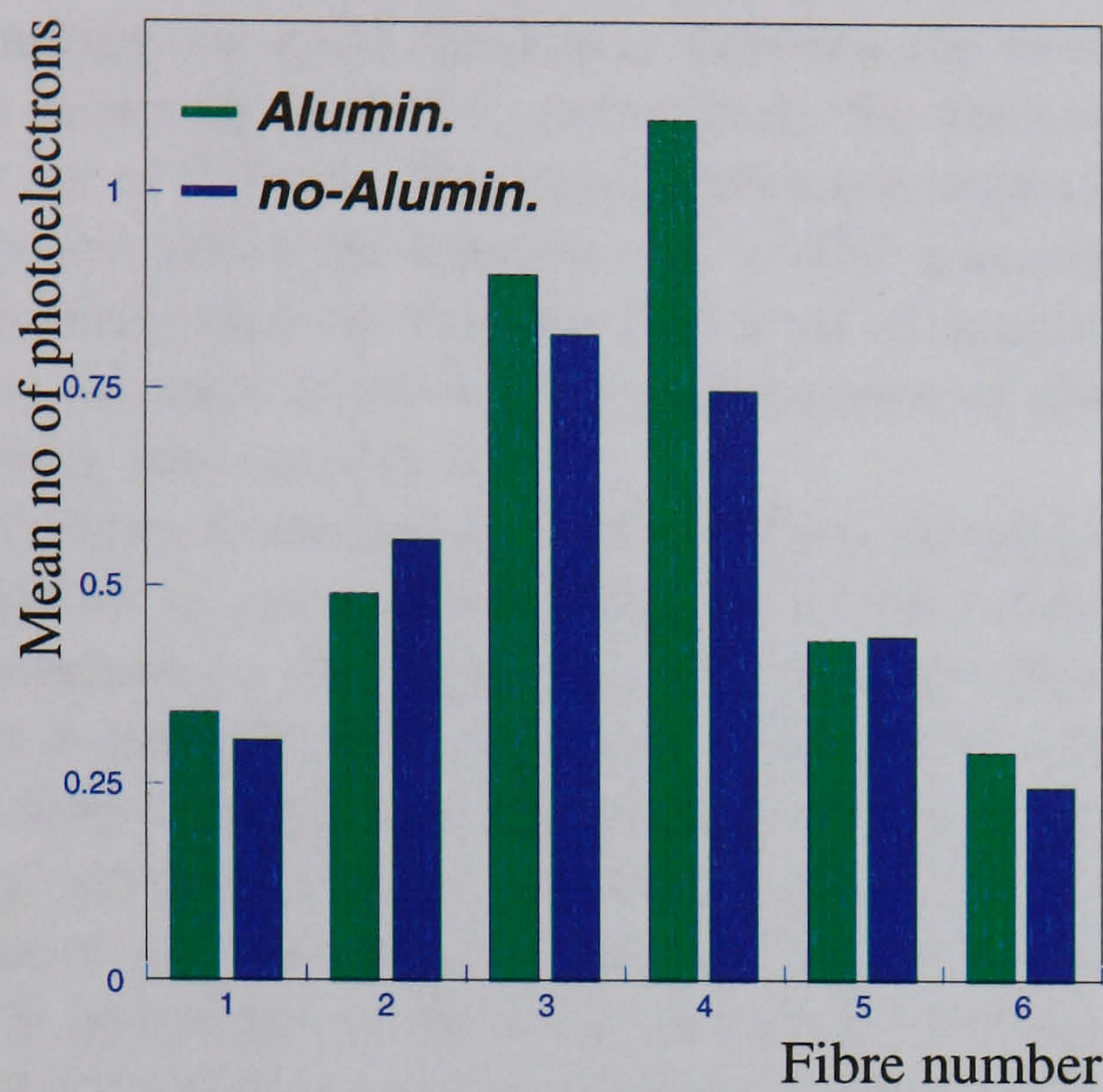


Figure 5.11: Output of individual 1 mm diameter fibres with one end aluminised to improve light output. The fibres are coupled to the top surface of the 5 mm thick crystal with gel. Also shown are the results for the non-aluminised 6 central fibres in figure 5.7 (5 mm / gel) for comparison.

Crystal	WSF	Coupling	Energy (keV)	nphe	nphe/MeV	ref	Source:
							O-Other authors T-This work
LSO:Ce	Y-11	clear epoxy	511	8	16	[192]	O
LSO:Ce	BCF-91A	optic. gel	511	8.6	17	[194]	O
LSO:Ce	BCF-91A	air	511	6.1	12	[194]	O
CsI(Na)	BCF-91A	clear epoxy	511	10	20	[193]	O
CsI(Na)	—	optic. gel	662	20	30	[194]	O
CsI(Na)	BCF-91A	silic. gel	122	3.8	31	fig. 5.7	T
CsI(Na)	BCF-91A	air	122	1.8	15	fig. 5.7	T

Table 5.2: Results of experiments to measure the average number of photoelectrons detected using bialkali PMTs to readout the WSFs. All the fibres are 1 mm round, double clad, manufactured by Kuraray (Y-11) or by Bicon (BCF-91A). The last 2 rows refer to work described above in figure 5.6.

trapping efficiency of WSFs; c) the low quantum efficiency (about 15% to 20%) of bialkali photocathodes for green light (500 nm).

It is worth noting the good agreement between the results obtained and the predictions shown in table 4.2, particularly for the case of the sum of the signals in a set of 7 fibres. The good agreement indicates that the basic general assumptions about the behaviour of a WSF gamma camera are correct and its behaviour may be explained by a set of simple principles. This encourages us to attempt to model the performance of alternative systems of similar geometry (see chapter 6).

As discussed above, 1 mm diameter round fibres are preferable due to their lower cost compared to square fibres while achieving a similar performance. It is also advantageous to use 1 mm rather than 2 mm diameter fibres since the former have a much smaller minimum bend radius, giving flexibility in the design of a camera which may be crucial in determining its compactness.

Gel coupling provides a larger number of photo-electrons than air coupling. Furthermore, the amount of light collected by the E-PMTs is greater with gel which is important to obtain good energy resolution.

The 3 mm thick CsI(Na) crystal provides similar light distributions over sets of WSFs on opposite sides of the crystal. These distributions are also similar to those obtained with WSFs coupled to the top surface of the 5 mm thick crystal. However, broader distributions are obtained for WSFs on the bottom surface of the 5 mm thick crystal and the effect this has on spatial resolution has to be assessed in order to choose the ideal thickness of the scintillator, bearing in mind the higher detection efficiency provided by thicker scintillators.

A simulation of the response of PMTs was developed and is presented in the following chapter. Using the experimental results for the output of WSFs presented above it is possible to simulate the behaviour of a WSF gamma camera composed of WSFs read out by individual PMTs. This allows predictions to be made on the spatial resolution of such a system.

The importance of photo-electron statistics for the overall detection efficiency of the system is discussed in section 4.3.2. There, the imaging efficiency is defined as the probability that, after a given gamma ray interaction inside the energy window, at least one photoelectron is produced by the set of WSFs. The total number of photo-electrons obtained for gel coupling in figure 5.6 is about 3.8 and, therefore, an imaging efficiency of about 98% is expected following the same arguments presented in that section.

Chapter 6

Monte Carlo simulation studies

The results presented in chapter 5 confirm the general predictions made in chapter 4 about the light levels at the wavelength-shifting fibres (WSFs) in the proposed WSF gamma camera. The first part of this chapter describes the use of a widely available Monte Carlo program to simulate the physical processes involved in the production of light trapped inside the fibres in a WSF gamma camera. The results obtained in chapter 4 are based on very general assumptions about the average values of light absorbed and trapped in WSFs. This Monte Carlo method provides more detailed information about the optical paths of individual photons inside the scintillator and the WSFs, allowing a more complete understanding of the parameters that determine the light levels at the WSFs. It can be regarded as a further check of our understanding of the formation of the observed signals.

The second part of the chapter describes a new and simple Monte Carlo simulation to predict the spatial resolution obtained given a set of values for the mean number of photons in a set of WSFs. It is based on the observed data for the output of photomultiplier tubes. Using the results in the previous chapter on the light levels of WSFs, the model allows a prediction of the spatial resolution of a WSF gamma camera in which each WSF is read out with PMTs similar to the PC-PMT in that chapter. The model is also used to simulate the spatial resolution of a WSF gamma camera with higher light levels at the WSFs and with photodetectors with better single electron resolution than the PC-PMT.

6.1 Simulation of a WSF gamma camera

6.1.1 The simulation packages

The simulation of a WSF gamma camera involves two distinct physical processes. The first is the deposition of gamma ray energy in the scintillator. For gamma rays of 140 keV, the main interactions to consider are photoelectric, in which a full energy deposition occurs, and Compton interaction where a gamma ray loses part of its initial energy [24]. The deposition of gamma ray energy in a scintillator is followed by the production of isotropically emitted photons. These photons may undergo successive interactions in the surrounding materials (e.g. reflection, refraction, absorption, transmission) which are the second type of physical processes to take into account.

The gamma ray interactions in the scintillator were simulated with the EGS4 Monte Carlo package ¹. This package has been extensively used in nuclear medicine to simulate the gamma ray interactions in several materials. In particular it has been used to study and optimize the geometry and the materials of the collimator and of the scintillator. A set of initial parameters is defined which includes the nature and dimensions of the materials used and the distribution of initial gamma rays (energy and direction). Using pre-defined tables containing the cross-sections for the various possible interactions in the materials chosen, EGS4 produces an output record specifying the nature and position of successive interactions in a material. It follows the successive photons and energetic electrons created in a cascade event (history) and allows a spatial map to be created with the energy loss for each history.

The simulation of light was performed with the public domain software package DETECT97 ². It is an optical ray tracing program to simulate the behaviour of light given the definition of a set of optical properties for the materials and the optical interfaces used. It allows the construction of several geometries using simple commands involving the generation of points and lines as well as planar, cylindrical, conical and spherical surfaces. Once the geometry is defined, each component (or object) is assigned a set of optical attributes.

Each history begins with the isotropic emission of a photon with an initial wavelength. When the photon travels inside a component it may be absorbed

¹Thanks are due to Kevin Johnson, Dept. Medical Physics and Bioengineering, UCL for setting up the EGS4 code for this study and also for useful discussions.

²DETECT97 [195] is an extended C version of DETECT [196] downloaded from <ftp://animal.rad.washington.edu>. Thanks are due to Dr. Tom Lewellen for downloading instructions.

in the bulk of the material, scattered or wavelength-shifted. The probabilities for each of these events are defined through their mean free paths and whether a photon undergoes any of these events before intersecting a surface is determined by a random sampling of exponential distributions. If absorption occurs, the history is terminated. In the case of scatter, the photon is re-emitted along a random direction chosen from an isotropic distribution. If a wavelength-shifting event occurs, the initial photon is absorbed and a new photon is isotropically emitted with a different wavelength. A different set of absorption and scatter mean free paths are pre-defined for the shifted photons.

When a photon intersects an optical interface several types of interactions may occur depending on the characteristics defined for the surface. There are 5 basic surface attributes in DETECT97:

DETECT Represents the light detector (e.g. a photocathode). If the photons intersect a DETECT surface, the history is terminated and a valid count is stored.

METAL Assumes a smooth surface with a metalised coating where perfect specular reflection occurs. A reflection coefficient may also be defined.

PAINT Assumes a diffuse reflective coating material where Lambertian reflection³ occurs.

POLISH Represents a polished surface which may or may not be in contact with other surfaces. If not, it is assumed to interface with vacuum. Depending on the difference between the refractive indices on both sides of the surface and on the angle of incidence of the photons with respect to the surface normal, the photons may either be reflected or transmitted (refracted) according to Fresnel's reflection formula

$$R = \frac{1}{2} \left[\frac{\sin^2(\theta_i - \theta_t)}{\sin^2(\theta_i + \theta_t)} + \frac{\tan^2(\theta_i - \theta_t)}{\tan^2(\theta_i + \theta_t)} \right]$$

and to Snell's law

³In a perfect Lambertian reflective surface the intensity of the reflected light along an angle θ with respect to the surface normal is independent on the direction of the incident light and is given by $I_\theta = I_\perp \cos(\theta)$, where I_θ is the intensity of reflected light along the direction given by θ and I_\perp is the intensity along the direction perpendicular to the surface. It can be shown that the luminance of these surfaces is independent of the viewing angle[197].

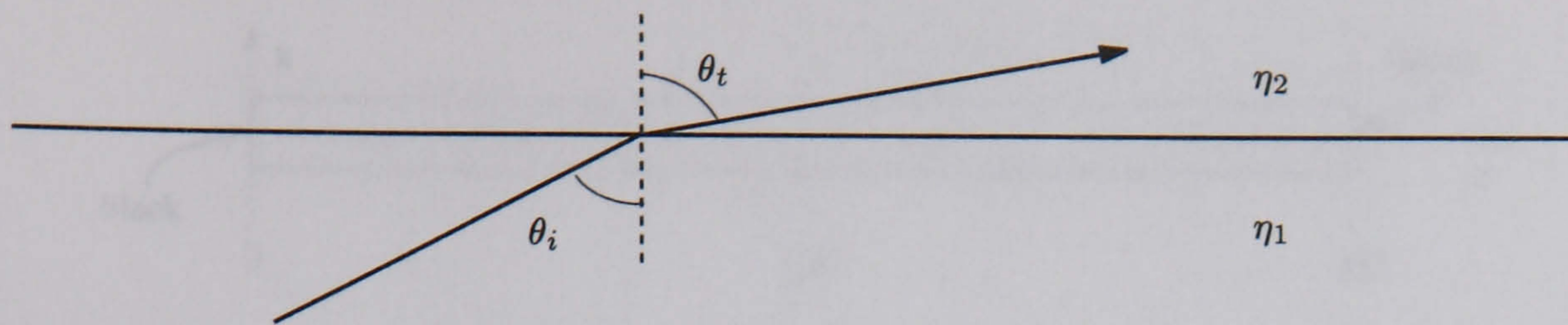


Figure 6.1: Definition of angles in Fresnel's reflection formula and Snell's law.

$$\eta_1 \sin(\theta_i) = \eta_2 \sin(\theta_t)$$

where the angles θ_t , θ_i are defined in figure 6.1, η_1 and η_2 are the refractive indices on both sides of the surface and R is the reflection probability. Snell's law, defines a minimum angle (critical angle), θ_c , below which total internal reflection occurs ($R=1$) $\sin(\theta_c) = \eta_2/\eta_1$.

If the surface is in contact with vacuum, a reflection coefficient may be defined to represent the probability that a transmitted photon is reflected back through the surface into the original component. This simulates a reflective material coating a polished surface with a small vacuum (or air) gap in between.

GROUND Simulates a roughened or ground surface. It is based on the same arguments on reflection and refraction described above for the POLISH surface, but in this case the orientation of the normal to surface is randomly sampled from a Lambertian distribution. As above, a reflection coefficient may be defined.

UNIFIED Allows the definition of a wide range of roughness values. In short, the photon is directed at a micro-facet whose normal makes an angle with the normal to the average surface normal. This angle is randomly sampled from a Gaussian distribution with a user defined standard deviation, allowing therefore some degree of control on the roughness of the surface. The POLISH and GROUND definitions are therefore special cases of this more general surface type. Some more definitions may be specified and are not described since no use is to be made of them (for a complete description see the DETECT97 User Manual that comes with the package distribution).

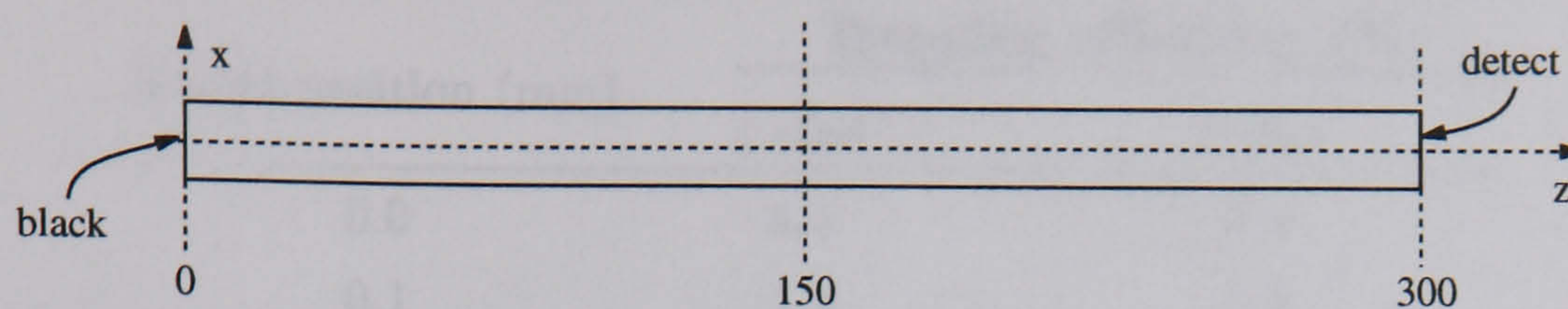


Figure 6.2: Geometry used for the simulation of light trapped inside WSFs. All dimensions in mm.

6.1.2 Light trapped in optical fibres

As mentioned in chapter 4 the trapping efficiency of round fibres depends on the location of photon generation along the fibre radius. The trapping efficiency for photons generated at several positions inside an optical fibre was estimated using DETECT97.

The geometry commands defined a 30 cm long round fibre. Both single clad and double clad fibres were simulated. For the latter case for example, there were 3 concentric cylinders defining the interfaces between the core, the claddings and the external environment (vacuum). Two planes perpendicular to the axis of the cylinders were defined representing the two ends on the fibres. The inner cylindrical surfaces were of the POLISH type. The outer surface was of type PAINT with a 0.0 reflection coefficient (black paint) to eliminate all the photons crossing into the outer cladding. One end of the fibre was painted black and the other was the DETECT surface. The definitions for a singly clad fibre were similar except for the fact that it only required the definition of 2 cylinders.

The refractive indices of the core, first cladding and second cladding were chosen according to the values specified for the Bicon BCF-91A WSF shown in table 4.1. The fibre had a 1 mm diameter core with cladding thickness also shown in that table.

A total of 100,000 photons were generated at different radial positions (e.g. along x) and at $z=150$ mm (see figure 6.2).

Table 6.1 shows the values obtained for the number of photons detected as a percentage of the total number of photons generated, which is the trapping efficiency of the fibre.

It can be observed that the trapping efficiency value for the double clad fibre for photons generated at the axis agrees with the value shown in table 4.1 obtained from an analytical calculation based on the difference in refractive indices of the core material and the claddings. For photons generated at a 0.45 radial distance, the trapping efficiency is about 2.5 higher than for

Radial position (mm)	Trapping efficiency (%)	
	1 clad	2 clad
0.0	3.4	5.6
0.1	3.5	5.6
0.2	3.7	6.1
0.3	4.3	7.0
0.4	5.8	9.4
0.45	8.7	13.6

Table 6.1: Trapping efficiency values for photons generated isotropically at different radial positions inside the fibre.

photons generated at the axis. However, as discussed in section 4.2.2, the former undergo a higher number of reflections due to their spiral trajectories and are more likely to be lost even for short fibres (e.g. 0.5 m).

In a practical situation where non-collimated light impinges sideways on the fibre, the distribution of the positions of generation of wavelength-shifted photons depends on the optical paths of the original photons inside the fibre and on the mean free path for these photons in the core material. In practice the photons are generated at a wide range of radial distances, defining an average trapping efficiency.

A similar simulation was carried out where the photons, instead of being generated at a fixed point, were generated at random positions inside a $0.318 \times 0.318 \text{ mm}^2$ region centered at the fibre axis⁴. The values for the trapping efficiency in this case are 4.1% and 6.7% for the single clad and the double clad fibres respectively.

6.1.3 One WSF coupled to a CsI(Na) crystal

Consider the simple geometry depicted in figure 6.3. A 1 mm diameter WSF is coupled to a 3 mm thick, $125 \times 125 \text{ mm}^2$ slab of CsI(Na). The crystal surface facing the fibre was chosen to be POLISH and all the other surfaces were black PAINT (0.0 reflection coefficient) to avoid the contribution of reflections inside the crystal.

The fibre was a 300 mm long Bicon BCF-91A as in the previous section. Its other dimensions and optical properties are shown in table 4.1. One fibre end was DETECT and the other was black PAINT. The 3 cylinders defining

⁴This is the area of a square that fits inside a 1 mm diameter

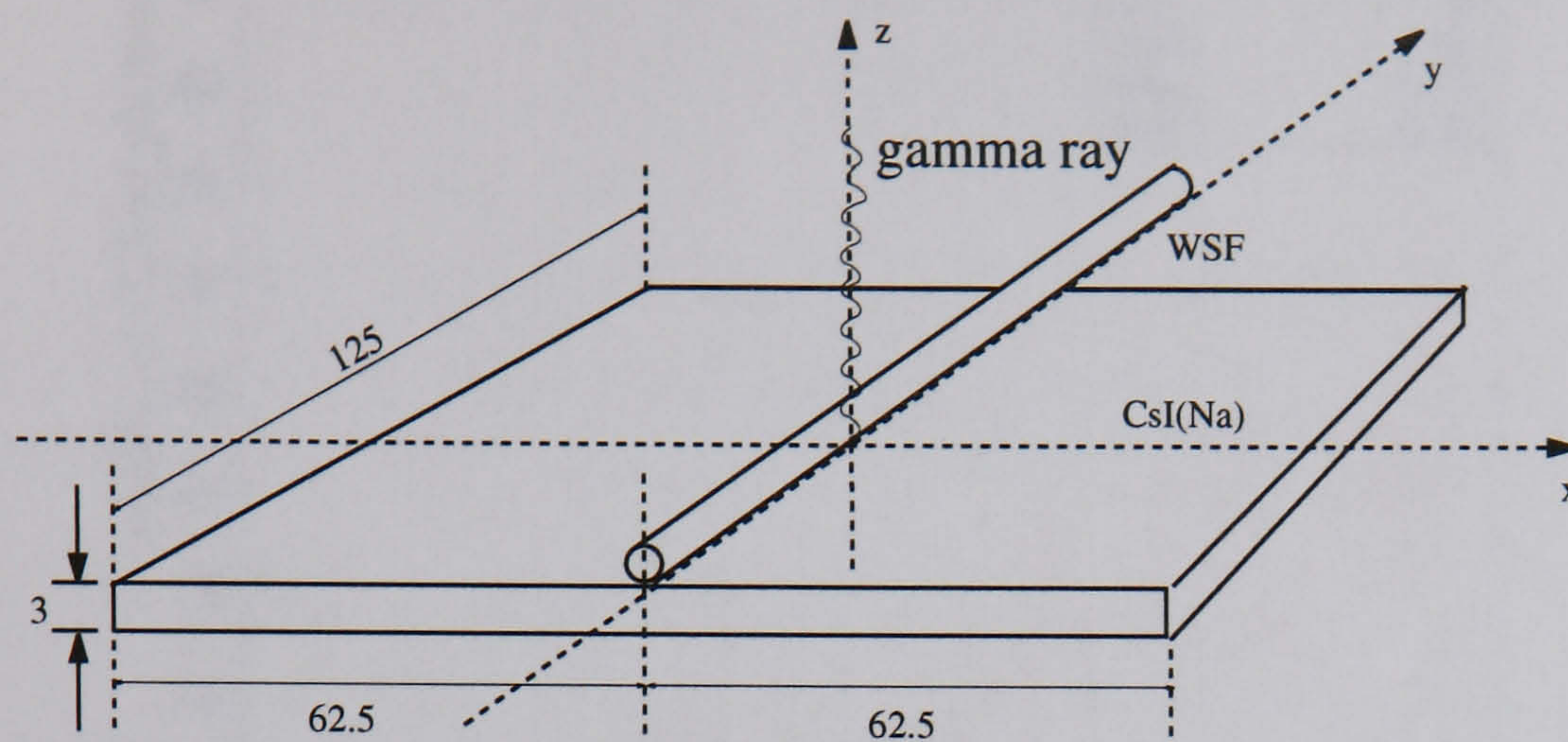


Figure 6.3: A 1 mm diameter WSF coupled to a 3 mm thick, $125 \times 125 \text{ mm}^2$ slab of CsI(Na). The gamma rays interact in the CsI(Na) generating scintillation light pulses. The dimensions are in mm and the objects are not to scale.

the fibre core and claddings were POLISH. There was a 0.1 mm gap between the fibre and the crystal. The refractive index of CsI(Na) is 1.84 and the surrounding medium is silicone optical gel, with 1.46 refractive index.

Radial position of wavelength-shifting events

A first simulation using DETECT97 was performed where 50,000 photons were generated at position $(x,y,z)=(0 \text{ mm}, 0 \text{ mm}, 1.5 \text{ mm})$, i.e., at the centre of the large surface of the crystal, and halfway along the crystal thickness.

Some of the scintillation photons exit the crystal and intercept the WSF. The mean free path for a wavelength-shifting event inside the fibre core was $300 \mu\text{m}$. The wavelength-shifted photons may be trapped inside the fibre, and the bulk absorption mean free path for wavelength-shifted photons was 3000 mm in the fibre core. The details of each photon history were recorded and the position for a wavelength-shifting event inside the fibre was determined.

Figure 6.4 shows the number of wavelength-shifting events as a function of the radial position inside the WSF where the events took place. The average radius is found to be 0.35 mm. This result is particularly important for the case of round fibres since their trapping efficiency strongly depends on the radial position of the wavelength-shifting event (table 6.1).

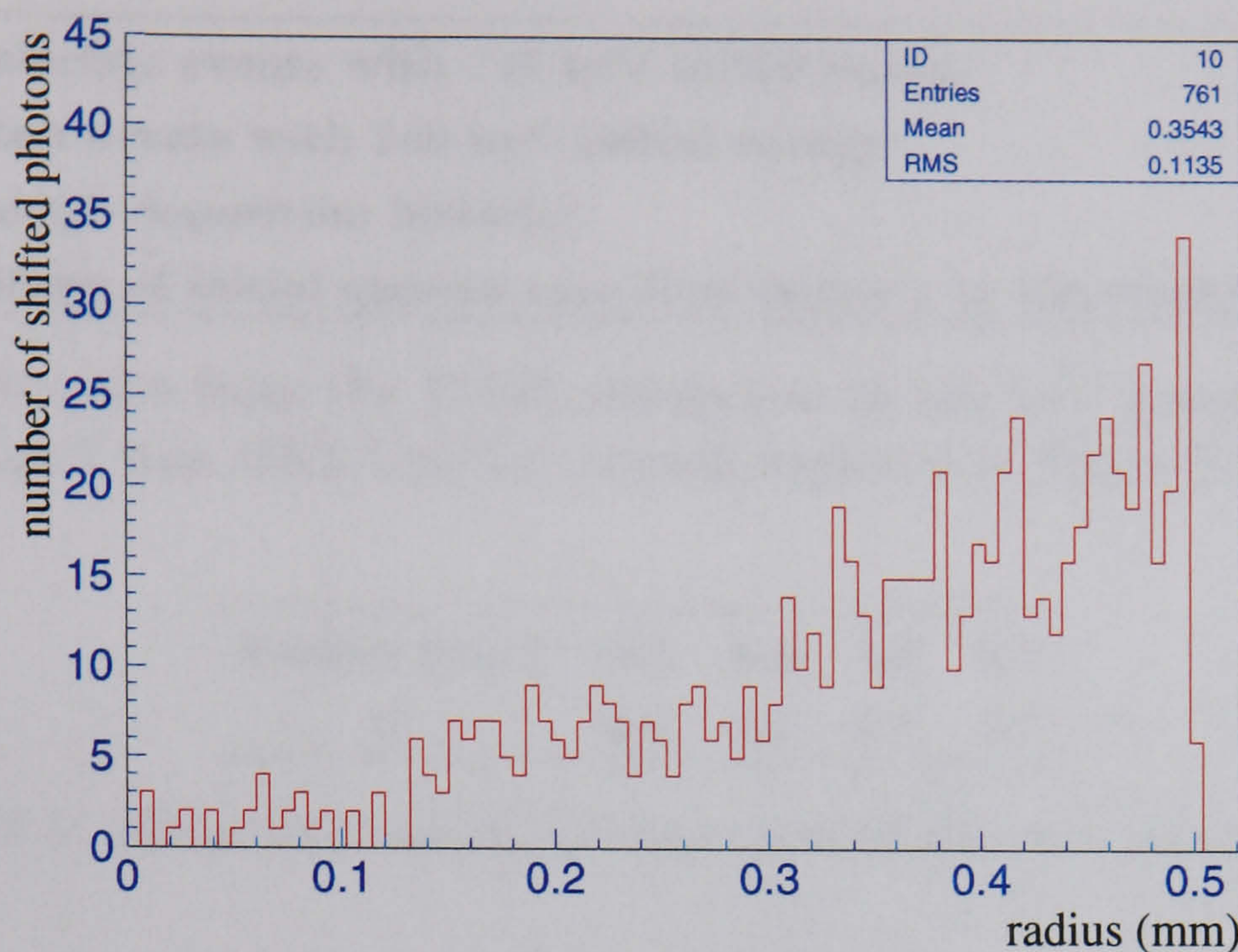


Figure 6.4: Number of wavelength-shifting events as a function of the radial position of the absorption point within the WSFs.

Gamma ray interactions

A more realistic simulation was performed using EGS4 to model a pencil beam of 140 keV gamma rays perpendicularly directed at the center of one of the large surfaces of the crystal, covering a circular spot of 0.01 mm radius. The EGS4 simulation recorded the photoelectric and Compton interactions in the scintillator and the respective positions for 10,000 gamma ray histories. The light yield of the scintillator was assumed to be independent of the energy deposited and equal to 37 photons/keV. In the case of a photoelectric interaction the gamma ray energy was assumed to be fully deposited at the position of interaction and is followed by the isotropic emission of 37×140 scintillation photons. For a Compton scatter interaction, there is isotropic emission of $37 \times E_r$ scintillation photons, where E_r is the energy of the recoil electron in keV (refer to ref. [24] for a description of the interactions of gamma radiation with matter). Table 6.2 shows the results obtained from the EGS4 simulation of gamma ray interactions in the 3 mm thick CsI(Na) crystal. The values are shown as the fraction of initial gamma rays in the simulation.

Following a Compton scatter interaction the scattered photon may either exit the crystal, undergo another Compton scatter or undergo a photoelectric interaction. If it exits the crystal after one or more Compton events the initial gamma ray energy is not fully deposited and the energy signal is likely to fall outside the energy window (see section 2.3.1). The results in the last

Photoelectric events with 140 keV initial energy	57.6%
Compton events with 140 keV initial energy	9.5%
Full energy deposition histories	64.3%
Percentage of initial gamma rays that interact in the crystal	67.1%

Table 6.2: Results from the EGS4 simulation of 140 keV gamma ray interactions in the 3 mm thick CsI(Na) crystal depicted in figure 6.3.

Radius (mm)	0.2	0.5	1.0	2.0
%	6.8	4.4	2.7	1.0

Table 6.3: Mean fraction of photons created above a given radius.

two rows in table 6.2 show that these events represent about 4% of the total number of gamma rays that interact in the crystal.

For full energy deposition events where one or more Compton interactions occur, fractions of the total number of scintillation photons are created in distinct locations inside the scintillator. The resulting spread of light contributes to a degradation of the spatial resolution.

Figure 6.5 shows the average fraction of the total number of photons created per gamma ray history as a function of the radius around the gamma ray beam ($\sqrt{x^2 + y^2}$, with x and y defined in figure 6.3). A summary of the results is shown in table 6.3, where the fraction of photons created above a given radius is tabulated.

It is seen that over 93% of the photons are created within a 0.2 mm radius around the pencil beam of gamma rays. This suggests that the contribution to the spatial resolution from the spread of light due to Compton interactions should only be significant for the cases where sub-millimeter spatial resolution is a requirement.

Tracing of optical photons

The EGS4 output file includes a list of positions inside the crystal where optical photons were generated. This list was then used by DETECT97 to simulate the subsequent fates of the photons. The number of gamma ray events for the simulations described in this section was 100.

Table 6.4 shows the results of the simulations for the cases of vacuum and optical gel surrounding media. The values for the average trapping efficiency agree with the results presented in section 6.1.2 for photons emitted at a

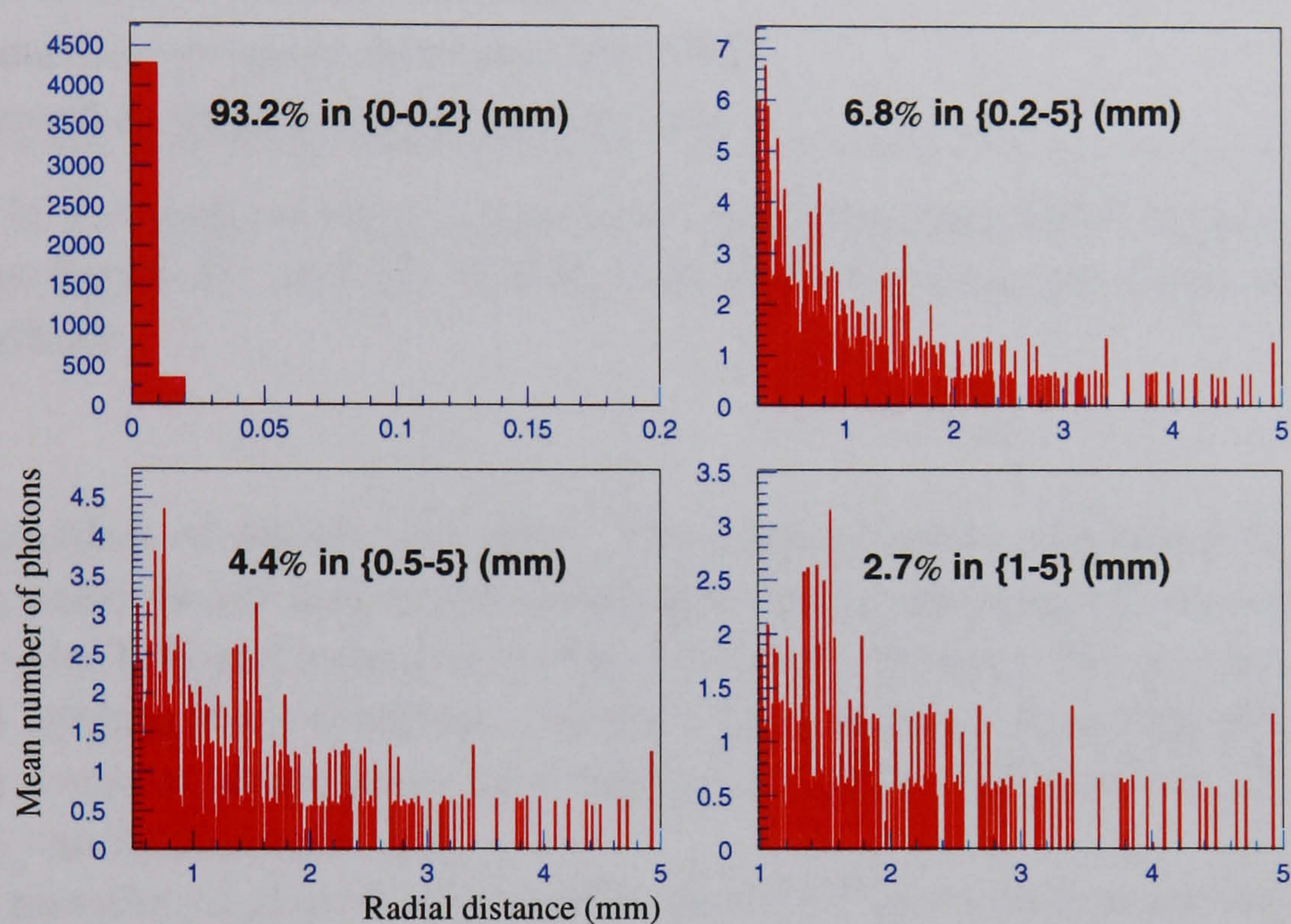


Figure 6.5: Mean number of scintillation photons created at a radial distance $\sqrt{x^2 + y^2}$ from the gamma ray beam due to Compton interactions, in the x, y plane defined in figure 6.3. Each plot also shows the fraction of photons for the corresponding range of radial values.

Average percentage of wavelength-shifted photons	6.5%
Mean number of wavelength-shifted photons	339
Mean number of wavelength-shifted photons detected	27
Mean trapping efficiency	$\frac{27}{339} \approx 7.9\%$

Table 6.4: Summary of the results obtained for the geometry depicted in figure 6.3.

Mean number of photons detected	9.3
Mean number of photoelectrons (QE=15%)	1.4
Mean number of photoelectrons (QE=20%)	1.9

Table 6.5: Estimate of the total number of photons on a WSF in the geometry shown in figure 6.3 and the number of photoelectrons produced in a PMT photocathode.

radial position of about 0.35 mm. The high trapping efficiency in vacuum was discussed above and is a consequence of the non-realistic assumption of perfect total internal reflection at the boundary between the second cladding and the surrounding medium. Assuming an average trapping efficiency of 7.9% in vacuum (the same as obtained for gel), the number of detected photons can be scaled to 13.

The number of photons detected in the WSF is overestimated because the DETECT97 package does not take into account some important factors. For example the spectral match between the scintillator emission and the fibre absorption. According to the discussion in section 4.2, this is assumed to be 46%. Another factor is the wavelength-shifting quantum efficiency of the fibre which is assumed to be 75% (see section 4.2). The average number of photons detected shown in the third row of table 6.4 can therefore be scaled to 9.3. This result may be used to estimate the number of photoelectrons produced by the WSF on a PMT. The results are shown in table 6.5 for two different photocathode quantum efficiencies (15% and 20%).

6.1.4 An idealised WSF gamma camera

The method described in the previous section was extended to simulate the properties of the idealised WSF gamma camera depicted in figure 6.6. The geometry is similar to the previous one (figure 6.3). In this case, there was a set of 7 close packed WSFs on each side of the CsI(Na) crystal -

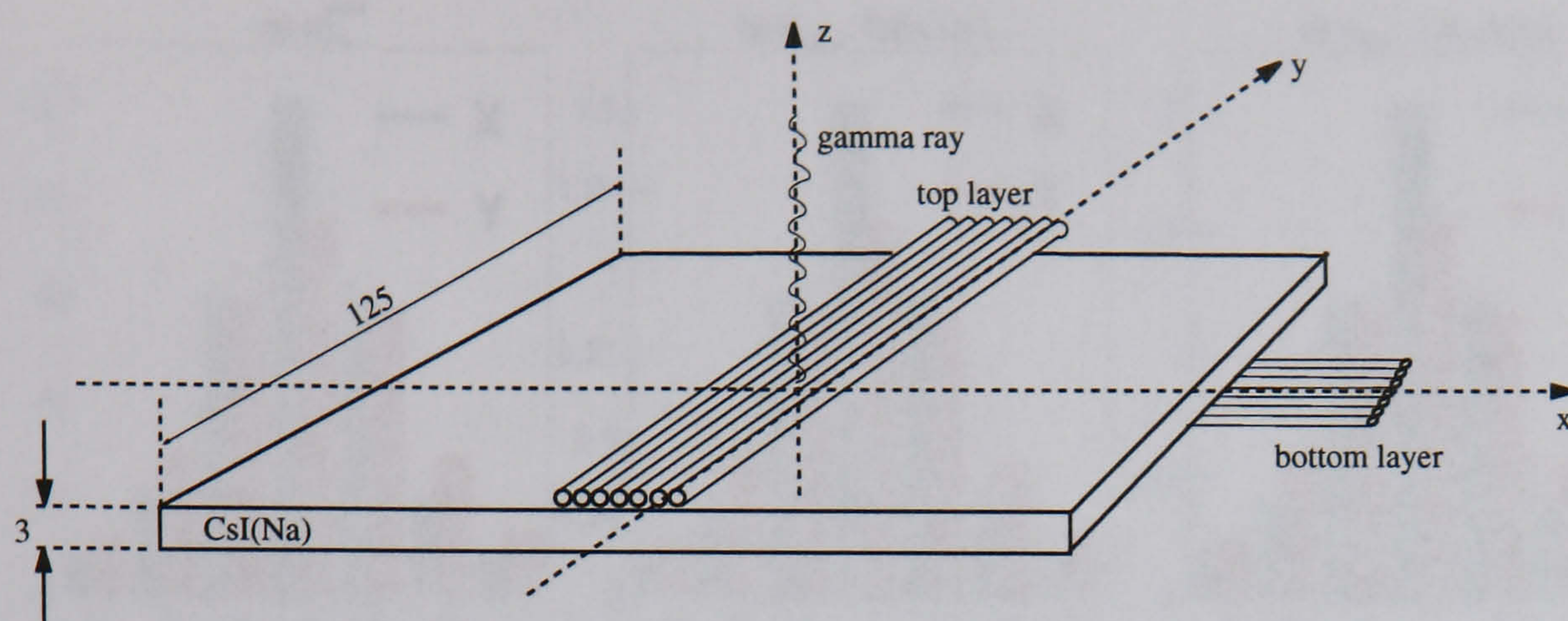


Figure 6.6: Geometry used to simulate a WSF gamma camera. The dimensions are in mm.

fibres $\{X_1, X_2, \dots, X_6, X_7\}$ on the top and $\{Y_1, Y_2, \dots, Y_6, Y_7\}$ on the bottom - and the collimated gamma ray beam was directed at the intercept of fibres X_4 and Y_4 . The two sets of fibres were perpendicular to each other and the dimensions of the fibres were the same as in the previous section. The large surfaces of the crystal were of type POLISH and the edges were GROUND, to approximately model the CsI(Na) crystal used in the previous chapter (section 5.2.2). A 1 mm thick PMT glass window was also introduced with a photocathode (DETECT surface) laid on the bottom surface to detect the energy signal. As before, the whole system was surrounded by a 1.46 refractive index medium (optical gel). The refractive index of the glass window was 1.46.

Signals from the WSFs

A total of 10,000 gamma ray histories was simulated. As in the previous section, one should also take into account the 75% wavelength-shifting quantum efficiency and the 46% spectral match between the CsI(Na) emission and the WSF absorption spectra as above. The corrected values n_{ph}^{cor} are plotted in figure 6.7 a), for the X and the Y fibres.

Figures 6.7 b) and 6.7 c) show the number of photoelectrons n_{phe} expected to be produced by each fibre on a PMT with 15% and 20% quantum efficiency, QE, taken from $n_{phe} = QE \times n_{ph}^{cor}$.

Table 6.6 shows a comparison between the simulation results and those obtained with the analytical model presented in section 4.3.1. The table shows the results for the number of photoelectrons, assuming a 15% quantum efficiency, with those shown in table 4.2 for gel coupling. It is observed that

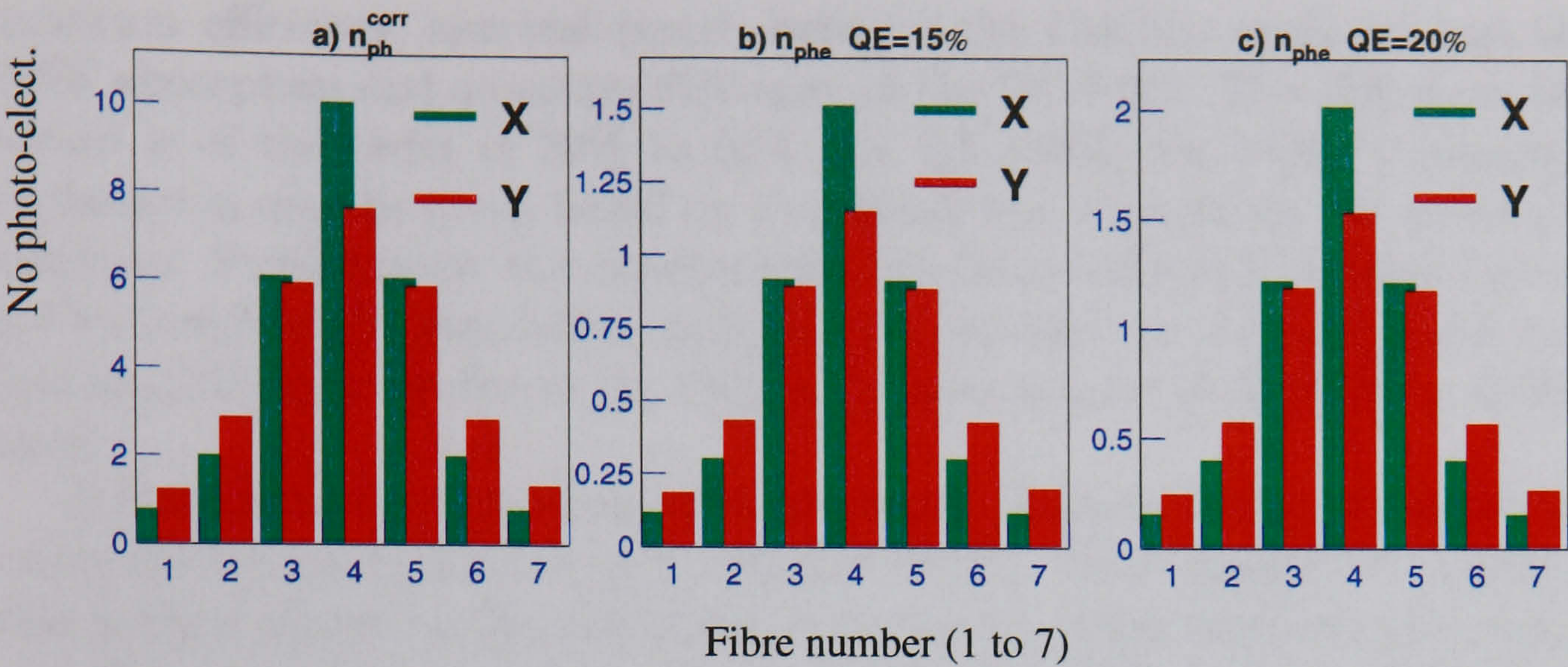


Figure 6.7: Simulation results for a) the number of photons, n_{ph}^{cor} , detected in each fibre and corrected as explained in the text; b) the number of photoelectrons expected to be produced in a PMT with 15% and c) 20% quantum efficiency.

Fibre	0	1	2	3	sum
n_{nphe}^i (simul)	1.5	0.9	0.3	0.1	4.1
n_{nphe}^i (calc)	2.0	0.52	0.14	0.03	3.4

Table 6.6: Comparison between the results obtained with the Monte Carlo simulations and the calculations in section 4.3 for the case of gel coupling.

there is good agreement, particularly for the case of the summed values. The values for each individual fibre are significantly different in the two methods, which may be explained by the different fibre cross-sections (square and round) and by the fact that the calculations in section 4.3.1 assume rectilinear photon trajectories for photons crossing boundaries between regions with different refractive indices. The simulation traces the optical paths with more accuracy, taking into account the refraction angles, defined by Snell's law (equation 4.1).

A comparison between the simulation and the results from the experiments presented in section 5.4 shows that, in practice, there is a lower number of photoelectrons than predicted by these simulations (assuming the quantum efficiency of the PC-PMT to be about 20% at 500 nm, as stated by the manufacturer). However, to obtain the results in figure 6.7 many approximate parameters were introduced: CsI(Na) light output, wavelength-shifting

quantum efficiency, spectral match between the CsI(Na) emission and the WSF absorption and quantum efficiency of the PC-PMT. The difference observed is of the order of 30% to 50% (for QE=20%) for which a plausible explanation may be given based on a combination of errors on the above parameters. Furthermore, the experimental results are affected by other factors not included in the simulation, such as, “air bubbles” in the optical gel, surface imperfections or dirt in the CsI(Na) crystal and/or in the WSF polished ends.

A fraction of the light created isotropically inside the scintillator directly exists the crystal and intercepts a layer of WSFs. As discussed in chapter 4, this is determined by the difference in refractive index between the crystal and the surrounding medium (figure 4.11). For this case the fraction of directly transmitted light is 39%⁵. From the simulation results, it is found that the total number of wavelength-shifted photons is 35.6% of the mean number of photons generated in the crystal. Therefore, most of the light directly exiting the crystal, and intercepting the fibres, is shifted.

6.2 Simulation of spatial resolution

From the above simulations and from the experimental results in the previous chapter it may be observed that the signals in the WSFs are localised mainly in about 5 fibres (1 mm diameter), which suggest that a good spatial resolution may be achievable. Assuming that each fibre is individually read out by a separate detector channel (like the PC-PMT in the previous chapter, for example) the position of gamma ray interaction may be estimated by a centroid algorithm using the signals from these PMTs. In order to predict the spatial resolution of such an imager, a Monte Carlo simulation program was developed (SR-SIM) to simulate the production of charge pulses in a PMT, given a mean number of photoelectrons produced in its photocathode and collected by the first dynode. Using the experimental results presented in the previous chapter for the mean number of photoelectrons produced by each WSF on the PC-PMT, it is possible to simulate the centroid algorithm and predict the spatial resolution obtained with such a system. This will be checked against experimental observations and used to predict the performance of further developments of the WSF camera.

⁵This is found by calculating the fraction of the solid angle defined in figure 4.11. Note that two identical solid angles are taken into account (18% fraction of solid angle each) defining cones of light exiting from the top and from the bottom surfaces of the crystal.

6.2.1 The simulation algorithm

Given a mean number of photoelectrons, μ , collected by the first dynode of a PMT, the probability of a particular event creating n photoelectrons collected by the first dynode is given by the Poisson distribution (equation 5.1).

The charge amplification process in the dynode stages for a single photoelectron is described by a Gaussian distribution of the charge variable, Q . The mean value $\overline{Q_1}$ is the single electron charge of the PMT and the standard deviation σ_1 of the Gaussian distribution is the single electron resolution. These two parameters can be obtained experimentally by fitting a Gaussian curve to the single photoelectron peak. The method to obtain this peak is described in section 5.2.4 and figure 5.2 shows a typical single photoelectron peak for the PC-PMT used. For n photoelectrons, the charge multiplication is also described by Gaussian distributions which are related to the single photoelectron response: the mean is $\overline{Q_n} = n\overline{Q_1}$ and the standard deviation is $\sigma_n = \sqrt{n}\sigma_1$.

In a practical low light level experiment, the charge distribution is a convolution between these Poisson and Gaussian distributions, as explained in section 7.3.4, and this process is simulated to generate the PMT response for each fibre.

A flow diagram of SR-SIM is shown in figure 6.8. The inputs of the program are:

1. the single photoelectron resolution, σ_1 , of the PMT. Unless otherwise mentioned the characteristics of the PMT are based on the measured performance of the PC-PMT (EMI 9124A) described in the previous chapter, with $\sigma_1=0.51$ photoelectrons.
2. the PMT threshold. If a PMT pulse is smaller than the threshold, the charge signal is given the value zero. Unless otherwise mentioned, and according to the experiments in the previous chapter, the threshold is chosen to be at 0.15 photoelectrons (see section 5.3).
3. the number, f , of WSFs to simulate;
4. the mean number of photoelectrons for each fibre $\{\mu^1, \dots, \mu^f\}$
5. the number of events, N , which represent the number of gamma ray histories producing a constant light level in the WSFs.

For each event j , SR-SIM samples from a Poisson distribution with mean μ^i to obtain the number of photoelectrons, n , to be amplified for fibre i . Then it samples from a Gaussian distribution with mean $n\overline{Q_1}$ and standard

deviation $\sqrt{n}\sigma_1$ to obtain the value of charge Q^i produced by the i^{th} fibre. The process is repeated for all the f fibres. The set of f values of Q is then used to calculate the centroid, C_j , for that event:

$$C_j = \frac{\sum_{i=1}^f iQ^i}{\sum_{i=1}^f Q^i}. \quad (6.1)$$

For a given set of initial parameters, the spatial resolution is taken from the width of the distribution of centroids.

6.2.2 Results

PMT pulse-height distribution

In order to verify that the program correctly simulates the response of a PMT, a first simulation was carried out for only one input μ and recording the pulse height distribution of the simulated PMT pulses. In this case the centroid calculation is not of interest. For two different values of μ , 0.9 and 3.7, the pulse-height distributions are shown in figure 6.9. These values of μ correspond to the values obtained experimentally and shown in figure 5.5 for the EMI-9124A photomultiplier. The excellent agreement between the experimental results and the simulations is evident.

Centroid distributions

The simulation of spatial resolution was performed using the mean numbers of photoelectrons per channel shown in figure 5.7 as inputs to SR-SIM. In this case the simulation recorded the centroids for multiple events by sampling a set of 9 fibres representing the simultaneous response of a set of 9 PMTs coupled to each fibre ⁶. Figure 6.10 shows the distribution of centroids obtained. The horizontal axis corresponds to the position found using equation 6.1. Since the fibres are 1 mm diameter, the results are assumed to be in millimeter units.

The lines represent Gaussian fits to the simulation data, the parameters of which are also shown in each plot. The full-width-at-half-maximum, FWHM, can be obtained from the relation $\text{FWHM}=2.35\text{Sigma}$.

In section 4.3.2 the imaging efficiency was defined as the fraction of events in which at least one fibre has a signal above threshold. Otherwise no position information can be obtained for that event. The results obtained from SR-SIM are summarised in table 6.7.

⁶In chapter 5 each fibre was read out separately.

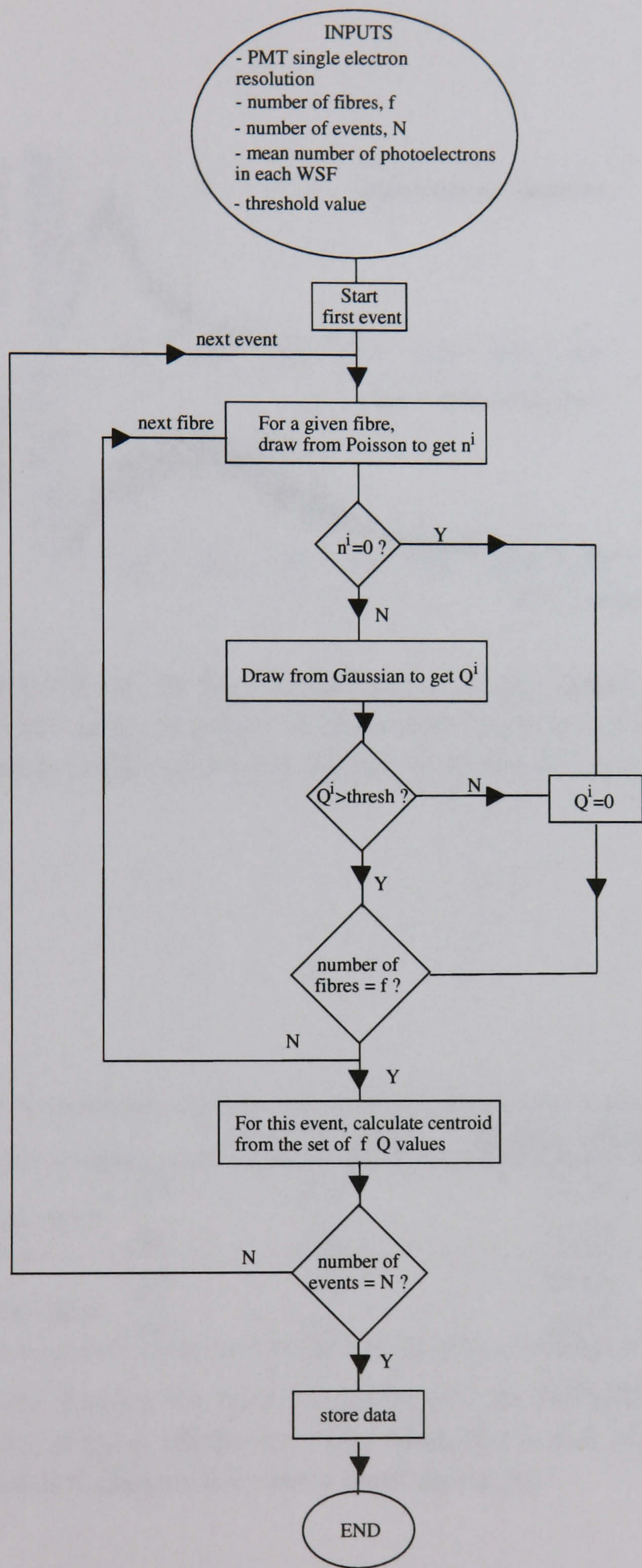


Figure 6.8: Flow diagram of the simulation program (SR-SIM) developed to simulate the spatial resolution of a WSF camera.

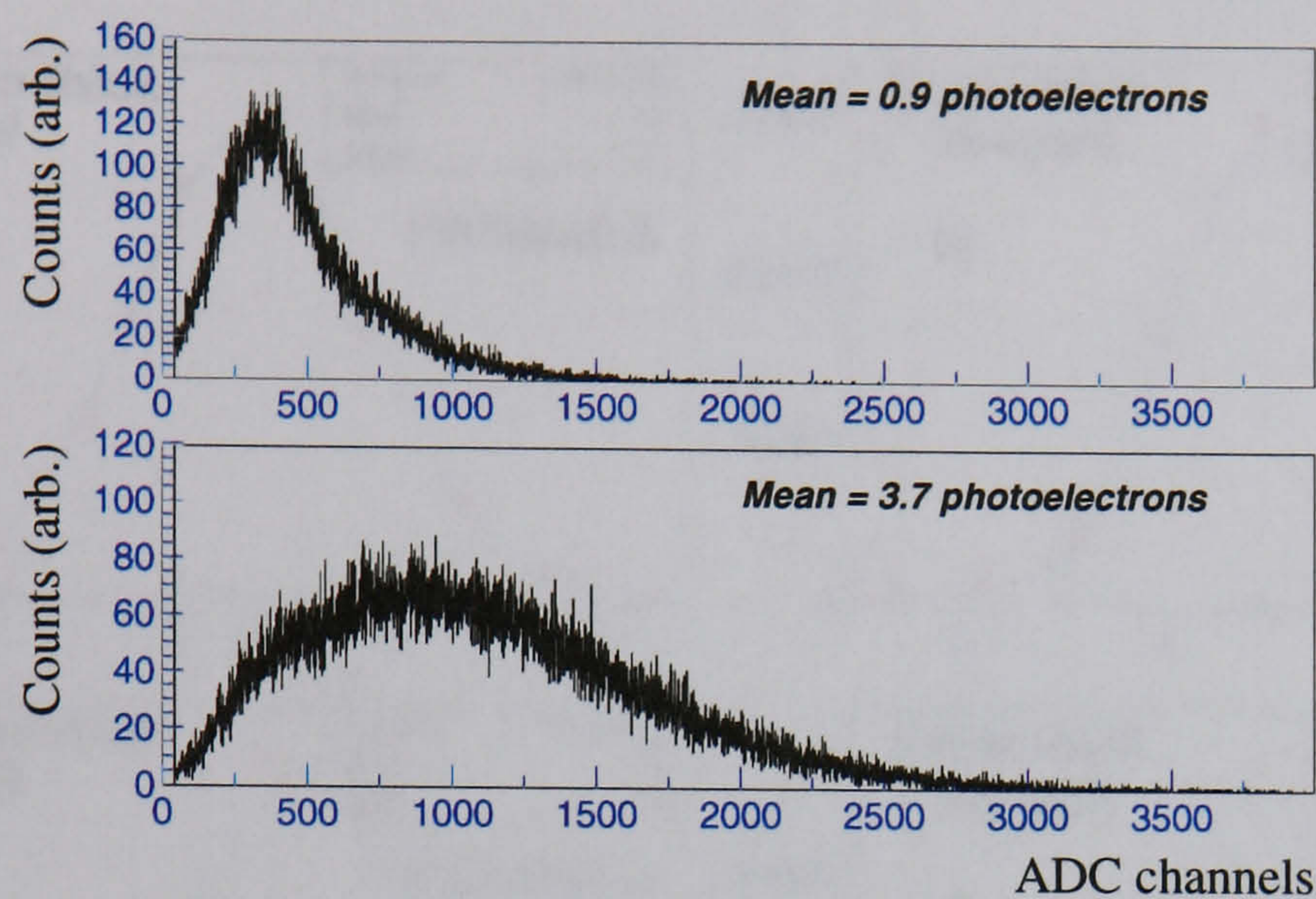


Figure 6.9: Results from SR-SIM for the pulse-height distributions obtained from a PMT. The mean number of photoelectrons is 0.9 and 3.7 and an excellent agreement with the results shown in figure 5.5 is observed.

		FWHM (mm)	Imaging efficiency
3 mm thick	gel	2.8	97.3%
	air	2.2	79.5%
5 mm thick	gel	2.8	96.9%
	air	2.5	76.5%

Table 6.7: SR-SIM results for spatial resolution, as FWHM of the centroid distribution, and imaging efficiency. The observed mean numbers of photoelectrons per channel (figure 5.7) were used as input.

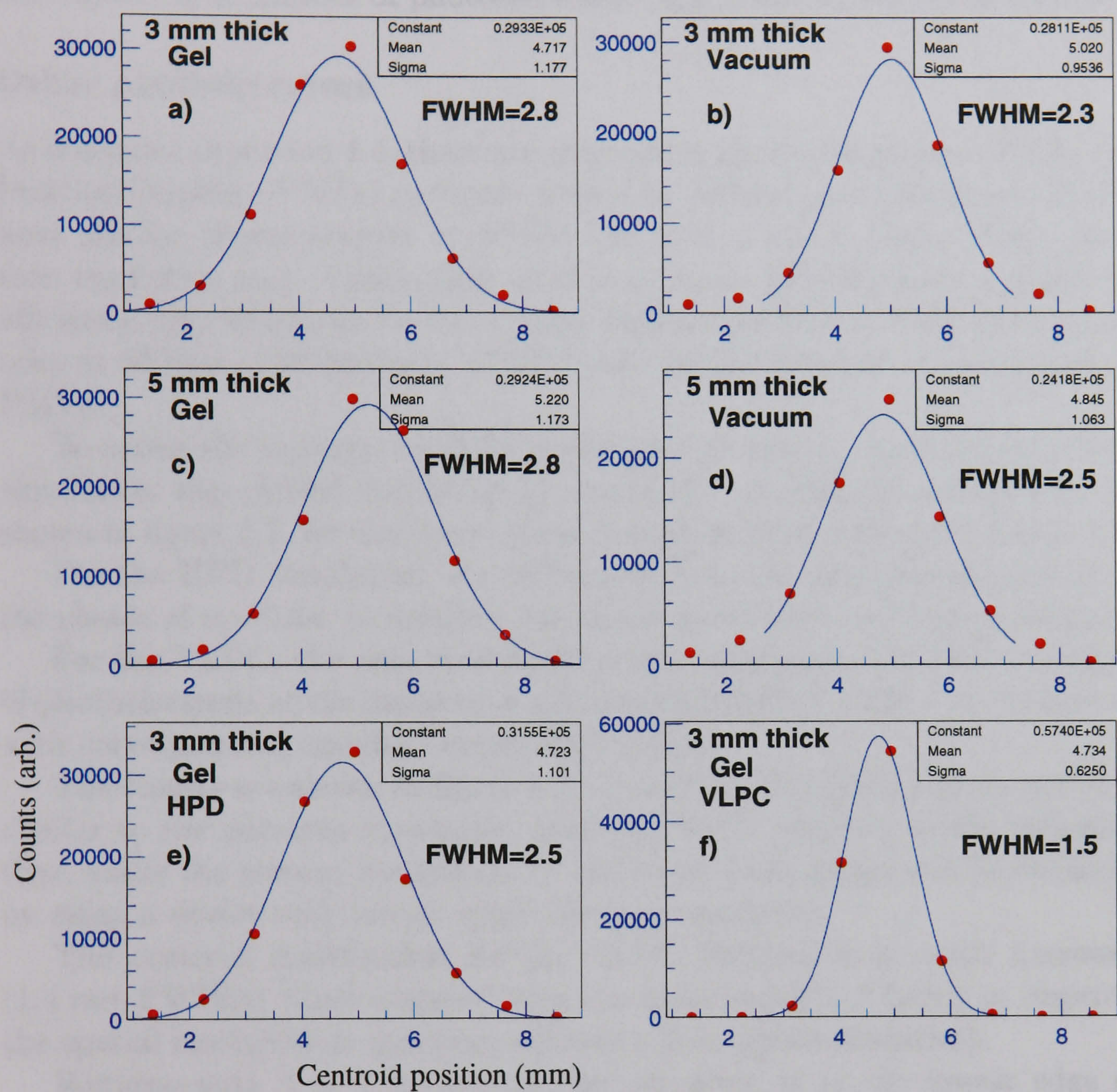


Figure 6.10: Spatial resolution results from SR-SIM: a), b), c) and d) - the inputs were the observed mean numbers of photoelectrons (figure 5.7); e) for a device with better single electron resolution than a PMT (e.g. HPH); f) for a device with high quantum efficiency (e.g. VLPC). Refer to main text for a complete description of the simulation parameters.

According to these simulations, the spatial resolution is expected to be better than 3 mm FWHM for all cases, which is comparable to current Anger cameras. The imaging efficiency is better for the cases of gel coupling due to the higher total number of photoelectrons (figure 5.6) in the set of 9 fibres.

Other photodetectors

As discussed in section 4.4, there are alternative photo-detectors to PMTs (or Position Sensitive PMTs) currently available. Hybrid photodetectors (HPD) have similar characteristics to PMTs but have a much better single electron resolution (σ_1). Visible light photon counters (VLPC) have a quantum efficiency, QE, which can be 3 to 4 times higher than that of PMT photocathodes at 500 nm. Furthermore, VLPCs have similar or better σ_1 compared to PMTs.

To assess the importance of these two parameters (σ_1 and QE), a similar simulation was carried out using as inputs the photoelectron distributions shown in figure 5.7, for the 3 mm thick crystal coupled with gel in figure 5.7.

For the HPD simulation, the difference from the previous simulation is the choice of $\sigma_1=0.04$, to simulate an almost ideal single electron resolution.

For the VLPC, the only modification was multiplying the mean number of photoelectrons at the input by 4, simulating therefore a QE 4 times higher, with corresponding smaller Poisson fluctuations.

The results are shown in figure 6.10 e) and f). The HPD results are very similar to the previous simulation assuming PMT readout, which indicates that, under the present conditions, no substantial advantage can be obtained by using a device with better single electron resolution.

The centroid distribution for the VLPC simulation is much narrower (1.4 mm FWHM) which suggests that the most important factor to improve the spatial resolution is quantum efficiency (i.e., photo-statistics).

Working with 3 to 5 photoelectrons per event is at the lowest edge of viability for the WSF gamma camera, because in a significant fraction of events only one fibre generates a signal in the photodetector. Increasing the quantum efficiency by a factor of 4 means that all events have signals in 2 or 3 fibres, giving a much smaller spread in the centroid distributions.

6.3 Discussion and conclusions

The simulation of the WSF camera presented in the first part of this chapter showed results consistent with previous experiments. The fundamental

physical interactions are modeled allowing accurate predictions for the light levels at the WSFs.

As seen from the experiments in the previous chapter, gel coupling provides higher light levels at the WSFs which is important to obtain high imaging efficiency. Moreover, gel coupling is also important to obtain a higher energy signal giving a better energy resolution compared to air coupling.

The simulation in the second part of the chapter predicts the spatial resolution of a WSF camera based on the experimental conditions presented in the previous chapter. A resolution better than 3 mm FWHM is predicted and the importance of gel coupling to enhance the imaging efficiency is confirmed. It is also predicted that a 4-fold increase in quantum efficiency would lead to a spatial resolution of 1.4 mm FWHM for the 3 mm thick crystal with gel coupling. This is possible with currently available VLPC technology. Recent developments in avalanche photodiode technology also promise higher quantum efficiency compared to PMT photocathodes.

Chapter 7

Evaluation of PSPMTs

7.1 Introduction

As described in chapters 3 and 4, PSPMTs are very promising devices for achieving good spatial resolution in nuclear medicine gamma-ray imaging. In particular, the metal channel dynode technology (section 3.2.2) provides very compact PSPMTs which are available with several anode configurations at a relatively low cost (\leq £1000).

This chapter describes experimental work on the evaluation of 3 types of metal channel dynode PSPMTs from the Hamamatsu R5900 series¹. The tubes differ mainly in their anode structure. The C8 model has 4+4 crossed-plate anodes whereas the M16 and M64 have arrays of 4×4 and 8×8 discrete anode pixels (see table 3.2).

The aim of these tests is to assess the suitability of these PSPMTs for use in small gamma cameras, in two distinct configurations: i) PSPMT directly coupled to scintillators and ii) PSPMTs to read out signals from wavelength-shifting fibres (WSF) in the WSF camera described in chapter 4. Although the three tubes are adequate for the former application, the C8 has the advantage of having a smaller number of anodes compared to the M16 and the M64.

In the WSF camera, for a given gamma-ray interaction, it is expected that more than one fibre is involved in the detection of light emitted from the scintillator, and a PSPMT reading out the fibre signals should be capable of separating the signals from each individual fibre. Therefore, the crossed-plate anodes have the disadvantage of position ambiguity for simultaneous events on several WSFs (see figure 3.16 and related discussion). For this

¹Hamamatsu Photonics K. K., Electron Tube Center, 314-5, Shimokanzo, Toyoota-village, Iwata-gun, Shizuoka-ken, 438-0193, Japan, www.hamamatsu.com.

reason, the C8 tests focus mainly on possible applications with direct coupling to scintillators. For the WSF camera application, the discrete anode pixel configuration (M16 and M64) with individual anode readout is more appropriate to avoid position ambiguity for simultaneous events on several WSFs.

7.2 Evaluation of the R5900-C8 PSPMT

The Hamamatsu R5900-C8 (hereafter C8) has a metal package encapsulation with external physical size of $25\times25\times20\text{ mm}^3$. According to the manufacturers' specifications [59] it has a bialkali photocathode with a wavelength of maximum response of 420 nm and an effective area of $22\times22\text{ mm}^2$. The optical interface is a 1.5 mm thick borosilicate glass window. The dynode multiplier structure consists of 10 stages of metal channel dynodes (figure 3.10) and a solid last dynode (DY11). According to the manufacturer, it achieves a gain of about 7×10^5 at the recommended operation voltage (- 800 V). Figure 7.1 gives an outline of the dimensions of the C8.

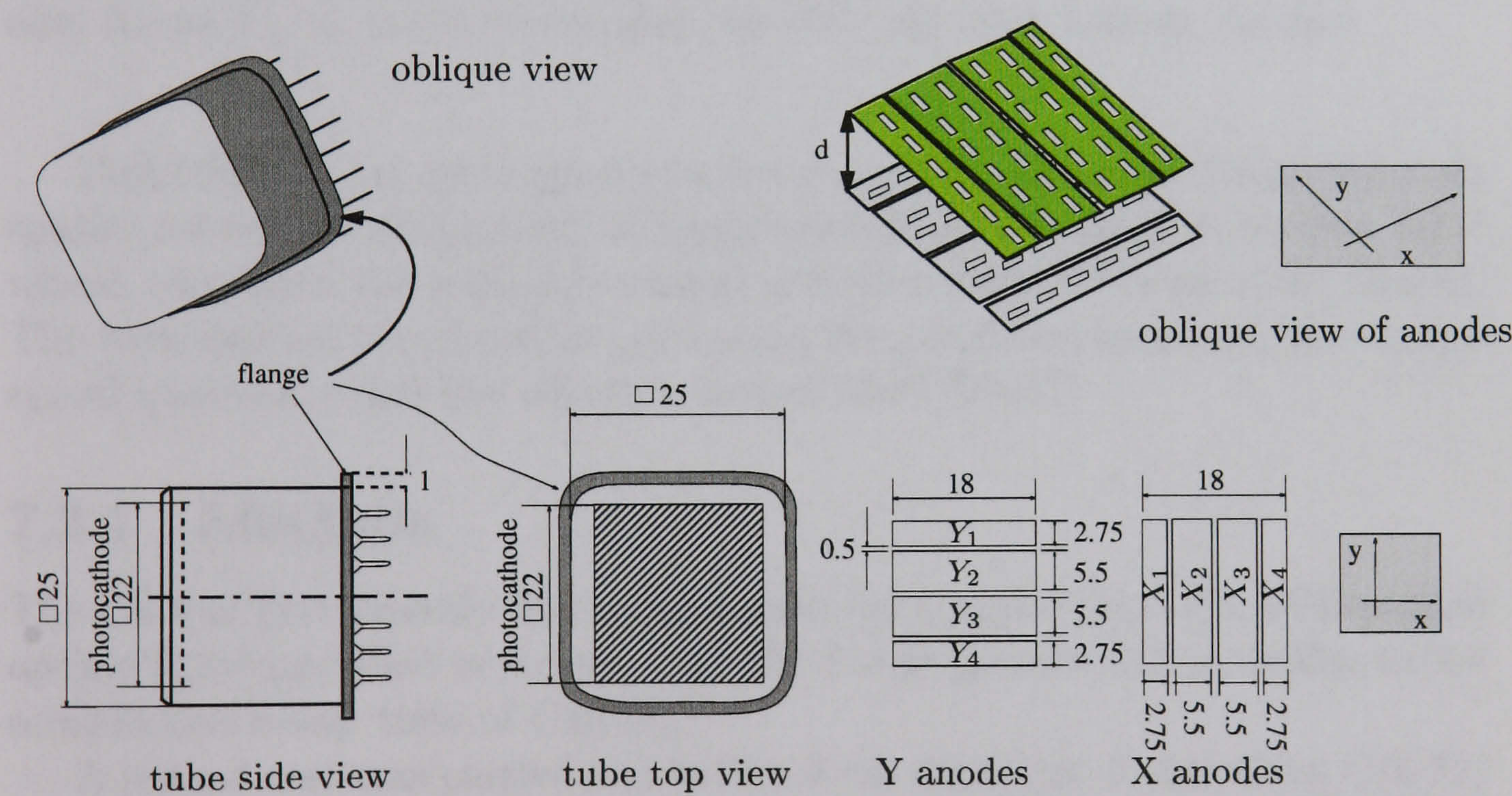


Figure 7.1: Schematic outline of the Hamamatsu R5900-C8. Side and top views of the tube are shown together with an outline of the position sensing 4X+4Y anodes. Dimensions in mm.

The anode structure is a set of 4+4 crossed-plates. The two sets of 4 perpendicular anodes are located between dynodes DY10 and DY11. Each

anode plate is about 0.5 mm thick and has several small rectangular holes to allow the transmission of charge to the last reflective dynode, as described in section 3.2.3.

The tube is connected to a Hamamatsu E678-32B socket, which has the dynode voltage divider depicted in figure 7.2.

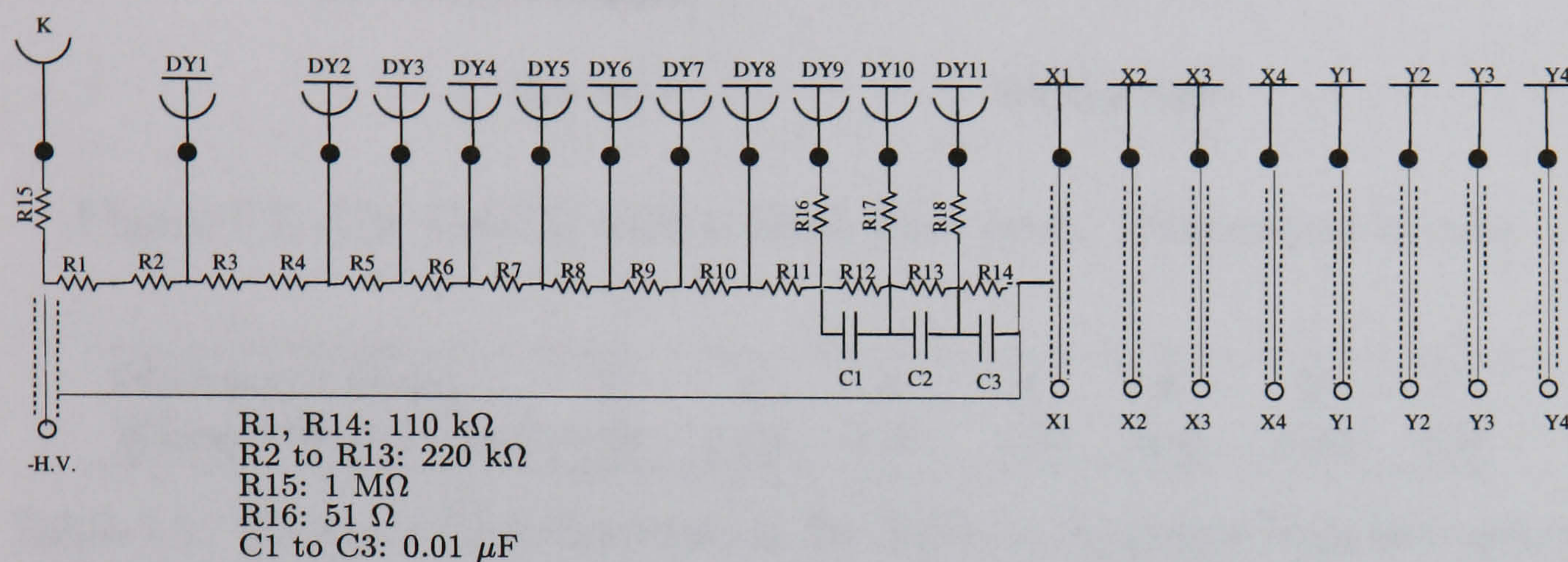


Figure 7.2: Schematic outline of the Hamamatsu E678-32B socket connected to the R5900-C8. DY1 to DY11 represent the 11 dynodes, K the photocathode, X₁ to X₄, Y₁ to Y₄ the anodes and -HV the high voltage applied.

This PSPMT can be coupled to a scintillator in a compact design of a high spatial resolution gamma-ray imaging module as discussed in section 3.3.2 where, to achieve the required imaging size several PSPMTs are close packed. The tests carried out aimed at evaluating the positional response, the energy signal uniformity and the effective area of the PSPMT.

7.2.1 Methods

The C8 was first directly illuminated with light pulses from the LED-pulsed optical fibre described in section 5.3. The 1.2 μ s pulse width is similar to the scintillation decay time of CsI(Tl).

A second test was carried out with a 9 cm diameter, 5 mm thick CsI(Tl) crystal coupled to the PSPMT. Since the crystal is larger than the PSPMT, a black tape mask was fitted on the crystal leaving two 25 \times 25 mm² regions at opposite faces to fit the PSPMT window (figure 7.3). In all the measurements one side of the crystal was coupled to the PSPMT with silicon gel and the opposite side was left uncovered. A 1 mm collimated beam of Tc^{99m} 140 keV gamma-rays was used to irradiate the crystal over the PSPMT. The lead collimator was 13 mm thick with a 1 mm diameter hole.

In these scans the high voltage across the C8 was set to -800 V.

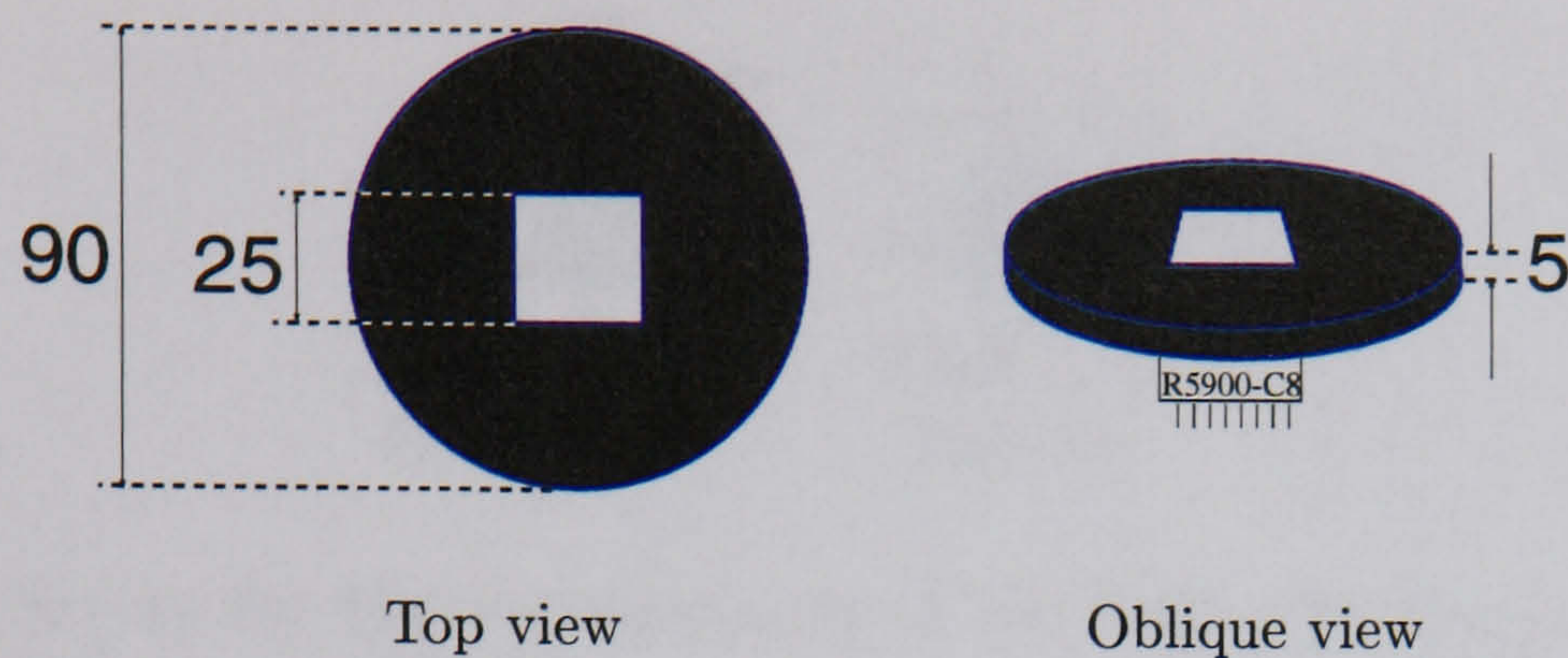


Figure 7.3: The CsI(Tl) with a black tape mask. Dimensions in mm.

Distance d (mm)	0	2	4	6	8	10	15
Width FWHM (mm)	0.66	0.80	1.20	1.90	2.40	2.90	4.20

Table 7.1: Width of light distribution for different distances from the optical fibre to the CCD.

Size of the light spot

As discussed in section 3.2.2, the spatial resolution of the metal channel PSPMTs is strongly determined by the light spread over the photocathode. If the C8 is coupled to a scintillator the light spread is determined by the dimensions of the crystal: for a single continuous crystal, its thickness; for a segmented array, the size of the elements.

The behaviour of the C8 for different light distributions at the photocathode was assessed by placing the end of the optical fibre coupled to the LED at different distances from the tube window. This created broader light distributions for increasing distances.

To determine the width of the distribution, a CCD camera was used to measure the light spot projected from the optical fibre (figure 7.4). The CCD was made by EEV Ltd. It has 388×287 square pixels each with 22×22 μm^2 , extending over a total area of 8.5×6.3 mm². For each distance two images were obtained, one with the LED switched on and the other with the LED switched off to measure the background. The background-subtracted images obtained and the intensity profiles are shown in figure 7.5. The profiles correspond to a row of pixels (horizontal, in the pictures) through the highest intensity pixel. Table 7.1 summarizes the results.

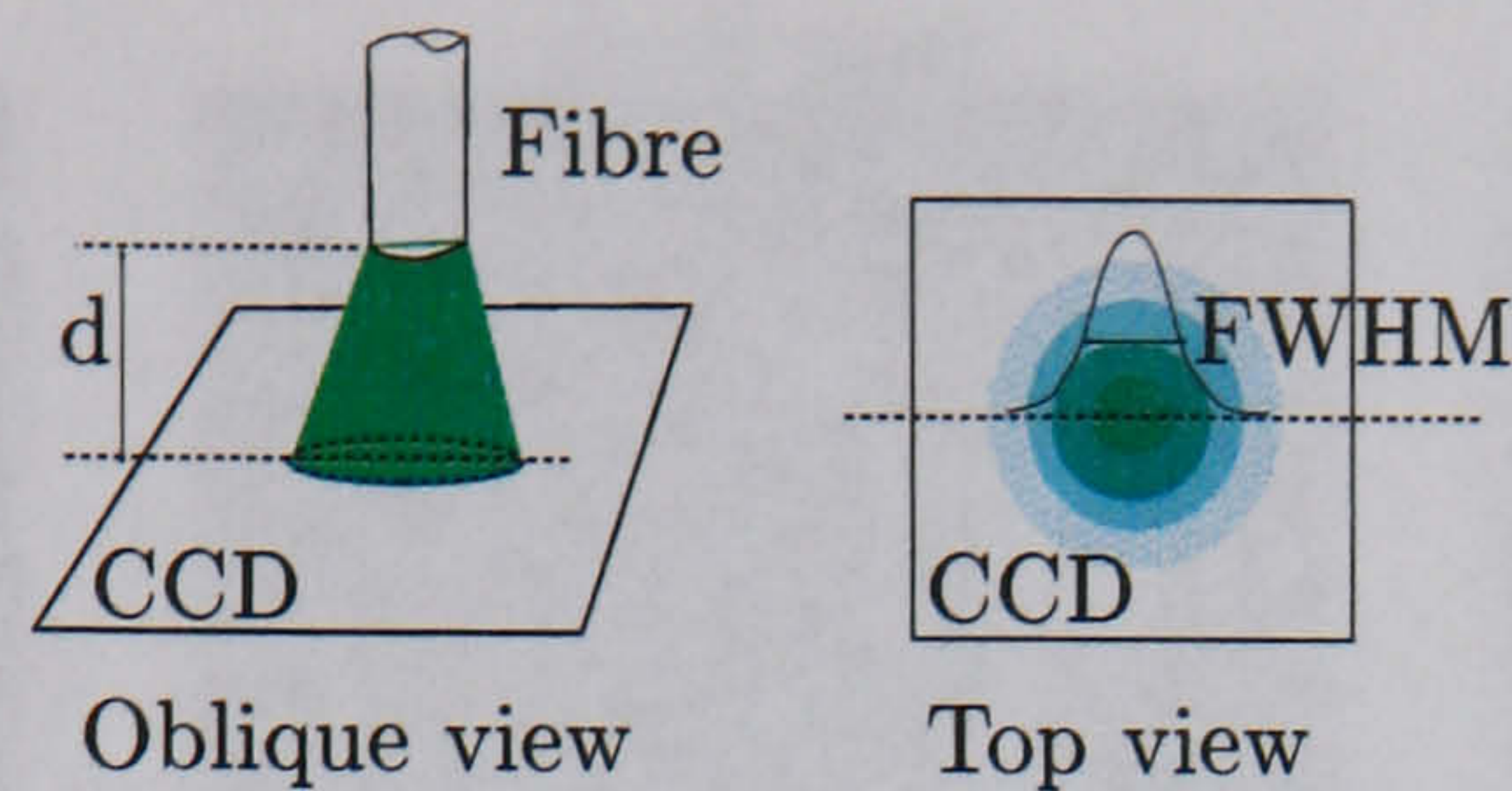


Figure 7.4: Set-up for the measurement of the light distribution created by the optical fibre on a CCD camera at a distance d from the fibre.

Scanning stage

The PSPMT was attached to a x-y scanning stage driven by stepper motors. The stage was controlled by the data acquisition PC, which also synchronised the motion of the PSPMT with the data acquisition described below.

The entrance window of the C8 was scanned with the LED-pulsed optical fibre. Three scans were performed with different distances d from the fibre to the tube window, $d=1, 7, 15$ mm. These correspond to light spot widths of 0.73, 2.15, 4.2 mm FWHM at the tube window, using linear interpolations between adjacent points of the results shown in table 7.1 for $d=1$ mm and $d=7$ mm. The LED light intensity was adjusted so that the signals created by the optical fibre were of the same order of magnitude (within $\pm 50\%$) as those obtained when a CsI(Tl) crystal coupled to the PSPMT was irradiated by a collimated beam of 140 keV gamma-rays.

The C8 was also coupled to the CsI(Tl) crystal shown in figure 7.3 and scanned with a 1 mm collimated beam of 140 keV gamma-rays from Tc^{99m} .

All scans were done at 1 mm steps covering a matrix of 24×24 points centered on the tube window. The true position of the fibre or of the gamma-ray beam is represented by the coordinates (x_j^f, y_k^f) , where j and k are indices with values from 1 to 24. The starting position (x_1^f, y_1^f) corresponds to the matrix corner above the anodes X_1 and Y_1 .

Readout electronics

The readout circuit is shown in figure 7.6. It is based on a readout circuit previously developed for the readout of a PSPMT in another application². Each anode signal is individually amplified and digitised. The signal from the last dynode is similarly amplified and used to trigger an acquisition.

²Thanks are due to Dr. Ian Cullum from the Institute of Nuclear Medicine of the Middlesex Hospital in London for designing and assembling the readout electronic circuit.

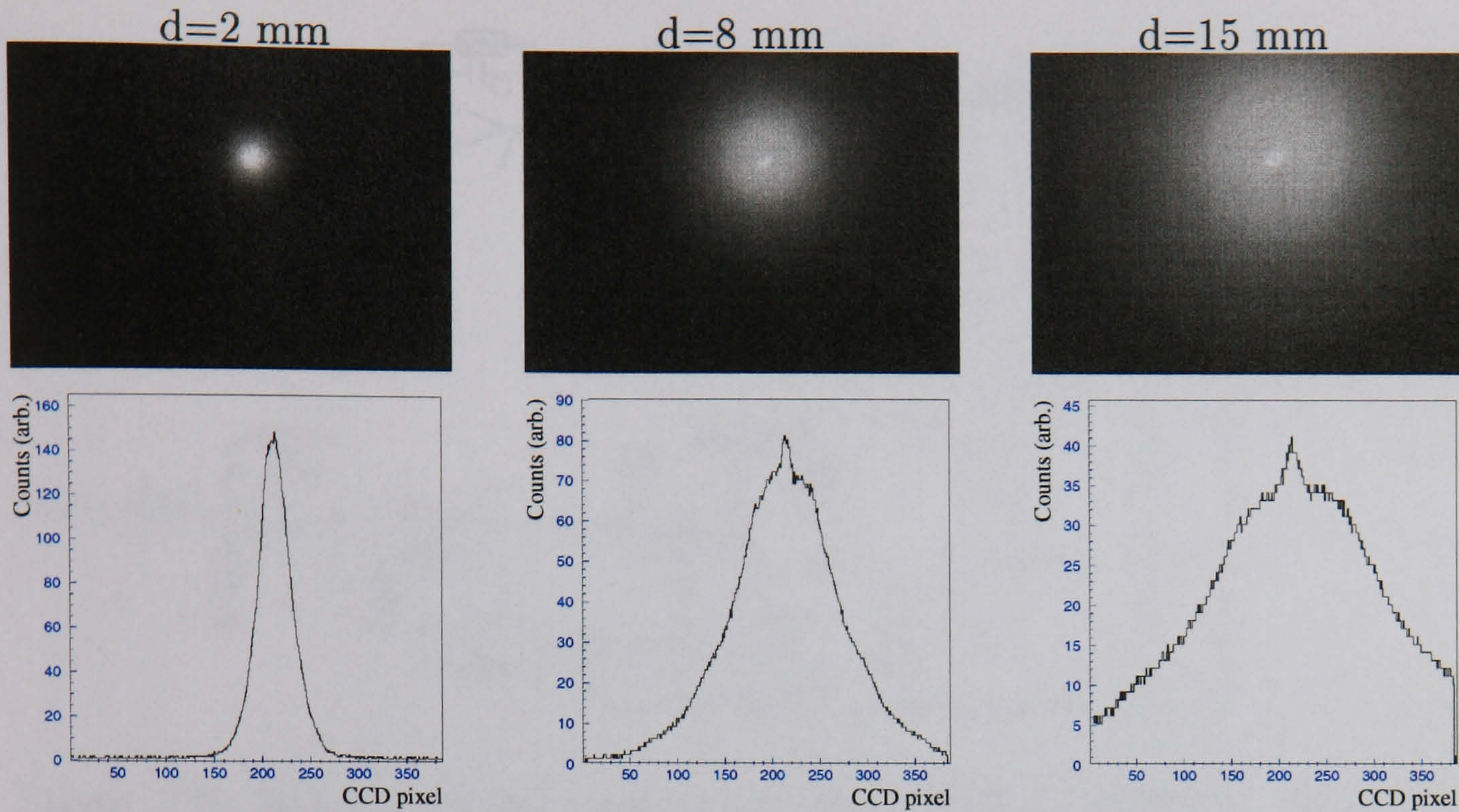


Figure 7.5: Results of the measurement of the light distribution created by the optical fibre on a CCD camera at a distance d from the fibre. Each image corresponds to a $8.5 \times 6.3 \text{ mm}^2$ area.

The signals from the anodes and the last dynode are amplified with two operational amplifier circuits. The first is a charge amplifier with an integration time $\tau = C_1 VR_1$. The integration time τ is chosen to be $2\mu\text{s}$ with $C_1 = 10\text{pF}$ and $VR_1 = 200\text{k}\Omega$ in both the LED and the scintillator tests. The second is a linear non-inverter amplification stage with variable gain $A_2 = 1 + VR_2/R_2$.

The amplified signal from the last dynode is compared with a fixed threshold voltage (comparator) producing a logic signal used to trigger the acquisition. This logic pulse is used for three tasks. The first is to produce the "hold" pulse for the sample-and-hold (S/H) module using a monostable. The monostable output has a variable width, ranging from $1\mu\text{s}$ to over $10\mu\text{s}$, adjusted by VR_3 . The second is to start the logic circuit that produces the addresses for two analogue multiplexers: one for the X signals and the other for the Y signals. These addresses determine which input signal is present at the multiplexer output. Both addresses are sequentially incremented in a repetitive cycle after a selectable number of pulses (16 in this case) from a 25 MHz clock. The third task is to trigger the digitising module.

The analogue-to-digital conversion was performed with a Signatec DA60

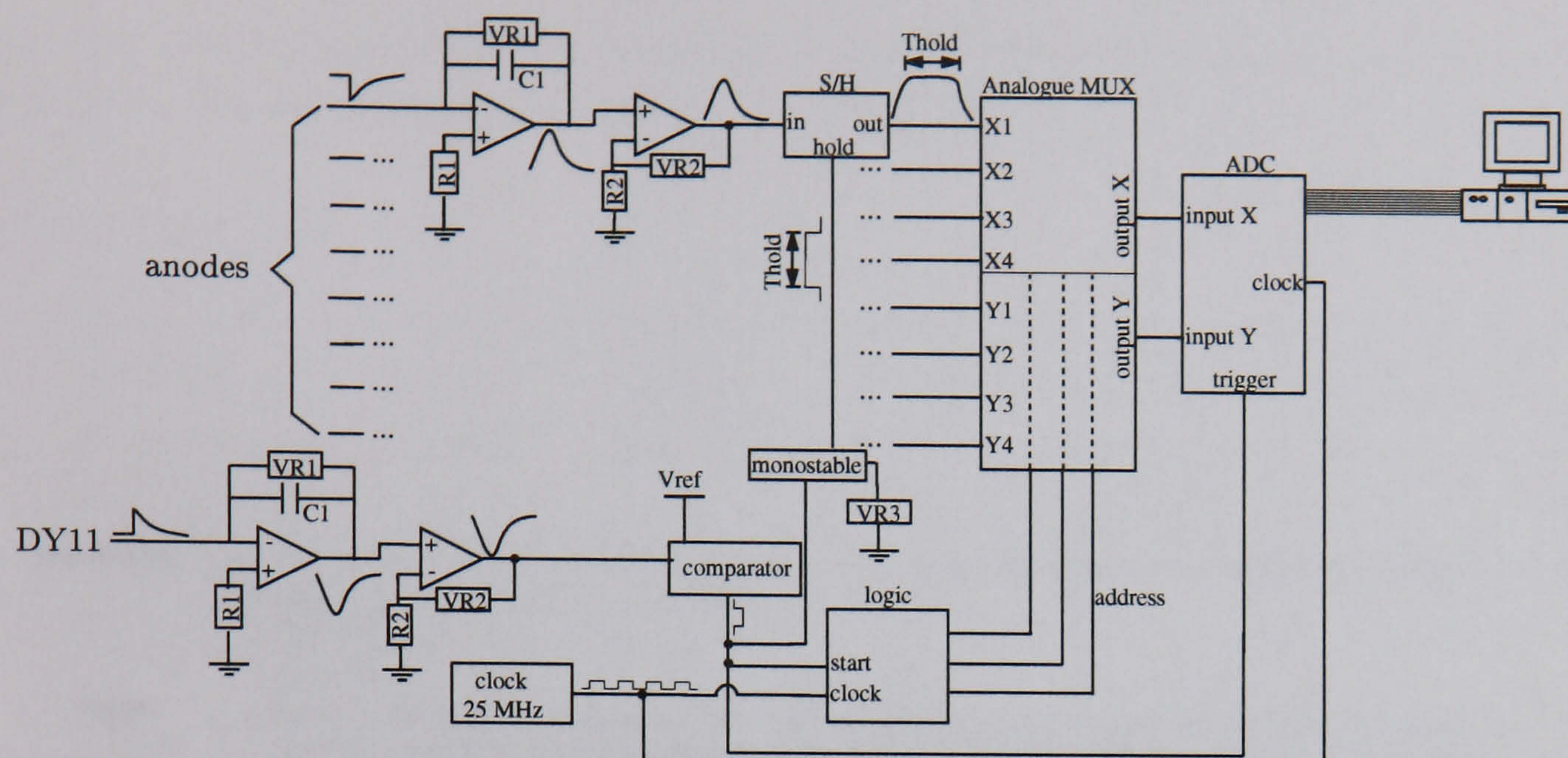


Figure 7.6: Readout circuit used to test the R5900-C8 PSPMT. DY11 corresponds to the last dynode signal, used as a trigger.

PC board for the ISA bus³. It has two inputs, each coupled to a 12-bit-ADC. The inputs are simultaneously sampled with a 30 MHz maximum sampling rate. For each trigger, it acquires a set of 96 samples for each input at the falling edge of an external clock pulse. The signal at the ADC inputs vary according to the analogue multiplexer output which is determined by the logic circuit shown in figure 7.6. Since the logic circuit switches the analogue multiplexer output every 16 clock cycles, there were 6 ($6 = 96/16$) sets of samples per trigger, each set corresponding to a different anode signal.

The ADC sampling is shown in figure 7.7 for one ADC channel corresponding to the set of four X anodes. The other ADC channel operates similarly to digitise the Y anodes. Notice that only the first four sets of 16 samples are used in the centroid calculation. All the samples are then transferred to two 256 ksamples on-board RAM chips, and subsequently to computer memory or hard disk for analysis and storage. When analysing the data the value for each anode was found by averaging the set of 8 samples shown in figure 7.7. These 8 samples were the “central” samples of the set of 16 samples for a given anode. The first and the last four samples were discarded to avoid distortions due electronic jitter caused by the analogue multiplexer address switching.

Before connecting the PSPMT the channels were calibrated with an electronic pulser (ORTEC model 480) and the second amplifier gain was adjusted

³Industry Standard Architecture, I/O bus standard for personal computers.

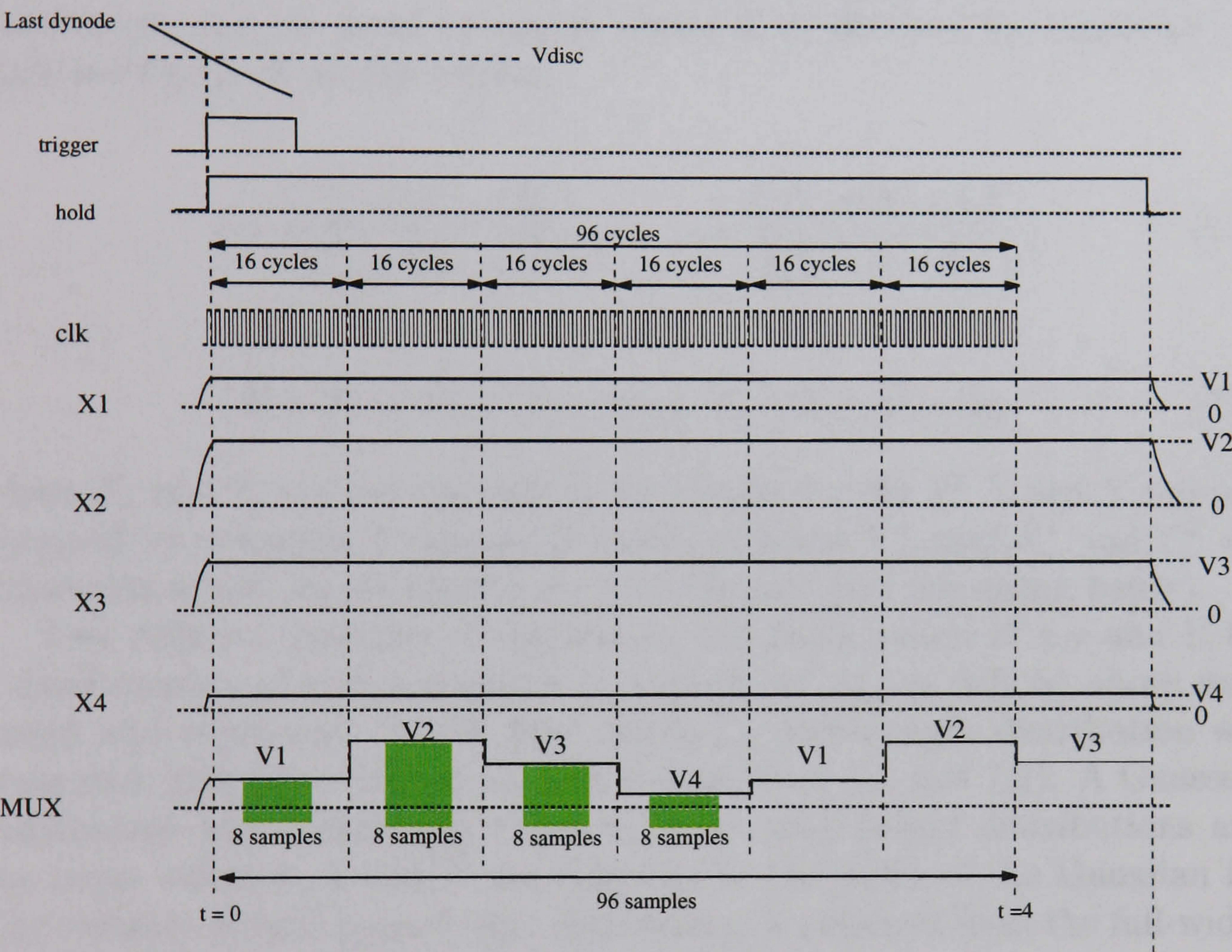


Figure 7.7: ADC sampling of the X anodes. The timing is shown in μs units.

so that the signals from the 8 anode-channels differ less than $\pm 2\%$ after digitisation, for the same input pulse.

Data analysis

A valid event is defined for a light pulse that generates a last dynode signal above threshold. This would be an LED pulse, in the case of the LED scans, or a gamma ray interaction, for the case of the gamma-ray scan. For each valid event the position coordinates x, y are found by a center of gravity calculation, and the total or energy signal E is obtained by summing the digitised signals of all the anodes:

$$x = \frac{\sum_{i=1}^4 i(X_i - X_i^T)}{\sum_{i=1}^4 (X_i - X_i^T)} \quad ; \quad y = \frac{\sum_{i=1}^4 i(Y_i - Y_i^T)}{\sum_{i=1}^4 (Y_i - Y_i^T)}; \quad (7.1)$$

$$E = X_1 + X_2 + X_3 + X_4 + Y_1 + Y_2 + Y_3 + Y_4. \quad (7.2)$$

where X_i and Y_i are the digitised pulse heights for the i^{th} X and Y anodes, obtained by averaging 8 samples as shown in figure 7.7, and X_i^T and Y_i^T are thresholds which are introduced for each channel (see discussion below).

Two different methods of calculating the mean values of x, y and E for a fixed number of events acquired at a point (x_j^f, y_k^f) as defined above were tested and compared. In the first method a pulse-height distribution was generated with the values of x, y and E (equations 7.1 and 7.2). A Gaussian distribution was numerically fitted to these pulse-height distributions and the mean values \bar{x} , \bar{y} and \bar{E} are taken to be the mean of the Gaussian fit. The variance of each pulse-height distribution is obtained from the full-width at half maximum (FWHM) of the Gaussian fit.

The second method differs in the calculation of \bar{x} , \bar{y} and the corresponding FWHM values. For each event, the x and y values obtained with equation 7.1 are used to fill a two dimensional histogram (image) representing the x and y directions. Two profiles are taken along perpendicular directions passing through the histogram pixel with maximum counts (figure 7.8), each pixel being 0.2 mm wide. The mean values of x and y and the respective variances are taken from a Gaussian fit of these profiles, as described above.

The two methods were found to produce very similar results (within $\pm 1\%$) for \bar{x} and \bar{y} as well as for the FWHM of the centroid distributions. All the results shown hereafter were obtained using the first method described.

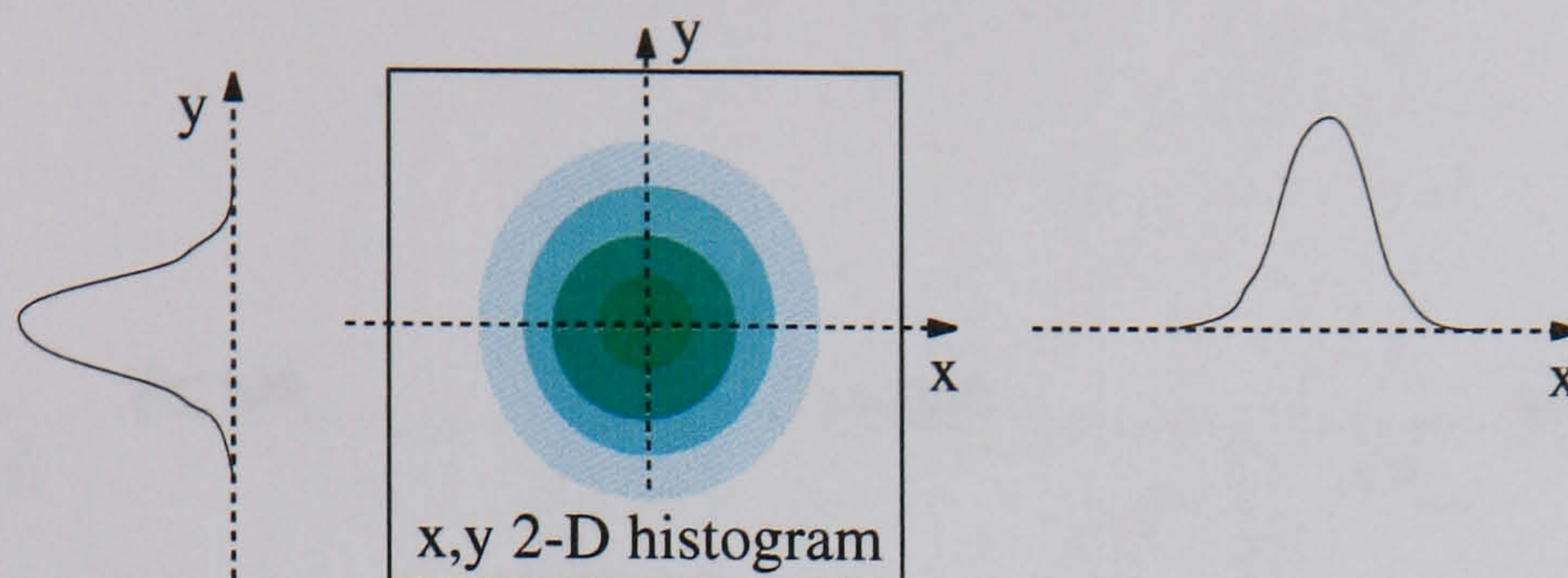


Figure 7.8: Illustration of a two dimensional histogram of the x and y centroids. Also shown are profiles along the x and y directions passing through the maximum pixel on the histogram.

7.2.2 Results from PSPMT scans

Spatial response: LED scans

For each fibre position (x_j^f, y_k^f) , a total of 21,840 events was acquired. Since the LED pulser was set to produce about 3,000 light flashes per second (figure 5.3), the expected total acquisition time at each fibre position should be about 7 seconds, if, for all the events, the last dynode signal was above threshold (figure 7.6), producing a trigger. The discriminator level was set to 25% ~ 40% of the average last dynode pulse height when the fibre was at the central region of the tube. An acquisition timeout was set to 20 seconds. If the total number of triggers during that period was less than 21,840 the response at that position was not considered in the data analysis.

Figure 7.9 shows results obtained for the 3 scans when the fibre was at distances $d=1, 7$ and 15 mm away from the C8 window. For each case the mean x position (\bar{x}) is shown as a function of x_j^f for a line y_k^f ($k=6, 12$ and 18). The error bars for each point represent the FWHM of the Gaussian fit to the pulse-height distribution of centroids discussed above.

The threshold values X_i^T and Y_i^T for a given anode are found prior to the centroid calculations, by analysing the pedestal peak of that anode when the fibre was far from it and at $d=1$ mm from the tube window. The thresholds are chosen to be the mean plus one standard deviation of the pedestal peak in that anode under those circumstances.

For $d=1$ mm there are flat regions which suggest no correlation between \bar{x} and x_j^f . This can be explained through an analysis of the signals from each individual anode. It is seen that in these flat regions the charge produced is mainly collected by a single anode which is a result of the small light spot size combined with the very low transverse charge spread provided by

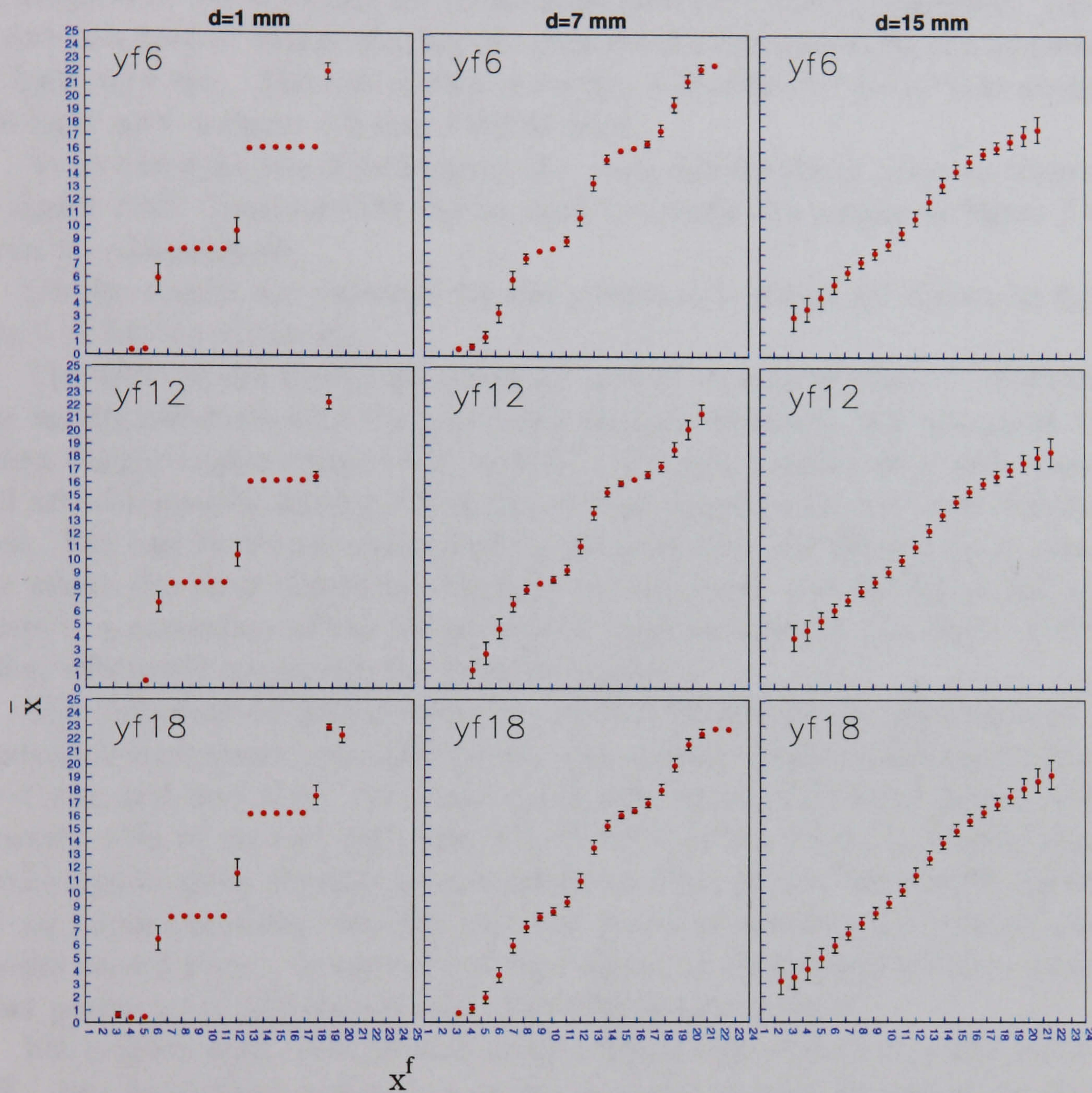


Figure 7.9: Average x position \bar{x} as a function of fibre position x_j^f for three y lines y_6^f , y_{12}^f and y_{18}^f . The error bars represent the FWHM of the pulse-height distribution of x centroids. Three cases are presented corresponding to a fibre-to-PSPMT distance $d=1, 7$ and 15 mm .

the metal channel dynode structure. Therefore, the centroid algorithm in equation 7.1 gives a constant value which is related to the number of the anode that collects the majority of the charge. The steep variations in \bar{x} correspond to regions where the fibre moved from above one anode to above its neighbour. For $d=7$ mm the correlation between \bar{x} and x_j^f improves. This is due to a greater charge sharing between anodes introduced by the increase in light spot size. The correlation is further improved for $d=15$ mm where the light spot is about 4.2 mm FWHM wide.

As an example, the distributions of x centroids for the y_{12}^f line are shown in figure 7.10. These are the curves used to obtain the results in figure 7.9 from the Gaussian fit.

Similar results are obtained for the y centroids, which are shown in figure 7.11 for the x line x_{12}^f .

The effect of the threshold values X_i^T and Y_i^T is seen in figure 7.12 where the results obtained with the previously defined thresholds are compared to using slightly higher values of X_i^T and Y_i^T . The new thresholds in each channel are obtained by adding 1% of the average signal to the previous thresholds. The results shown correspond to the scan with the fibre at $d=15$ mm, for which the most significant changes are observed. As the figure shows, there is a correction of the reconstructed position towards the edges of the tube, effectively increasing the linearity region.

The definition of spatial resolution as the FWHM of the centroid distributions is inadequate, specially for the case of narrow light distributions (e.g. $d=1$ mm and $d=7$ mm). For these cases, the values of \bar{x} and \bar{y} do not vary linearly with x_j^f and y_k^f and, also, the FWHM of the centroid distributions varies significantly, depending on whether the fibre is over the central region of one anode (narrower distribution) or it is over a boundary between anodes (wider distribution). A measure of the spatial resolution along x at a given fibre position (x_j^f, y_k^f) should take these effects into account.

For a given scan position and along a given scan direction, a parameter SR_{x_j} can be defined which is a measure of the spatial resolution at that position and along that direction:

$$SR_{x_j} = \frac{\Delta_{x_j}}{FWHM_j} \quad (7.3)$$

where

$$\Delta_{x_j} = \frac{(\bar{x}_j - \bar{x}_{j-1}) + (\bar{x}_{j+1} - \bar{x}_j)}{2} = \frac{\bar{x}_{j+1} - \bar{x}_{j-1}}{2} \quad (7.4)$$

the metal channel dynode structure. Therefore, the centroid algorithm in equation 7.1 gives a constant value which is related to the number of the anode that collects the majority of the charge. The steep variations in \bar{x} correspond to regions where the fibre moved from above one anode to above its neighbour. For $d=7$ mm the correlation between \bar{x} and x_j^f improves. This is due to a greater charge sharing between anodes introduced by the increase in light spot size. The correlation is further improved for $d=15$ mm where the light spot is about 4.2 mm FWHM wide.

As an example, the distributions of x centroids for the y_{12}^f line are shown in figure 7.10. These are the curves used to obtain the results in figure 7.9 from the Gaussian fit.

Similar results are obtained for the y centroids, which are shown in figure 7.11 for the x line x_{12}^f .

The effect of the threshold values X_i^T and Y_i^T is seen in figure 7.12 where the results obtained with the previously defined thresholds are compared to using slightly higher values of X_i^T and Y_i^T . The new thresholds in each channel are obtained by adding 1% of the average signal to the previous thresholds. The results shown correspond to the scan with the fibre at $d=15$ mm, for which the most significant changes are observed. As the figure shows, there is a correction of the reconstructed position towards the edges of the tube, effectively increasing the linearity region.

The definition of spatial resolution as the FWHM of the centroid distributions is inadequate, specially for the case of narrow light distributions (e.g. $d=1$ mm and $d=7$ mm). For these cases, the values of \bar{x} and \bar{y} do not vary linearly with x_j^f and y_k^f and, also, the FWHM of the centroid distributions varies significantly, depending on whether the fibre is over the central region of one anode (narrower distribution) or it is over a boundary between anodes (wider distribution). A measure of the spatial resolution along x at a given fibre position (x_j^f, y_k^f) should take these effects into account.

For a given scan position and along a given scan direction, a parameter SR_{x_j} can be defined which is a measure of the spatial resolution at that position and along that direction:

$$SR_{x_j} = \frac{\Delta_{x_j}}{FWHM_j} \quad (7.3)$$

where

$$\Delta_{x_j} = \frac{(\bar{x}_j - \bar{x}_{j-1}) + (\bar{x}_{j+1} - \bar{x}_j)}{2} = \frac{\bar{x}_{j+1} - \bar{x}_{j-1}}{2} \quad (7.4)$$

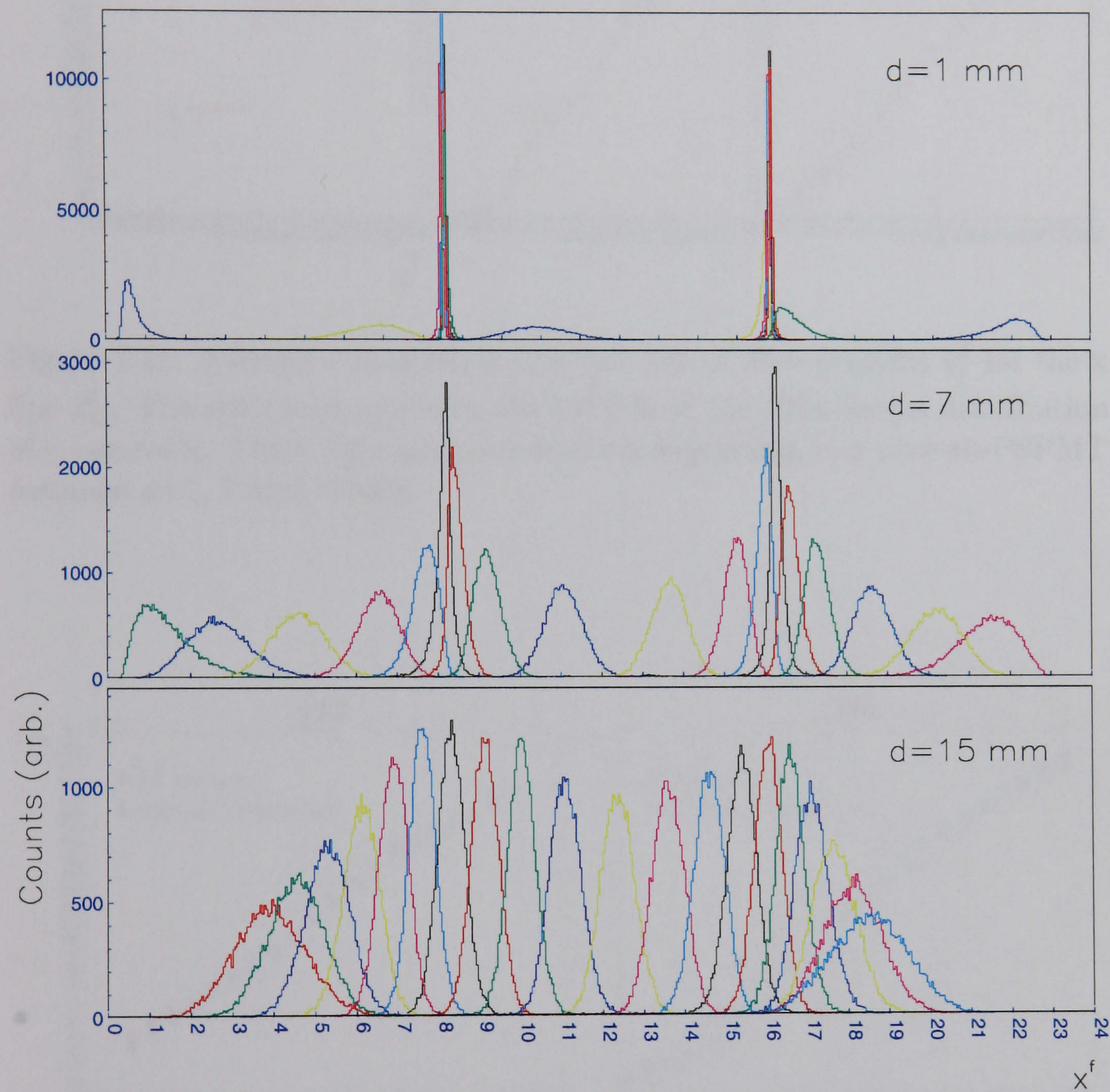


Figure 7.10: Distributions of x centroids for the 24 x_j^f points along the Y_{12}^f line.

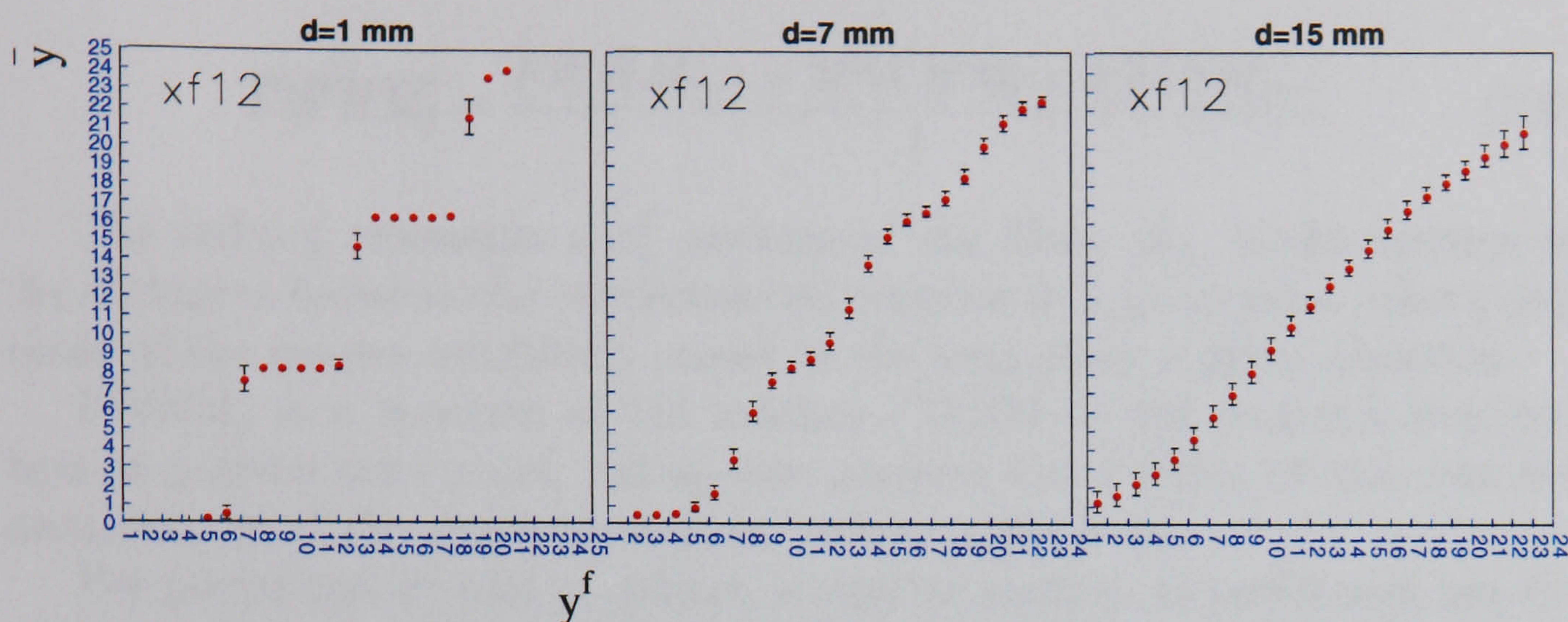


Figure 7.11: Average y position \bar{y} as a function of fibre position y_j^f for the x line x_{12}^f . The error bars represent the FWHM of the pulse-height distribution of y centroids. Three cases are presented corresponding to a fibre-to-PSPMT distance $d=1$, 7 and 15 mm.

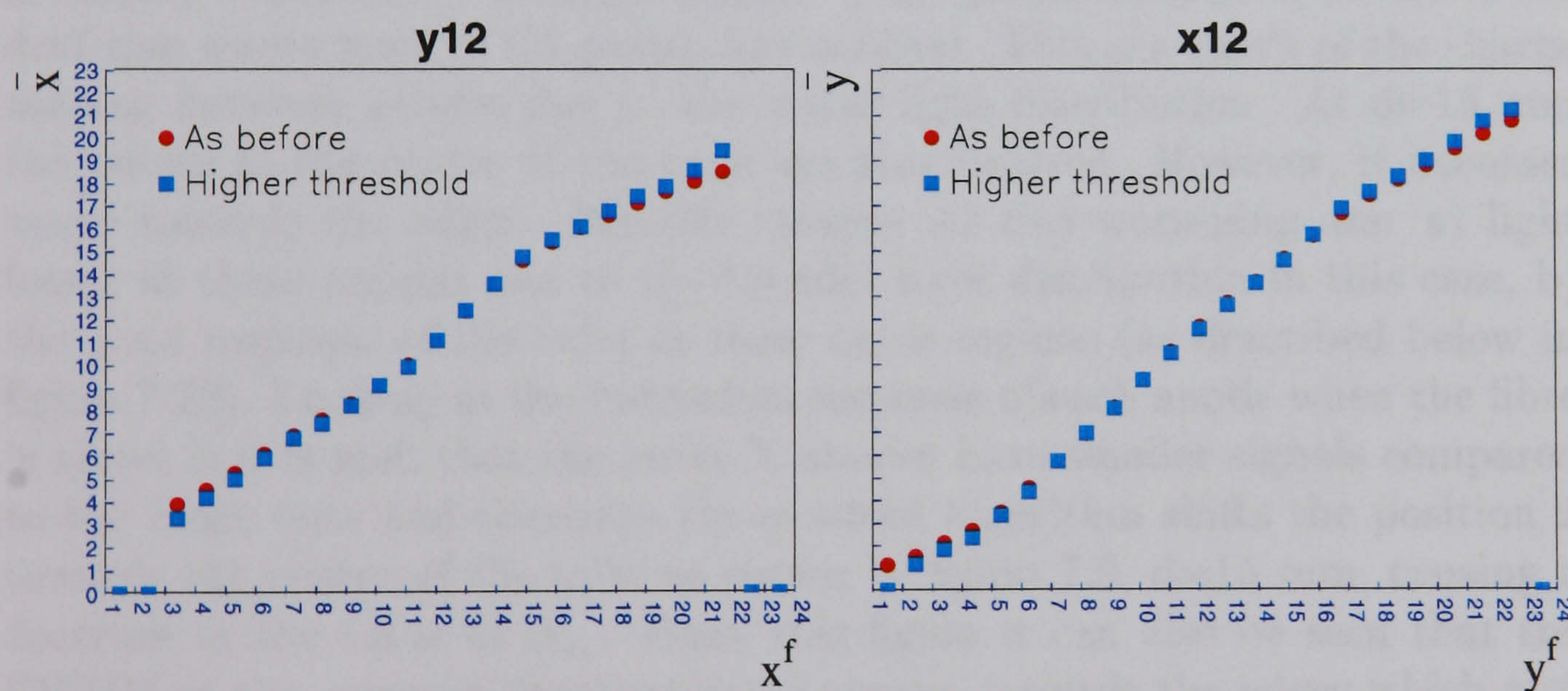


Figure 7.12: Average x and y positions \bar{x} and \bar{y} as a function of fibre position x_j^f and y_k^f for the y and x lines y_{12}^f and x_{12}^f . The fibre-to-PSPMT distance d is 15 mm. Results with a higher threshold are compared to the previously shown results.

and

$$\overline{FWHM_j} = \frac{FWHM_{j-1} + 2FWHM_j + FWHM_{j+1}}{4}. \quad (7.5)$$

The index j represents a x_j^f position of the fibre. Δ_{x_j} is the average of the distances between the reconstructed centroid at a given scan point j and those of the nearest neighbour points in the scan along a given direction.

$FWHM_j$ is a measure of the average FWHM of the centroid distribution at a given scan point, taking into account the FWHM of the centroid distributions of the nearest neighbour points in the scan.

For peripheral x_j^f and y_k^f points, a similar analysis is performed but involving only one nearest neighbour. For a given scan step size along the x direction (in this case 1 mm), if $SR_x > 1$ at a given position (x_j^f, y_k^f) , the calculated x position is considered resolved from its immediate neighbours and the scan step size is an upper limit to the spatial resolution at that point. The same discussion applies to the spatial resolution along the y direction, defined by SR_y . Figure 7.13 shows the values of SR_{x_j} for the y line y_{12}^f . For $d=1$ mm there are regions where some of the scan points are not resolved from their neighbours for the 1 mm step size of the scan. These regions correspond to the flat regions in figure 7.9 for $d=1$ mm where the charge is mainly collected by a single anode. The spatial resolution is better for $d=7$ mm where most of the points are resolved. This is a result of the charge sharing between anodes due to the wider light distribution. At $d=15$ mm the points at the centre of the tube are also resolved. However, it becomes worse towards the edges. Possible reasons for this worsening are: a) light losses at these regions due to the broader light distribution in this case, b) the poor response of the tube at these outer regions (as described below in figure 7.22). Looking at the individual response of each anode when the fibre is above it it is seen that the outer X anodes have smaller signals compared to the inner ones and therefore the centroid algorithm shifts the position \bar{x} towards the center of the tube as shown in figure 7.9, $d=15$ mm, causing a decrease in the value of Δ_{x_j} . From this figure it can also be seen that the FWHM of the centroid distributions increases towards the edges which also worsens the spatial resolution.

On the contrary, the outer Y anodes show a very similar response to the inner ones and the position distortion is reduced. The tube has an extended region of sensitivity along the y direction as seen in figure 7.11, for $d=15$ mm. As a consequence, the spatial resolution along y , particularly for $d=15$ mm, is better towards the edges compared to the x direction, as shown figure 7.14.

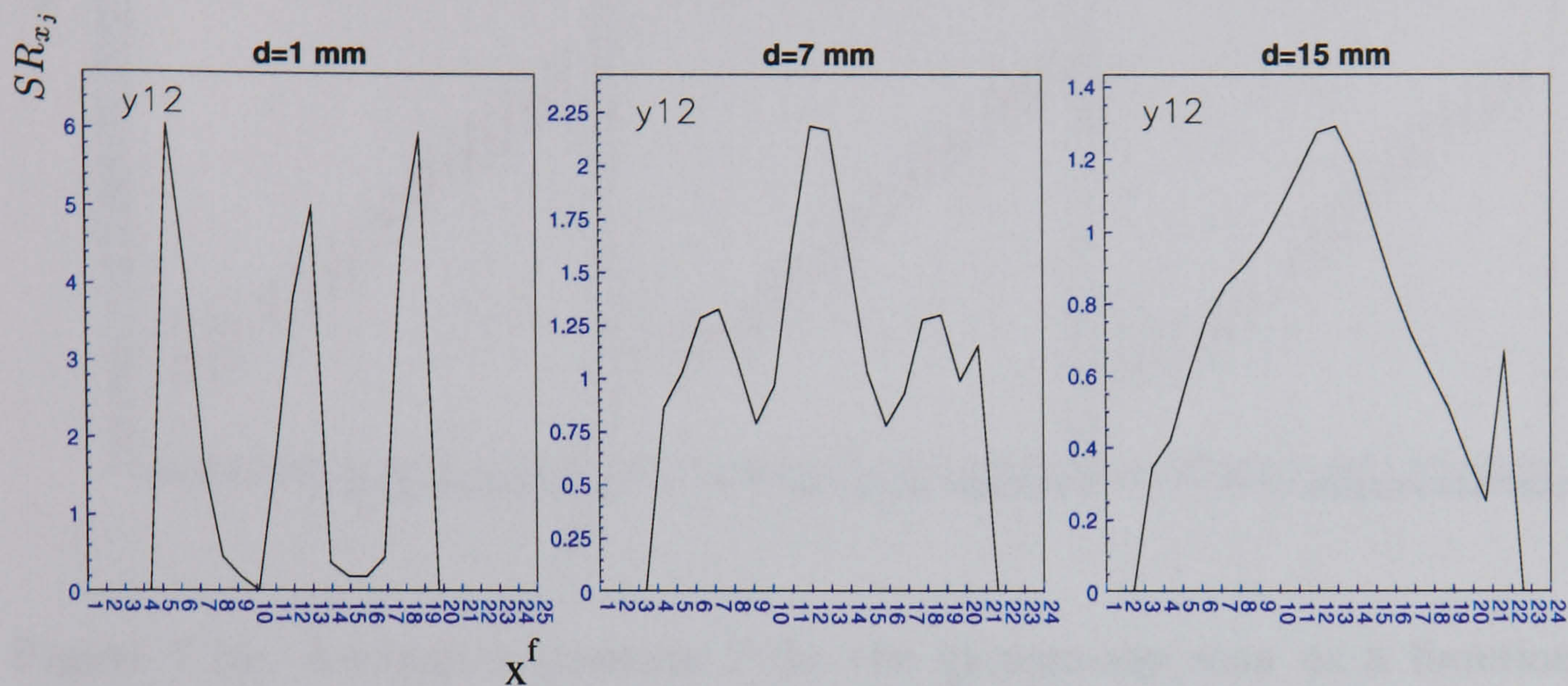


Figure 7.13: SR_{x_j} as a function of x_j^f for y_{12}^f and for fibre-to-PSPMT distances of $d=1, 7$ and 15 mm. Since the scan step size is 1 mm, if $SR_{x_j} > 1$ the spatial resolution at that point is at least 1 mm.

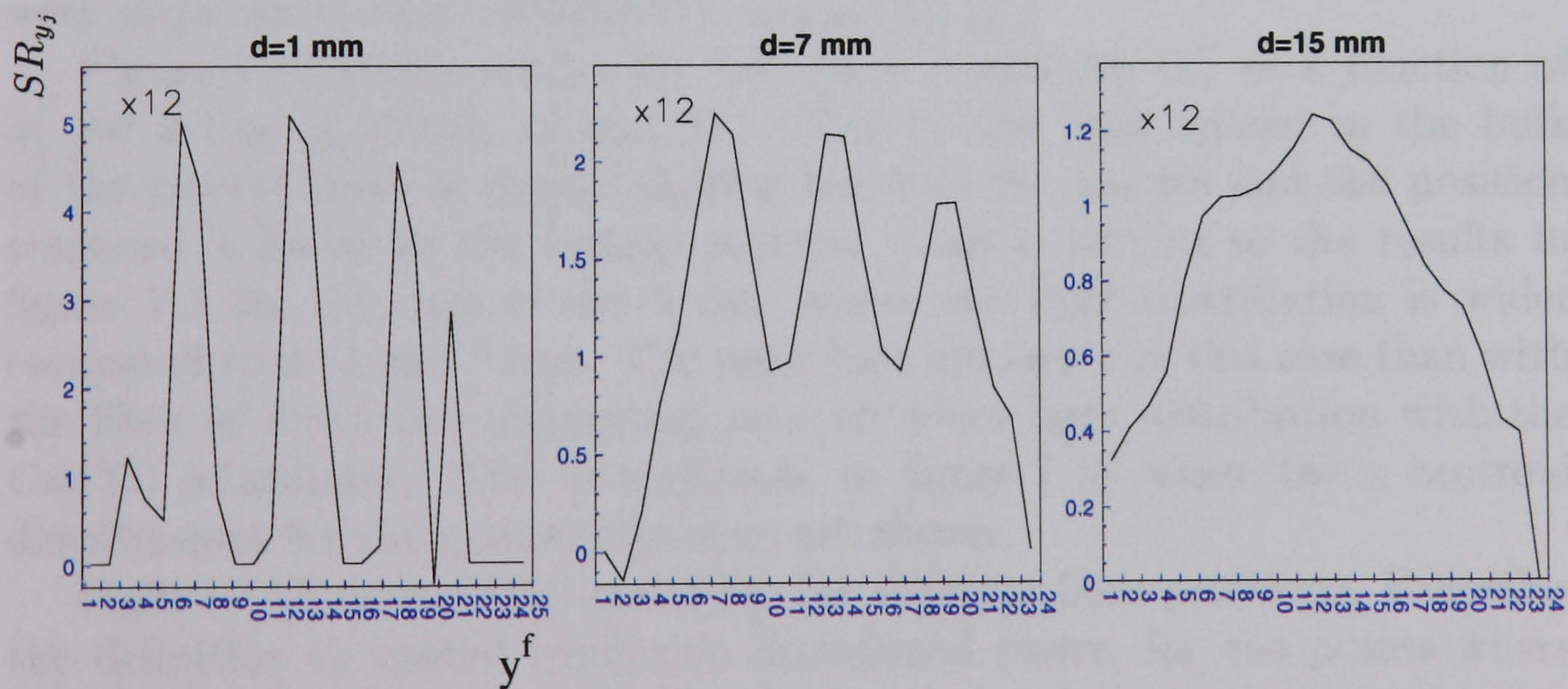


Figure 7.14: SR_{y_j} as a function of y_j^f for x_{12}^f and for fibre-to-PSPMT distances of $d=1, 7$ and 15 mm. Since the scan step size is 1 mm, if $SR_{y_j} > 1$ the spatial resolution at that point is at least 1 mm.

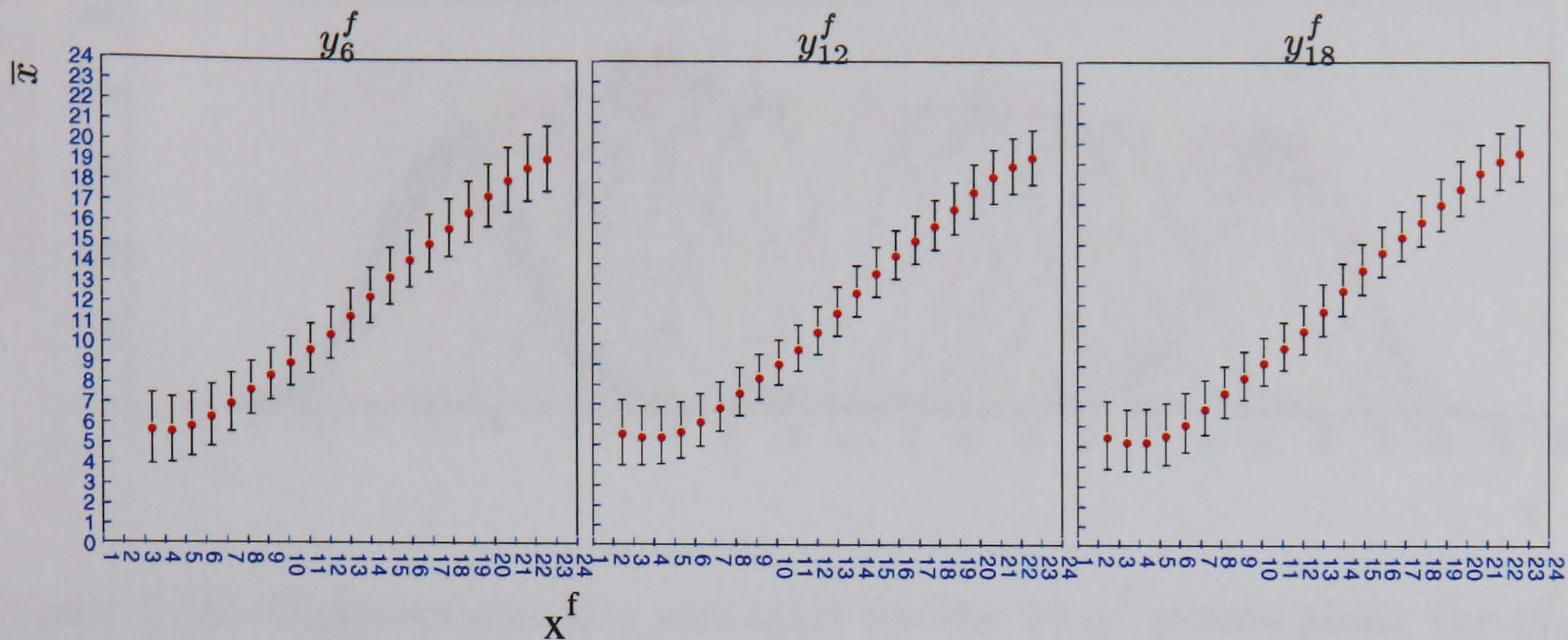


Figure 7.15: Average x position \bar{x} for the gamma-ray scan as a function of collimator position x_j^f for three y lines y_6^f , y_{12}^f and y_{18}^f . The error bars represent the FWHM of the pulse-height distribution of x centroids.

Spatial response: gamma-ray scan

A similar scan was performed with the CsI(Tl) crystal described above coupled to the C8. The acquisition timeout was adjusted to 30 seconds to correct for the lower event rate compared to the LED pulser. Again, 21,840 events were acquired at each collimator position (x_j^f, y_k^f) .

Figure 7.15 shows results for the mean x position (\bar{x}) as a function of x_j^f for a line y_k^f ($k=6, 12$ and 18). Due to the light spread in the bulk of the crystal there is charge sharing between the anodes and the position response is linear in the central regions. This is similar to the results in figure 7.9 for the case of $d=15$ mm where the light distribution is wider compared to $d=1$ and 7 mm. The error bars are larger in this case than with the fibre at $d=15$ mm suggesting an even wider light distribution with the CsI(Tl) scintillator. This is confirmed in figure 7.16 where the x centroid distributions for the gamma-ray scan are shown.

Figure 7.17 shows SR_{x_j} and SR_{y_j} for different fibre positions. Following the definition of spatial resolution introduced above, for the points where $SR_{x_j} > 1$ and $SR_{y_j} > 1$ an upper limit to the spatial resolution is the step size. To find an upper limit to the resolution, the calculations in equation 7.3 are performed for scanning points separated by 1 mm, 2 mm and 3 mm, and it is found that, for the later case, the conditions $SR_{x_j} > 1$ and $SR_{y_j} > 1$ are met in a region of about 15×15 mm² in the centre of the tube. Since this is not the case for points separated by 2 mm, the spatial resolution is between

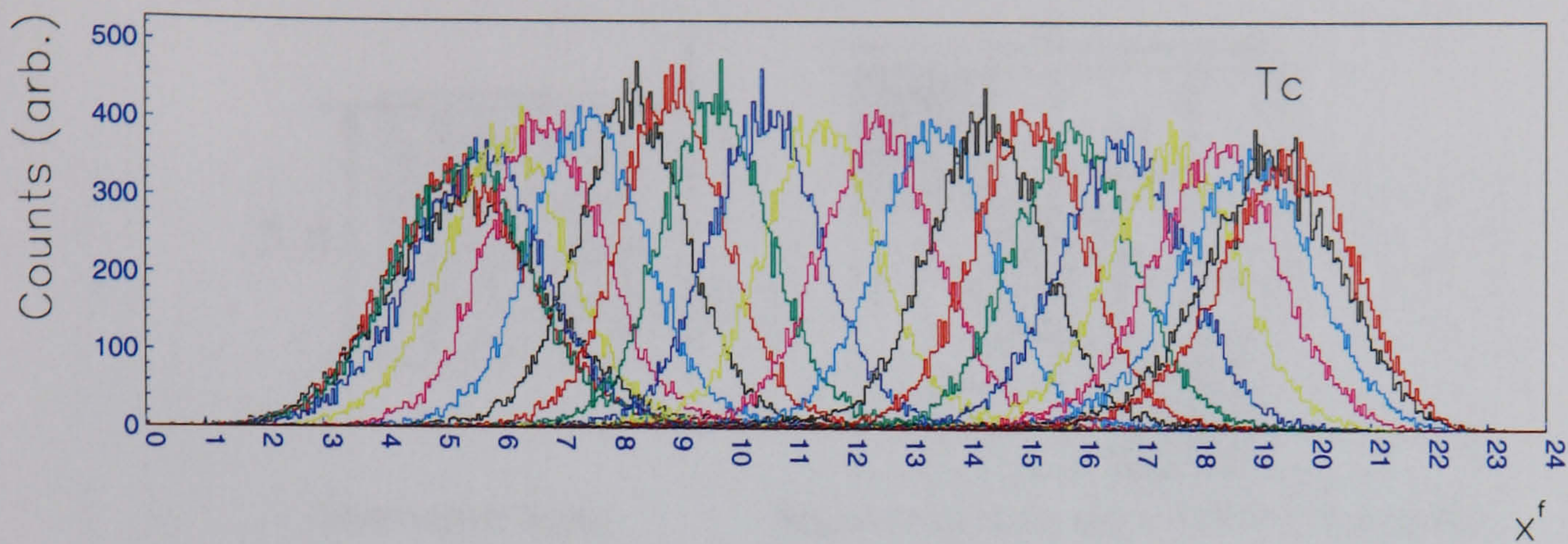


Figure 7.16: Distributions of x centroids for the 24 x_j^f points along the y_{12}^f line, for the gamma-ray scan.

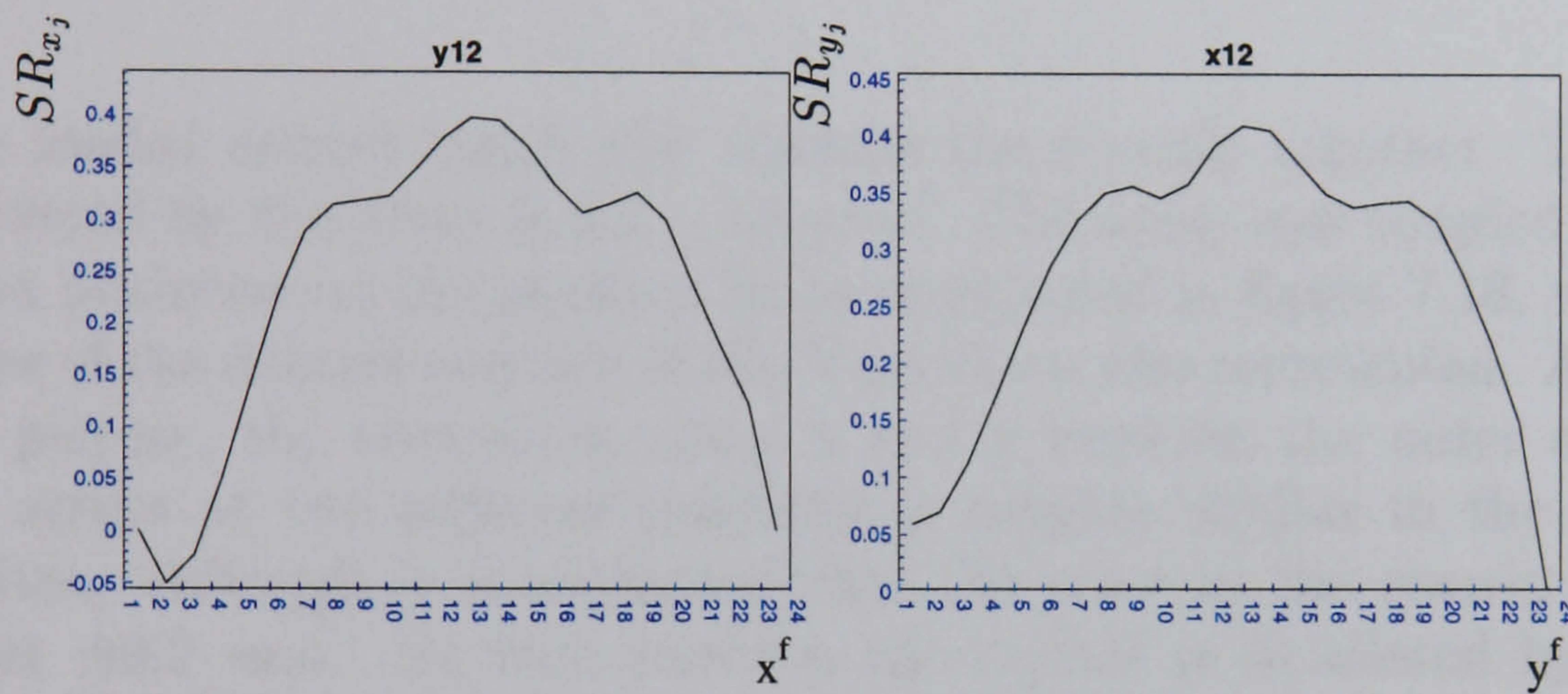


Figure 7.17: SR_{x_j} as a function of x_j^f for y_{12}^f and SR_{y_j} as a function of y_j^f for x_{12}^f , for the gamma-ray scan.

2 and 3 mm in this central region.

Due to the linear behaviour in the central regions, the spatial resolution can alternatively be defined as the FWHM of the pulse-height distribution of the x centroids at these regions. Spatial resolution values between 2.2 mm FWHM and 3 mm FWHM are obtained with this method for the central region of $15 \times 15 \text{ mm}^2$, in good agreement with the previous method.

Spatial response: image of a segmented pixel array

A 5×5 array of CsI(Tl) crystals was coupled to the C8. Each crystal segment is $1 \times 1 \times 5 \text{ mm}^3$ and there are 0.2 mm gaps between the segments. The gaps are filled with a diffuse white reflector material (based on a titanium

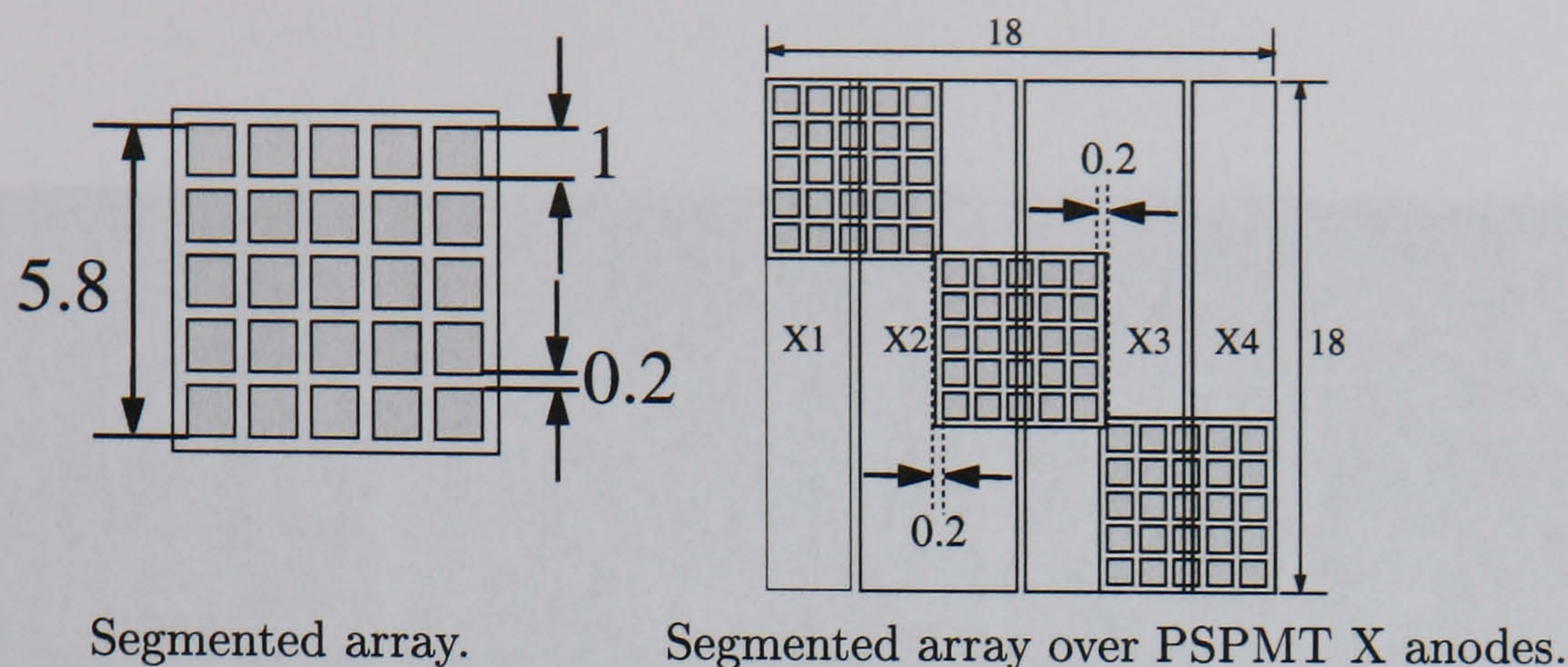


Figure 7.18: Schematic representation of an array of 5×5 CsI(Tl) crystal array and its position with respect to the PSPMT X anodes. All dimensions in mm.

dioxide loaded epoxy) which also cements the crystals together. The total area covered by the array is $5.8 \times 5.8 \text{ mm}^2$. The array was coupled in three different positions on the photocathode as depicted in figure 7.18, where an estimate of the relative position of the X anodes is also represented. As shown in the picture, the separation along x and y between the outer segments of the arrays at two adjacent positions is roughly similar to the segment separation, although it is estimated that the error in the matrix position is about $\pm 0.2 \text{ mm}$. At each position the crystal is irradiated by a non-collimated Co^{57} source (122 keV gamma-rays) located at the center of the array and 2 cm above its top surface.

The images obtained are shown in figure 7.19. For each image most of the 25 pixels are visible and differentiated. However, as expected from the LED scans, the reconstructed positions of any two segments located above the central regions of the inner anodes (X_2 , X_3 , Y_2 and Y_3) are closer than for segments above anode boundaries, and the former are therefore less easily distinguished. A superposition of these three images is shown in figure 7.20, where the difficulty in distinguishing the segments located above the central regions of the anodes is also visible.

Spatial response: discussion

The spatial response of the tube is clearly related to size of the light distribution over the photocathode.

For single continuous crystals the light spread is mainly determined by the thickness of the crystal. For a 5 mm thick CsI(Tl) a 3 mm spatial resolution

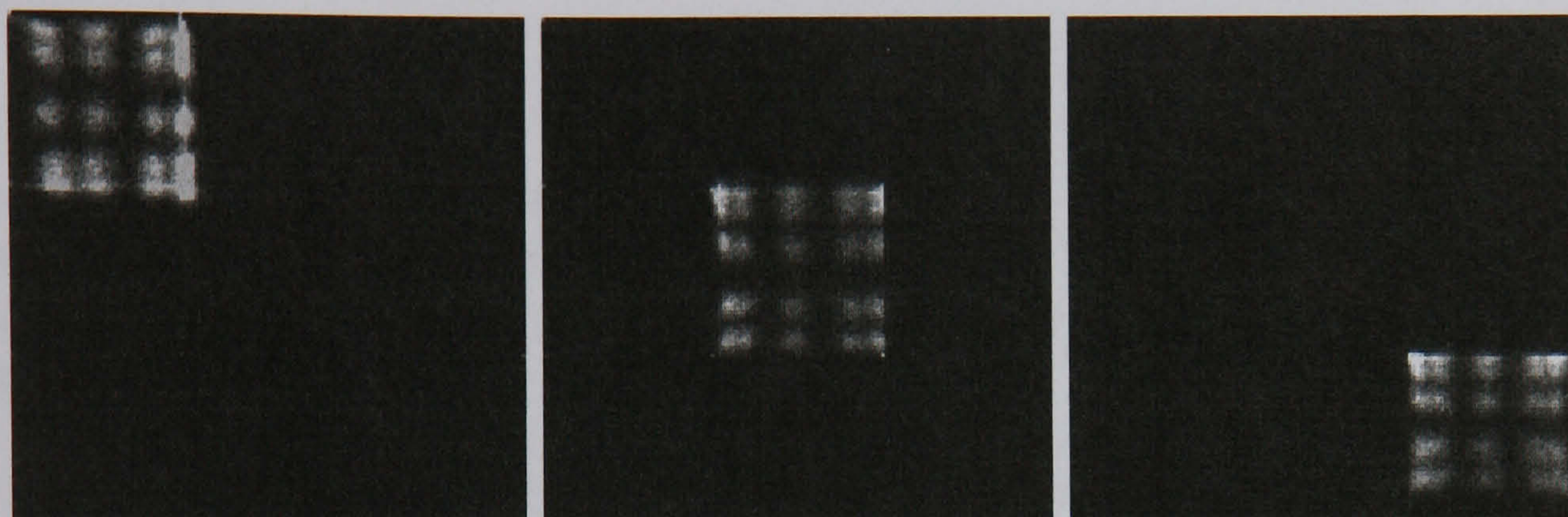


Figure 7.19: Images of the segmented crystal array coupled to the R5900-C8 and irradiated by 122 keV gamma-rays.

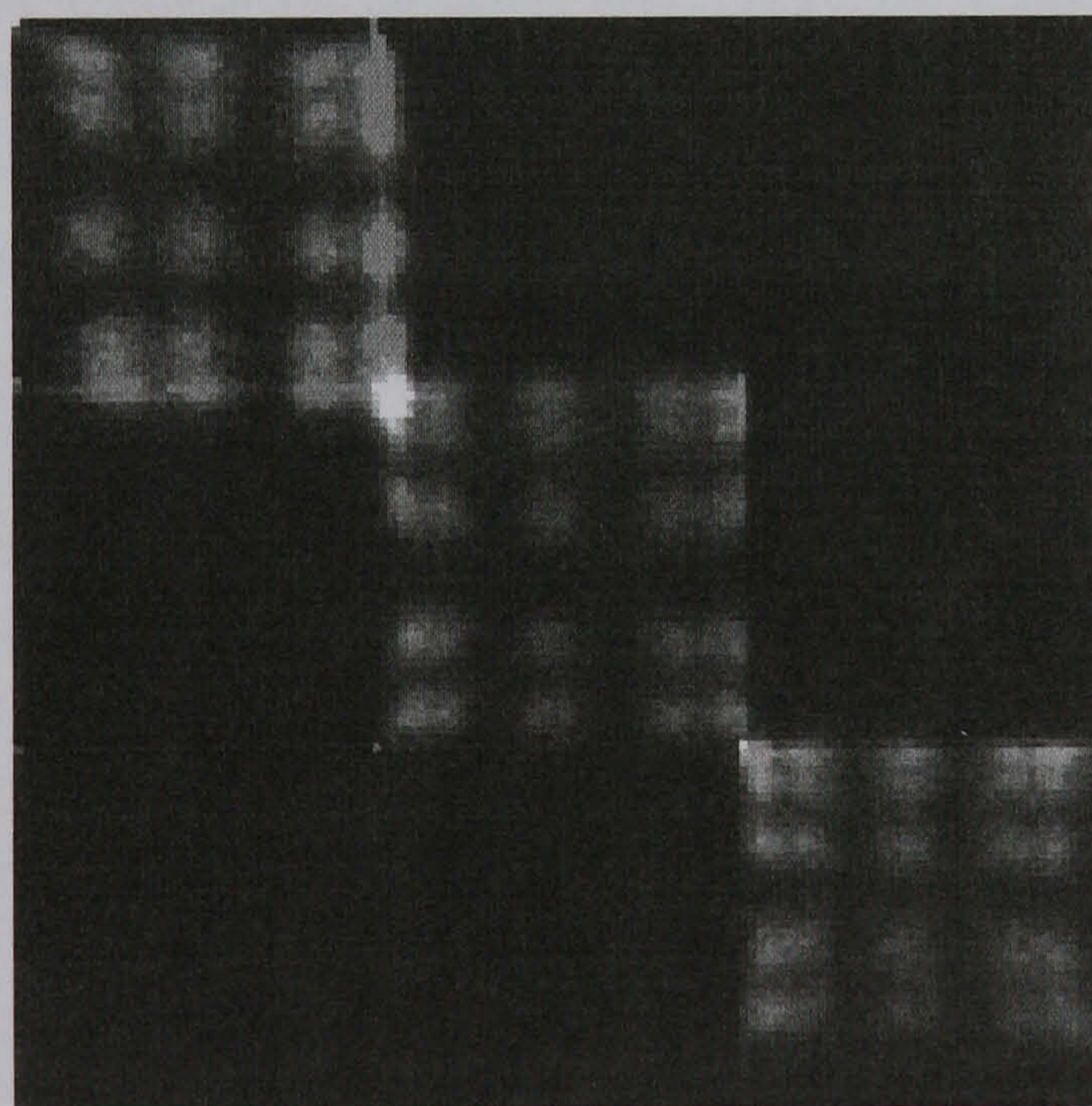


Figure 7.20: Superposition of the images of the segmented crystal array shown in figure 7.19.

is obtained. Due to the light spread over the PSPMT window there is charge sharing between the anodes and therefore good position linearity is achieved (figure 7.15).

A large area device (e.g. $10 \times 10 \text{ cm}^2$) can be assembled with arrays of C8s and a single crystal. This has been attempted by R. Pani et al [198] obtaining spatial resolution values between 2.5 and 4 mm FWHM for several crystals coupled to the tube with light guides. The combined thickness of the crystal and the light guide vary from 2 to 5 mm, which is in agreement with the results described above.

For segmented crystal arrays, the light spread is determined by the size of the crystal segments. Ideally it is desirable to be able to separate all the segments in the image in order to correctly identify the segment of interaction. In this case the spatial resolution of the system is determined by the segment size. The ability to separate adjacent segments depends on the size of the segment, which determines the light spread and the minimum centre-to-centre segment separation.

The results obtained show that for a segment size of about $1 \times 1 \text{ mm}^2$, the spatial resolution obtained is poor in some regions above the central regions of the C8 anodes, where adjacent segments are not separated. For segments greater than $2 \times 2 \text{ mm}^2$ the crystal separation should be achieved according to the results of the LED scan at $d=7 \text{ mm}$. This is confirmed by the results of other authors using pixels segments of $2 \times 2 \text{ mm}^2$ or larger [198, 199].

Energy response

Typical energy pulse-height distributions for the LED scan and for the gamma-ray scan at (x_{12}^f, y_{12}^f) are shown in figure 7.21. For the gamma-ray scan, the energy resolution is 37% FWHM, calculated from equation 3.1, where the values for the mean energy and standard deviation are taken from a Gaussian fit to the 140 keV peak. This result is probably due to the inefficiency in light collection for the geometry used. The same crystal coupled to a larger single anode PMT (2" circular EMI 9656) gave an 18% FWHM energy resolution when irradiated by the same Co^{57} gamma-ray source.

Figure 7.22 shows a two dimensional plot of the mean energy response \bar{E} at a fixed position of the fibre or the gamma-ray collimator (x_k^f, y_k^f) . For the LED scan at $d=1 \text{ mm}$, there are significant local variations. These are smoothed out for broader light distributions as in the LED scan at $d=7 \text{ mm}$. In this case, for the $18 \times 18 \text{ mm}^2$ region covered by the anodes the energy response is uniform to within $\pm 40\%$. For $d=1 \text{ mm}$ and $d=7 \text{ mm}$, it can be seen that, on average, there is an extended response along the y direction compared to the x direction.

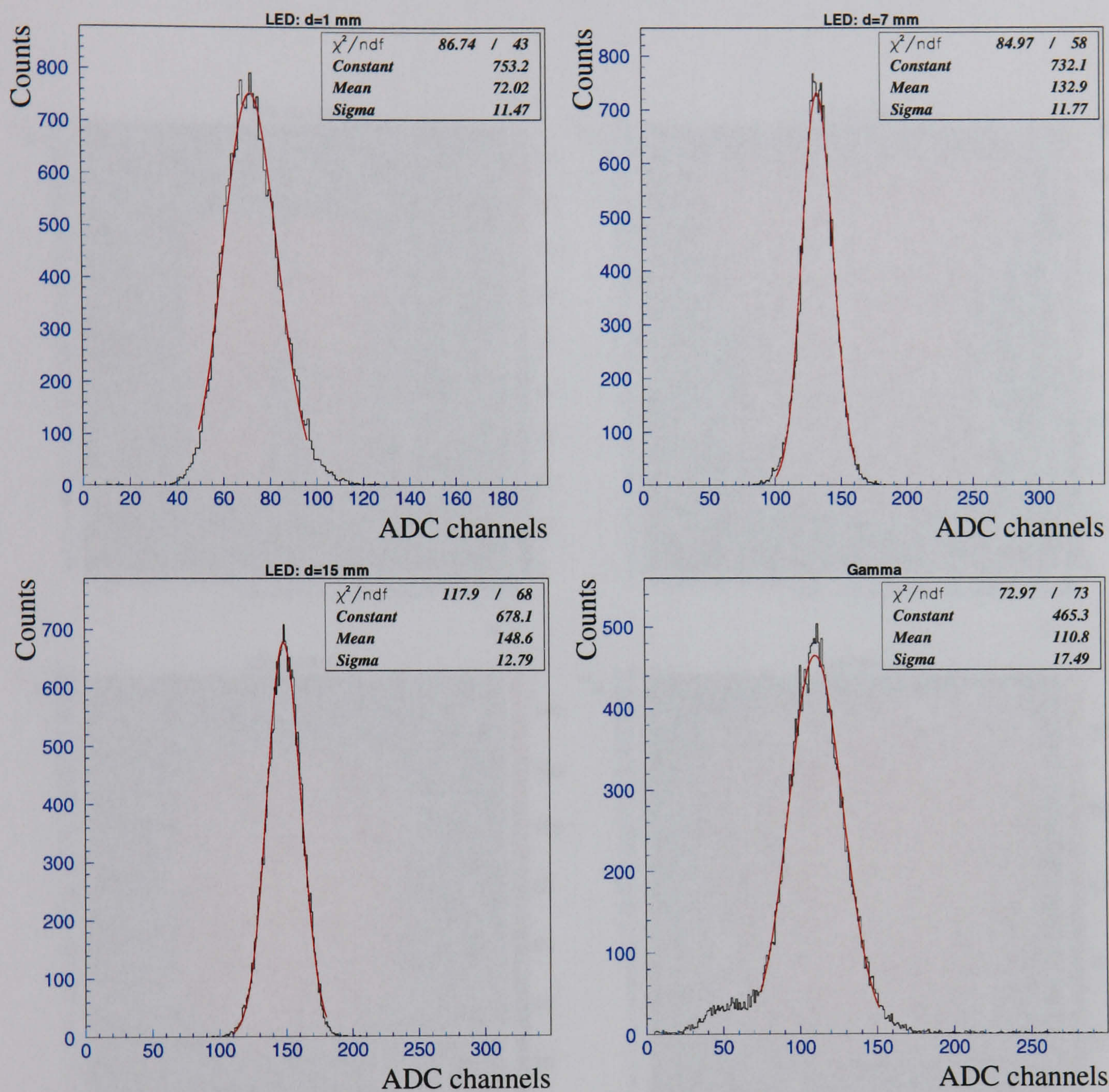


Figure 7.21: Pulse-height distributions for the energy signal for the LED scans and for the gamma-ray scan. Constant, Mean and Sigma are the parameters of the Gaussian distribution fitted to each pulse-height distribution. The energy resolution is calculated from $\frac{2.35\text{Sigma}}{\text{Mean}}$, where $2.35\text{Sigma} = \text{FWHM}$ for a Gaussian curve. The low tail peak observed for the gamma-ray scan distribution corresponds to the escape peaks of Cs and as well as to the characteristic K_α and K_β lines of the Pb collimator.

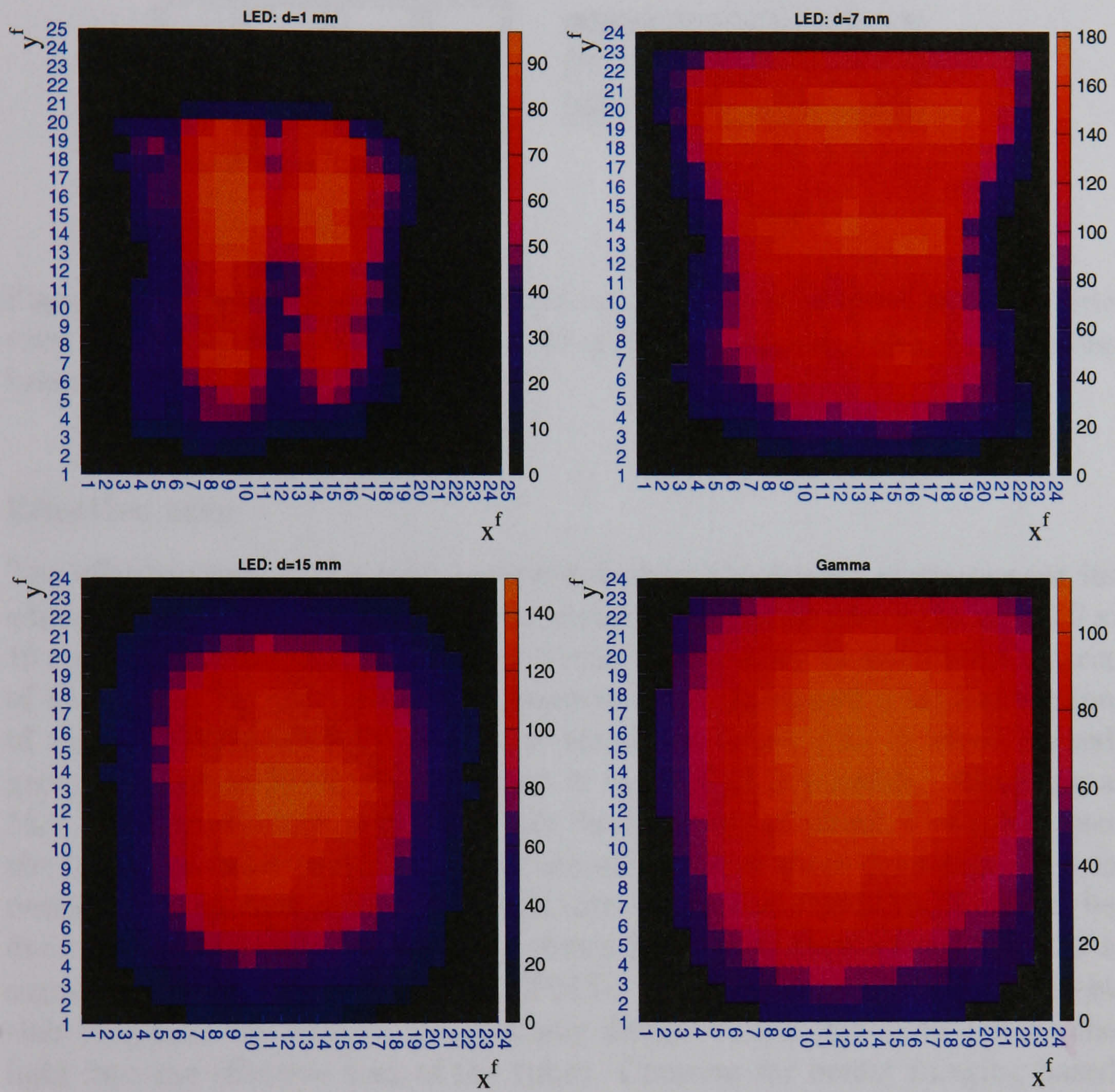


Figure 7.22: Mean energy \bar{E} as a function of the position of the fibre or the gamma-ray collimator (x_k^f, y_k^f) .

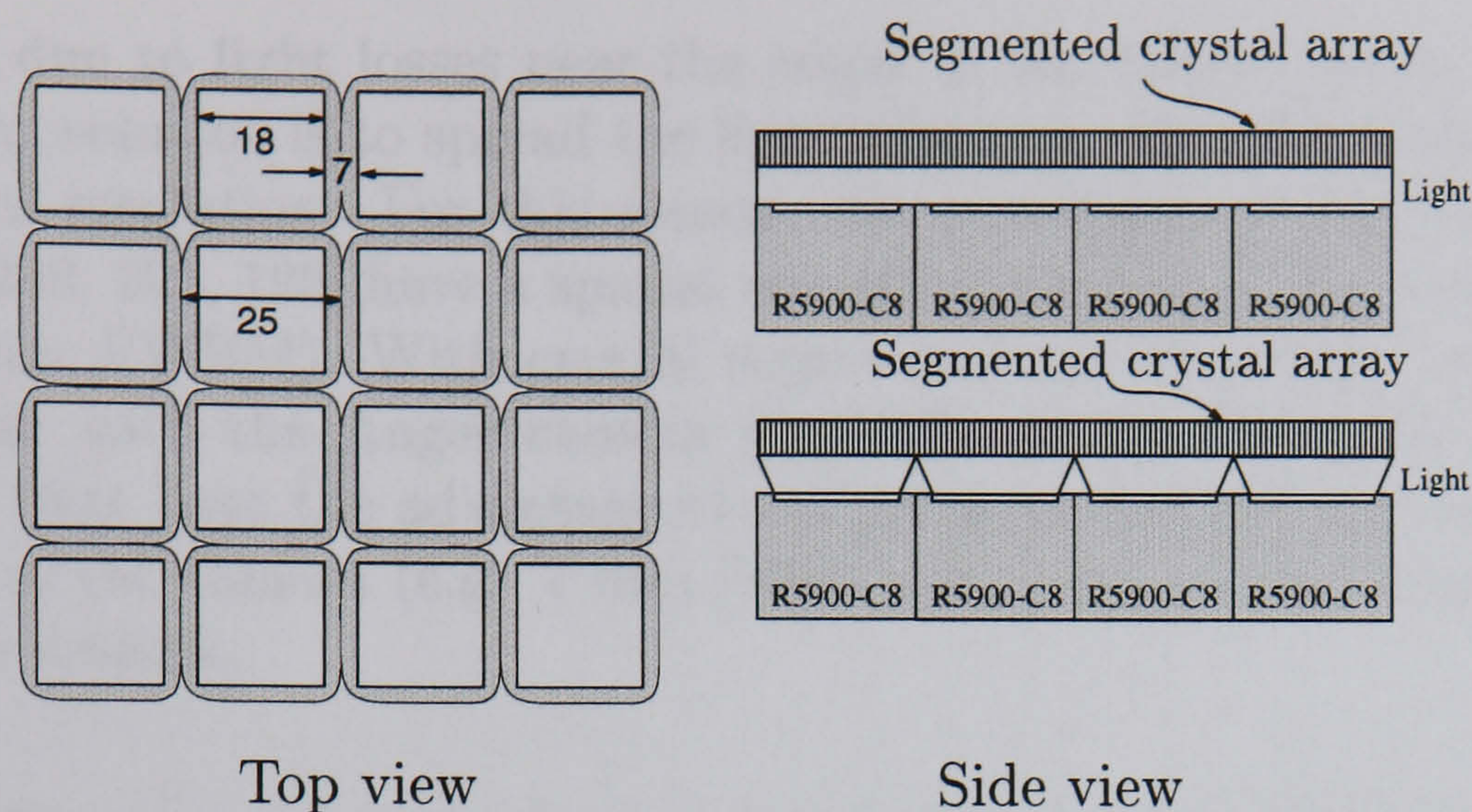


Figure 7.23: Schematic representation of an array of 4×4 C8s. The side view shows two possible techniques to allow imaging over the dead regions between PSPMTs.

Effective area

The effective area of the tube is determined by the poorer response near its edges. To build a gamma camera for breast imaging, an area of at least $10 \times 10 \text{ cm}^2$ is required, and, therefore, it would be necessary to assemble a matrix of 4×4 C8s. For this purpose, Hamamatsu has developed a similar version of the R5900-C8 without the flange shown in figure 7.1. A close packed geometry similar to the one depicted in figure 7.23 is possible. Assuming a $18 \times 18 \text{ mm}^2$ effective area, there are dead regions of about 7 mm between the tubes. In order to detect events occurring above these dead regions, it is necessary to spread or guide the light into the closest PSPMTs. This can be done by introducing light guides as shown in the side view where, between a segmented crystal array and the PSPMTs, one may introduce a transparent slab to spread the light or use specially designed light guides to convey the light into the effective area of the tubes. Cameras for breast imaging based on these concepts have been developed recently by other authors [200, 201] with scintillation pixels of $3 \times 3 \text{ mm}^2$ FWHM.

7.2.3 Discussion

The intrinsic properties of the R5900-C8 make it very promising for small gamma cameras with good spatial resolution. However, it is necessary to assemble a matrix of these tubes to obtain a camera with an adequate size for most nuclear medicine applications (e.g. breast imaging). This introduces

problems due to light losses near the edges of the tubes. As in the Anger camera the solution is to spread the light which, on the other hand, worsens the spatial resolution. For this reason, the prototypes developed by other authors [200, 201, 198] have a spatial resolution similar to the Anger camera (3 to 4 mm FWHM). With crystal segmentation, the energy resolution is worse than with the Anger camera (typically about 18 to 20% FWHM). However, they have the advantage of compactness and smaller dead area at the edge of the camera (e.g. 7 mm [200]) compared with at least 5 cm for the Anger camera.

7.3 Evaluation of the R5900-M16 PSPMT for use with Wavelength-Shifting Fibres

The Hamamatsu R5900-M16 (hereafter M16) has similar external dimensions to the C8. It has a borosilicate glass window and a bialkali photocathode with a wavelength of maximum response of 420 nm. According to the quantum efficiency curves in the M16 data sheet [202], the quantum efficiency at 500 nm is about 12%. The photocathode effective area is $17.5 \times 17.5 \text{ mm}^2$. The dynode structure is a 12 stage metal channel dynode which, according to the manufacturer, achieves a gain of about 3.3×10^6 at the recommended operation voltage (- 800 V), with the standard Hamamatsu linear voltage divider (section 7.3.2). The maximum operating voltage is rated at - 1000 V.

The anode structure is an array of 4×4 square solid pixels. Each anode pixel is $4.5 \times 4.5 \text{ mm}^2$ with a 0.5 mm spacing between adjacent anodes.

The individual segmented anode structure and the low transverse diffusion of the charge cloud provided by the metal channel dynode make this PSPMT very attractive for optical fibre readout. The aims of these tests are to assess the suitability of the M16 for the readout of low light level signals from 1 mm round wavelength-shifting fibres (WSF), used in the WSF gamma camera described in chapter 4. As discussed in section 4.4 the basic requirements for the WSF readout sensor in this application are good single electron resolution, low inter-pixel cross-talk and uniformity of response between different anodes. The evaluation that follows aims at characterising the M16 performance according to these parameters (it is also described in detail in ref. [203]).

7.3.1 Light source

Three M16s (tubes A, B and C) were tested with light pulses from a double clad, 1 mm round, blue-to-green WSF (Bicron BCF-91A). A blue emitting

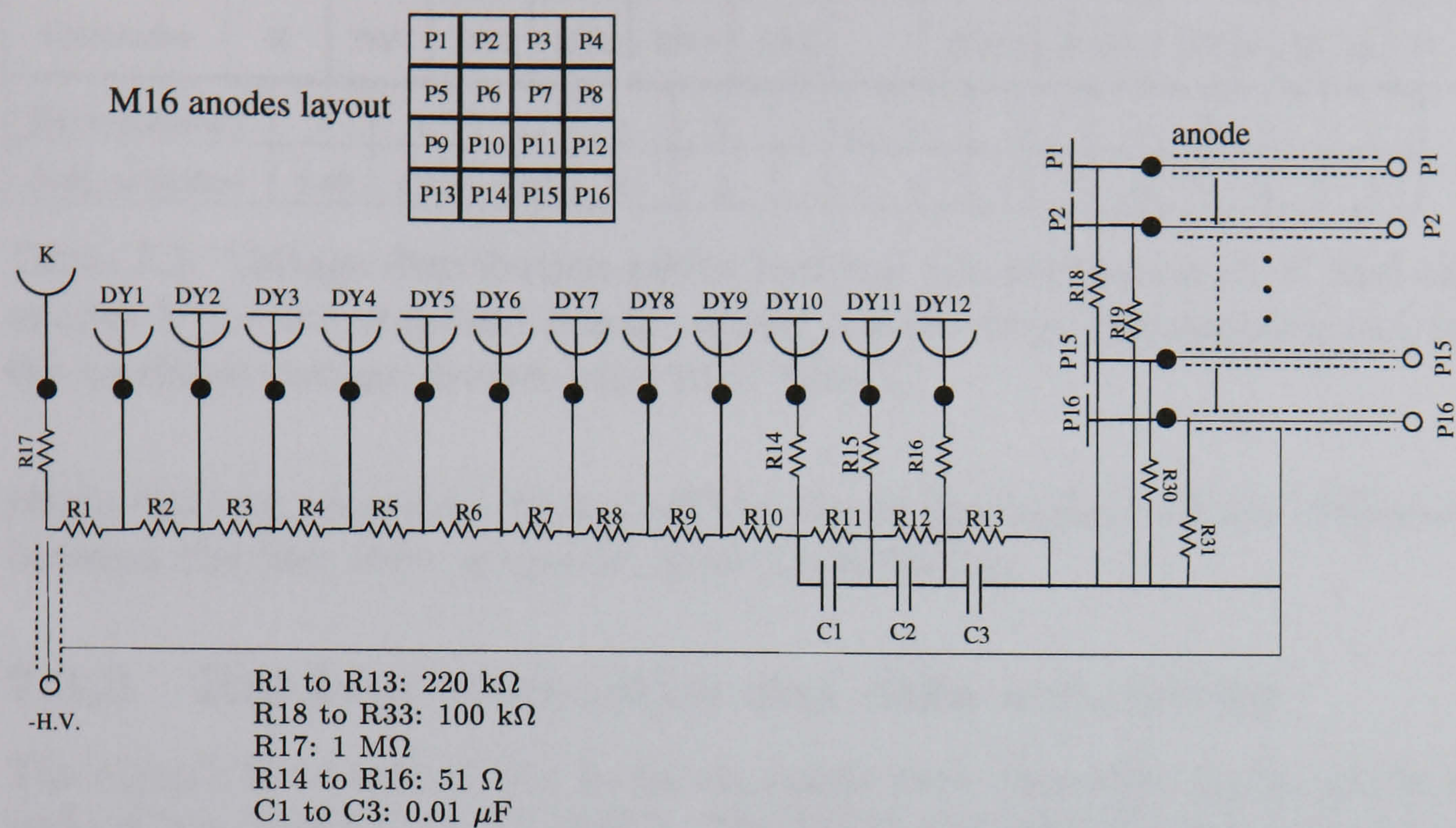


Figure 7.24: Schematic outline of the Hamamatsu linear voltage divider connected to the M16. DY1 to DY12 represent the 11 dynodes, K the photocathode, P1 to P16 the anodes and -H.V. the high voltage applied. Also shown is a layout of the anodes of the M16.

LED, with maximum emission at 400 nm was pulsed with an electronic pulser, model HP 215A from Hewlett Packard. The LED illuminated one end of the WSF (maximum emission at 500 nm) and the other end of the fibre was used to illuminate the PSPMT window. The pulser provides adjustable pulse width, pulse attenuation and frequency. The pulse rate was chosen to be 10 kHz and the width and attenuation were adjusted in order to produce an average number of photo-electrons between 1 and 3 on each tube. This was achieved with pulse widths between 8 and 12 ns.

7.3.2 Voltage divider circuit

Tubes A and B were encapsulated as single modules (Hamamatsu H6568) including a linear voltage divider, i.e., one which applies a constant voltage difference between consecutive dynodes. This voltage divider is similar to the one described above for the C8 and is depicted in figure 7.24.

Tube C was bought separately from its voltage divider. For comparison, it was tested both with the standard Hamamatsu linear voltage divider (figure 7.24) and with a modified version of it to try and optimize its single

Electrodes	K	DY1	DY2	DY3	DY4	DY5	...	DY10	DY11	DY12	DY13	P
Ratio-standard	1	1	1	1	1	1 ... 1		1	1	1	1	
Ratio-modified	2.43	2.43	2.43	1	1	1 ... 1		1	1	1	1	

Table 7.2: Voltage distribution ratios between the photocathode K and the anodes P for the standard linear voltage divider from Hamamatsu and for the modified voltage divider used with Tube C.

photo-electron response. This modified circuit has higher voltage difference between the first three stages as shown in table 7.2.

7.3.3 Readout electronics and data acquisition

The signals from each of the 16 anode pixels were connected to 16 inputs of two LeCroy 2249A CAMAC ADCs. The 2249A is 12-channel charge integrating ADC, with 10 bit resolution and a channel width of $w = 0.25 \text{ pC/channel}$. The ADC gate signal was provided by the pulser and was synchronised with the LED pulse. The CAMAC modules were controlled by a VME data acquisition system ⁴.

7.3.4 Data analysis for low light level measurements

For a given position (x_j^f, y_k^f) of the fibre at the photocathode of the M16, we are interested in calculating the number of photo-electrons collected and amplified by the dynode structure, the amplification gain and the cross-talk between anode pixels (signal sharing).

Assume that the number of photons hitting the photocathode obeys a Poisson distribution with mean m . The conversion of photons into electrons at the photocathode, with quantum efficiency QE, and the subsequent electron collection by the first dynode, with collection efficiency ε_c , can be described as binomial processes. Thus, the distribution of the number of photo-electrons collected by the first dynode is a convolution between these Poisson and binomial distributions which gives a Poisson distribution with mean $\mu = m\varepsilon_c\text{QE}$.

For a single photo-electron collected by the first dynode, the charge amplification process in the dynode structure produces a charge distribution which is usually well described by a Gaussian distribution with mean Q_1 and

⁴Thanks are due to Dr. Jenny Thomas from the Department of Physics and Astronomy, UCL, for help and advice in setting up the data acquisition system, as well as making available some PSPMTs for testing.

standard deviation σ_1 . The value of Q_1 is a measure of the mean gain \bar{G} of the charge multiplier and can be calculated from the charge distribution measured by the ADC for single photo-electron events. The relation between Q_1 and \bar{G} is

$$Q_1 = \frac{e\bar{G}}{w} \quad (7.6)$$

where e is the elementary electron charge, w the ADC channel width and Q_1 is therefore measured in number of ADC channels.

The width σ_1 of the single photo-electron peak, sometimes called the single electron resolution of the tube, can also be expressed as number of ADC channels.

The ideal response of the tube to more than one photo-electron can be described by a convolution between the Poisson distribution with mean μ and this Gaussian distribution, assuming that the amplification processes induced by each photo-electron are mutually independent.

This ideal response $R_{ideal}(x)$, where x represents the ADC channel, can therefore be expressed as

$$R_{ideal}(x) = \sum_{n=0}^{\infty} \frac{\mu^n e^{-\mu}}{n!} \frac{1}{\sigma_1 \sqrt{2\pi n}} e^{-\frac{(x-nQ_1)^2}{2n\sigma_1^2}}. \quad (7.7)$$

A more realistic response function has also to take into consideration the charge generated by noise from the electronics and from the tube. The former noise contribution (electronics) is responsible for a non-zero width of the pedestal defined as the pulse height distribution obtained when zero photoelectrons are released from the photocathode, and is usually associated with low charge processes (e.g. leakage current in amplifiers). With the electronic system used to read out the M16s the electronic noise is low since the charge is directly integrated in the ADC without an amplification stage, unless otherwise mentioned. Therefore, the pedestal signals are very narrow (1 channel wide) and this source of noise is not considered significant.

The latter noise contribution (from the tube) is related to probabilistic processes such as thermal-emission of photoelectrons by the photocathode or to events initiated by photoelectrons that are not collected by the first dynode but instead are collected by one of the following dynode stages and subsequently amplified with a lower and variable gain. These sources of noise can be represented by an exponential function. The thermal-emission component of this exponential noise was estimated by placing the tubes in

the dark, with no light signals present, and gating the ADC randomly. It was found that the total number of pulses above electronic pedestal in all the anodes was less than 0.5% of the total number of gate signals. The other components of the exponential noise are related to the light measurements and are therefore more difficult to measure. In what follows, this exponential component is not considered significant.

The ideal response in equation 7.7 is therefore assumed to be a good approximation of the charge distributions for the M16s. These charge distributions may be fitted by the function $R_{ideal}(x)$ to obtain the parameters μ , Q_1 and σ_1 which are the mean number of photo-electrons collected by the first dynode, the gain and the single electron resolution of the tube.

Another method of calculating μ and Q_1 is simply to count the number of events in the pedestal. Then, assuming again a Poisson distribution for the number of photoelectrons collected by the first dynode, μ is found by

$$\mu = -\ln \left(\frac{N_{zeros}}{N_{total}} \right) \quad (7.8)$$

where N_{zeros} is the number of events in the pedestal and N_{total} is the total number of events. The value of Q_1 is obtained by

$$Q_1 = \frac{\bar{x}}{\mu} \quad (7.9)$$

where \bar{x} is the mean ADC channel x for the charge distribution obtained.

The first method is hereafter referred to as FIT and the second as NZEROS. The FIT method uses the minimisation and error analysis package MINUIT⁵. The choice of method depends on the characteristic performance of a given tube. As described below, tube A has a very good single electron resolution and the FIT method gives very consistent results. For this tube, both methods were applied and compared and the results for μ and Q_1 were proven to be consistent to within $\pm 5\%$. For tubes B and C, only the NZEROS method was used.

7.3.5 Optimisation of PSPMT response

The response of the M16s depends on the high voltage (-H.V.) applied. In order to choose the optimum -H.V. value for each tube, the fibre was positioned

⁵MINUIT - function minimization and error analysis, CERN program library, CERN Geneva, Switzerland.

above one anode and the pulse-height distributions of charge were analysed. The response of all the other anodes was consistent with the results shown, as will be seen in detail in section 7.3.6.

The details of the measurements presented in this section are shown in appendix C. A summary of the most significant results follows.

Tube A

For HV=-950 V and HV=-900 V the single photo-electron peak was clearly separated from the pedestal and the peak corresponding to two photo-electrons is also visible (see figure C.1). All the results shown for tube A in this chapter are taken at -950 V. The gain \bar{G} of the tube at HV=-950 V is about 10 ADC channels, which corresponds to about 1×10^7 .

The response of tube A was compared to that of a standard single anode photomultiplier, EMI 9124 from Electron Tubes, with a nominal quantum efficiency of 20% at 500 nm, when illuminated with the same light pulses (see figure C.2). The mean number of photoelectrons found by the NZEROS method is 2.7 and 1.9 for the EMI 9124 and the M16 respectively. The difference is consistent with the two photocathodes having quantum efficiency of 20% and 13% respectively at 500 nm as specified.

Tube B

For tube B the best separation between the single photo-electron peak and the pedestal is obtained at -HV=-1000 V (see figure C.3). All the results shown for this tube in this chapter were taken at this -HV setting.

Tube C

A comparison between the standard Hamamatsu voltage divider and the modified voltage divider (section 7.3.2) was done by measuring the response of tube C with both dividers (see figures C.4 and C.6).

A much better separation between the single photo-electron peak and the pedestal was obtained with the modified voltage divider, demonstrating the optimization provided by this divider for single photo-electron detection. All the results for tube C shown in this chapter were taken at -HV = -1000 V and with the modified voltage divider.

7.3.6 Results from scans

A complete evaluation of the response of tubes A, B and C was carried out by scanning the entrance window with the WSF pulsed by the blue LED at a

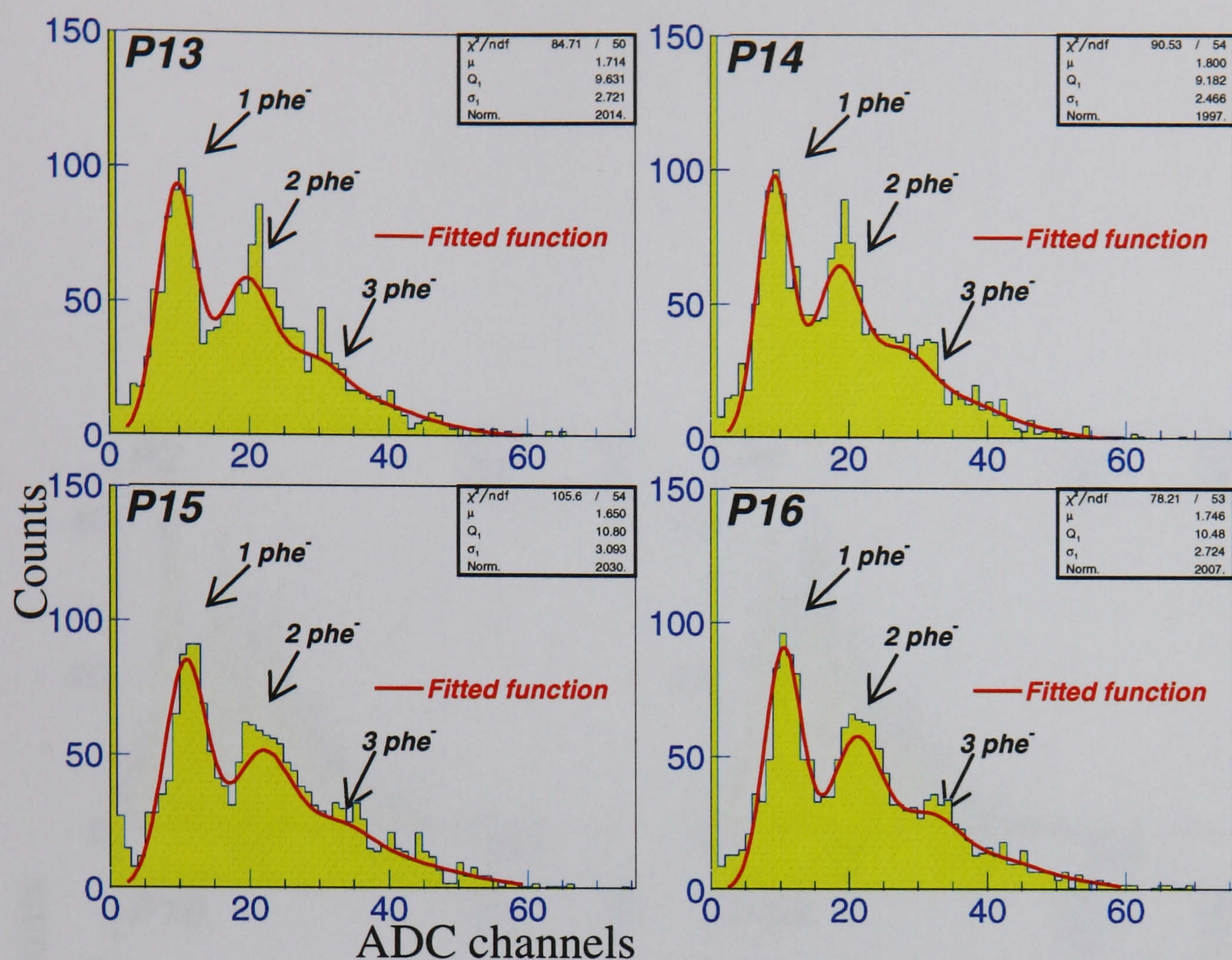


Figure 7.25: Typical charge distributions for 4 anodes of tube A with the same pulse from the fibre.

distance of less than 1 mm from the tube window. The scan step was 1 mm for tubes A and B and 0.5 mm for tube C. As mentioned above, the high voltage settings were -950 V for tube A and -1000 V for tubes B and C.

The number of events acquired at each fibre position (x_j^f, y_k^f) was 2,000 for tubes A and B and 1,000 for tube C. The pulser settings were altered between scans and therefore no absolute comparison should be made between the responses of the tubes.

Examples of the charge distributions obtained for four M16 anodes are shown in figures 7.25, 7.26 and 7.27. Each plot corresponds to the response of a given anode during the scan when the fibre is in the centre of the pixel. For tube A the response is fitted with equation 7.7 to find the values of μ , Q_1 and σ_1 with the FIT method. These plots demonstrate the similarity between the anode responses within a given tube.

Figure 7.28 shows the mean value in ADC channels of the charge distri-

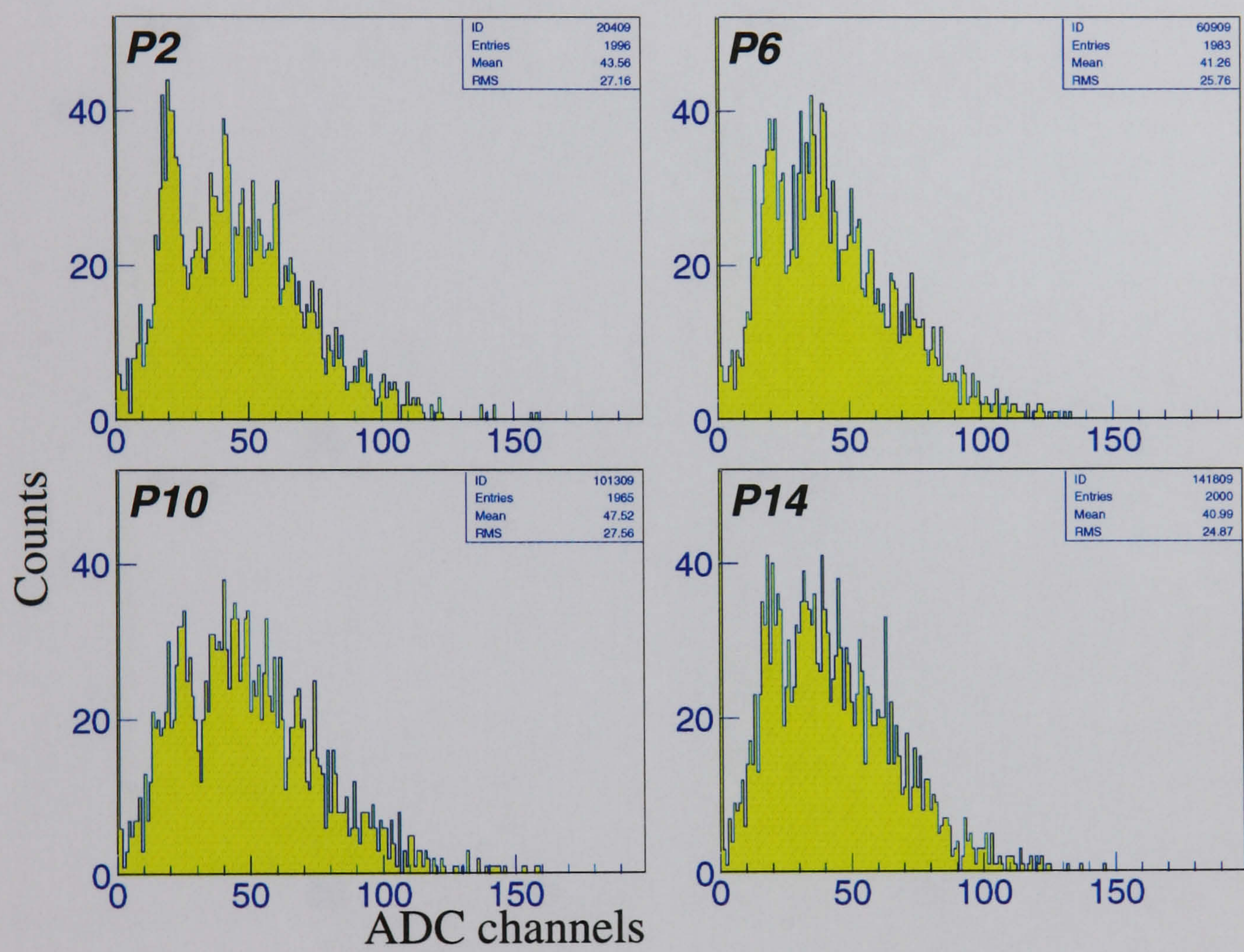


Figure 7.26: Typical charge distributions for 4 anodes of tube B.

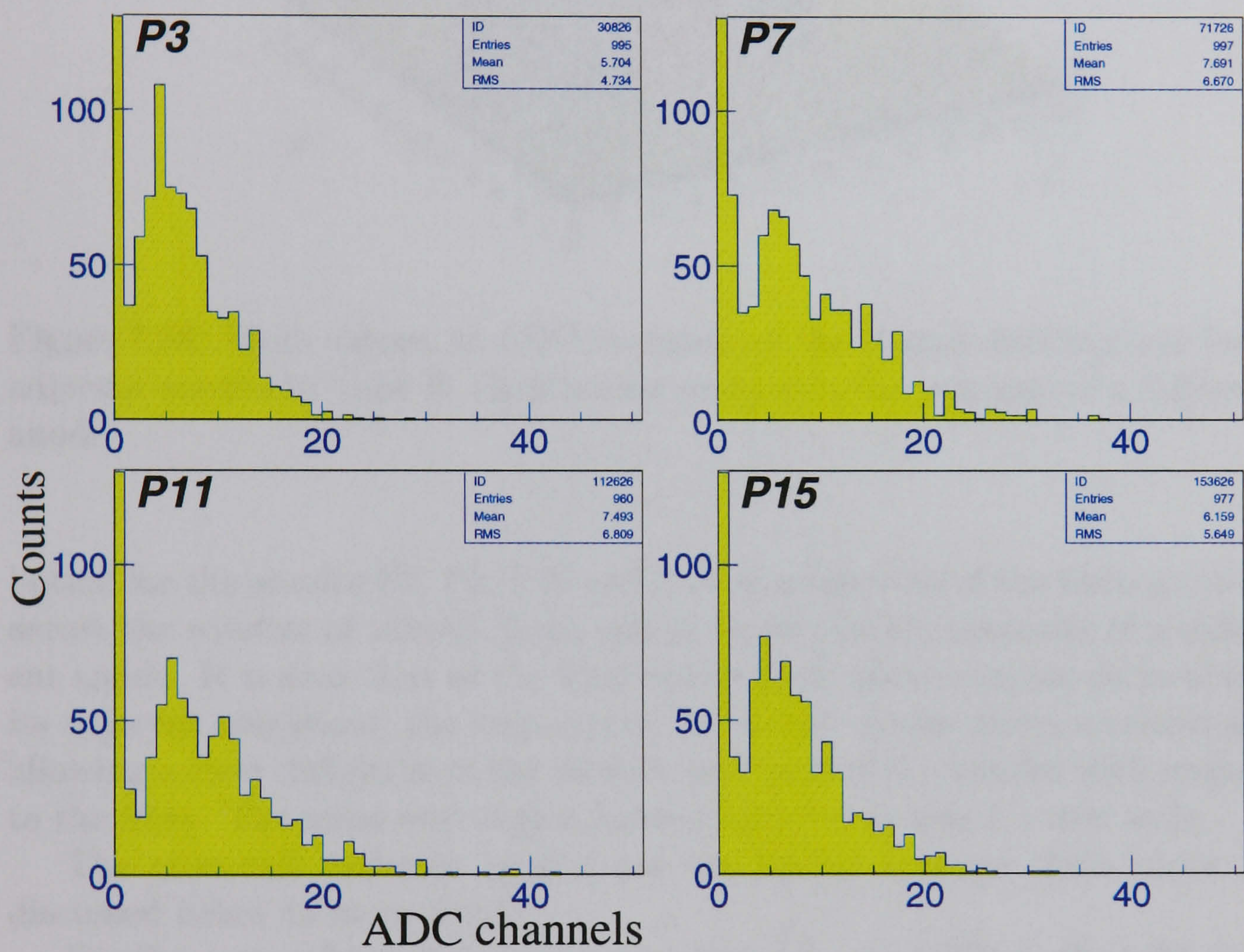


Figure 7.27: Typical charge distributions for 4 anodes of tube C.

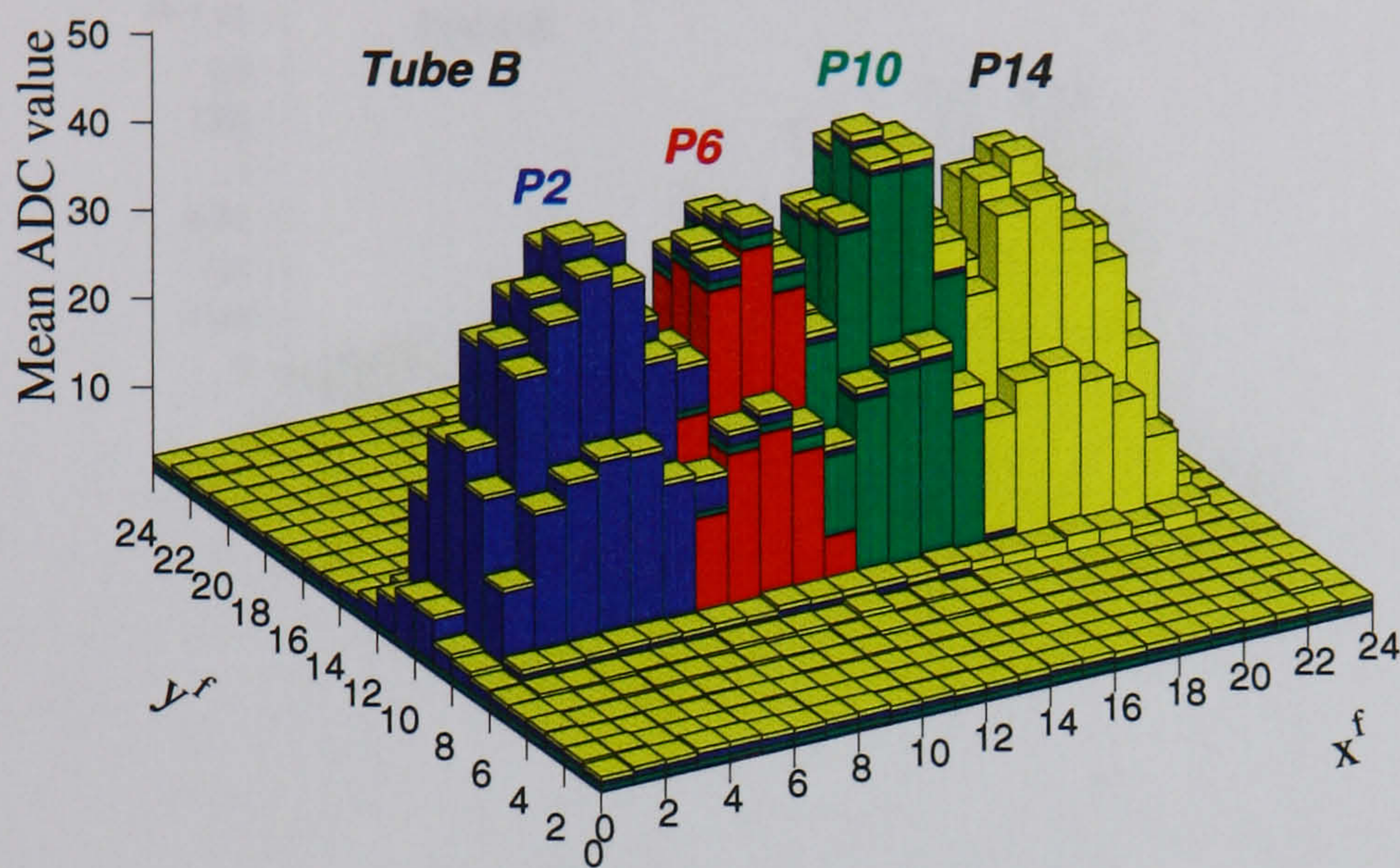


Figure 7.28: Mean values, in ADC channels, of the charge distributions for 4 adjacent anodes in tube B. Each colour represents the response of a different anode.

bution for the anodes P2, P6, P10 and P14 as a function of the fibre position across the window of tube-B. Each colour represents the response of a different anode. It is seen that as the fibre moves from above one anode to above its adjacent neighbour, the response of the former anode drops immediately allowing a clear definition of the relative positions of the anodes with respect to the fibre. The cross-over region between anodes is about 1 mm wide.

The cross-talk between anodes can be defined through these plots, as discussed below in more detail.

For the narrow light distributions produced by the WSF at the tube window, each M16 can therefore be considered as 16 separate PMTs. Thus, in analysing the data from the scans, the calculation of the number of photoelectrons described in section 7.3.4 is done for each individual anode separately.

The number of photo-electrons μ for the response of anodes P13, P14, P15 and P16 of tube A as a function of the fibre position is shown in figure 7.29, where the FIT method is used. Similar plots are shown in the same figure for anodes P2, P6, P10 and P14 of tube B and P3, P7, P11 and P15 of tube C. For these tubes μ is calculated with the NZEROS method.

After a careful inspection of the response of all the anodes in all three tubes, the relative position of the 16 anodes in each tube is established and a

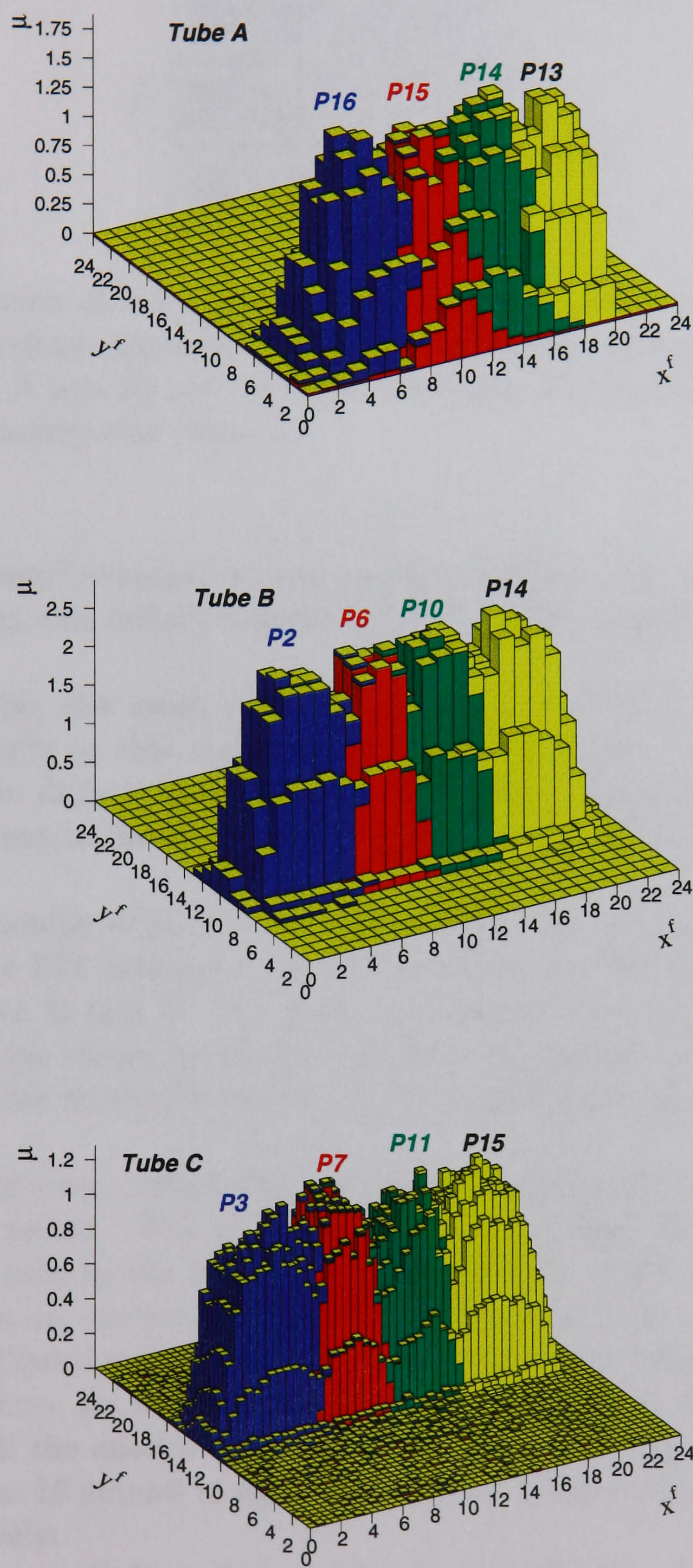


Figure 7.29: Number of photo-electrons for 4 adjacent anodes in a) tube A, b) tube B and c) tube C. Each colour represents the response of a different anode.

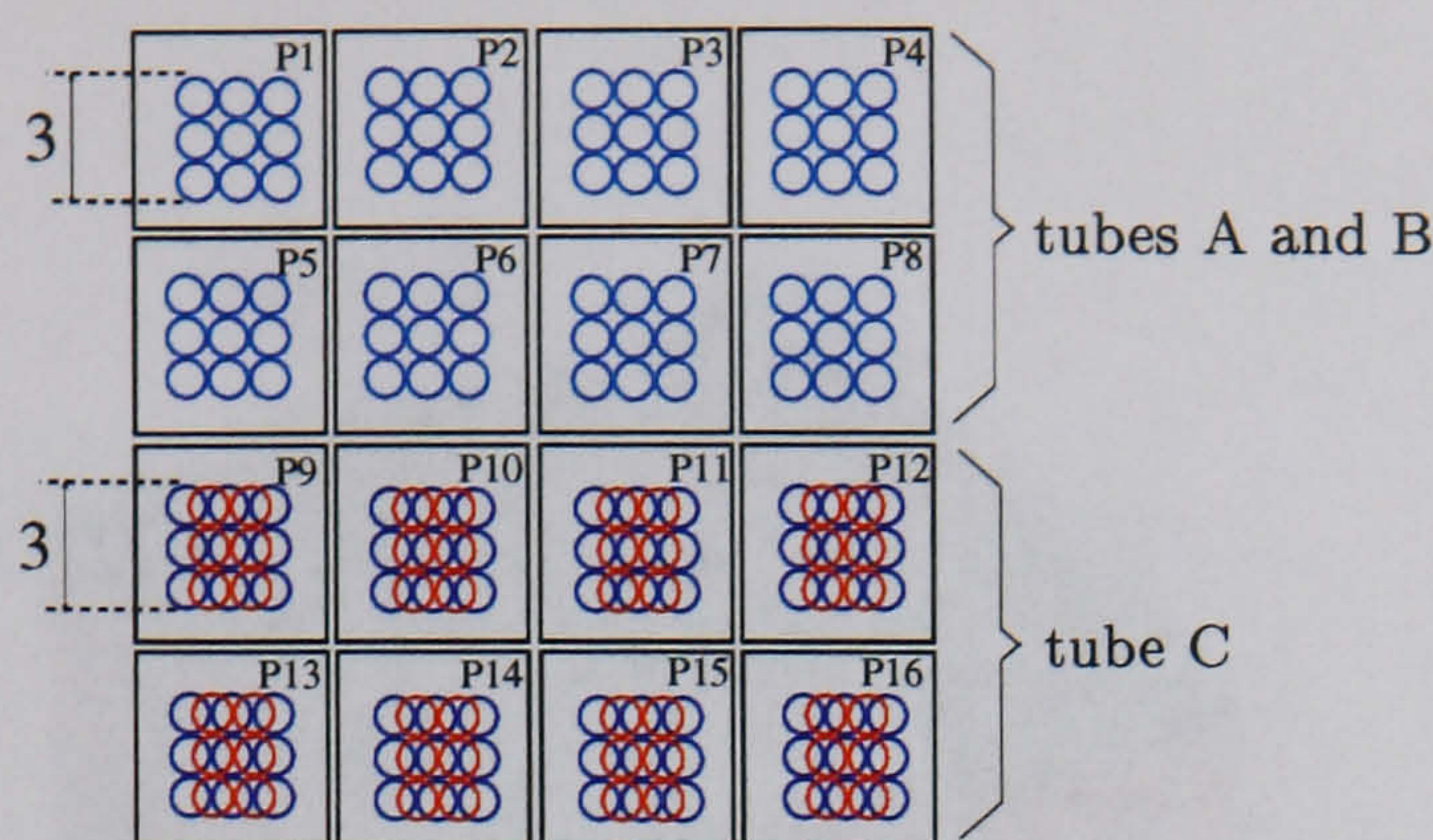


Figure 7.30: Matrix of $3 \times 3 \text{ mm}^2$ scan regions centered at each anode. The first 8 anode positions represent the pattern of the 9 points at the 1 mm scan step size (tubes A and B) and the last 8 positions represent the 25 points at the 0.5 mm scan step size (tube C).

region of $3 \times 3 \text{ mm}^2$ centered in each anode is defined. For scan step sizes of 0.5 mm or 1 mm this defines matrices of 25 or 9 fibre positions respectively (figure 7.30).

For each tube, the mean response of a given anode is obtained by averaging the results in this matrix of $3 \times 3 \text{ mm}^2$ regions. A corresponding rms value is also defined with the set of 9 (tubes A and B) or 25 (tube C) points in each matrix, which is a measure of the uniformity of a given anode (rms_P).

The mean number of photo-electrons obtained for each anode is shown in figure 7.31. The FIT method is used for tube A and the NZEROS method is used for tubes B and C. The green shading at the top of each column represents the rms values for the sets of scanning points in each matrix.

The results for anode P1 of tube C are not available due to a bad connection.

The values of rms_P within one anode are less than 10% for all the anodes in the 3 M16s tested. The rms variation of the mean response of the 16 anodes in each tube is 3%, 5% and 30% for tubes A, B and C respectively.

Similar plots are shown in figure 7.32 for the gain \bar{G} as a function of the fibre position. Equation 7.6 is used to obtain \bar{G} from the values of Q_1 . Again, the values of rms_P on the 9 or 25 \bar{G} measurements in each anode are less than 10% for all the anodes in the 3 M16s tested. The rms variation of the mean gain of the 16 anodes in each tube is 18%, 9% and 29% for tubes A, B and C respectively.

The total cross-talk for a given anode pixel is defined as the ratio between the number of photo-electrons μ in that pixel and the sum of μ in all the other

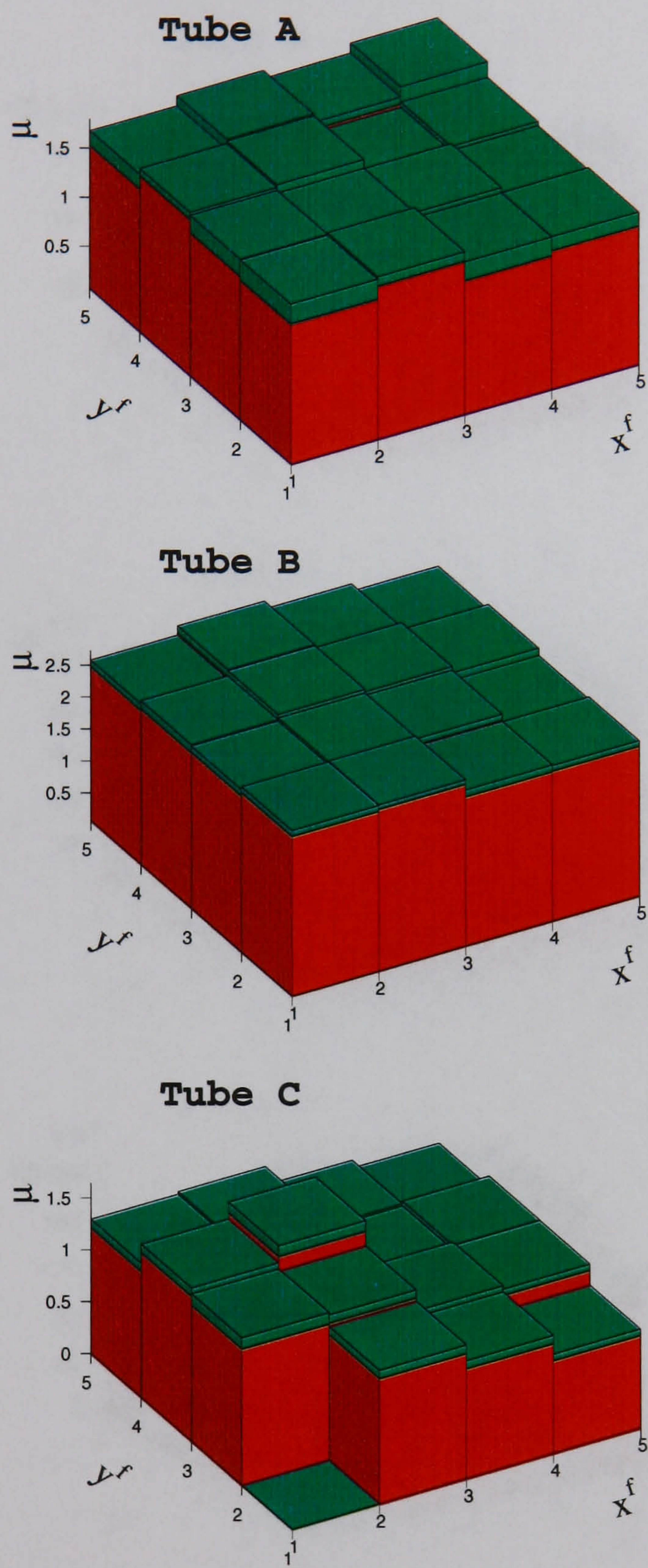


Figure 7.31: Mean number of photo-electrons per anode for the three M16s using the same input pulse. The green shading at the top of each column represents the rms of the 9 (or 25) measurements at each anode position.

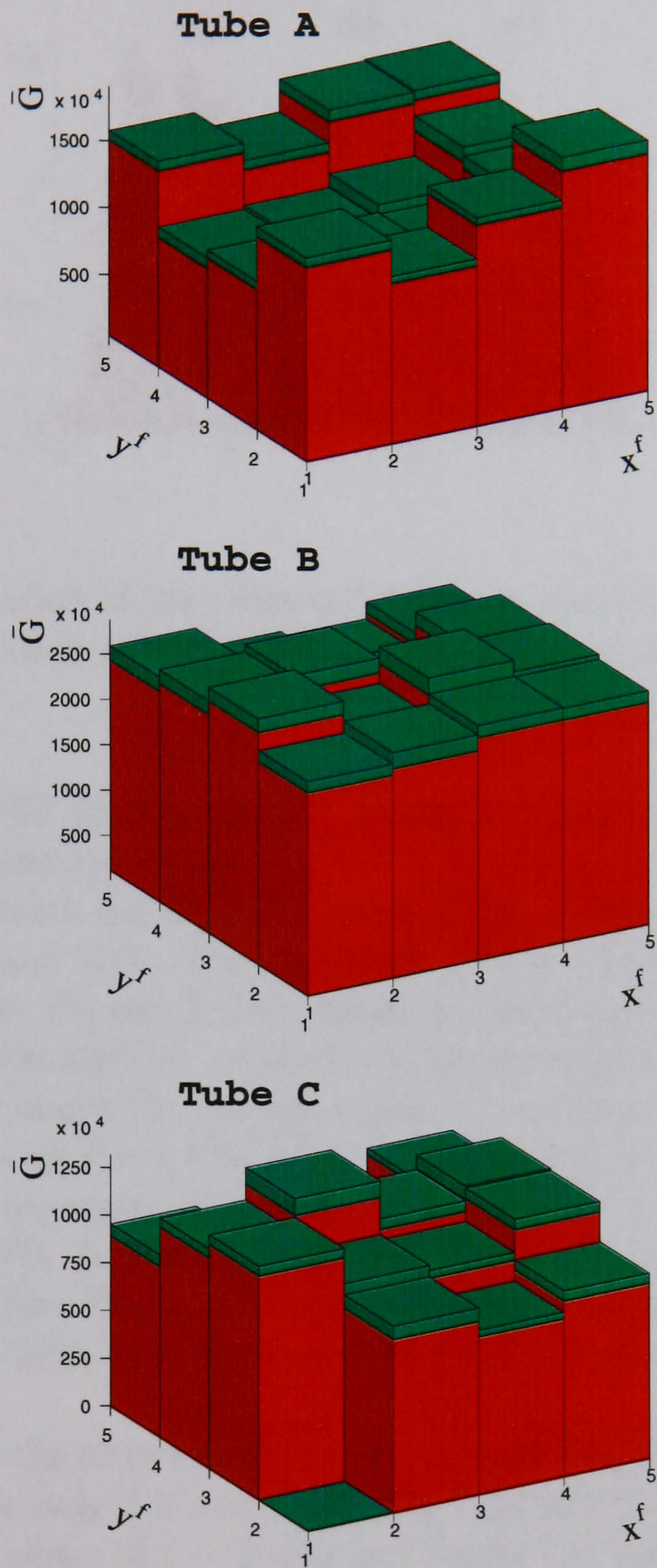


Figure 7.32: Gain \bar{G} per anode for the three M16s calculated from equation 7.6. The green shading at the top of each column represents the rms of the 9 (or 25) measurements at each anode position.

7.3.7 Discussion

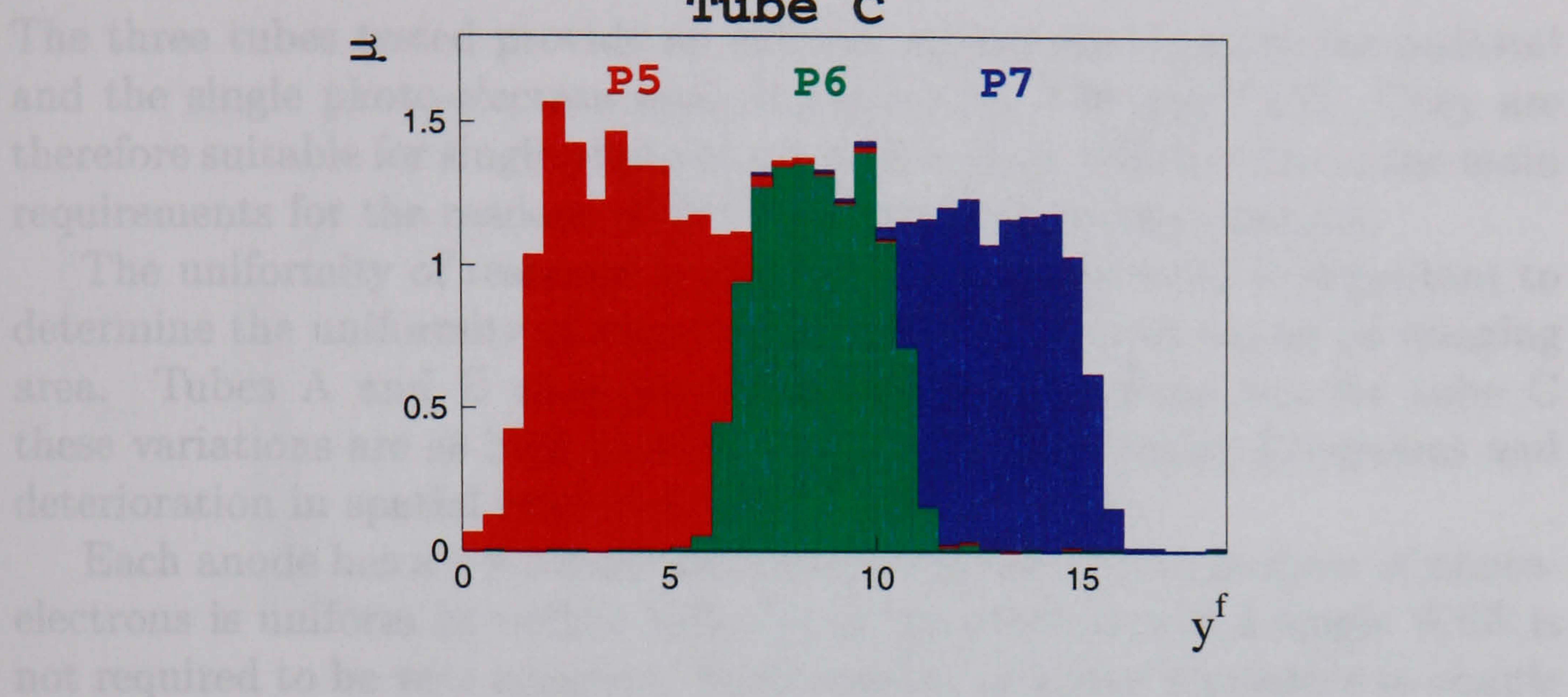


Figure 7.33: Illustration of the cross-talk between nearest neighbours for line x_{18}^f across tube C. Each colour represents the response of a different anode.

pixels, when the WSF fibre is directly above that particular anode pixel. It is expressed in percentage values.

The total cross-talk for all the anodes of the 3 tubes tested was found to be between 3% and 10%. The cross-talk from a single nearest neighbour is typically less than 1% and from a diagonal neighbour it is typically 0.5%. Figure 7.29 illustrates the low cross-talk between nearest neighbour pixels if the fibre is located above the central region of an anode. For better visualisation, a profile along the x line x_{18}^f is shown in figure 7.33 for the case of tube C, where the responses of anodes P7 and P5 are super-imposed on the response of anode P6. It is seen that, when the fibre is at the center of P6, the contributions from P5 and P7 are very small compared to that of P6. Likewise, when the fibre is at the center of P5 or P7, the contribution of P6 is very small.

As stated above the fibre was at less than 1 mm from the PSPMT window. Since the window is only 1.5 mm thick, the light distribution over the photocathode is of the order of $1 \sim 2$ mm (see figure 7.5) which is much smaller than the size of the anodes. The low cross talk observed is also a demonstration of the very low transverse diffusion of the charge cloud through the metal channel dynode stages.

7.3.7 Discussion

The three tubes tested provide an efficient separation between the pedestal and the single photo-electron peak (figures 7.25, 7.26 and 7.27). They are therefore suitable for single photo-electron detection, which is one of the main requirements for the readout of WSFs in the WSF gamma camera.

The uniformity of response in number of photoelectrons is important to determine the uniformity of response of the WSF camera across its imaging area. Tubes A and B show small inter-anode variations but for tube C these variations are as high as 30%, which may cause image distortions and deterioration in spatial resolution of the WSF camera.

Each anode has a $3 \times 3 \text{ mm}^2$ area where the response in number of photoelectrons is uniform to within 10%. Thus the alignment of a single WSF is not required to be very accurate. Furthermore, it makes it possible to couple more than one WSF to each anode (up to 9) to multiplex the WSF readout and therefore simplify and reduce the cost of the whole readout system.

The requirements for gain uniformity are not as important since it may be corrected by using variable gain amplifiers or through software.

The cross-talk between pixels is low and therefore an M16 can in practice be treated as 16 independent PMTs. It is therefore expected that a system based on M16s might behave according to the predictions made in the previous chapter, where a WSF gamma camera based on individual PMTs is simulated.

The major disadvantage of the M16 is its relatively low quantum efficiency of only $\sim 13\%$ at 500 nm. In all other aspects it is a suitable choice for the readout of the WSF gamma camera.

7.4 Preliminary investigation of an R5900-M64 PSPMT

The Hamamatsu R5900-M64 (M64) has very similar physical characteristics to the M16 described above. One of the main differences is the anode pattern. The M64 has an 8×8 individual anode array, each with an area of $2 \times 2 \text{ mm}^2$ and separated by a 0.25 mm gap (anodes P1 to P64). The recommended operating voltage is also - 800 V (maximum of - 1000 V) at which a gain of 3×10^5 is obtained, using the Hamamatsu voltage divider for this tube. The voltage distribution of this non-linear divider is shown in table 7.3.

The tests on an M64 were carried out using the same electronic readout system and the same LED-pulsed WSF described above for the M16 evaluation. The fibre was positioned to give the best response on anode P5 (at

Electrodes	K	DY1	DY2	DY3	DY4	DY5	...	DY9	DY10	DY11	DY12	P
Ratio	3	3	3	1	1	1 ... 1		1	1	2	5	

Table 7.3: Voltage distribution ratio for the Hamamatsu M64.

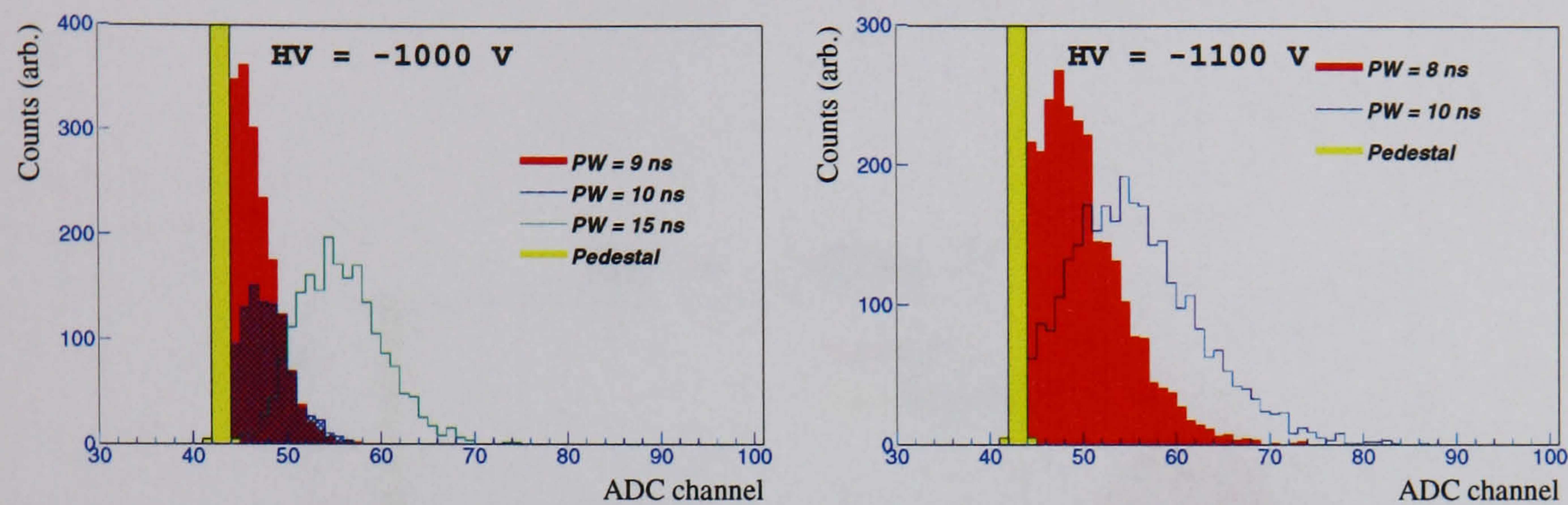


Figure 7.34: Charge distributions for anode P5 of the M64 at low light levels. PW is the width of the pulse across the LED.

less than 1 mm from the window) and basic measurements of the charge distributions were taken for different - HV settings and different light levels.

Figure 7.34 shows the charge distributions obtained for anode P5 for two -HV settings. Each plot shows the distributions for different light levels (PW is the width of the pulse across the LED).

Note that for low light levels, the signal is not clearly separated from the pedestal, even at a voltage -HV = 1100 V which exceeds the maximum recommended voltage for the tube. The M64 is found to have a lower gain compared to the M16 which agrees with the manufacturer’s specifications.

Other authors [204] have used a modified voltage divider, similar to the one described in section 7.3.2, and obtained an excellent separation between the single photoelectron peak and the pedestal. They were able to visualise the peaks corresponding to up to three photoelectrons, in a very similar way to the plots shown in figure 7.25 for the M16-A tube.

Figure 7.35 shows the response of anode P5 for higher light levels. It also shows the corresponding responses of the nearest neighbour anodes P4 and P6 to illustrate the very small inter-pixel cross-talk of the M64.

Due to the small area of each anode, the size of the light spot at the photocathode should be of the order of the anode size. The fact that the M64 exhibits such a low cross-talk is another confirmation of the low transverse diffusion of the electronic charge through the metal channel dynode stages. From this point of view the M64 is a very attractive choice for the readout of

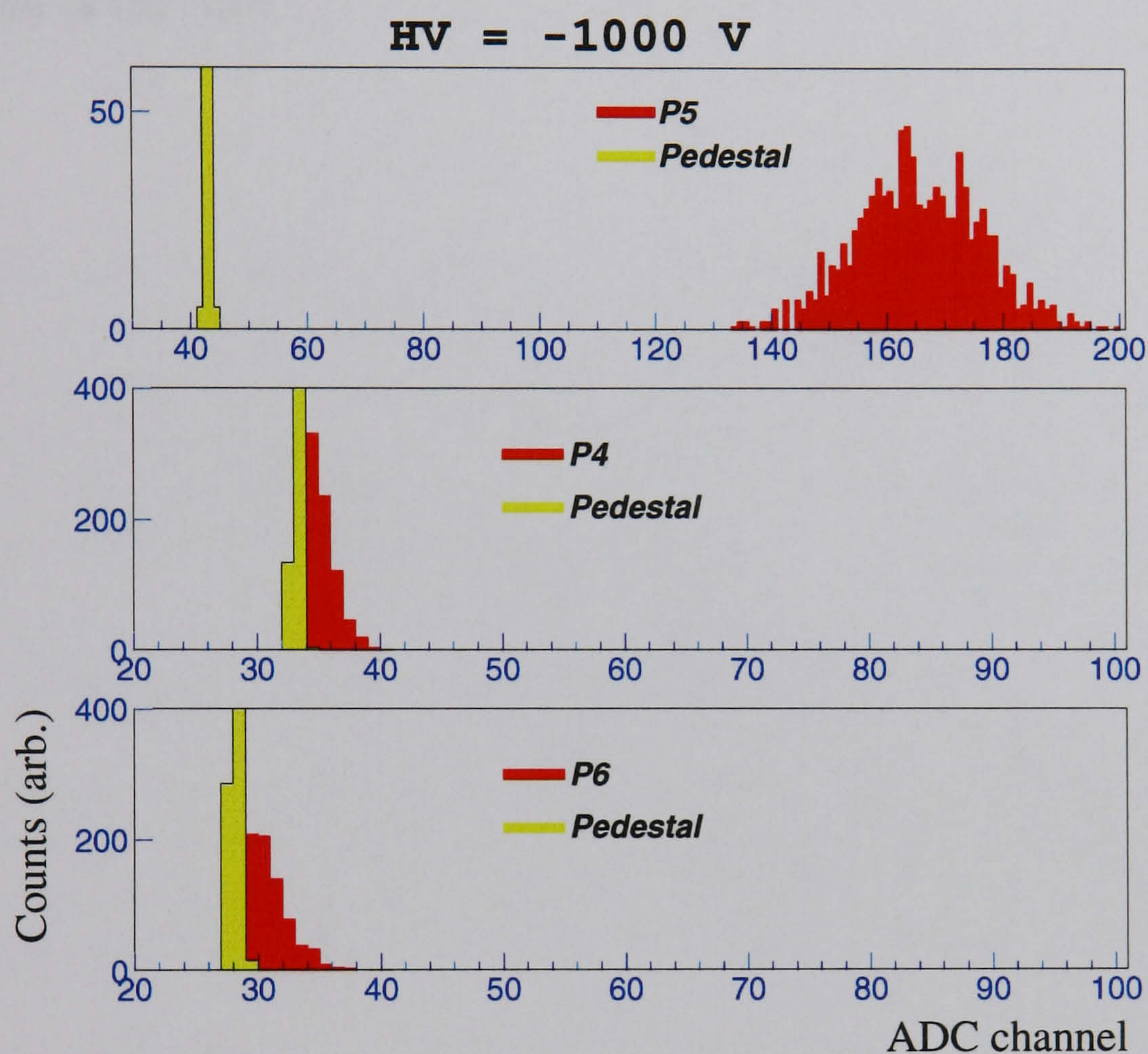


Figure 7.35: Charge distributions for the adjacent anodes P4, P5 and P6 of the M64, with the fibre placed to give the best response on anode P5. The pedestals are obtained from another independent measurement.

a large number (64) 1 mm diameter fibres, acting almost as 64 independent PMTs.

These preliminary studies, together with recent results from other authors, show that the M64 is an excellent candidate for the readout of the WSF gamma camera. It has the same dimensions as the M16 but provides four times more readout channels at approximately the same cost. The low transverse diffusion of charge of the metal channel dynodes provides low cross talk between anodes allowing an efficient one-to-one mapping of 64 WSFs to the anodes of the M64.

Chapter 8

WSF gamma camera prototype

The results in the previous chapters indicate that the WSF gamma camera design is very promising for nuclear medicine imaging. To confirm this, a WSF gamma camera prototype was built, based on the conceptual diagram shown in figure 4.1, as previously reported in ref. [205]. The imaging characteristics of the prototype were evaluated, with particular focus on spatial resolution, energy resolution, detection efficiency and uniformity of response.

8.1 Description of the prototype

The prototype can be divided into 5 main components: i) the scintillation crystals, ii) the WSFs, iii) the photo-detectors for WSF readout, iv) the photo-detectors for the readout of the energy signal and v) the readout electronics and data acquisition software.

8.1.1 Scintillation crystals

The two CsI(Na) slabs used in the experiments described in chapter 5 were used for the WSF gamma camera prototype. The crystals, manufactured by Hilger Crystals¹, had a $128 \times 128 \text{ mm}^2$ area and different thickness of 3 mm and 5 mm.

For comparison, two other scintillation crystals were evaluated: a $120 \times 120 \text{ mm}^2$, 4 mm thick CsI(Na) crystal manufactured by Bicron Corp.² and a $52 \times 52 \text{ mm}^2$, 5 mm thick NaI(Tl) crystal from Hilger Crystals. The NaI(Tl) crystal was encapsulated, to protect from moisture, between two $800 \text{ }\mu\text{m}$ glass sheets. These two scintillators were mainly used to compare the light

¹Hilger Crystals, Westwood, Margate, Kent, CT9 4JL, UK.

²Bicron, 12345 Kinsman Road, Newbury, Ohio, 44065-9677, USA.

output and energy resolution of the crystals directly coupled to a PMT, without WSFs (see appendix B). However, a preliminary experiment was also carried out with the WSFs coupled to the NaI(Tl) crystal to compare with the CsI(Na) based WSF camera prototypes. All the details and results of this evaluation are presented in appendix E.

Figure D.1 in appendix D is a photograph of the four scintillators.

8.1.2 Wavelength-shifting fibres

The fibres used were 1 mm diameter Bicon BCF-91A, blue-to-green WSFs (see table 4.1 for details of fibre properties).

A total of 64 fibres were cut in 30 cm long pieces, both ends polished and one end aluminised until it showed total opacity under microscope inspection³. The 64 fibres were not sufficient to cover the entire 128×128 mm². However, it allowed testing of the intrinsic imaging characteristics of the camera over a smaller area, using two of the previously tested Hamamatsu R5900-M16 position sensitive photomultiplier tubes.

To cover the remaining area of the crystal there was a second set of 192 fibres, each cut in 13 to 15 cm long pieces. The ends of these fibres were neither polished nor aluminised since they were not used for imaging. Their presence was important to test the energy resolution of the WSF camera in a realistic setup, where all the light from the crystal passes through a layer of WSFs.

8.1.3 Photo-detectors for WSF readout

Two R5900-M16 Hamamatsu PSPMTs were used to read out the signals from the fibres. An evaluation of both tubes is presented in section 7.3. Referring to the naming convention in that section, the tubes used are tubes B and C. Tube M16-B was encapsulated in a standard Hamamatsu module with a linear voltage divider. Tube M16-C was connected to a customized voltage divider which optimized the single photo-electron response as described in section 7.3.

These two M16s provided a total of 32 independent WSF readout channels. For each CsI(Na) crystal used in the prototype (3 and 5 mm thick), two different configurations were tested: i) one WSF coupled to each M16 anode and ii) two WSFs coupled to each M16 anode.

In all cases, the x direction was measured by the bottom layer of WSFs, i.e., the WSFs between the crystal and the E-PMTs (X WSFs), which were

³Thanks are due to Mr. Derek Thomas, Department of Physics and Astronomy, UCL, for aluminising the fibres.

read out by tube B, whereas tube C read out the top layer of WSFs (Y WSFs).

8.1.4 Photo-detectors for the energy signal readout

A 2×2 array of square PMTs was used to collect the energy signal (E-PMTs). The E-PMTs were manufactured by Photonis, Imaging Sensors⁴ (model X3392B). They had a 76×76 mm² entrance window with a 72×72 mm² photocathode area, and were closely packed to optimize light collection. According to the manufacturer, their bialkali photocathode had a quantum efficiency of $\approx 30\%$ and 20% for 420 and 500 nm respectively. Using the appropriate Photonis voltage divider (model VD282K), the 8-stage box-and-linear dynode structure provided a gain of $\approx 2.5 \times 10^5$ at an operating voltage of -1000 V. Unless otherwise mentioned, the four tubes were operated at -1000 V.

The 2×2 matrix of E-PMTs (figure D.2 in appendix D) was close-packed and coupled to a 5 mm thick perspex slab (*energy light-spreader*) with silicon gel.

8.1.5 Readout electronics and data acquisition software

Figure 8.1 shows a schematic representation of the electronics readout system. Its building blocks are a set of custom built amplifier boards⁵, two 16-channel ADC boards for the PCI bus and the PC-based data acquisition software.

Amplifier Boards

The amplifier boards contained several channels of signal shaping and amplification. There were two basic types of channels depending on the PMT being read out, the R5900-M16 or the E-PMT.

The basic structure of each type of channel is shown in figure D.3 in appendix D. The output of each channel was connected to an ADC input channel for digitisation.

The four E-PMT channels were also summed with the two circuits shown in the lower part of figure D.3. One summed signal was connected to an ADC input channel, providing a total energy signal (*hardware sum*). The digitised values of the four original E-PMT signals were summed via the data

⁴Photonis Imaging Sensors

⁵Thanks are due to Dr. Ian Cullum, Institute of Nuclear Medicine, Middlesex Hospital, London, for designing the amplifier boards.

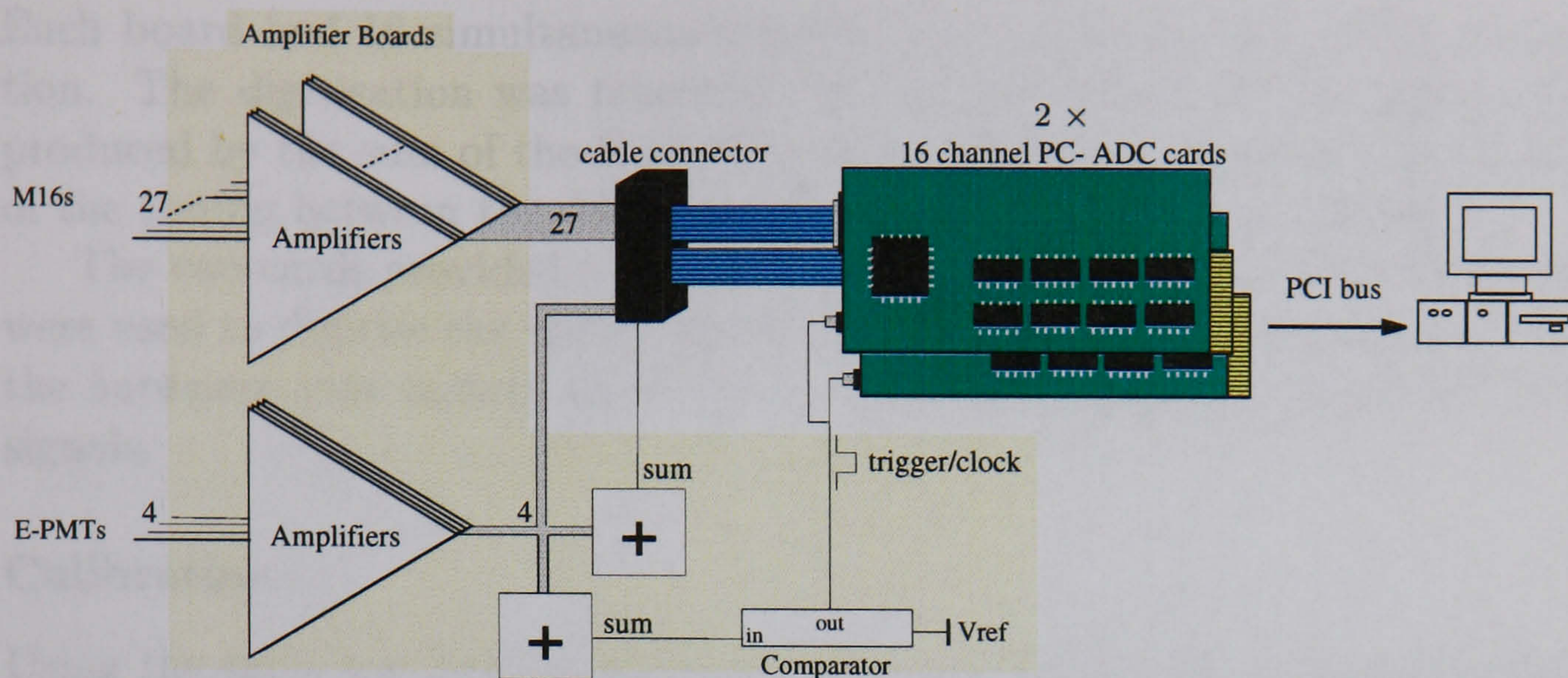


Figure 8.1: Diagram of the electronics readout system. See text for a detailed description.

acquisition software (*software sum*) allowing a comparison with the *hardware sum*.

The second summed signal was connected to a comparator. For signals above an adjustable reference voltage the comparator output was used to generate a “hold” signal for the sample-and-hold circuit and a logic pulse to be supplied to the ADC boards to initiate the digitisation (ADC trigger).

The sample-and-hold circuit was not used in the measurements presented in this chapter, since it greatly adds to the complexity and cost of the system while only leading to a small improvement in the pulse-height spectrum of the M16 tubes at low light levels.

Comparing the typical low light-level pulse-height spectrum for an M16 channel shown in figure D.5 with the spectra shown in figure 7.25 using the CAMAC based readout system with the same M16, it is seen that a similar separation between the pedestal and the single photoelectron peak is obtained. The peak corresponding to two photoelectrons is also visible with both readout systems. These results confirm the efficient performance of the customised readout system.

PCI ADC cards

The digitisation was carried out by two PCI-416L2A ADC cards manufactured by Datel⁶. The boards were controlled by a PC with Windows NT.

⁶DATTEL, Inc, 11 Cabot Boulevard, Mansfield, MA 02048-1151, USA.

Each board had 16 simultaneous-sample input channels with 12 bit resolution. The digitisation was triggered by the falling edge of the logic pulse produced by the sum of the E-PMT signals. Refer to appendix D for details of the timing between the ADC trigger and the signals to be digitised.

The two cards provided a total of 32 digitising channels. Since 5 channels were used to digitise the energy signal (one for each E-PMT and another for the *hardware sum* signal), there were only 27 channels left to read out M16 signals.

Calibration

Using the same low light level signal from an M16, all the readout channels were calibrated by adjusting the gain of the amplifiers so that the single photoelectron peak in the pulse height distributions had a similar mean value to within $\pm 10\%$.

Data acquisition software

The KmaxNT⁷ data acquisition software was used to read-out the digitised values from the ADC cards. It allows real-time data acquisition, image display and data storage.

For each acquisition, an energy window was chosen on the pulse-height distribution of the *hardware sum*, and only events falling inside this window were taken into account for the image formation. For each such event, a position (x, y) was calculated by finding the centroids of the WSF signals for both directions:

$$x = \frac{\sum_{i=1}^m i \cdot X_i}{\sum_{i=1}^m X_i} \quad ; \quad y = \frac{\sum_{i=1}^m i \cdot Y_i}{\sum_{i=1}^m Y_i} \quad (8.1)$$

where X_i and Y_i are the pedestal subtracted signals on the i^{th} fibre in each direction. Of the 27 available digitising channels, 13 were allocated to X WSFs (tube M16-B) and the remaining 14 to Y WSFs (tube M16-C).

Variations in response from different fibres may create distortions in the centroid calculation. In a full clinical system, a calibration of the response of all the fibres would have to be made, for instance, by scanning the camera with a collimated beam of gamma rays. Such a scan was made to estimate the

⁷Sparrow Corporation, Mississippi, USA, www.sparrowcorp.com.

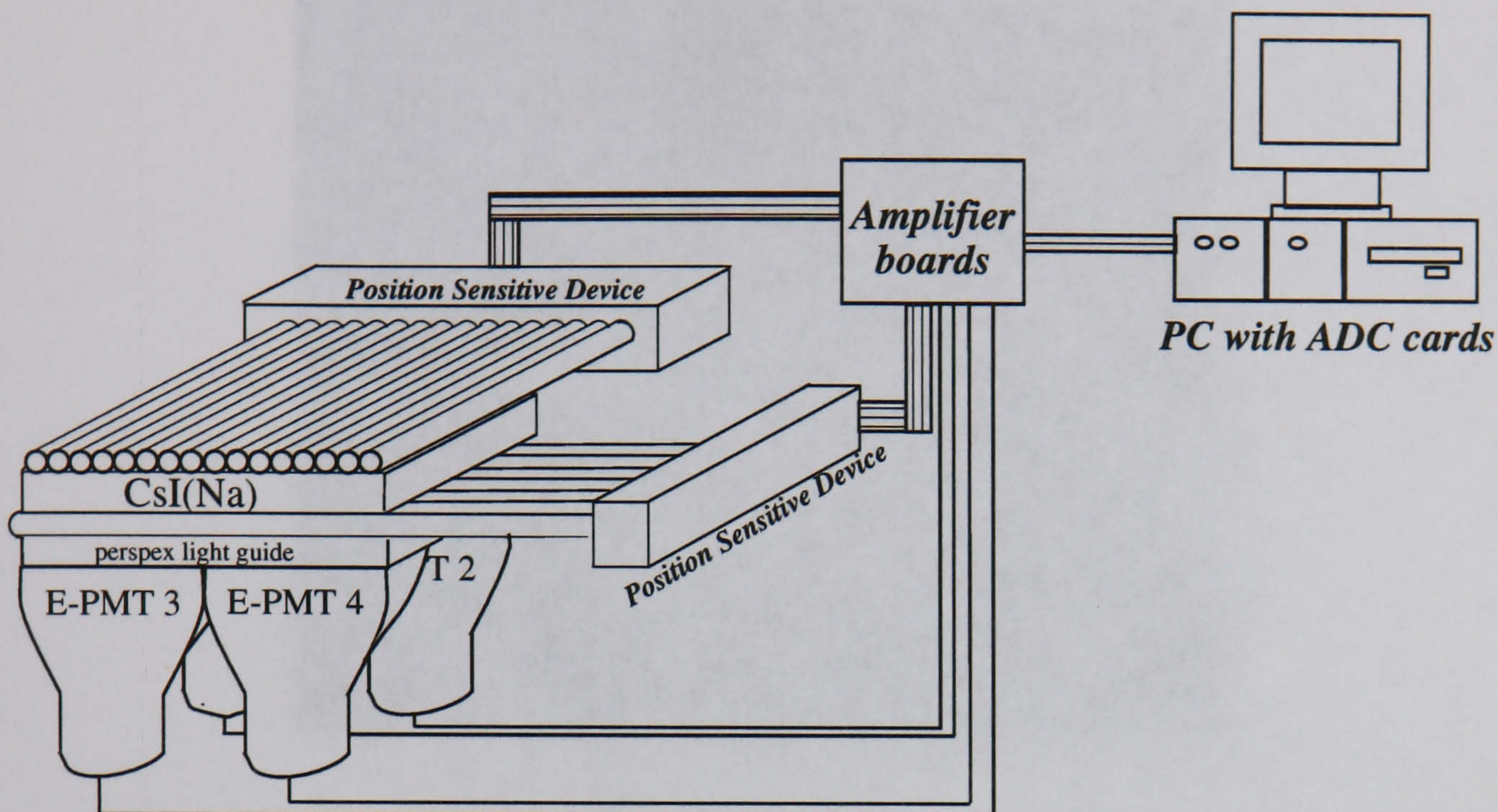


Figure 8.2: Diagram of the WSF camera prototype. Note that in practice the WSFs are bent in order to be coupled to the windows of the M16s in a 4×4 square array.

response variations for different WSFs and is described below. However, no correction algorithm was applied when calculating the centroids with equations 8.1.

8.1.6 The prototype

Figure 8.2 shows a schematic of the prototype with the main building blocks described above.

As shown in figure 8.3, the fibres were slightly bent in order to be coupled to the anodes of the M16.

As mentioned above, the system was assembled and tested with both CsI(Na) scintillators from Hilger Crystals. For each crystal two configurations were evaluated:

1. a single WSF coupled to each M16 pixel, providing an imaging field of view of $13 \times 14 \text{ mm}^2$;
2. two WSFs coupled to each M16 pixel, providing an imaging field of view of $26 \times 28 \text{ mm}^2$;

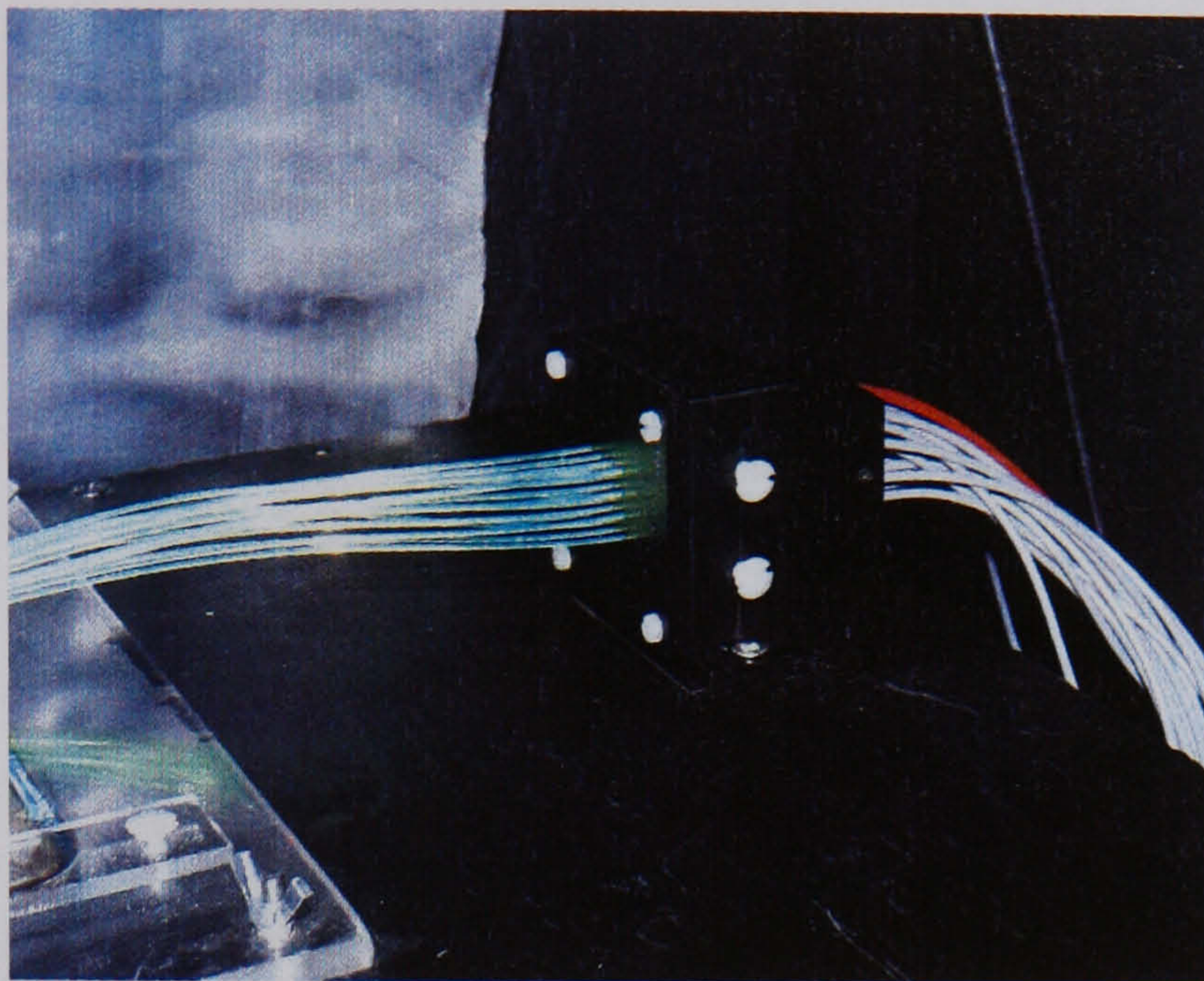


Figure 8.3: Photograph of the WSFs coupled to an M16.

For the first case, the index i in equation 8.1 takes consecutive values from 1 to 13 for x and from 1 to 14 for y . For the second case, i takes only odd values from 1 to 25 for x and from 1 to 27 for y , since each imaging pixel is 2 mm wide for this case.

Figure 8.4 shows the relative positions of the E-PMTs, the crystal and the WSFs. The imaging region is the total area covered by the WSFs being read out by the M16s (a maximum of 26 for x and of 28 for y).

8.2 Evaluation of the scintillation crystals

Before assembling the prototype with the WSFs, the two CsI(Na) scintillators from Hilger Crystals were evaluated.

Each crystal was directly coupled, with silicon gel, to the perspex slab, which was coupled with gel to the array of E-PMTs. A collimated beam of predominantly 122 keV gamma rays from a Co^{57} source was used to irradiate the scintillator. The gamma ray collimator was 13 mm thick and has a 1 mm diameter hole. It is shown in figure 5.1.

A comparison in figure D.6 between the energy pulse-height distributions for the *hardware sum* and for the *software sum* shows that very similar results are obtained, and, in particular, the energy resolution obtained from both distributions is practically identical. All the results shown in this chapter for the energy signal refer to the *hardware sum*, which is simpler to implement since it requires only one ADC channel.

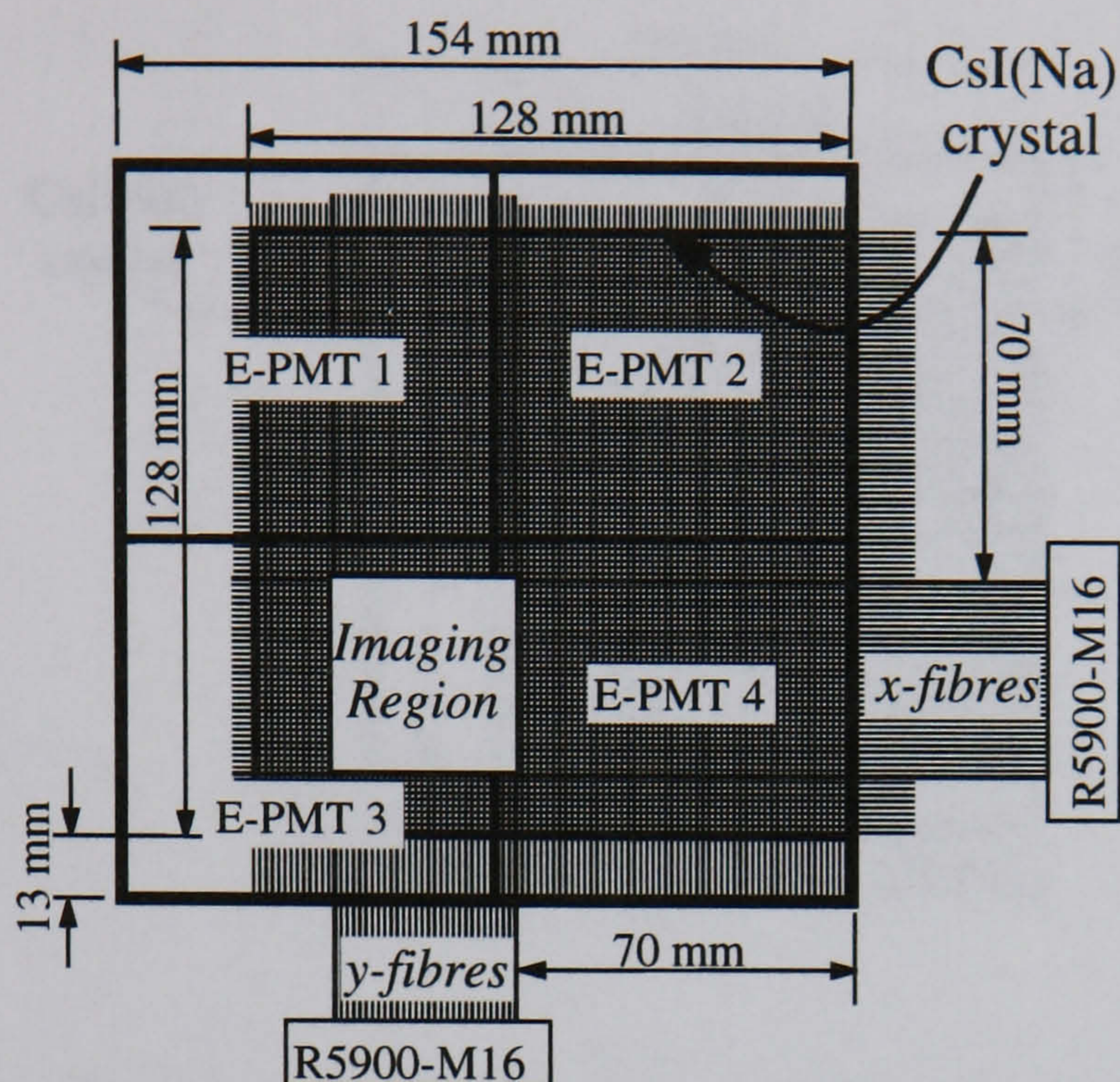


Figure 8.4: Diagram of the top view of the set-up showing the relative position of the E-PMTs, the scintillator and the WSFs.

The energy resolution is calculated using equation 3.1 and subtracting the electronic pedestal (ADC channel 74) from the mean of the energy distribution.

The relative position of the E-PMTs, the scintillator and the beam of gamma rays is shown in figure 8.5. Recall that the crystals have the same dimensions, except for their thickness.

A comparison between coupling the 3 mm thick crystal to the *energy light-guide* with and without silicone gel is presented in appendix D (figure D.7). It can be seen that, with gel, the energy signal is about 60% higher than without gel, which gives a better energy resolution for the former case (19% compared to 23% FWHM). As demonstrated in chapter 5, gel coupling also optimizes the light collected by the WSFs, and is therefore used for the experiments described in this chapter.

Figure 8.6 shows the pulse-height distribution of the energy signals. The energy resolution is calculated from the mean (pedestal subtracted) and the sigma values obtained from Gaussian fits to the pulse-height distributions.

The energy resolution is $\approx 19\%$ FWHM for both crystals. Furthermore, the mean value of the peak (in ADC channels) is also very similar indicating an approximately equal light collection for both scintillators. This is a result of the very similar geometry of the crystals and also indicates that the total

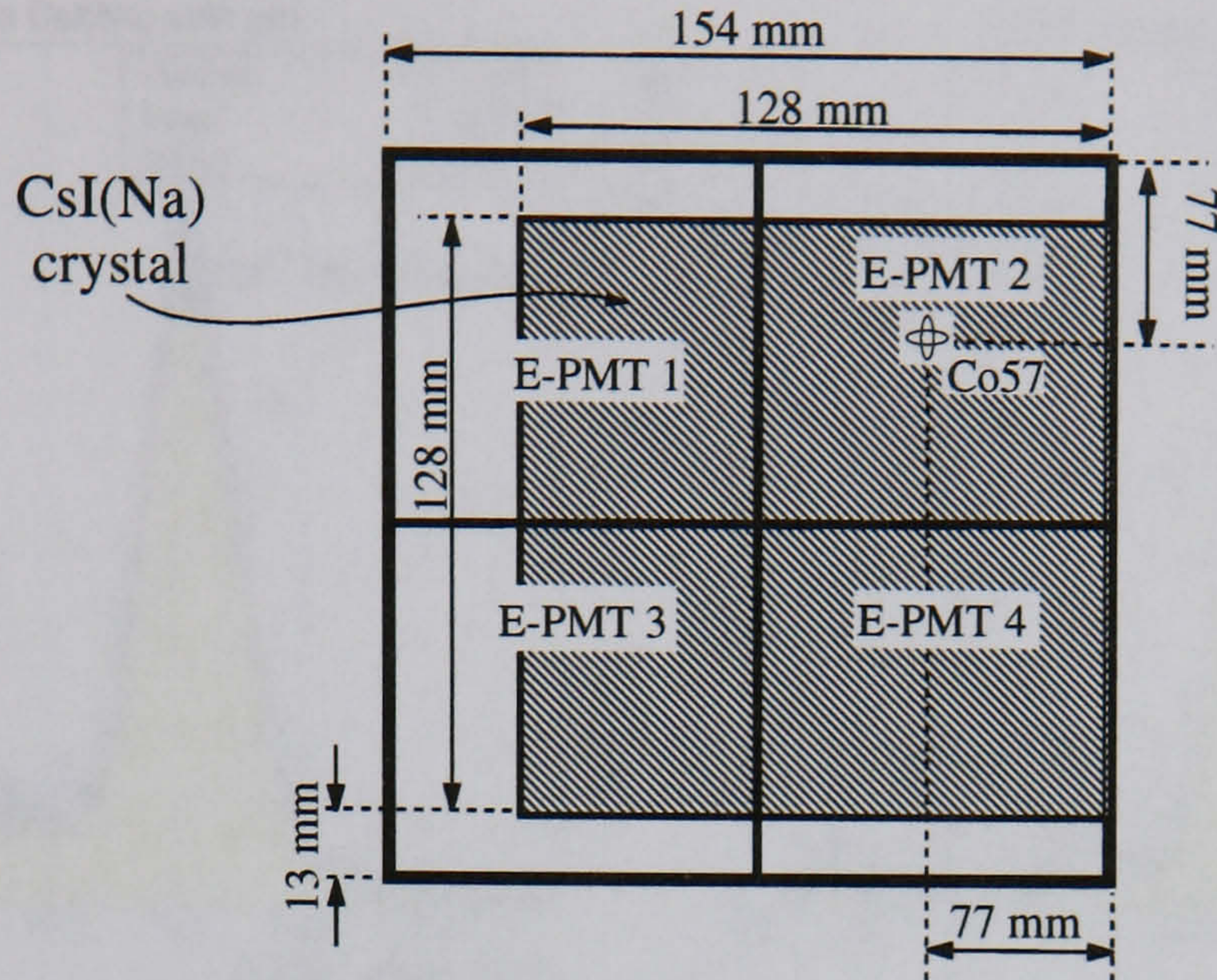


Figure 8.5: Diagram showing the relative position of the E-PMTs, the scintillator and the beam of gamma rays.

light output must be similar for each.

When the top surface of the 5 mm crystal was covered with 3 layers of white teflon tape to increase the light collection an increase of 25% in the energy signal was observed, with an improvement in the energy resolution to 18% FWHM.

In appendix B there is a detailed study of the energy resolution and light output of the four scintillators described in section 8.1.1. It is seen that the CsI(Na) scintillators evaluated provide a worse energy resolution compared to a NaI(Tl) scintillator (19% compared to 14%). This worse resolution obtained with CsI(Na) is linked to a lower light output and to a higher contribution of the terms R_T^2 and R_i^2 in equation 3.5.

8.3 Light collected by the WSFs and M16s

8.3.1 Experimental procedure

The prototype was fully assembled with the WSFs as described in section 8.1. Unless otherwise mentioned, the evaluation of the detector was carried out using a collimated beam of Co^{57} gamma rays. The beam was collimated with the previously described 13 mm thick lead collimator with a 1 mm diameter hole.

Following gamma ray interactions in the crystal, energy signals were gen-

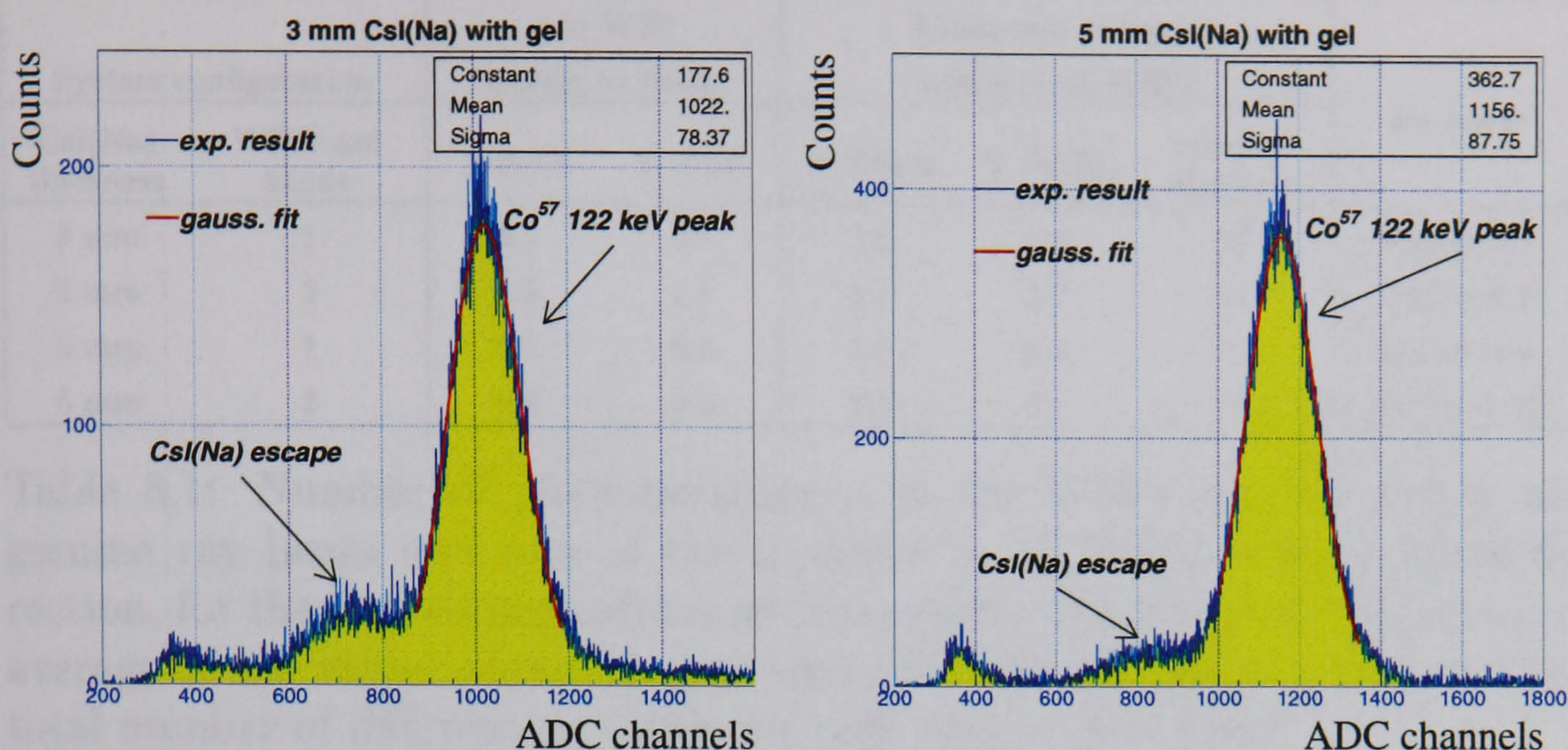


Figure 8.6: Pulse-height distribution of the energy signal, for the 3 and the 5 mm thick crystals.

erated. If a signal was above the pre-defined reference voltage in the comparator (see figure D.3), an ADC trigger was produced initiating the digitisation of all ADC input channels. For each position of the collimator, the data acquisition software recorded the data for 51,200 ADC triggers.

An energy window was selected around the mean position of the 122 keV gamma ray peak in the *hardware sum* pulse-height distribution. Pulse-height distributions for the M16 signals only used events whose *hardware sum* was within the energy window. For these events, the (x, y) centroids were calculated using equation 8.1 and an (x, y) image histogram was updated with the corresponding (x, y) values.

The mean number of photoelectrons μ created in each anode of the M16s was calculated following the method described in section 5.2.4. N_T in equation 5.3 is the number of events inside the energy window. As described in that section, the number of background events are subtracted from N_T and N_{th} in equation 5.3.

The procedure of aligning the collimator position x^{col}, y^{col} with respect to the position of the X and Y WSFs, has an experimental accuracy of ± 0.5 mm. The errors in the experimental procedure were evaluated by repeating the positioning of the collimator over a fibre and measuring its output. The results of the evaluation of μ by this procedure agreed within $\pm 10\%$.

System configuration		μ in WSF closest to beam		Mean sum of the μ values in all WSFs			Example
CsI(Na) thickness	WSFs per anode	X WSF	Y WSF	X WSFs	Y WSFs	number of points	
3 mm	1	0.7	0.7	3.6	2.8	26	Figure 8.7
3 mm	2	0.9	1.1	4.1	2.7	54	Figure 8.8
5 mm	1	0.3	0.8	3.0	2.4	5	Figure 8.9
5 mm	2	0.5	0.8	3.3	3.1	5	Figure 8.10

Table 8.1: Number of photoelectrons μ in the WSFs directly below the gamma ray beam and sum of the μ values in all WSFs along a given direction, for the four configurations of the system. The summed values are an average of the values obtained at several different collimator positions. The total number of different positions for each case is also shown.

8.3.2 Results

The results obtained for the four configurations of the system are summarised in table 8.1. The table shows the numbers of photoelectrons μ for the fibres directly below the gamma ray beam as well as the sum of the μ values in all the WSFs along one direction. The results for the sums are average values taken at different positions of the collimator over the imaging region. The number of different points for each case is also shown in the table.

Figure 8.7 shows the mean number of photoelectrons μ for each WSF for the case of one WSF per M16 pixel and for the 3 mm thick CsI(Na) crystal.

For the WSFs directly below the gamma ray beam (X7 WSF and Y10 WSF) the mean number of photoelectrons measured is ~ 0.7 . This result compares to the ~ 0.9 mean shown in figure 5.7, obtained with the EMI 9124A PMT and with a NIM-based readout system, for the same CsI(Na) crystal. This reduction is not surprising, given the lower quantum efficiency of the PSPMT compared with the EMI 9124A.

The collimator scanned the imaging region with 1 mm steps along two lines defined by a X WSF and a Y WSF. It is observed that, for each scan, the response of the scanned fibre varies by $\pm 5\%$.

The output of the fibres laid perpendicularly to each line of scan, and located directly below the gamma ray collimator, was measured. The response variations from fibre to fibre are $\pm 20\%$ for the X WSFs and $\pm 50\%$ for the Y WSFs. These variations are mainly caused by a poor response associated with 2~3 fibres in each set. To confirm that the variation was not associated with the M16 response or readout electronics, the WSFs were moved to different M16 pixels and the same low response was observed for the same

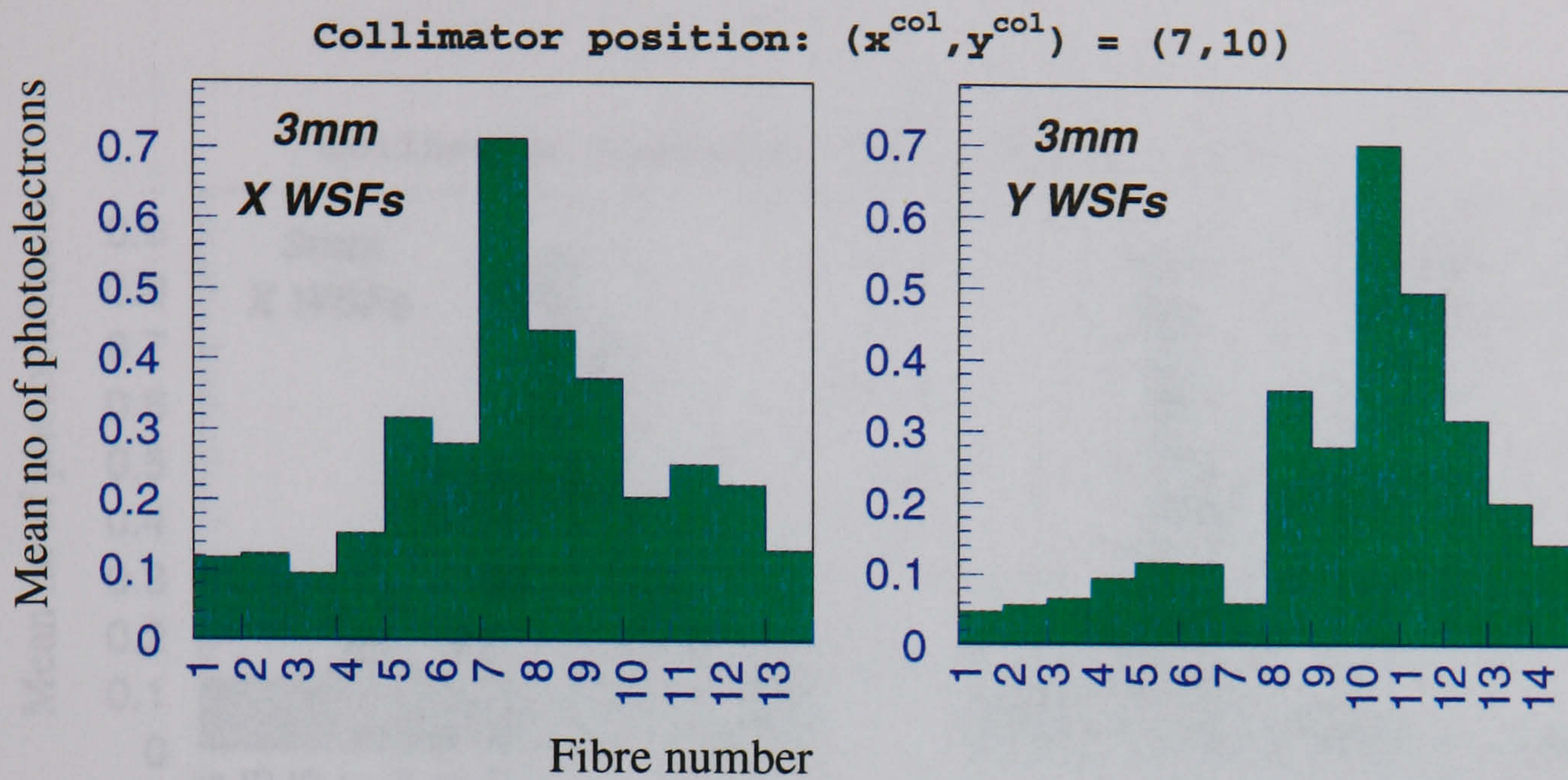


Figure 8.7: Mean number of photoelectrons μ for the X WSFs and the Y WSFs coupled to the 3 mm thick CsI(Na) crystal.

fibres.

These variations are possibly associated with some degree of non-uniformity in coupling the WSFs to the crystal and also to the uncertainty in the position of the gamma ray collimator over the WSFs. Such large variations were not found in the simpler set-up used in the experiments described in chapter 5, indicating that a much higher uniformity is achievable.

The results for the sum of the mean number of photoelectrons are 3.6 for the X WSFs and 2.8 for the Y WSFs, which compare to ~ 3.7 obtained in chapter 5 and shown in figure 5.6.

A similar experiment was carried out with two WSFs per M16 pixel. In this case the position x^{col}, y^{col} of the gamma ray beam was approximately above fibres X15 and Y9 of the 26×28 set of WSFs. The results are shown in figure 8.8, where each bin of the histogram corresponds to 2 WSFs.

The sums of the μ values are similar to those obtained with 1 WSF per M16 anode, a configuration with half the number of fibres (13×14). This shows that the light signal is confined to a region of less than $13 \times 14 \text{ mm}^2$ as predicted in previous chapters.

Figure 8.9 shows the mean number of photoelectrons μ for the X and Y WSFs for the case of one WSF per M16 pixel, and for the 5 mm thick CsI(Na) crystal.

For the WSFs directly below the gamma ray beam, X7 WSF and Y7 WSF, the mean number of photoelectrons measured is ~ 0.3 and ~ 0.8 respectively. The lower signal in the central X WSF is due mainly to two reasons. The first

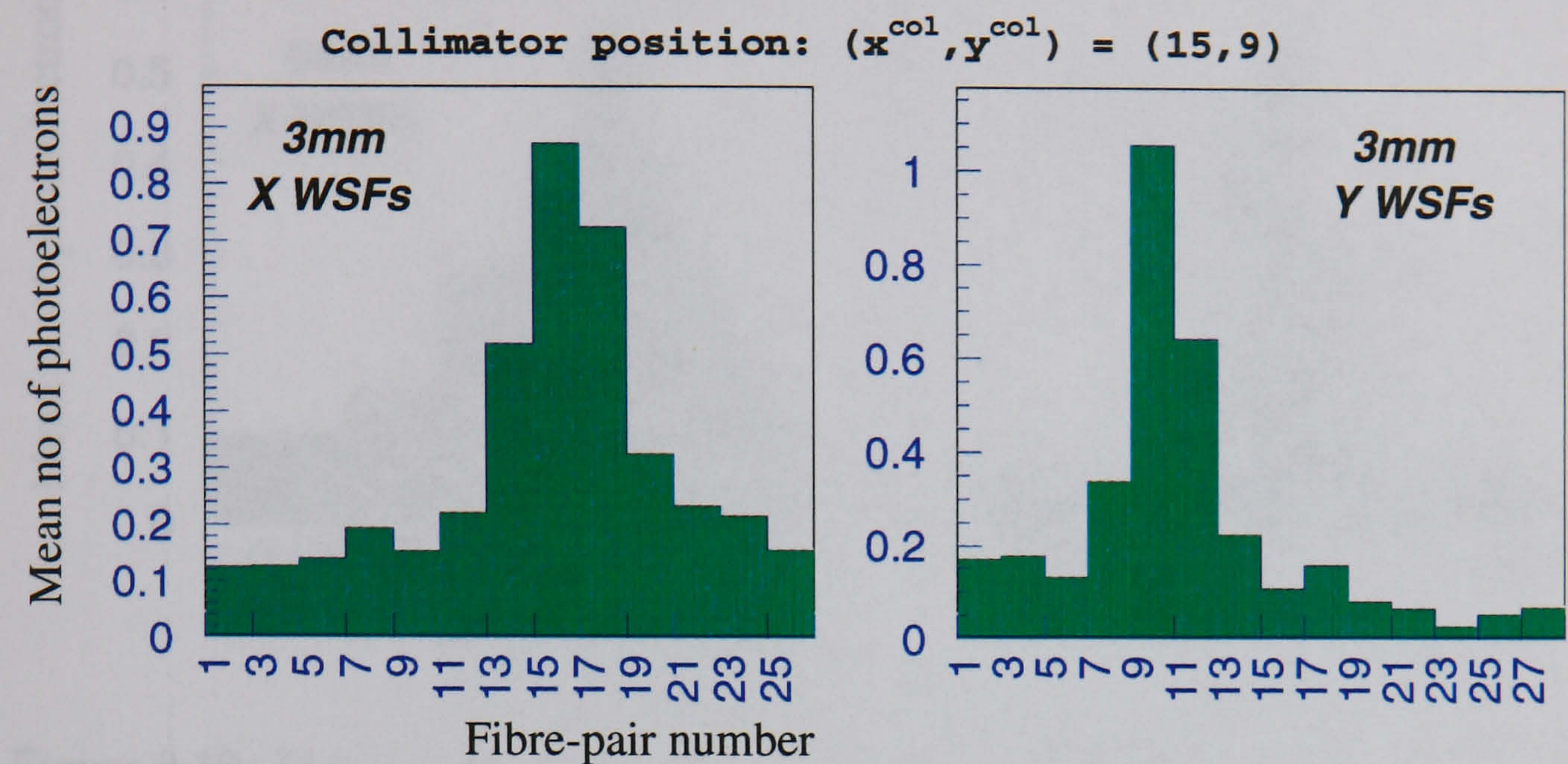


Figure 8.8: Mean number of photoelectrons μ for each pair of WSFs coupled to an M16 anode for the 3 mm thick CsI(Na) crystal.

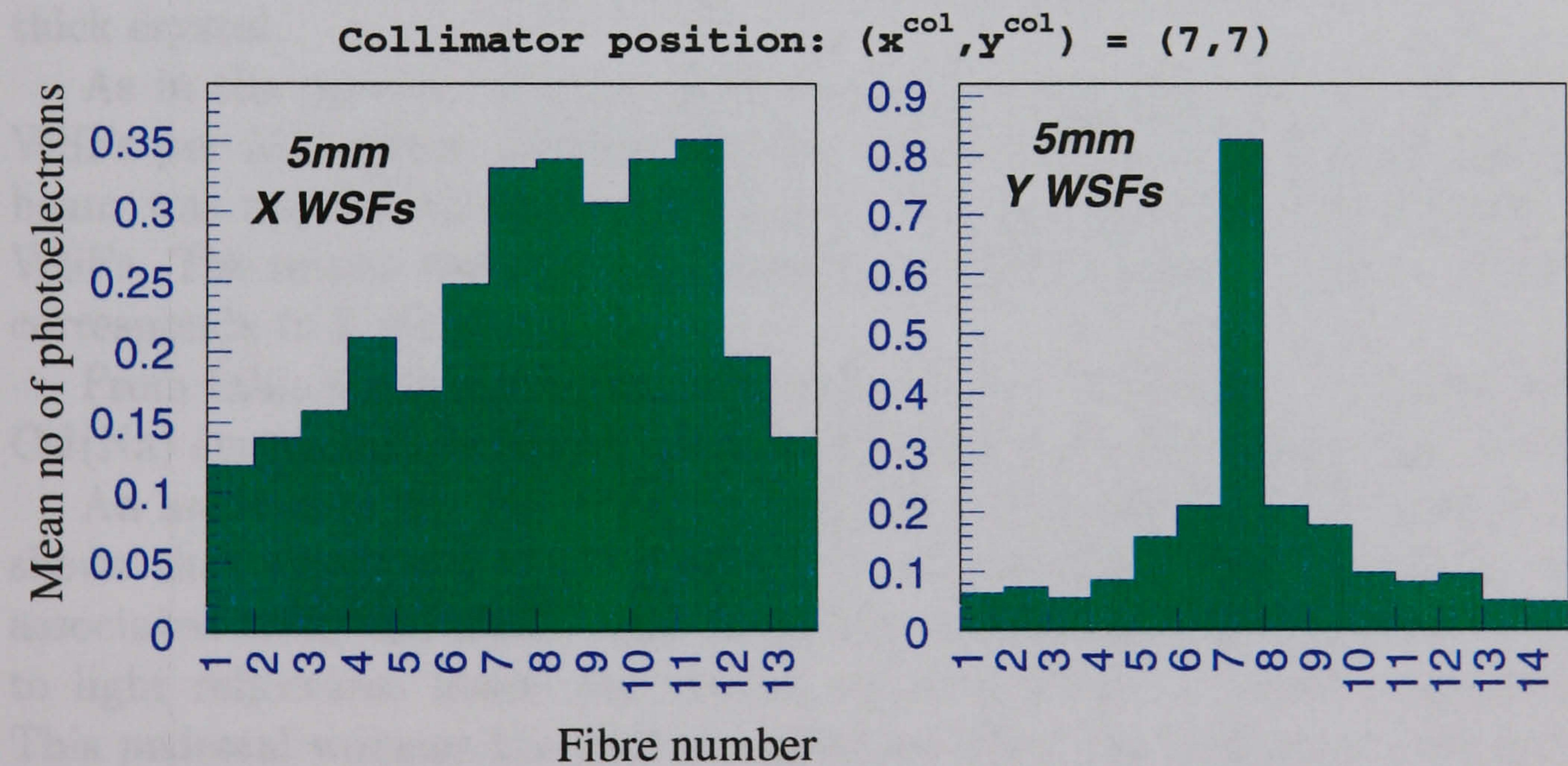


Figure 8.9: Mean number of photoelectrons μ for the X WSFs and the Y WSFs coupled to the 5 m thick CsI(Na) crystals.

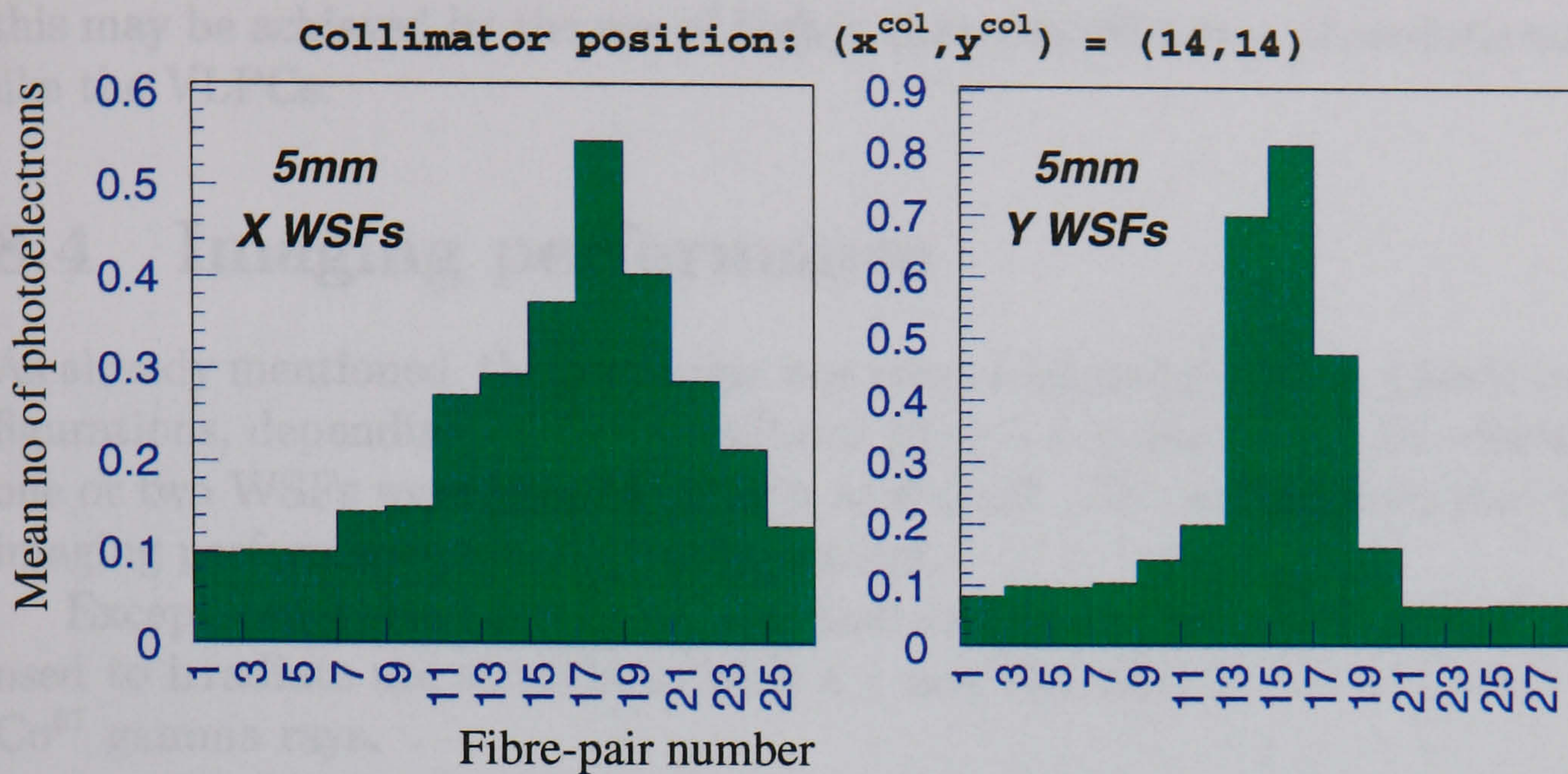


Figure 8.10: Mean number of photoelectrons μ for each pair of WSFs coupled to an M16 anode for the 5 mm thick CsI(Na) crystal.

is the poor response of the X7 and X8 WSFs compared to the neighbouring fibres. The second is the broader light distribution over the X WSFs which are coupled to the CsI(Na) opposite to the gamma ray entrance surface. This effect was previously observed and described in figure 5.8 and related text. The Y WSFs show a similar behaviour to the results obtained with the 3 mm thick crystal.

As in the previous section, a similar experiment was carried out with 2 WSFs per M16 pixel. In this case the position x^{col}, y^{col} of the gamma ray beam was approximately above fibres X14 and Y14 of the 26×28 set of WSFs. The results are shown in figure 8.10, where each bin of the histogram corresponds to 2 WSFs.

From table 8.1 it is seen that the sums of the μ values for the 5 mm thick CsI(Na) crystal are similar to the ones obtained with the 3 mm thick crystal.

An analysis of the plots obtained for different positions of the collimator, shows that there is a small pedestal in all the plots. This is clearly not associated with the direct light from the scintillator and is probably due to light reflections inside the crystal which generate a small background. This pedestal worsens the spatial resolution when the position is calculated using the centroid calculation in equation 8.1. A cluster algorithm, where the position is calculated based on the signals of a selected number of fibres, may provide a better resolution. For such an algorithm, it would be important to have higher output from the photodetectors reading out the WSFs, in order to be able to correctly define the clusters. As mentioned in previous chapters,

this may be achieved by the use of higher quantum efficiency photodetectors, like the VLPCs.

8.4 Imaging performance

As already mentioned, the prototype was assembled and tested in 4 basic configurations, depending on the scintillator (3 or 5 mm thick) and on whether one or two WSFs were coupled to each M16 pixel. This section describes the imaging performance for each configuration.

Except otherwise mentioned, the lead collimator described earlier was used to irradiate the scintillator with a 1 mm diameter collimated beam of Co^{57} gamma rays.

8.4.1 Spatial resolution

Figure 8.11 shows the images obtained for each configuration when the gamma ray beam is in a central region of the imaging area. For each measurement, there are approximately 35,000 events inside the energy window, and the centroids in x and y are calculated from equation 8.1.

Profiles across the highest intensity pixel, along the lines depicted in figure 8.11, are shown in figure 8.12. For some gamma ray events, there are no photoelectrons generated in the M16s by any fibre. In these cases the centroid is assigned a value of zero, which correspond to the lowest bins in the profiles shown.

The full width at half maximum (FWHM) of each profile was calculated. These FWHM values are considered to be an approximation to the intrinsic spatial resolution for each configuration.

For the 3 mm thick crystal the spatial resolution along X and Y is very similar, and ranges from 3 to 4 mm FWHM, for different positions over the imaging region, for the case of one WSF per M16 anode. For two WSFs per anode, the spatial resolution is about 6 mm FWHM.

For the 5 mm thick crystal, the spatial resolution along Y is consistently better than along X. This is a result of the broader light distribution over the X WSFs which are coupled to the CsI(Na) surface opposite the gamma ray entrance surface. For one WSF per anode, the spatial resolution along X is about 6 mm FWHM, compared to 3-4 mm FWHM along Y. Note that the latter value is very similar to that obtained with the 3 mm thick crystal. For two WSFs per anode, a resolution of 4 mm FWHM along Y and of 8 mm FWHM along X is observed.

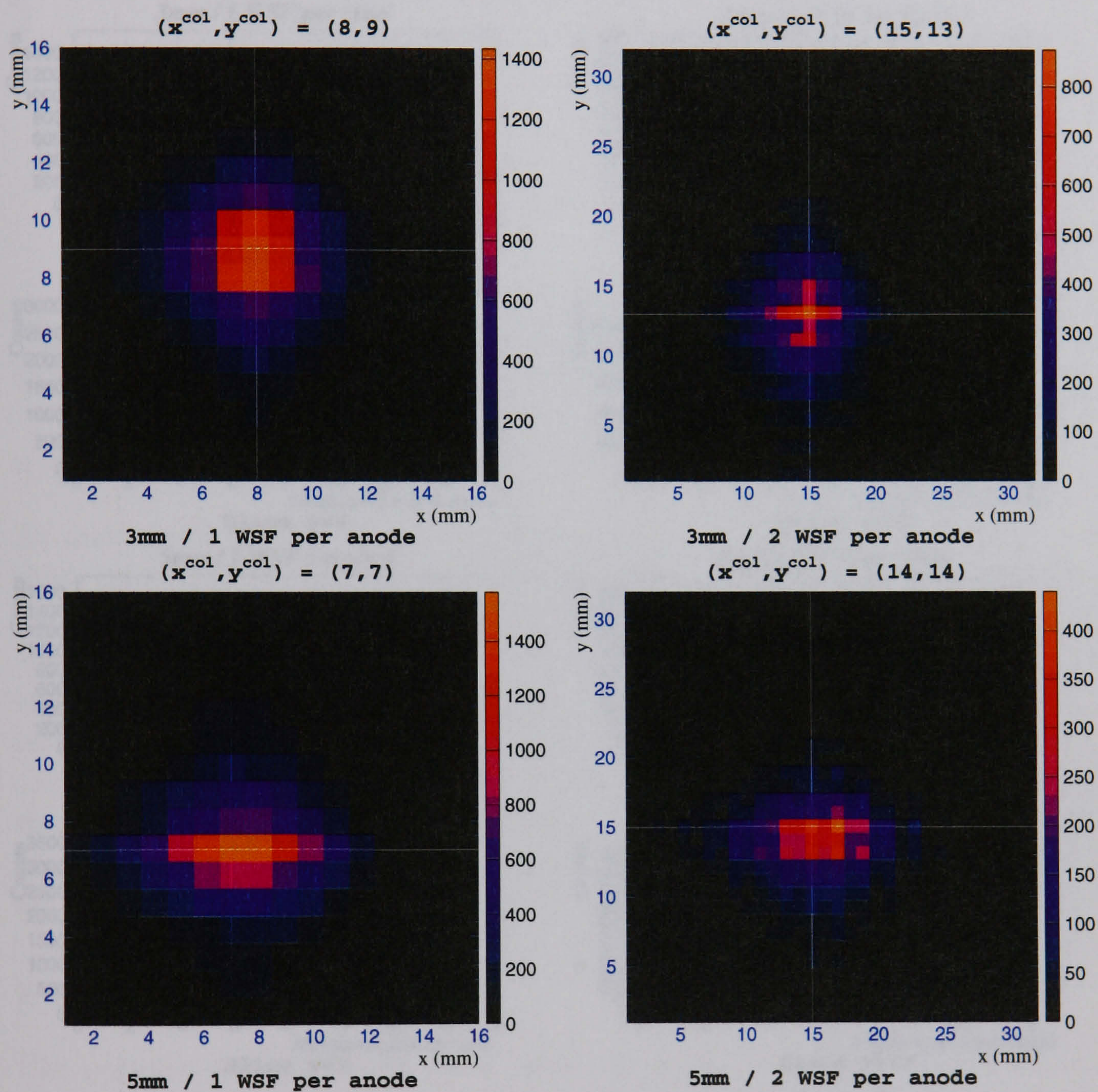


Figure 8.11: Point source images for each of the 4 configurations studied. Note the different scales in the images on the left (1-16 mm) compared to the images on the right (1-32 mm).

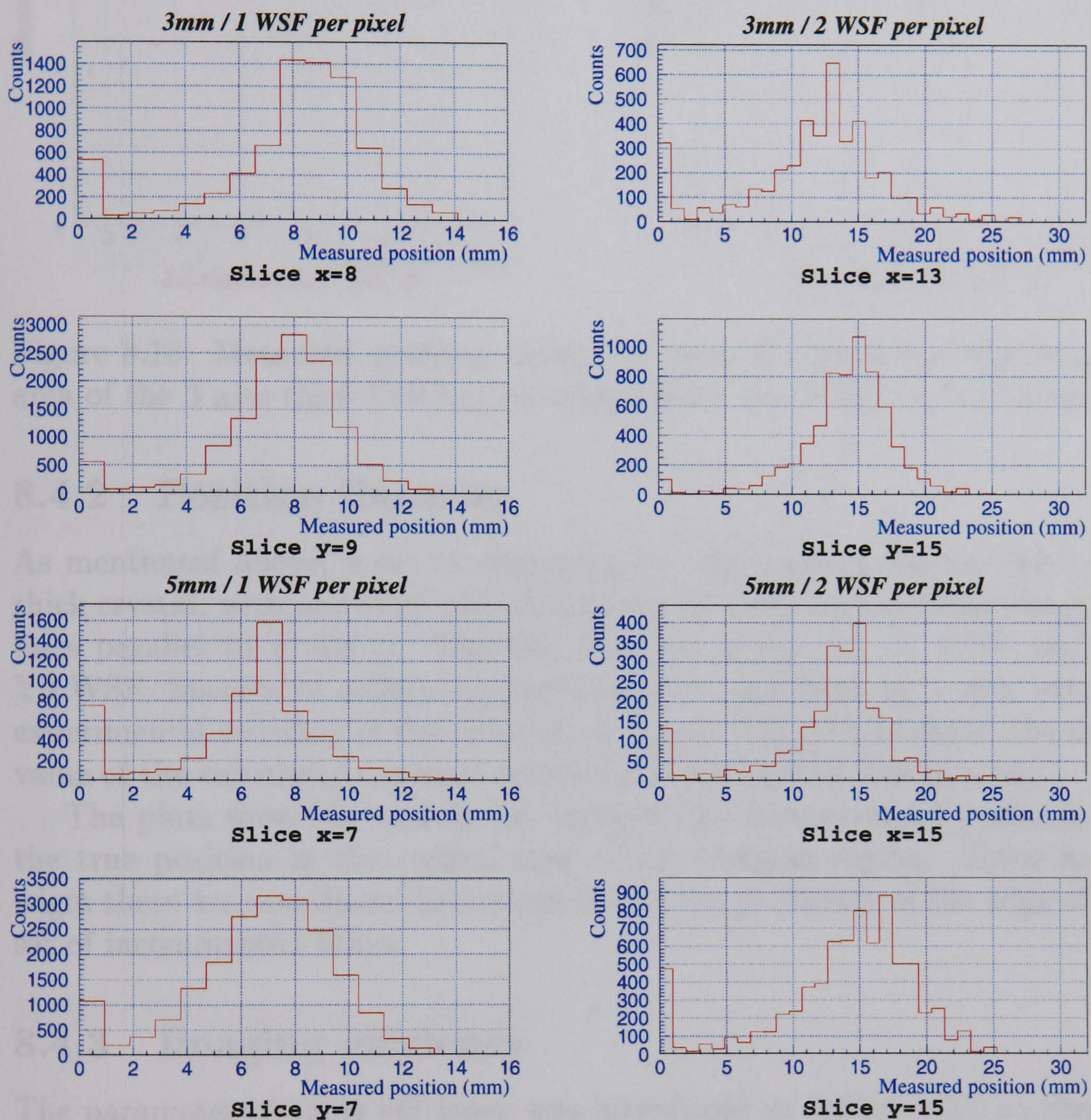


Figure 8.12: Profiles across the highest intensity pixels in figure 8.11. Note the different scales in the plots on the left (1-16 mm) compared to the plots on the right (1-32 mm).

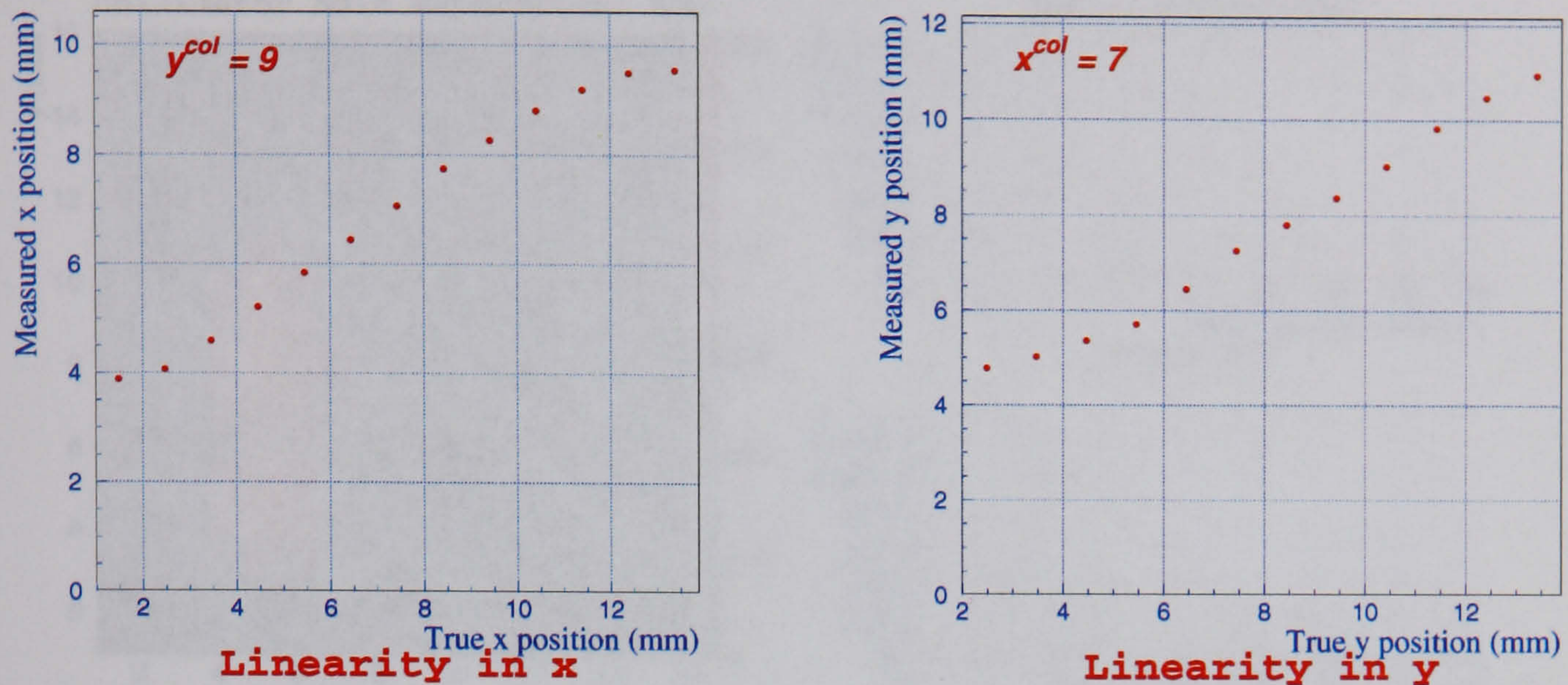


Figure 8.13: Measured position along two lines of scan across the imaging area of the 3 mm thick CsI(Na) prototype with one WSF per M16 anode.

8.4.2 Position linearity

As mentioned above, a set of measurements was carried out for the 3 mm thick crystal, with one WSF per M16 anode, at different positions along two lines parallel to x and y . The two lines are along the X7 WSF and the Y9 WSF. Successive collimator positions were separated by 1 mm with an experimental accuracy of the order of ± 0.1 mm. Figure 8.13 shows the mean value of the calculated centroid distributions along each line of scan.

The plots show the correlation between the reconstructed position and the true position in the central area of the imaging region. Towards the edges there are non-linear distortions due to the proximity of the edge of the set of instrumented fibres.

8.4.3 Imaging efficiency

The parameter imaging efficiency was introduced in section 4.3.2 to characterise a loss in gamma ray detection sensitivity of a WSF imager due to the low light levels in the WSFs. There are some cases where, for a given gamma ray interaction with full energy deposition, there are no photo-electrons in either layer of WSFs (X or Y), in which case there will not be a valid image point.

By comparing the number of events inside the energy window with the number of events in the final image for the cases presented in section 8.3, it is found that the imaging efficiency is higher than 90% for all cases.

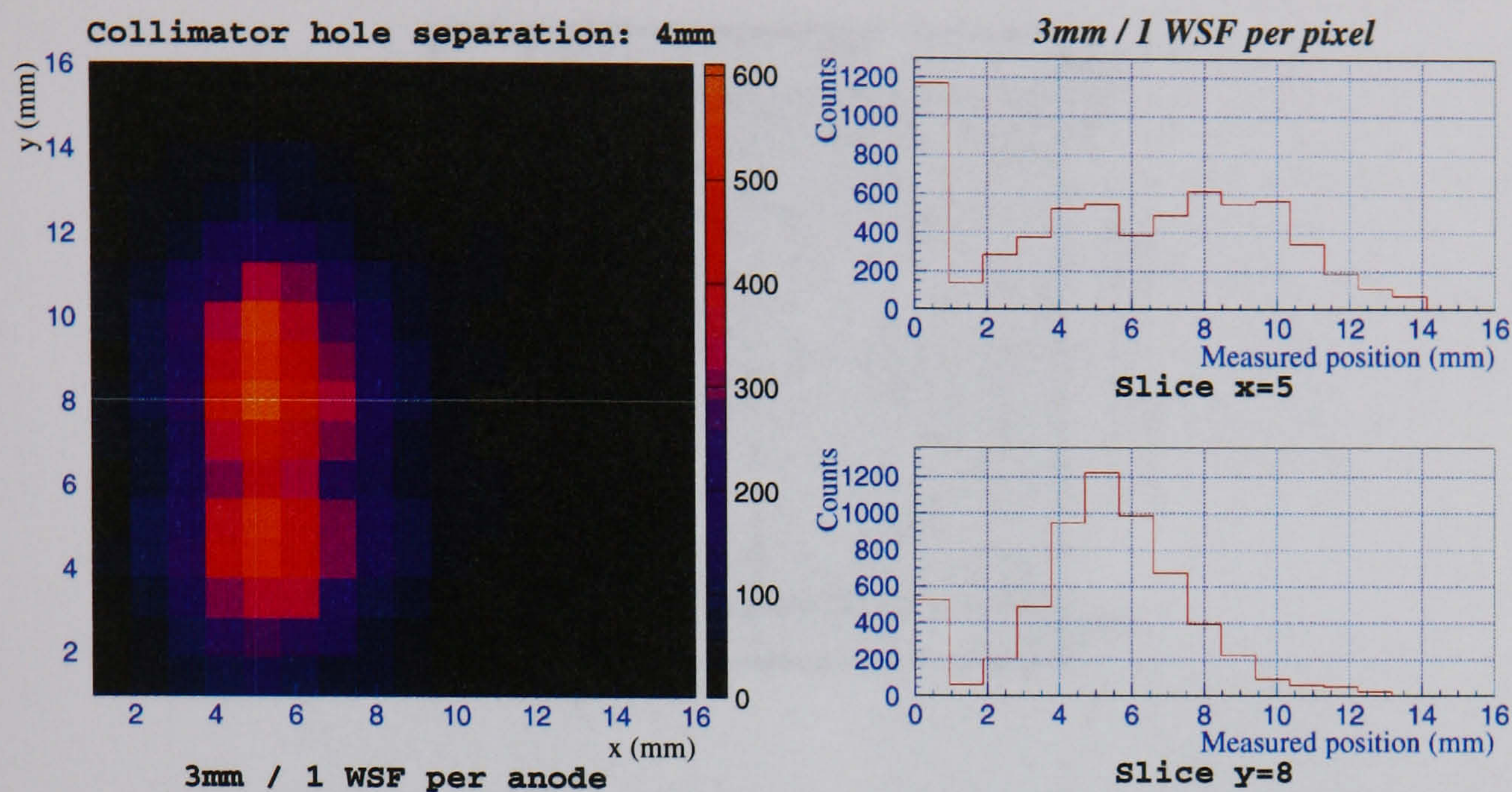


Figure 8.14: Image of two points separated by 4 mm, using the 3 mm thick CsI(Na) and with 1 WSF coupled to each M16 anode. The corresponding profiles along the lines shown in the image are also shown.

8.4.4 Image of two points

A lead slab with two 1 mm diameter holes separated by 4 mm was used to obtain the image shown in figure 8.14 using a Co^{57} gamma ray source.

Also shown are the profiles along the lines depicted in the image. The distance between the holes is of the order of the spatial resolution of the system and, as can be observed from the profiles, the two points are on the edge of being distinguished along Slice $x=5$.

8.5 Energy response

8.5.1 Energy resolution

It can be seen in appendix B that the energy resolution obtained with the CsI(Na) crystals coupled directly to the *energy light-spreader* is 19% FWHM. Coupling the fibres to the crystals in the WSF camera configuration, the energy signal drops to about 60% of the result obtained with the “bare” crystal, with a corresponding energy resolution of $\sim 23\%$ FWHM.

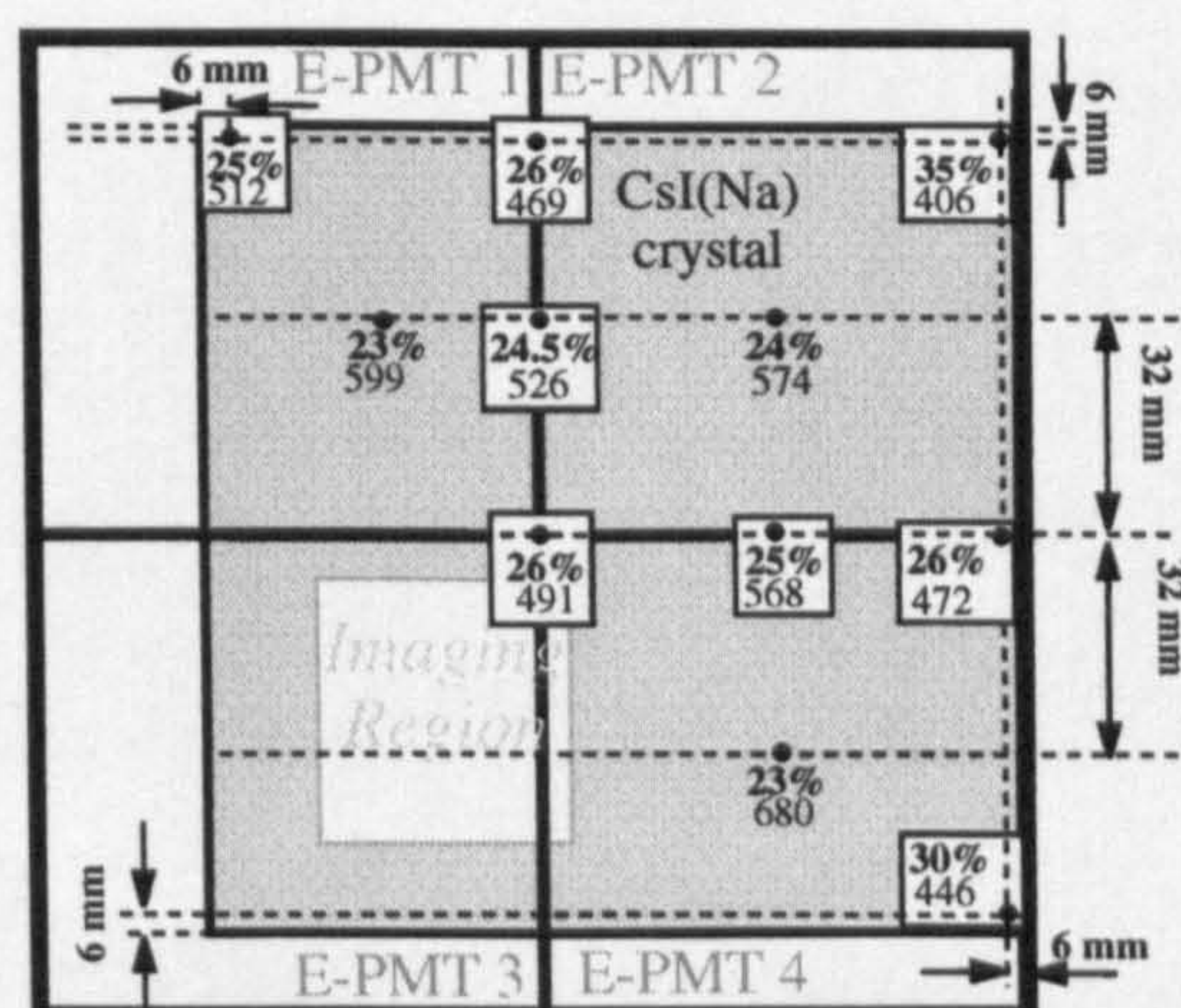


Figure 8.15: Energy response for some selected points on the 3 mm CsI(Na) crystal. Values in bold correspond to energy resolution (FWHM) and the values below these are the mean position of the energy peak in arbitrary units (ADC channels).

8.5.2 Energy uniformity

The uniformity of the energy signal is illustrated in figure 8.15 for the 3 mm thick CsI(Na). The crystal was irradiated with the collimated beam of Co^{57} gamma rays at the points indicated in the figure. These were selected in order to show the highest energy signals, at the central regions of the E-PMTs, as well as the lowest ones, at the edges of the E-PMTs and at the edges of the crystal.

A maximum variation of the energy signal of 40% is observed which is associated with a variation in energy resolution from 23% to 30% FWHM.

8.6 Monte Carlo simulations for a high quantum efficiency device

The functionality of the Monte Carlo program SR-SIM previously developed and described in section 6.2, was extended in order to simulate an imager.

The centroids for two different sets of fibres were calculated and the corresponding image was built, assuming the sets of fibres to be perpendicular.

Using the distributions of the mean number of photoelectrons per WSF obtained experimentally (section 8.3) it is possible to create images similar to those in figure 8.11. The other inputs to the program are the single electron

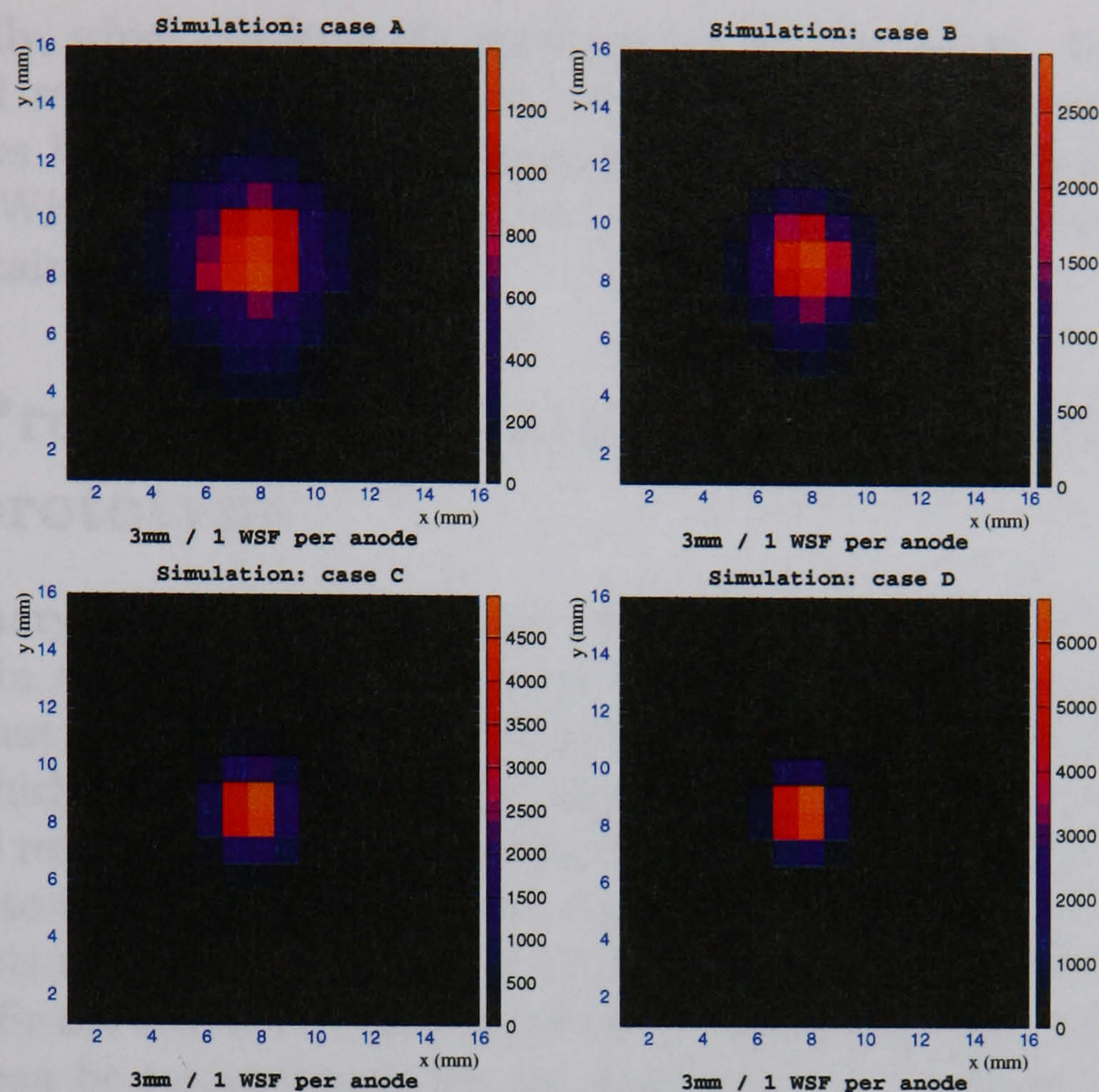


Figure 8.16: Results of the Monte Carlo simulations for case A - using the experimental results for the WSF output; case B - twice the output per WSF; case C - four times the output per WSF and case D - six times the output per WSF .

resolution of M16-B and M16-C which are 0.2 and 0.3 respectively.

Figure 8.16 shows three images obtained using the experimental results corresponding to figure 8.11, for the 3 mm thick CsI(Na) with 1 WSF per M16 anode, as input to the modified SR-SIM.

For the first case (A), the mean number of photoelectrons in each WSF is the same as obtained experimentally. For cases B, C and D, the mean number of photoelectrons per fibre is multiplied by 2, by 4 and by 6, to estimate the potential effect of using a higher quantum efficiency device as discussed in section 6.2.2. Since the quantum efficiency of the M16 at 500 nm is approximately 12%, these inputs simulate devices with 12%, 24%, 48% and 72% quantum efficiency. The higher quantum efficiency values might be achieved with currently available silicon photodetectors, like the previously discussed VLPCs. For all cases, a total of 35,000 events was simulated.

For case A, the simulated image is very similar to the one obtained ex-

perimentally, which confirms the accuracy of the simulation. In particular the spatial resolution obtained is 4.5 mm FWHM. For the cases of 2, 4 and 6 times higher output, the spatial resolution improved to 3.3, 2.4 and 1.9 mm FWHM respectively, with an obvious impact on the point source images obtained.

8.7 Preliminary investigation of a NaI(Tl) WSF prototype

A preliminary evaluation of the 5 mm thick NaI(Tl) (section 8.1.1) coupled to WSFs in a WSF camera configuration is presented in appendix E. It is found that the signals from the WSFs are higher than with the CsI(Na) crystals which agrees with the higher light output of the NaI(Tl). However, the spatial resolution obtained is worse (6-7 mm FWHM), particularly when compared to the 3 mm thick CsI(Na) crystal.

A simple study of the behaviour of the centroid calculation for the case where WSFs are coupled to the edge of the crystal was carried out. From the results it can be extrapolated that the dead areas at the edges of a camera with a 3 mm thick crystal should be of about 3 mm or less.

8.8 Discussion and conclusions

The results obtained and described throughout this chapter confirm the earlier predictions that the WSF gamma camera is a promising concept for Nuclear Medicine imaging.

The light levels at the WSFs agree with previous results with different photodetectors and readout systems. The mean number of photoelectrons per gamma ray event in each set of fibres (X WSFs and Y WSFs) is in the range of 2.5 to 3.5 which is enough to provide an overall imaging efficiency greater than 90% in all cases studied.

The spatial resolution obtained with the 3 mm thick CsI(Na) crystal is in the range of 3 to 4 mm FWHM for both directions, which is comparable to the 3.5 mm FWHM intrinsic resolution of the Anger camera. For the 5 mm thick CsI(Na) crystal, the spatial resolution is between 3 and 4 mm FWHM for the direction associated with the top layer of WSFs (i.e., the fibres coupled to the gamma ray entrance surface). In the direction associated with the bottom layer of WSFs the resolution is approximately 6 mm FWHM.

The Monte Carlo simulation developed (SR-SIM) predicts a spatial resolution improvement for higher number of photoelectrons per fibre. Starting

with a spatial resolution of 4.5 mm FWHM for the numbers of photoelectrons obtained experimentally, the simulation predicts an improvement to 3.3, 2.4 and 1.9 mm FWHM for 2, 4 and 6 times the numbers of photoelectrons respectively. As discussed in section 4.4.4 this may be achieved by the use of silicon based devices, such as VLPCs, which have a quantum efficiency up to 6 times higher than that of the M16.

The energy response obtained with the CsI(Na) crystals was shown to be worse than that obtained with the NaI(Tl) crystal. In particular, a poorer energy resolution of 19% compared to 14% is achieved with the bare crystals directly coupled to the E-PMTs. However, the spatial resolution obtained with the NaI(Tl) crystal is worse, mainly due to its larger thickness. Coupling the WSFs to the CsI(Na) crystals, the energy signal drops and the energy resolution obtained is 23%.

Preliminary experimental data taken near the edge of a 5 mm thick NaI(Tl) crystal indicates that the dead areas near the boundaries of the crystals should not be greater than 6 mm. For thinner crystals, like the CsI(Na) used in this chapter, an even smaller dead region of 3 mm or less may be achieved. This is a significant improvement compared to the Anger camera, where the dead areas at the edges are of the order of 3 to 7 cm.

Chapter 9

Conclusions and Future Work

9.1 Conclusions

Anger cameras are general purpose imagers, usually large enough to allow whole-body imaging. However, for specific imaging of small organs, the size of the Anger camera is a major drawback in obtaining optimal images. It is also expensive. For cases like breast cancer, which have a very high incidence in women, it is clearly justified to develop application-specific imagers. These should provide better performance and therefore assist in early tumor detection with a significant impact on the survival rates.

The proposed design of the wavelength-shifting fibre (WSF) camera is inherently flexible. The camera may be built in a variety of shapes to suit the clinical needs, and it is easily scalable. These features can potentially improve the images by allowing better positioning of the camera close to the patient. It can also avoid strong background from other organs like the heart and the liver.

Before building a camera prototype, an evaluation of the main components was carried out. The output of WSFs coupled to scintillators was measured, showing that the amount of light at the fibres per gamma ray interaction is sufficient to be easily detected with currently available photodetectors. Several PSPMTs were evaluated with special attention to their low light level response, demonstrating the excellent photon counting characteristics of the Hamamatsu R5900-M16 tubes.

The prototype developed showed an intrinsic spatial resolution of 3-4 mm FWHM, which is comparable to currently available Anger cameras. The resolution was clearly limited by low photon statistics. A Monte Carlo simulation predicts a significant improvement in spatial resolution to less than 2 mm FWHM by simply replacing the PSPMTs with higher quantum

efficiency devices. Visible light photon counters (VLPCs) meet this requirement and are available and extensively used in high energy physics experiments. The compact design and better intrinsic spatial resolution compared to the Anger camera promises significant improvements to the overall spatial resolution of the system.

The energy resolution of the WSF camera (23% FWHM) is worse than that of the Anger camera (10% FWHM). It is arguable however that through a better positioning of the camera, a significant amount of scatter can be avoided and therefore a much less stringent energy resolution may be acceptable. An accurate assessment of this trade-off is not available yet although some preliminary studies confirm to some extent that argument.

The results show that a much smaller dead region at the edges is achievable with the WSF camera than with Anger cameras. A region of less than 3 mm is to be expected which represents a major improvement compared to 3–5 cm in Anger cameras.

The materials and technology used are inexpensive. An estimate of the cost, based on the price of each component, including the detector with a collimator, the electronics, data acquisition software and computer, gives a total of about £20,000.

9.2 Future Work

Further work is needed in two distinct areas. The first is the development of an imager for clinical use, with the techniques established in this thesis. Clinical experience will provide the best assessment of the camera and will help to define the most convenient size and shape for it. It is also important to understand the impact of a worse energy resolution compared to Anger cameras, which may or may not have implications on the camera design.

Secondly, research is required into using VLPCs as a replacement for PSPMTs. The techniques for operating VLPCs can be easily borrowed from high-energy physics experiments where very similar WSF readout has been performed. The cryogenic techniques required to cool these devices may have to be optimised for operation in a clinical environment. This approach offers excellent spatial resolution which may cause a significant impact in image quality and specially in the detection of smaller tumours which is the final goal of the development of new gamma cameras for scintimammography.

Appendix A

Energy resolution of inorganic scintillators coupled to PMTs

Several studies have been dedicated to establish the relative importance of the three terms in equation 3.5 to determine the energy resolution R of the most common inorganic scintillators. A summary of the most important findings follows. Refer to the main text in section 3.1.3 for some of the definitions of abbreviated terms and variables used in this discussion.

A.1 PMT resolution

The PMT resolution, R_{PMT} , depends on the mean number of photoelectrons created ($\bar{n}_{phe} = \bar{N}_{ph}\bar{T}$) and the variance of the dynode multiplication process $v(G)$. It is known to be one of the most relevant factors determining the energy resolution obtainable with scintillation counters. This term can be estimated experimentally by illuminating the PMT with a light flasher which delivers $N_{ph} \pm \sqrt{N_{ph}}$ per pulse. The value of $v(G)$ can be measured by analysing the width of the single photoelectron peak (see section 5.3 for an example of the single photoelectron peak of a PMT).

The joint contributions from R_T and R_i can be estimated experimentally by measuring R and R_{PMT} . The value of R is obtained by analysing the signals from a scintillator coupled to a PMT, when the scintillator is irradiated with a gamma ray source. R_{PMT} is found by illuminating the same PMT with a light flasher whose intensity is adjusted to create a charge Q similar to that created with the scintillator. Figure A.1 shows a schematic representation of typical data obtained using this technique. Similar curves are obtained for various types of scintillators [27, 206, 207].

Using this technique, several authors have reported that the combined

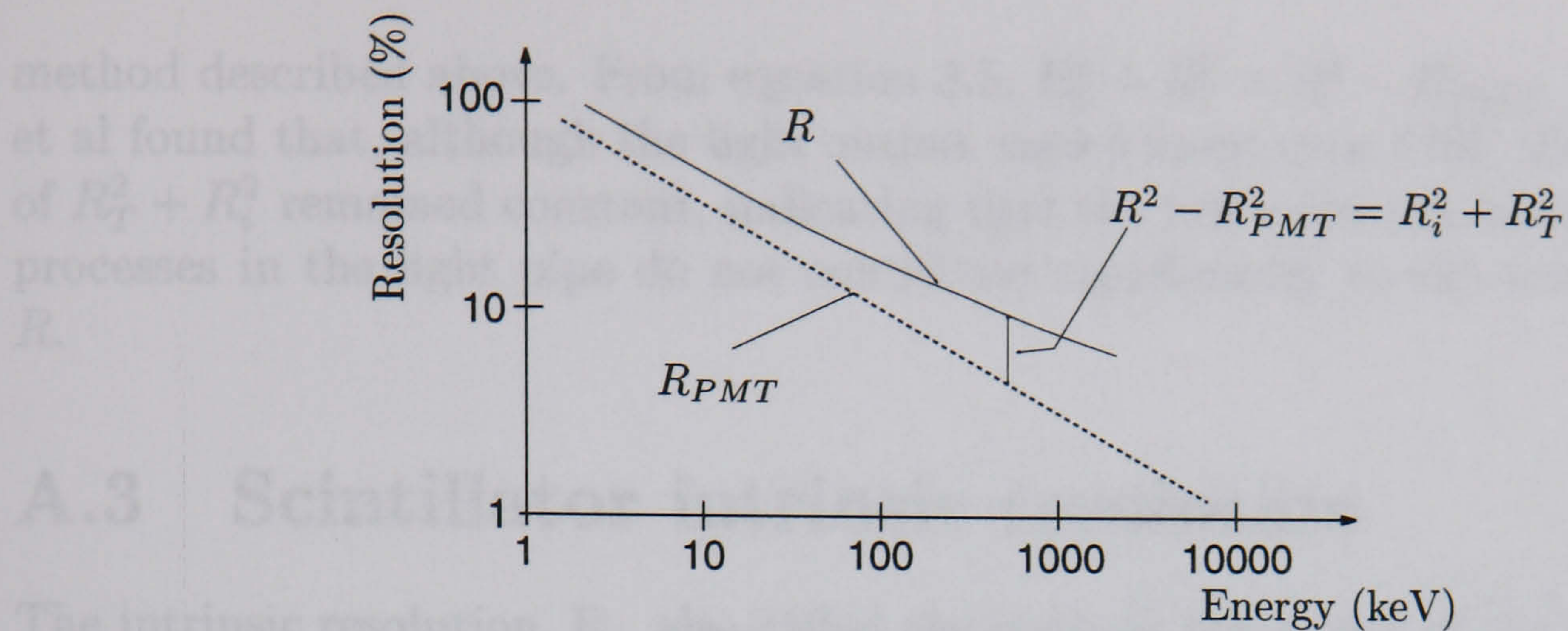


Figure A.1: Schematic curves for the energy resolution R obtained with a scintillator coupled to a PMT compared to the resolution R_{PMT} obtained with a light flasher directly coupled to the PMT.

effect of R_T and R_i is of the same order as R_{PMT} [208, 206] for NaI(Tl). A review of the response of several scintillators to gamma rays by P. Dorenbos et al [209] arrived at the same conclusion for many other scintillator materials, e.g. CsI(Tl), CsI(Na), BGO, LSO.

The individual contributions of R_T and R_i are not easily measurable. However, some experimental results together with theoretical and Monte Carlo studies have been made by several authors to try to clarify this question, some of which are discussed below.

A.2 Transfer resolution

The transfer resolution, R_T , is related to the fluctuations in the probability that a given scintillation photon created in the crystal results in a photoelectron collected by the first dynode of the photomultiplier tube. These fluctuations can arise from several factors such as the variable wavelength of the photon, the quantum efficiency of the photocathode at this wavelength, the spatial uniformity of the photocathode, the angle of incidence of the photon on the photocathode, the reflective coating on the crystal's edges and their surface treatment, the optical coupling between the crystal and the PMT, the collection efficiency of the first dynode.

In an attempt to estimate the importance of the transfer efficiency Kelley et al [208] used different light pipes, each with different light attenuation, to couple a NaI(Tl) crystal to a PMT. The value of R for 662 keV gamma rays was measured for each case and R_{PMT} was found with the light flasher

method described above. From equation 3.5, $R_T^2 + R_i^2 = R^2 - R_{PMT}^2$. Kelley et al found that, although the light output varied more than 50%, the value of $R_T^2 + R_i^2$ remained constant, indicating that the reflection and absorption processes in the light pipe do not contribute significantly to the resolution R .

A.3 Scintillator intrinsic resolution

The intrinsic resolution, R_i , also called the intrinsic line-width of the scintillator, represents the statistical fluctuations in the production of scintillation photons $v(N_{ph})$.

For an ideal scintillator, the light output (defined by the number of photons N_{ph}) should be proportional to the gamma ray energy deposited. However, it is known that for most scintillators the light output per unit energy L_γ deposited varies with the energy of the incident gamma rays [210, 211, 209]. Generally these variations are particularly high for incident gamma rays of less than 100 keV and can be as large as 30%. Figure A.2 shows some examples of L_γ versus incident gamma ray energy or gamma response curves. For an ideal scintillator the response should be a horizontal line.

For the gamma ray energies in nuclear medicine (maximum 511 keV), a total absorption gamma ray interaction in the scintillator may occur through a single photoelectric event or by one or more Compton events followed by a photoelectric final absorption. In either case, one or more energetic electrons are created. Since the scintillation is generated through the energy loss of these electrons, the non-proportional response in figure A.2 must be due to a non-proportionality of the light yield to energetic electrons [212, 213, 214, 215, 216, 207].

A monoenergetic source of gamma rays interacts in the scintillator creating different numbers of electrons with different sets of energies depending on the specific history of a given event, which is statistically determined by the cross-sections for the successive interactions. Due to the non-proportional electron response, the light yield for a given gamma ray interaction depends on the particular electron distribution generated, which adds to the statistical fluctuations of N_{ph} .

Fluctuations in the photon production may also arise from a non-uniform distribution of the activator sites throughout the crystal volume, causing light output variations depending on the location of the gamma ray interaction.

Based on these considerations, the intrinsic resolution can be divided in two independent components

where R_{int} refers to intrinsic resolution distribution in the crystal and R_{ext} refers to the proportionality of scintillation response. R_{int} can be identified as R_{ext} . Some authors have shown that R_{int} is dependent of the size of the crystal, indicating that R_{int} is not a constant.

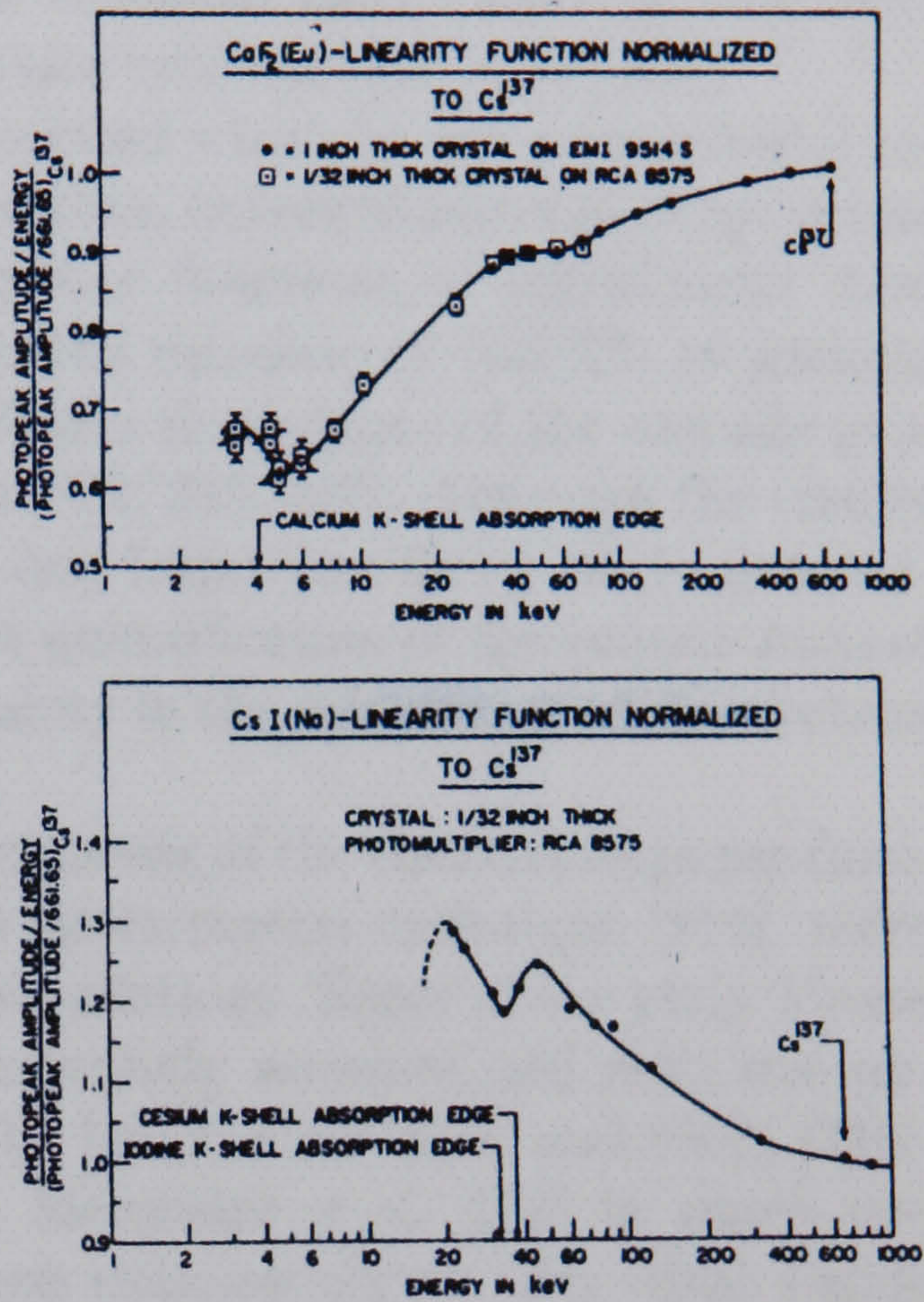
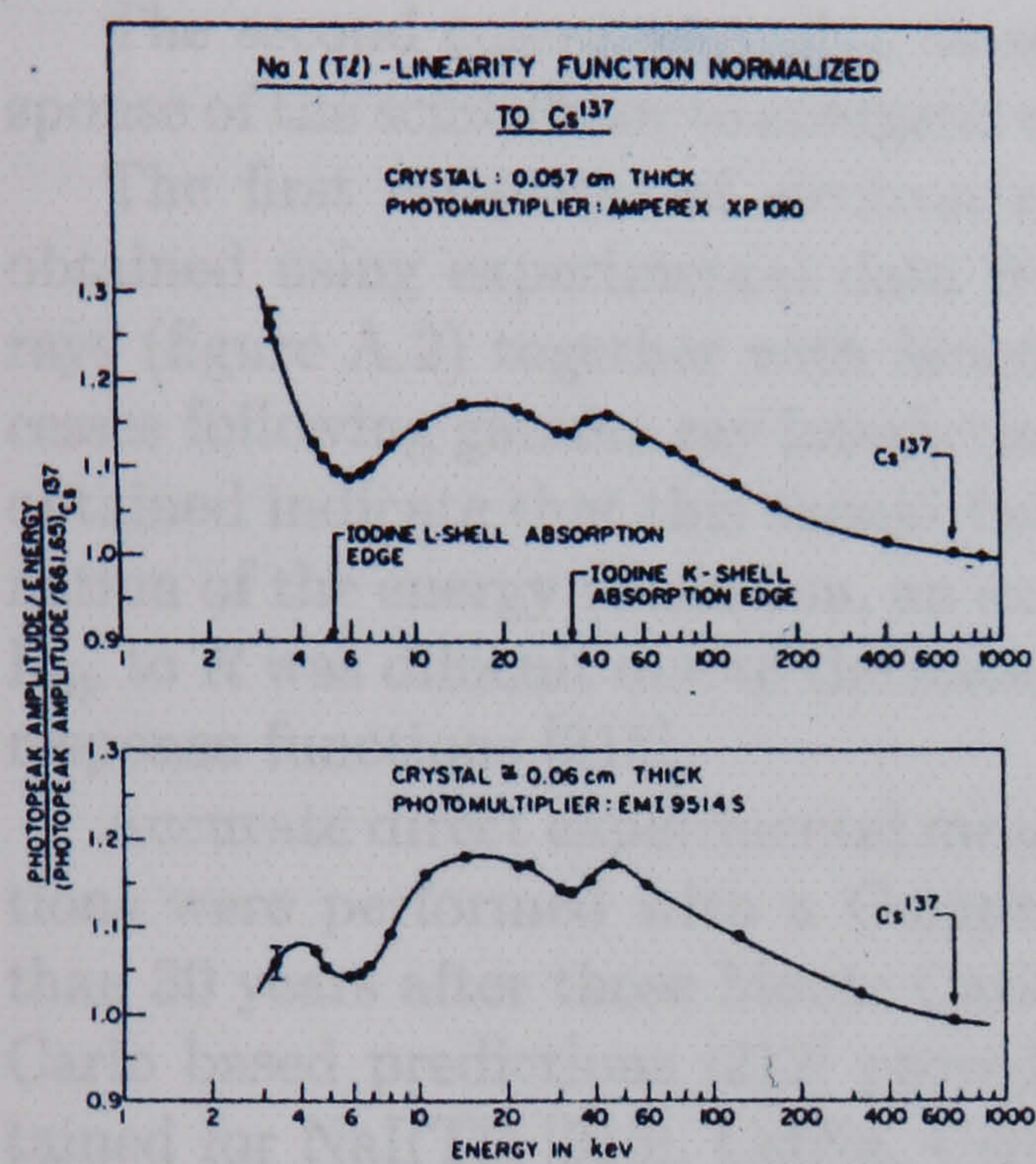


Figure A.2: Gamma ray response functions for some common scintillators [209] - NaI(Tl), CsI(Na) and CsI(Tl) . The plots show the gamma response (light yield per unit of gamma ray energy) as a function of the gamma ray energy. Being correlated to the electron response functions, these curves indicate a strong contribution of non-proportionality to the energy resolution of the scintillation counter.

$$R_i^2 = R_{inh}^2 + R_{np}^2.$$

where R_{inh} refers to fluctuations due to inhomogeneity of activator site distribution in the crystal and R_{np} refers to fluctuations due to the non-proportionality of scintillation response.

R_{inh} can be minimized by the improvement of crystal growing techniques. Some authors have shown that, for NaI(Tl), the resolution R is almost independent of the size of the crystal for a similar light collection efficiency, indicating that R_{inh} should not be a major contribution to R [208].

The second component, R_{np} , is associated with the non proportional response of the scintillator to energetic electrons, or scintillator non-proportionality.

The first estimates of electron response functions of scintillators were obtained using experimental data from the response of NaI(Tl) to gamma rays (figure A.2) together with Monte Carlo simulations of the cascade processes following gamma ray interactions [212, 213, 217]. Although the results obtained indicate that this should be a very important factor in the determination of the energy resolution, an exact quantification of the contribution of R_{np} to R was difficult due to the uncertainty in the calculation of the electron response functions [218].

Accurate direct experimental measurements of the electron response functions were performed with a Compton spectrometer technique [214], more than 30 years after those Monte Carlo simulations. Some of the early Monte Carlo based predictions [212] proved extremely accurate and data was obtained for NaI(Tl) [215], CsI(Na), CsI(Tl), BGO, LSO, YAP and CaF₂ [216]. Figure A.3 shows the results from W. Mengesha et al. [216] in which two general shapes were found for the electron response curves. The alkali halide scintillators have a maximum response at 10 keV whereas the electron response of the other scintillators increases monotonically with electron energy. From the curves, it is seen that, of the alkali halides, CsI(Na) has the higher non-proportionality to energetic electrons. Also interesting to note is that YAP's response approximates that of an ideal scintillator, i.e., its electron response function is approximately a horizontal line.

As discussed above, the contributions to R , other than R_{PMT} , are a combination of several factors. In most cases, it is not possible to establish the absolute contribution of the non-proportionality since there are many other factors involved (e.g. R_{inh} , R_T). Based on these accurate measurements of the electron response functions, Valentine et al [207] estimated this contribution by convoluting the response functions of figure A.3 with electron energy distributions found by Monte Carlo methods for a given gamma ray energy. The results obtained for NaI(Tl) and LSO show that R_{np} should be a major

contribution to R .

Experimental evidence of this fact has also been found in recent results for high quality YAP samples which show an excellent total energy resolution of $R=4.38\%$ for 662 keV gamma rays with a PMT contribution of $R_{PMT}=4.18\%$, indicating that the contributions R_i and R_T resolution add up to only 1.3%, the best result ever observed for a scintillator [30]. This is consistent with the close to ideal response of YAP to electrons as shown in figure A.3. This indicates that there is in fact a strong correlation between the non-proportional light output of scintillators and the total energy resolution.

Another experimental indication of this correlation is the poor energy resolution found for LSO despite its relatively high light yield [157], which can be explained by the strong non-proportionality to electrons shown in figure A.3.

In summary, results and calculations up-to-date seem to indicate that the major contributions to R come from R_{np} and R_{PMT} for gamma ray energies between 30 and 1000 keV.

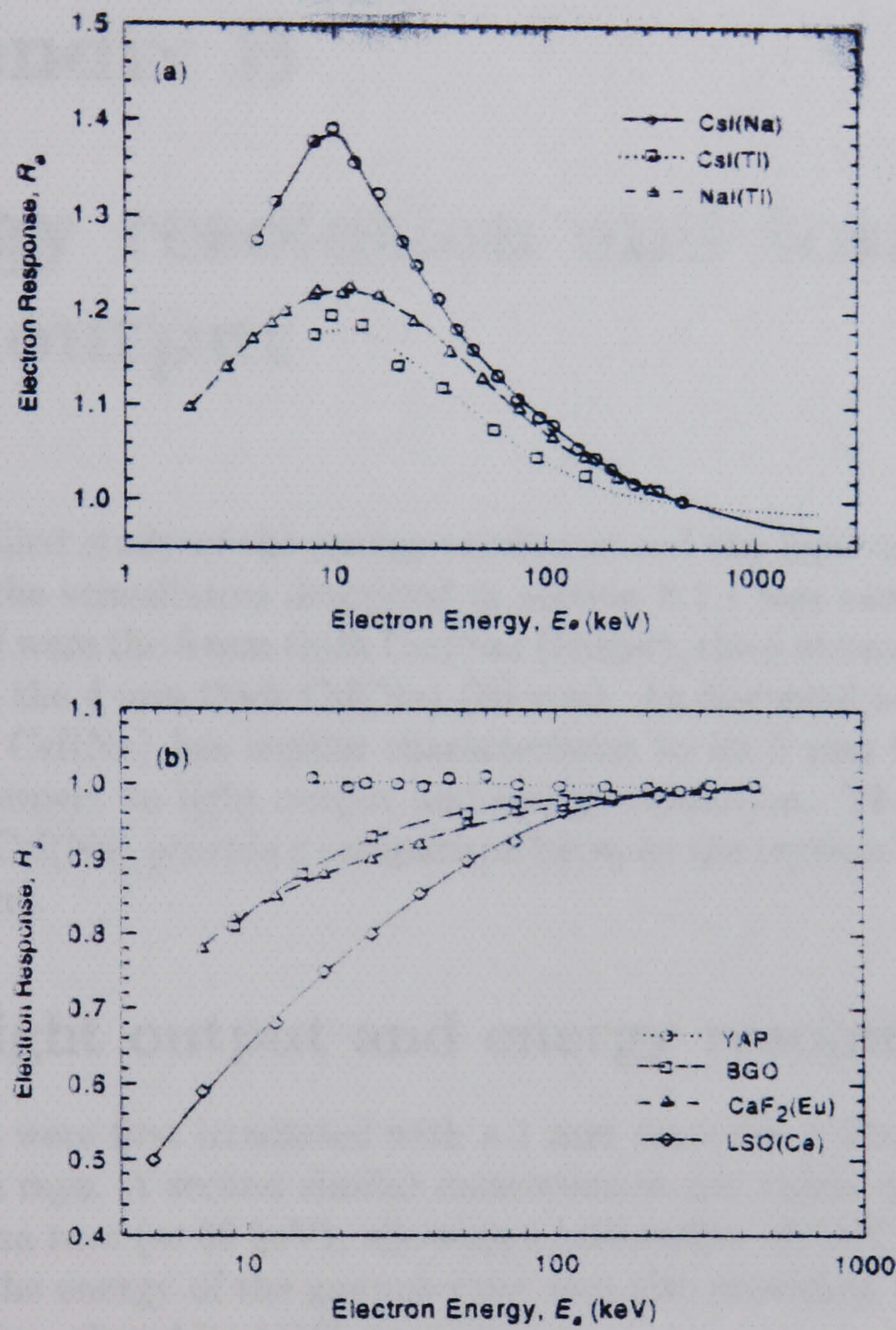


Figure A.3: Electron response functions for some common scintillators [216]. The plots show the electron response (light yield per unit of electron energy) as a function of the electron energy.

Appendix B

Energy resolution and total light output

A more detailed study of the energy resolution and the light output of three of the four the scintillators described in section 8.1.1 was carried out. The crystals used were the 5 mm thick CsI(Na) (Hilger), the 5 mm thick NaI(Tl) (Hilger) and the 4 mm thick CsI(Na) (Bicron). As discussed section 8.2, the 3 mm thick CsI(Na) has similar characteristics to its 5 mm thick counterpart, with respect to light output and energy resolution. The tests on the 4 mm thick CsI(Na) provide a comparison between the crystals from different manufacturers.

B.1 Light output and energy resolution

The crystals were first irradiated with a 1 mm diameter collimated beam of Co^{57} gamma rays. A second similar measurement was taken with a beam of Am^{241} gamma rays (≈ 60 keV), allowing a calibration of ADC channels as a function of the energy of the gamma rays, and also providing an estimate of the electronic pedestal in ADC channels.

The relative position of the CsI(Na) crystals, the E-PMTs and the gamma ray beams is shown in figure 8.5. The smaller NaI(Tl) crystal was centered on E-PMT2 (in the same figure), with the gamma ray beams centered on the crystal.

Table B.1 shows a summary of the result, including calculations performed on the gamma ray peaks in the pulse-height distributions obtained for each acquisition, for two different signals: i) the energy signal from the *hardware sum* and ii) the signal from E-PMT2. Since the area of the NaI(Tl) crystal is smaller than the entrance window of the E-PMTs, almost 100% of

Crystal (thickness)	gamma-ray energy (keV)	ADC mean		ADC rms		Energy Resolution	
		HS	E-PMT2	HS	E-PMT2	HS	E-PMT2
CsI(Na) (5mm)	60	280	234	25.6	25	21.5%	23%
	122	569	475	48.6	41.2	20%	19.5%
NaI(Tl) (5mm)	60	391	394	25.4	25.2	15.3%	15.2%
	122	795	802	48.2	48.5	14.2%	14.3%
NaI(Tl) (5mm)with teflon	60	454	460	36.5	36.5	18%	18%
	122	922	937	51.5	52.7	13%	13%
CsI(Na) (4mm)	60	276	225	23.9	24.9	20.3%	23.2%
	122	562	458	43.8	38.3	18.3%	18.6%

Table B.1: Results of the evaluation of the scintillation crystals without WSFs coupled to their surfaces. The values for the ADC mean (after pedestal subtraction) and rms are in arbitrary units (ADC channels). A Gaussian distribution is fitted to the 122 keV peak and the energy resolution is calculated using equation 3.1. For each measurement the values shown correspond to the *hardware sum* signal (HS) and to the E-PMT2 signal.

the light is collected by E-PMT2 for this crystal. For the larger CsI(Na) crystals, it is seen that about 90% of the signal is collected by E-PMT2 and, therefore, the *hardware sum* signal is about 10% higher than the E-PMT2 signal. These results are taken from Gaussian fits to the pulse-height distributions (similar to those in figure 8.6).

The results for the two CsI(Na) crystals from different manufacturers are very similar. On the other hand the NaI(Tl) crystal provides a higher signal and better energy resolution, possibly due to a higher light output.

After the first measurement, the NaI(Tl) crystal was covered with two layers of a white teflon sheet to increase the light collection. The corresponding results are also shown in the table. This led to a 20% signal increase, with a small improvement in energy resolution from 14% to 13%.

B.2 Components of the energy resolution

As discussed in section 3.1.3, the energy resolution of a scintillation counter can be separated into several components. The component corresponding to the PMT resolution can be estimated by illuminating the PMT directly with a light flasher which delivers $N_{ph} \pm \sqrt{N_{ph}}$ photons per pulse (i.e., whose emission follows Poisson statistics for large N_{ph}). This method also allows

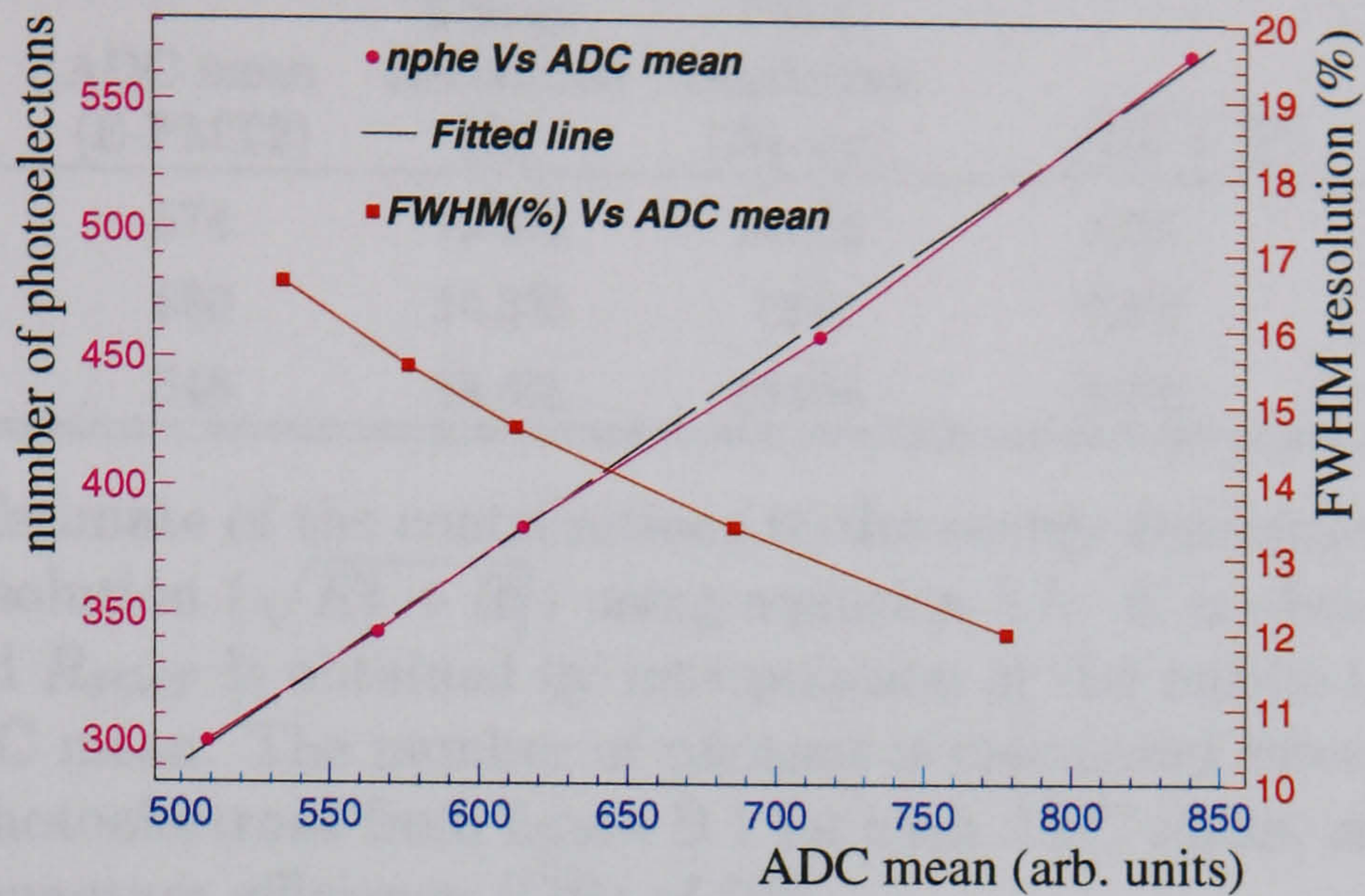


Figure B.1: Composed plot showing both the number of photoelectrons \bar{n}_{phe} and the peak resolution (in % FWHM) as a function of the ADC mean for the LED measurements.

an estimate of the mean number of photoelectrons released from the photocathode, using equation 3.4.

For this purpose, the LED pulsed optical fibre described in section 5.3 was used to directly illuminate the center of the photocathode of E-PMT2. Several measurements were taken with different LED intensities, by adjusting the variable resistor VR shown in figure 5.3. The LED intensities were chosen so that the corresponding means of the ADC peaks covered the range of ADC means obtained for the 122 keV peaks for the three crystals above.

For each LED pulse-height distribution, the mean and the standard deviation of the peak were measured and the mean number of photoelectrons \bar{n}_{phe} released by the photocathode was calculated using equation 3.4, where $\bar{n}_{phe} = \bar{N}_{ph}T$. The calculation assumes a value of $v(G)$ of 0.5 which is typical for a PMT. This is however an empirical choice and a ± 0.2 variation is plausible. Therefore the calculations involving this parameter are affected accordingly and the results shown include an error estimate which takes this variation into account.

Figure B.1 shows a plot of \bar{n}_{phe} against the ADC mean assuming $v(G) = 0.5$. The good fit to a straight line indicates that the LED emission follows a Poisson distribution as assumed in equation 3.4. The same figure shows a plot of the LED peak resolution (defined similarly to the scintillation counter energy resolution) against the ADC mean.

Crystal (mm thick.)	ADC mean (E-PMT2)	Energy Resolution (R)	PMT resolution (R_{PMT})	$\sqrt{R_T^2 + R_i^2}$	N_{ph} (QE=20%)
CsI(Na) (5)	574	19.5%	15.4%	12%	1740 ± 233
NaI(Tl) (5)	830	14.3%	12%	7.5%	2805 ± 374
CsI(Na) (4)	548	18.6%	15.9%	9.7%	1649 ± 219

Table B.2: Estimate of the contributions to the energy resolution other than the PMT resolution ($\sqrt{R_T^2 + R_i^2}$) using equation 3.5. R is obtained experimentally and R_{PMT} is obtained by interpolation of the results in figure B.1 for each ADC mean. The number of photons is calculated interpolating the number of photoelectrons from figure B.1 for each ADC mean, and assuming an average quantum efficiency (QE) of 20%.

Comparing these curves with the results in table B.1 for the ADC mean and the energy resolution obtained with the scintillators, it is possible to estimate two characteristic features of each scintillator:

1. the contribution to the energy resolution R from the transfer resolution and from the scintillator intrinsic resolution. Refer to section 3.1.3, equation 3.5. The value of R_{PMT} for a given ADC mean obtained in a scintillator measurement is estimated by interpolation from the results of the LED measurements (figure B.1).
2. the number of photons hitting the photocathode assuming an average quantum efficiency of 20%. As above, the results for each ADC mean are obtained by interpolation from the results of the LED measurements (figure B.1).

The results are shown in table B.2, where the values for the scintillators listed correspond to the 122 keV gamma ray pulse-height distributions. The errors associated with the number of photons are derived from the ± 0.2 variation in $v(G)$.

The results in the table show that the joint contribution of R_i and R_T is higher for the CsI(Na) crystals than for the NaI(Tl) crystal, which agrees with the results obtained by other authors as discussed in section A.3. In particular, refer to figure A.3, showing the higher non-proportionality to energetic electrons for CsI(Na) compared to NaI(Tl), and related discussion.

This effect leads to worse energy resolution R for CsI(Na) compared to NaI(Tl). Furthermore, as seen above, the signals obtained with the CsI(Na)

crystals were smaller compared to those obtained with the NaI(Tl) crystal, which also contributes to a worse energy resolution.

Appendix C

Operation settings of the R5900-M16s

C.1 Tube A

Figure C.1 shows charge distributions for anode P3 of tube A. Each plot corresponds to a different high voltage. For HV=-950 V and HV=-900 V the single photo-electron peak is clearly separated from the pedestal and the peak corresponding to two photo-electrons is also visible.

From the position of the single photo-electron peak at HV=-950 V it is possible to establish that the gain \bar{G} is about 10 ADC channels, which corresponds to a gain of 1×10^7 .

The response of tube A was compared to that of a standard single anode photomultiplier, EMI 9124 from Electron Tubes, when illuminated with the same light pulses. This PMT has a nominal quantum efficiency of 20% at 500 nm and therefore it is expected to produce a higher number of photo-electrons than the M16. Figure C.2 shows the charge distributions for both tubes. For the EMI 9124 the peaks corresponding to 1 and 2 photo-electrons are not obviously separated as for the M16, indicating poorer single electron resolution. The mean number of photoelectrons is found by the NZEROS method and is 2.7 and 1.9 for the EMI 9124 and the M16 respectively. The difference is consistent with the two photocathodes having quantum efficiency of 20% and 13% respectively at 500 nm as specified.

C.2 Tube B

The response of tube B to an 8 ns wide input pulse for different high voltages is shown in figure C.3 for anode P3. The best separation between the single

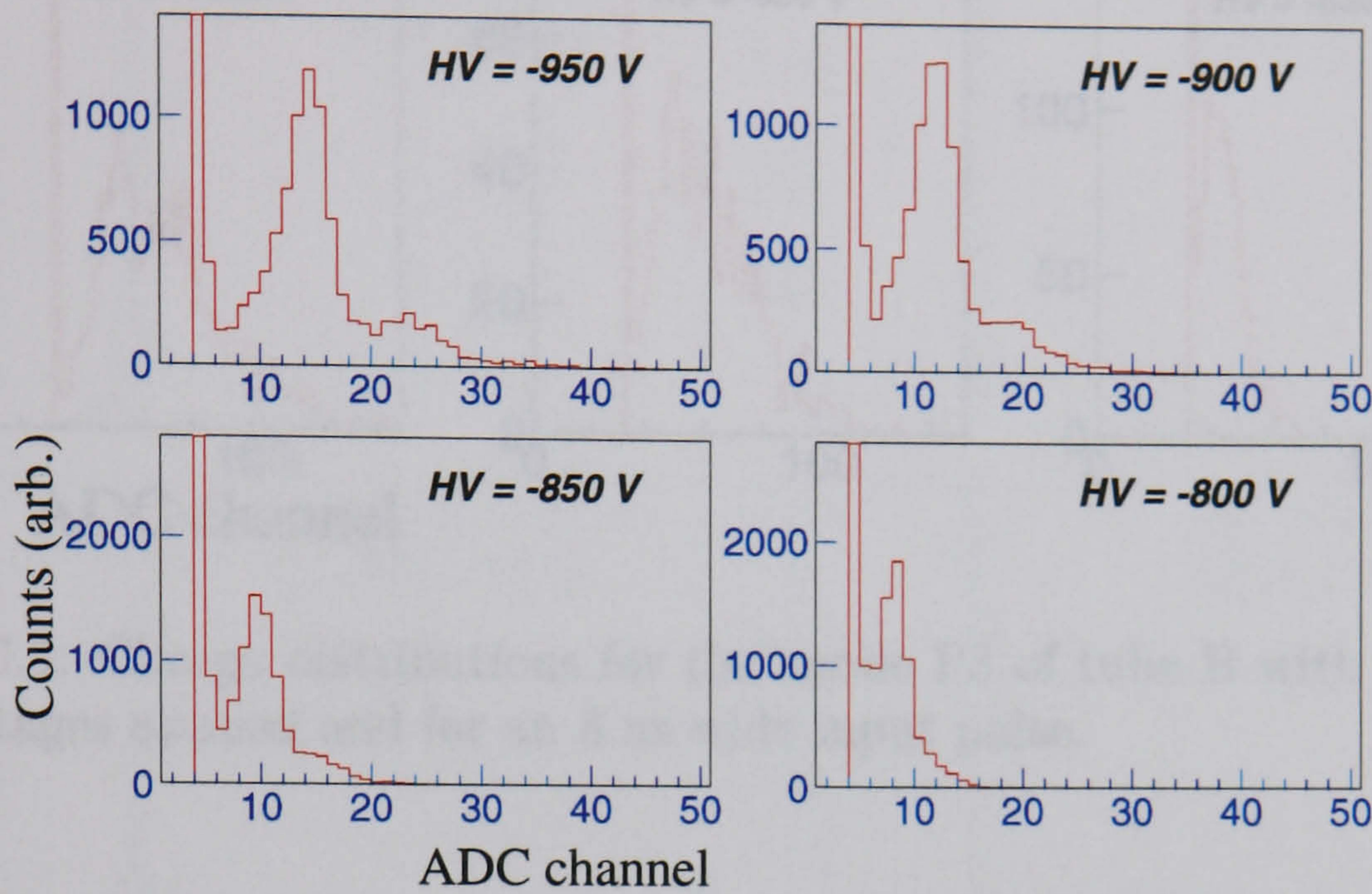


Figure C.1: Charge distributions for the anode P3 of tube A with different high voltages applied and for the same 10 ns wide input pulse.

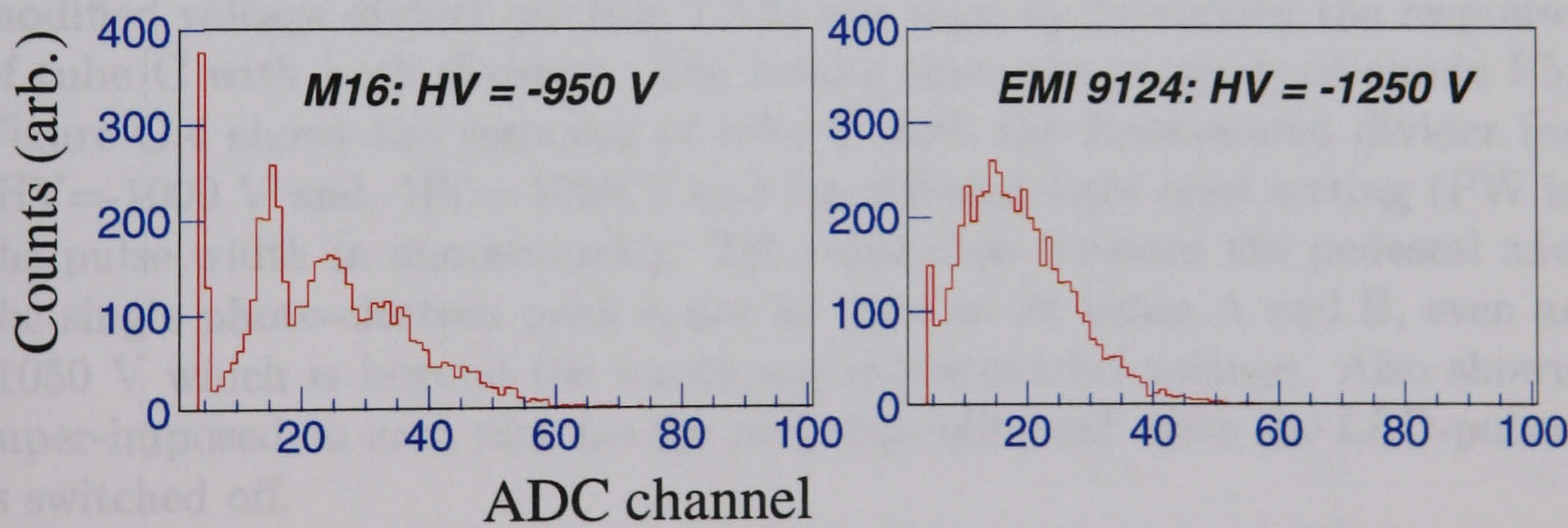


Figure C.2: Charge distributions for the EMI 9124 and for the anode P3 of tube A for the same pulser settings. A -1250 V high voltage is applied to the EMI 9124.

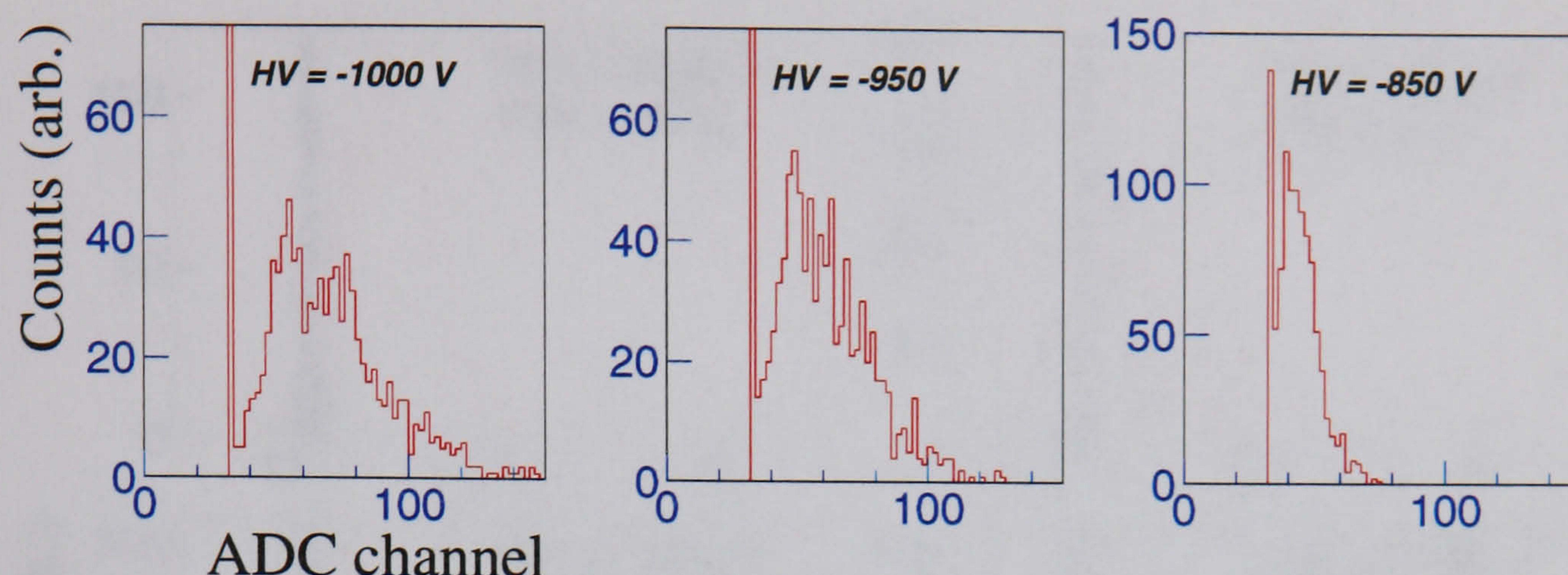


Figure C.3: Charge distributions for the anode P3 of tube B with different high voltages applied and for an 8 ns wide input pulse.

photo-electron peak and the pedestal was obtained at $-HV=-1000$ V, for which the tube showed stable operation. From the position of the single photo-electron peak at $HV=-1000$ V (ADC channel 20) it is seen that tube B has higher gain than tube A.

C.3 Tube C

A comparison between the standard Hamamatsu voltage divider and the modified voltage divider (section 7.3.2) was done by measuring the response of tube C with both dividers. The results show the response of anode P5. Figure C.4 shows the response of tube C with the Hamamatsu divider for $-HV=-1000$ V and $-HV=-1050$ V and for different light level setting (PW is the pulse width in nanoseconds). The separation between the pedestal and the single photo-electron peak is not as clear as for tubes A and B, even at -1050 V which is beyond the maximum recommended voltage. Also shown super-imposed on each plot are the pedestals obtained when the LED-pulser is switched off.

In order to see the signals in more detail, they were amplified using a LeCroy 612A amplifier and the charge distributions obtained with the same ADC are shown in figure C.5 for $-HV=-1000$ V. The pedestal is wider for this case due to higher electronic noise as discussed above, and the single photo-electron peak is not very well separated from the pedestal due to the lower gain of this tube compared to tubes A and B.

Figure C.6 shows the response of tube C with the modified divider.

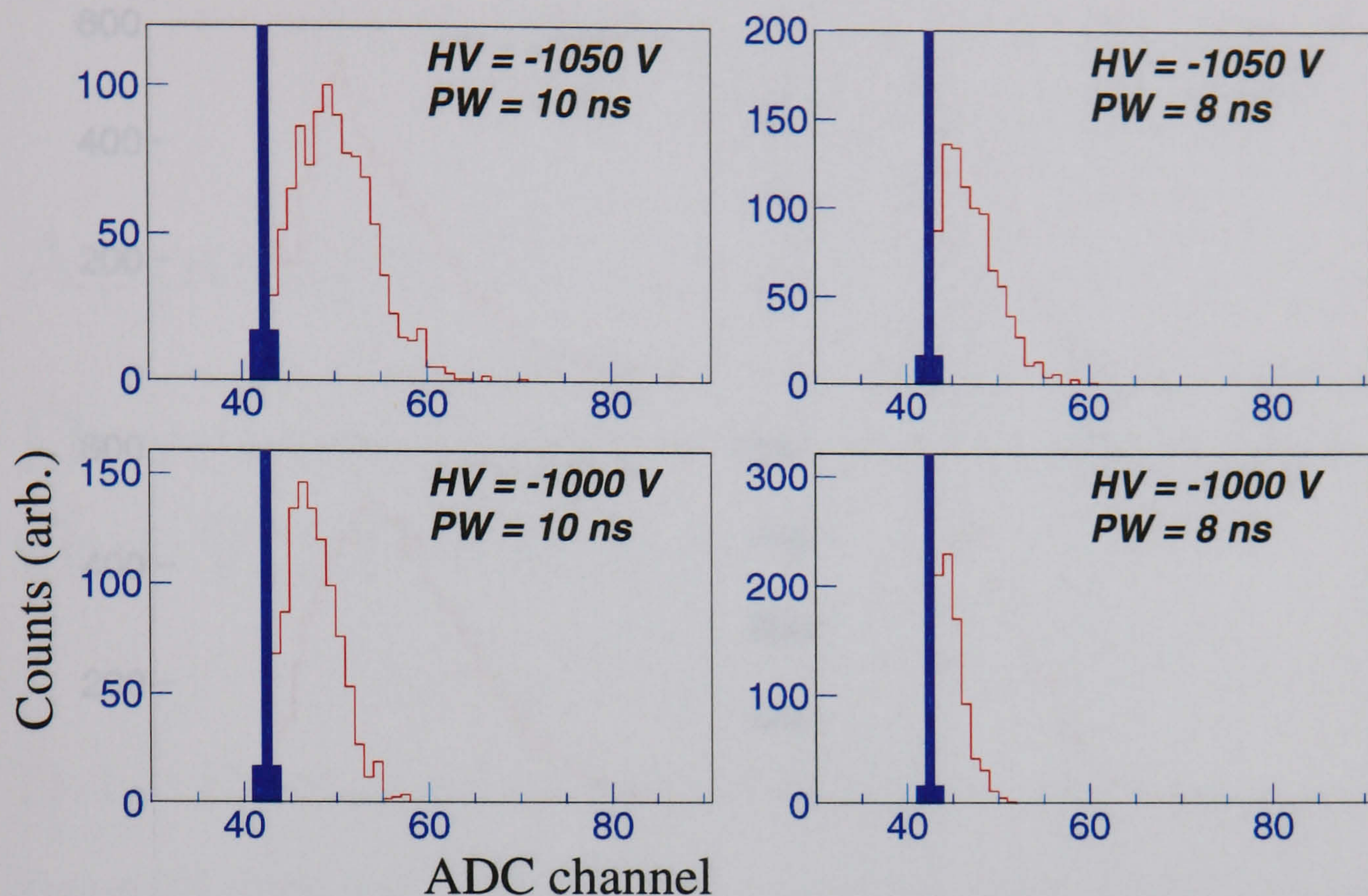


Figure C.4: Charge distributions for the anode P5 of tube C for different high voltages applied. The Hamamatsu voltage divider is used. The pedestal obtained when the LED pulser is switched off is super-imposed on each plot.

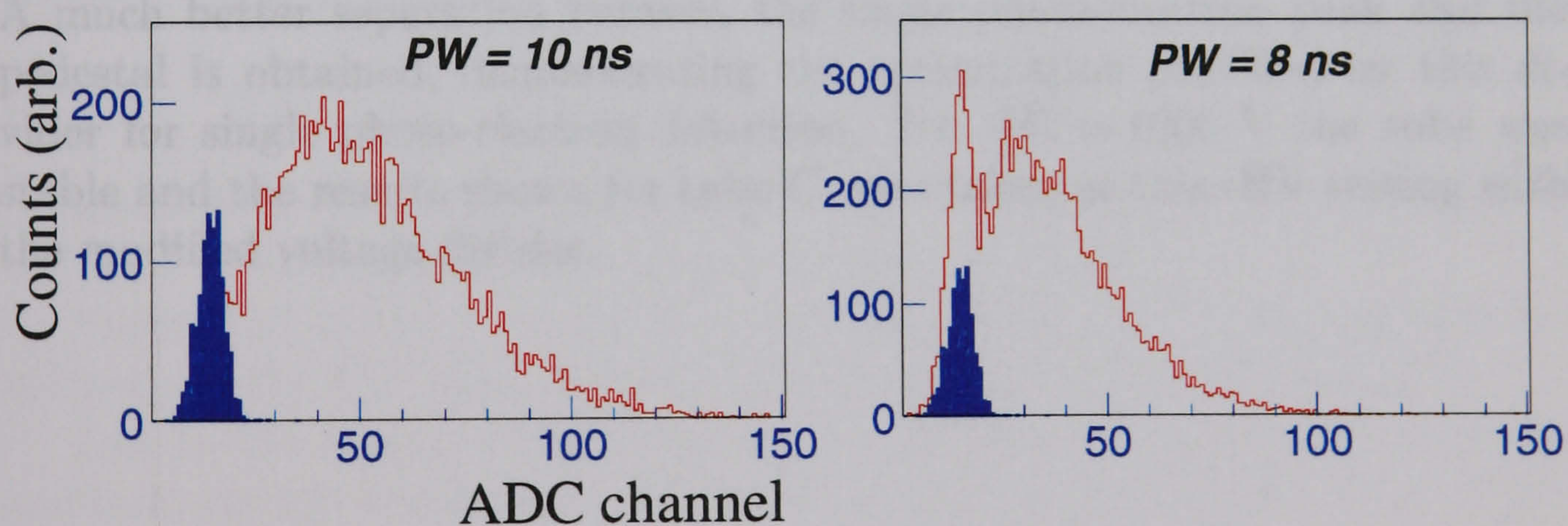


Figure C.5: Charge distributions for the anode P5 of tube C. The M16 signals are amplified with a LeCroy 612A amplifier and the Hamamatsu voltage divider is used. The pedestal obtained when the LED pulser is switched off is super-imposed on each plot.

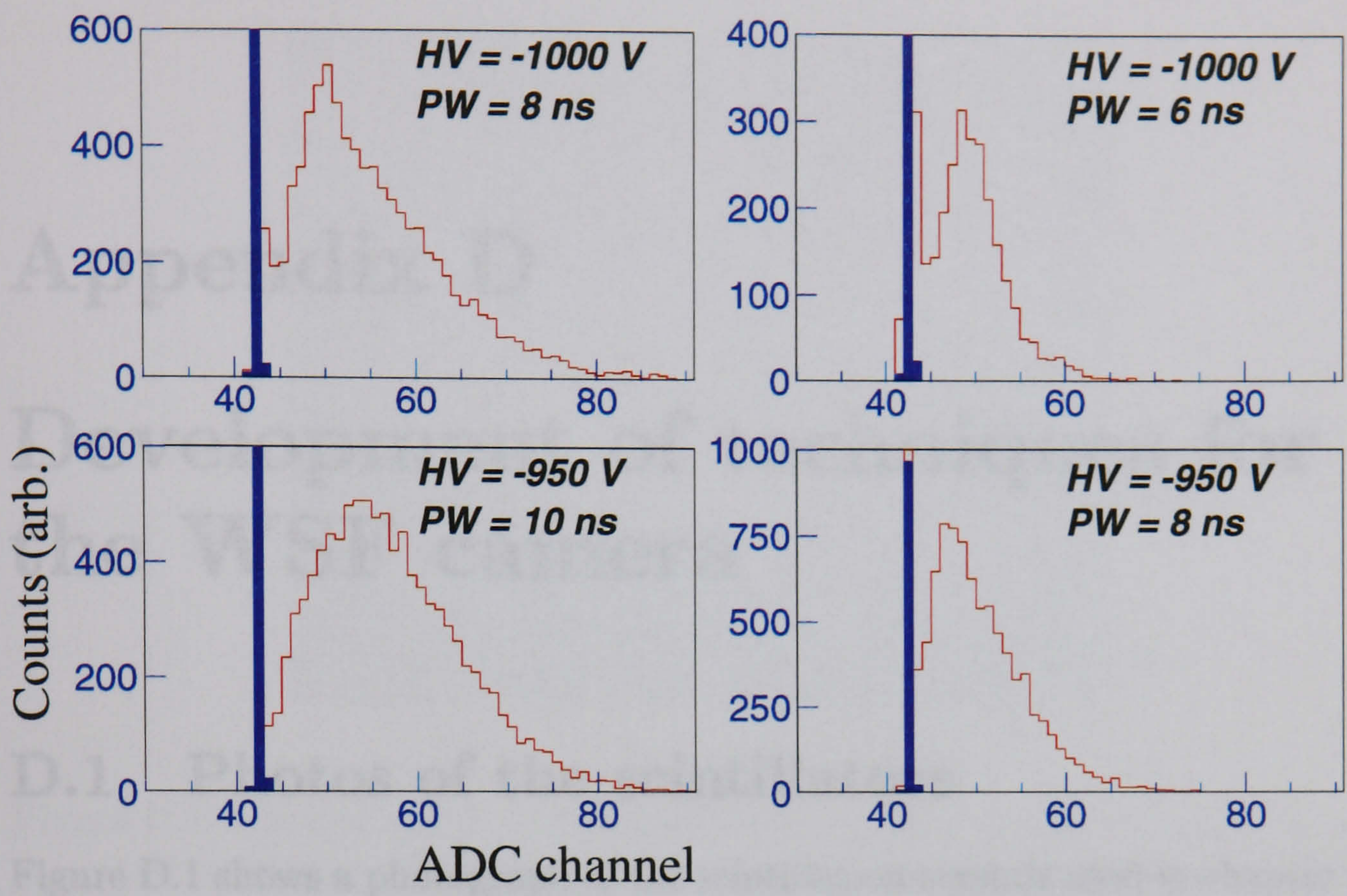


Figure C.6: Charge distributions for the anode P5 of tube C with different high voltages applied. The modified voltage divider is used to optimise the single photo-electron response. The pedestal is shown in blue.

A much better separation between the single photo-electron peak and the pedestal is obtained, demonstrating the optimization provided by this divider for single photo-electron detection. For $-HV=-1000\text{ V}$ the tube was stable and the results shown for tube C were taken at this $-HV$ setting with the modified voltage divider.

Appendix D

Development of techniques for the WSF camera

D.1 Photos of the scintillators

Figure D.1 shows a photograph of the scintillation crystals used in chapter 8.

D.2 Photo of the E-PMTs

Figure D.2 shows a photograph of the array of E-PMTs used in chapter 8.

D.3 Electronics readout

D.3.1 Readout channels and timing

Figure D.3 shows a diagram of the electronic readout system developed for the WSF gamma camera prototype described in chapter 8.

Figure D.4 shows a timing diagram of the electronic readout system developed for the WSF gamma camera prototype described in chapter 8.

Due to the similar performance obtained with and without the sample-and-hold circuit, the experiments presented in chapter 8 do not use sample-and-hold.

The ADC triggers on the falling edge of the trigger pulse which has an adjustable width. The trigger width was adjusted so that its falling edge occurs simultaneously with the peak of the M16 pulses.

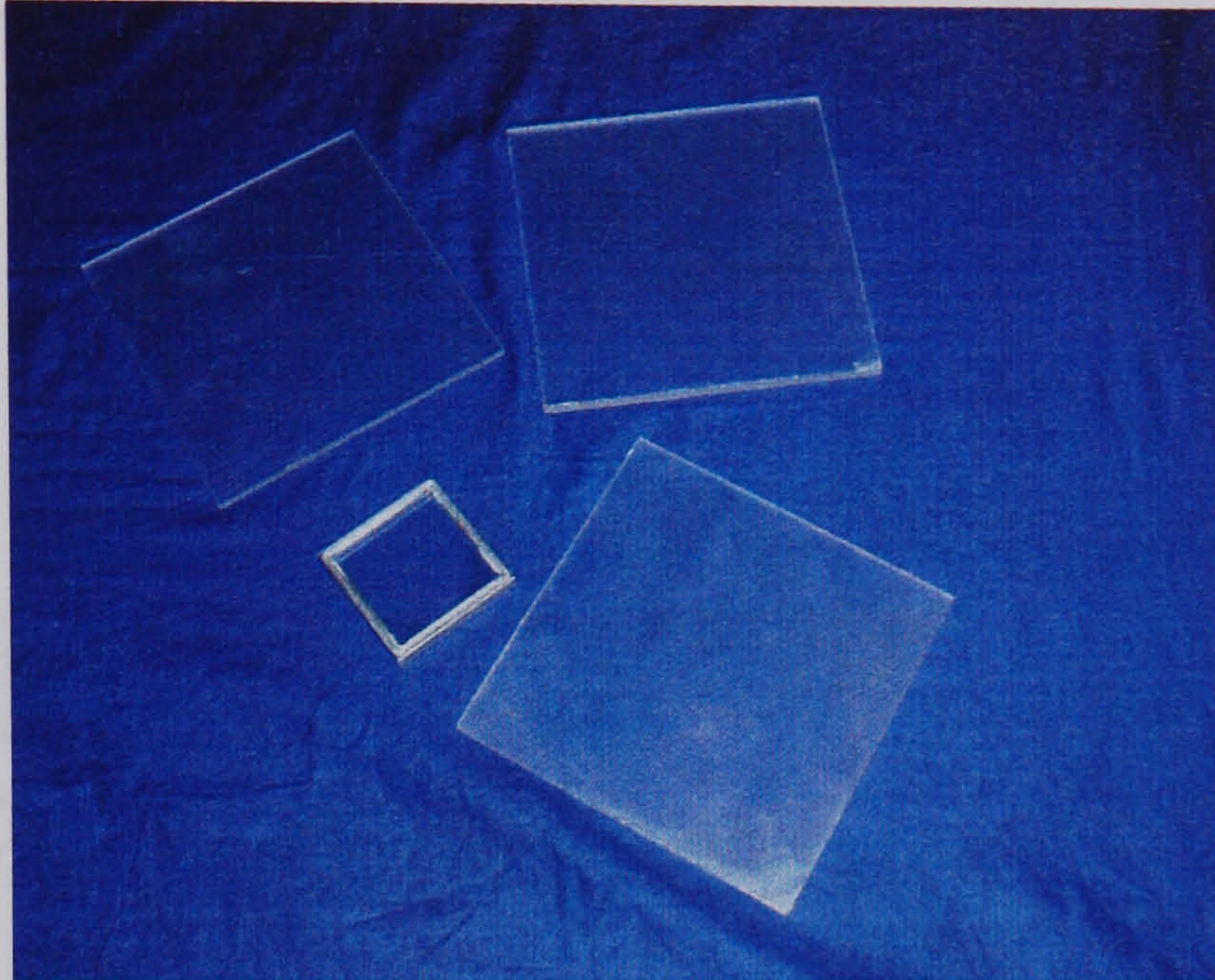


Figure D.1: Photograph of the 4 scintillation crystals used in the experiments described in chapter 8. Crystals 1 and 2 were also used in the experiments described in chapter 5.

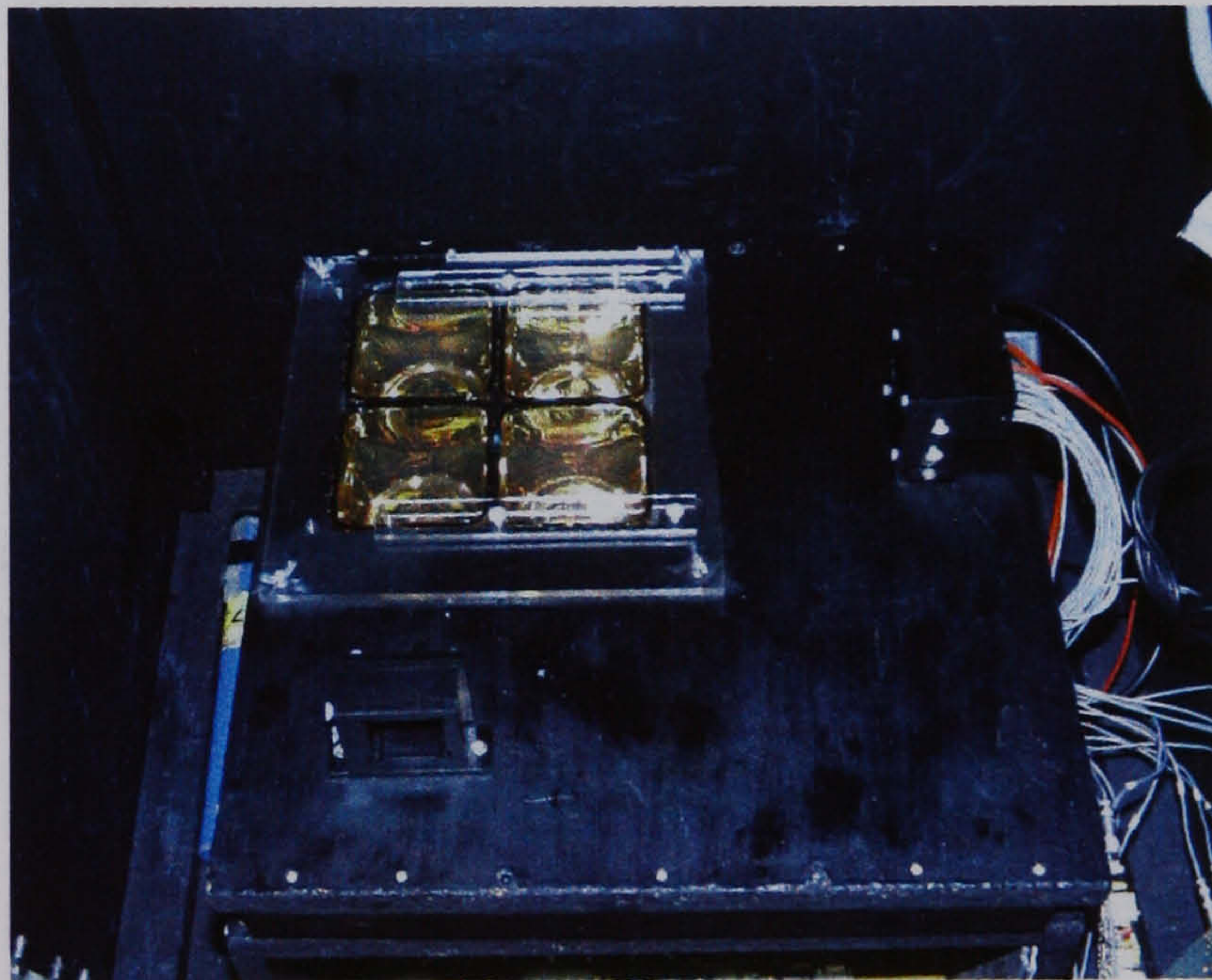


Figure D.2: Photograph of the 4 E-PMTs assembled in a 2×2 matrix for the experiments described in chapter 8.

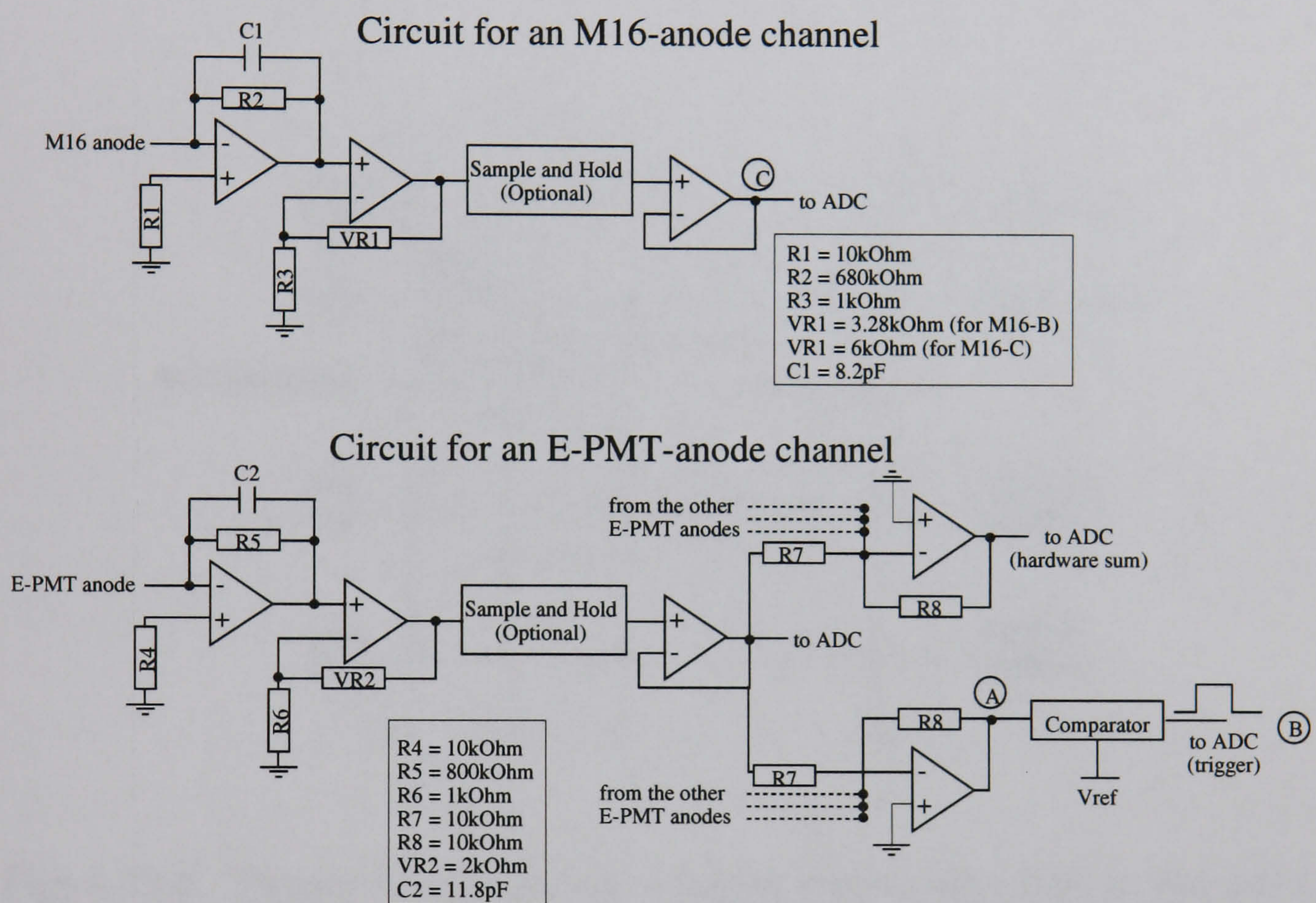


Figure D.3: Diagram of the two types of readout channels used in the experiments described in chapter 8: for the M16 channels and for the E-PMT channels.

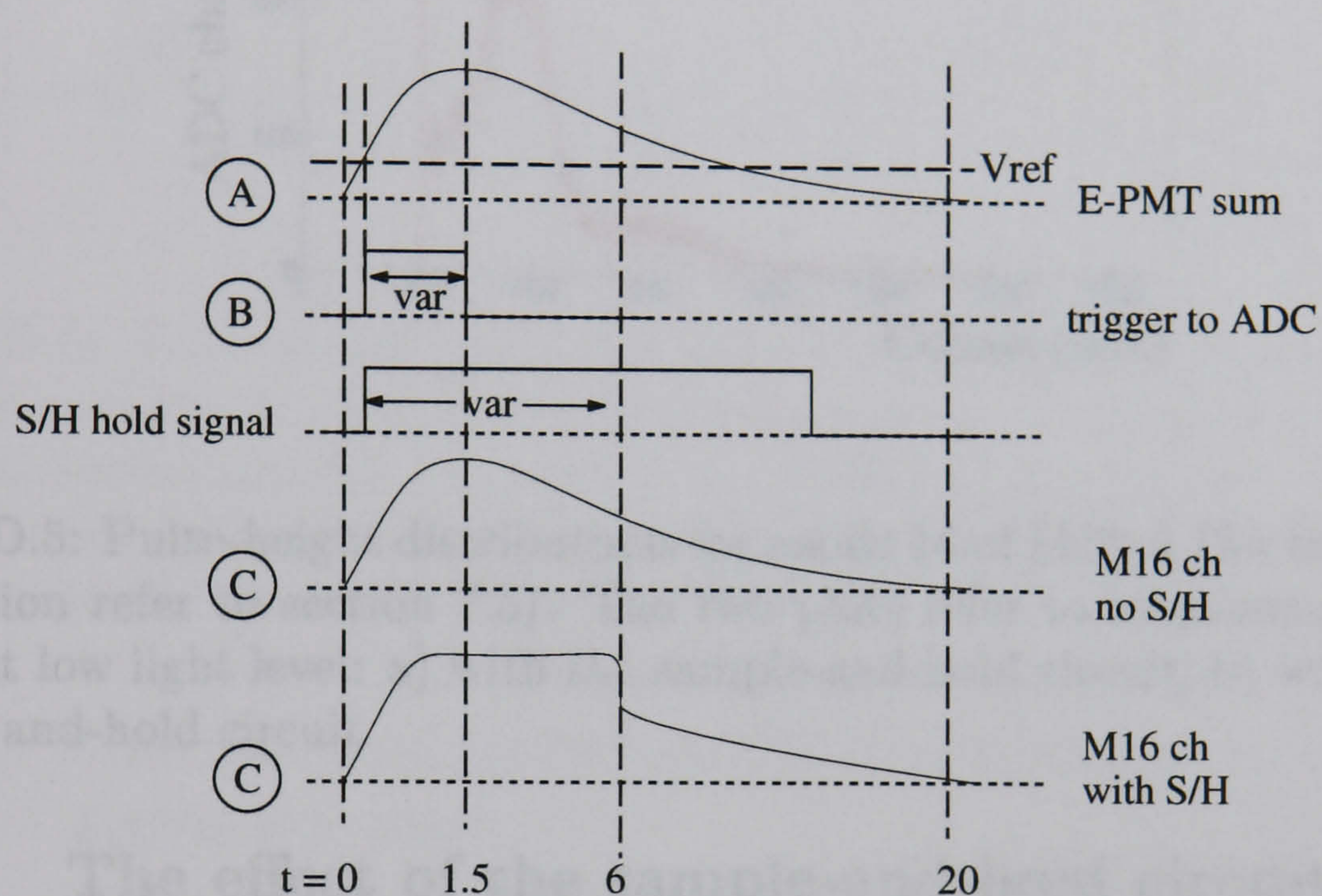


Figure D.4: Timing diagram for the readout system described in chapter 8. The numeric values are in μs units and the signals correspond to the points A, B and C in figure D.3. Typical signals for the M16 channels are shown for the cases where the sample-and-hold circuit was used and for no sample-and-hold.

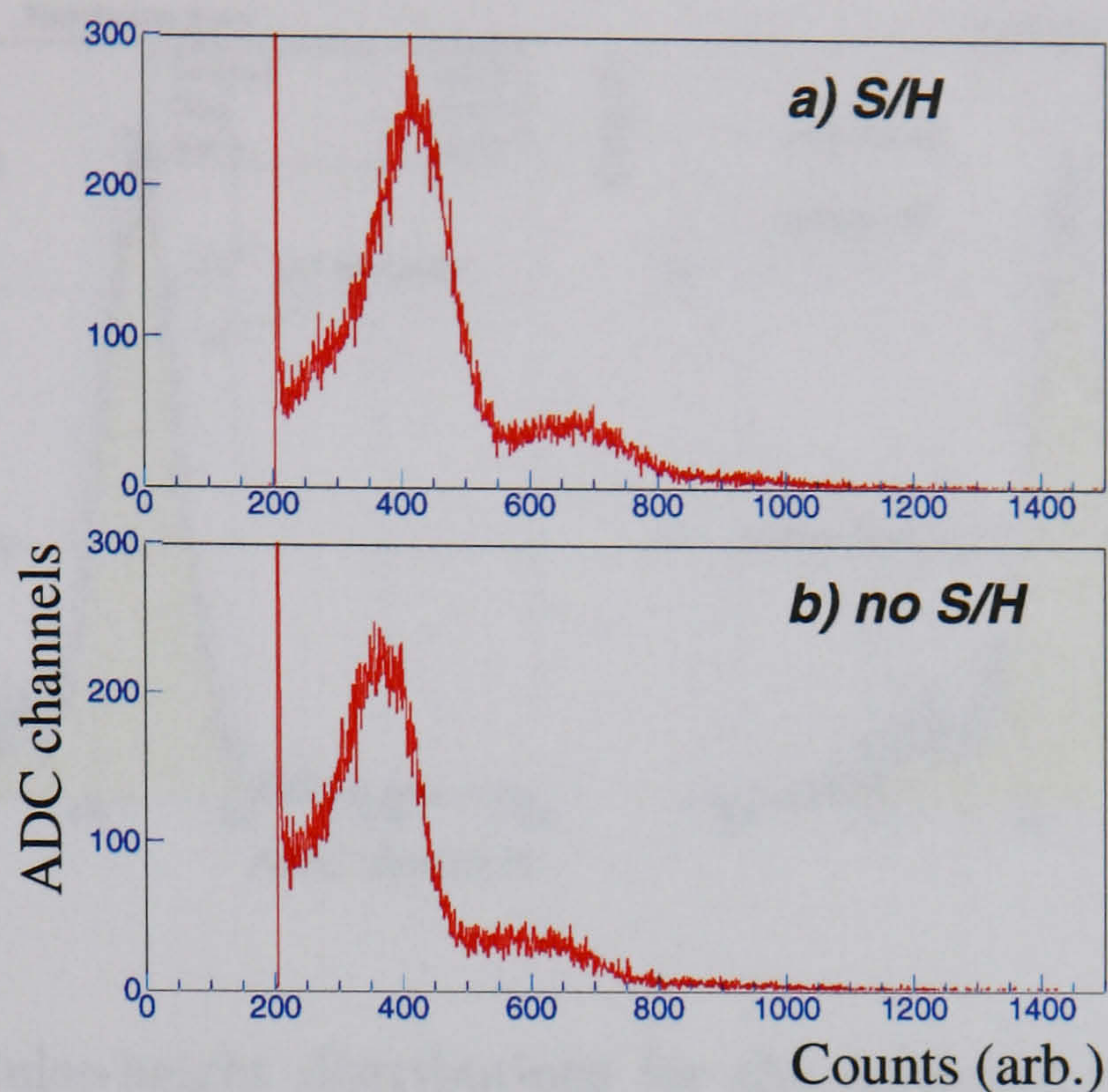


Figure D.5: Pulse-height distributions for anode 16 of M16-A (for the naming convention refer to section 7.3). The two plots refer to measurements at a constant low light level: a) with the sample-and-hold circuit; b) without the sample-and-hold circuit.

D.3.2 The effect of the sample-and-hold circuit

Figure D.5 shows the pulse-height spectrum for an M16 anode for two different configurations of the readout electronics used in chapter 8: a) with the sample-and-hold circuit and b) without the sample-and-hold circuit.

Both measurements were carried out with the experimental set-up described in section 5.2 with the 5 mm thick CsI(Na) crystal. The signal from the 5" E-PMT was used as the energy signal and to generate the ADC trigger, and fibre 5 in figure 5.1 was read out with anode 16 of the M16-A PSPMT (refer to section 7.3 for a description of this PSPMT).

It is seen that the two distributions are very similar, and therefore, for simplicity, no sample-and-hold is used in the measurements shown in chapter 8.

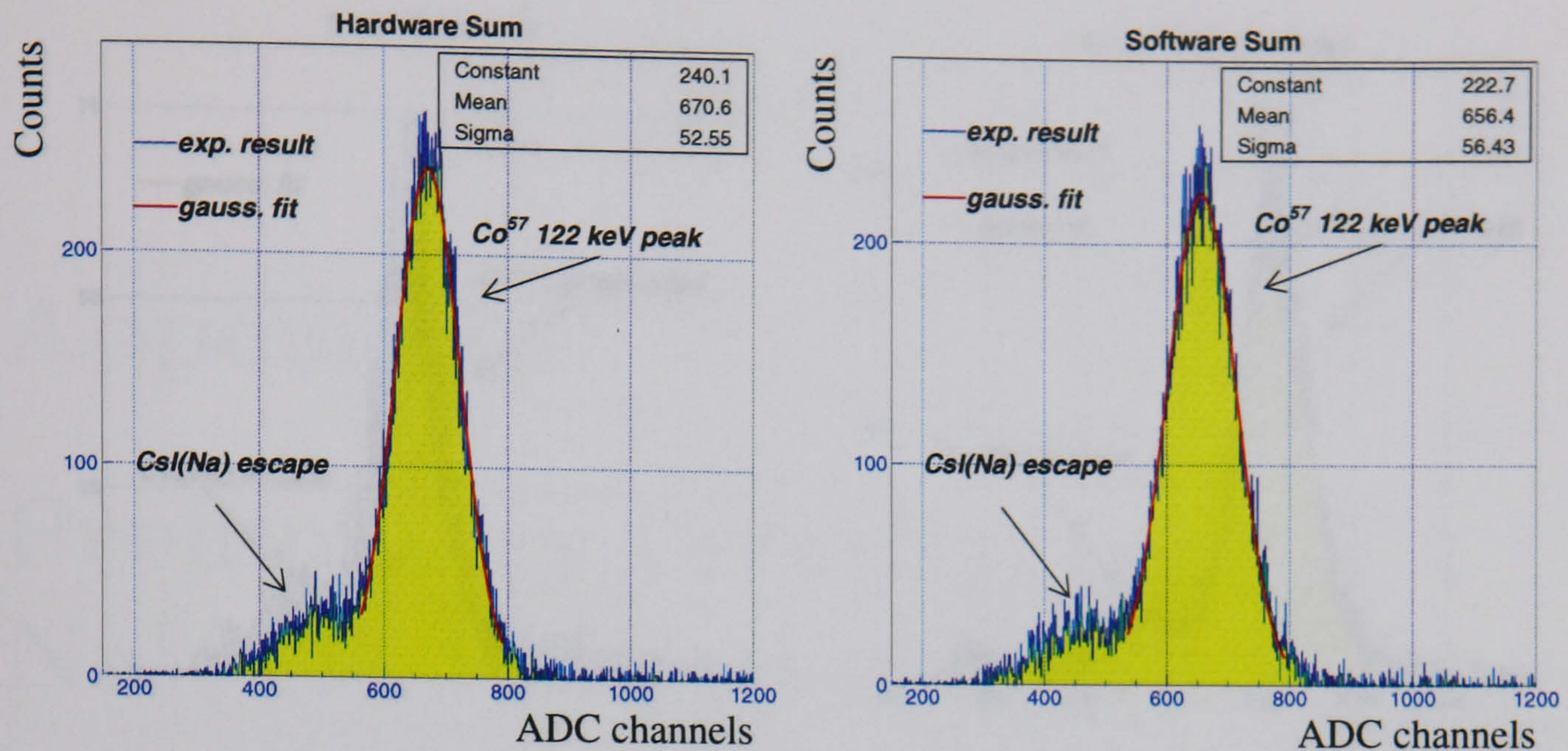


Figure D.6: Pulse-height distributions for the *hardware sum* and for the *software sum* for the setup described in section 8.2. Both plots refer to the same measurement made with the 3 mm thick CsI(Na) crystal. The values for Constant, Mean and Sigma correspond to the parameters obtained for the Gaussian-fit function depicted.

D.3.3 Comparison between the *hardware sum* and the *software sum*

Typical pulse-height spectra for the energy signal using the *hardware sum* and the *software sum* are shown in figure D.6 for the same measurement, using the readout system developed for the WSF gamma camera prototype described in chapter 8. It is seen that the spectra are very similar, a result which is consistent for all measurements made. This led to the use of the *hardware sum* to characterise the energy signal of the WSF camera prototype, due to its simplicity (requires only one ADC channel).

D.4 Energy signal from the scintillators

A comparison between coupling the 3 mm thick CsI(Na) crystal to the *energy light-guide* with and without silicon gel is presented in figure D.7. The relative position of the E-PMTs, the Co^{57} source and the crystal is illustrated in figure 8.5.

The energy signal with gel coupling is about 60% higher. The energy resolution is 23% FWHM without gel (i.e., air coupling) and 19% FWHM

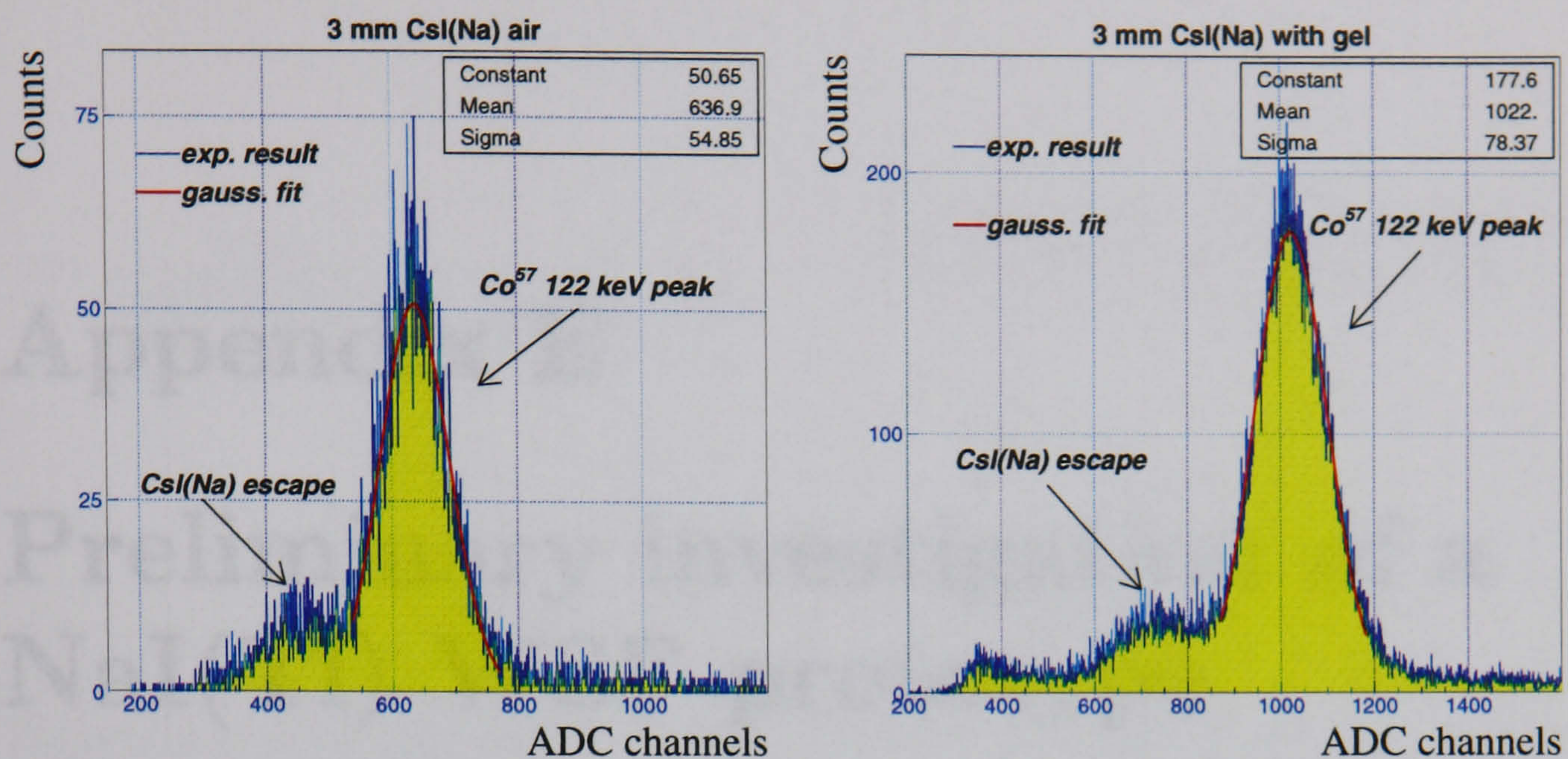


Figure D.7: Pulse-height distributions for the the 3 mm thick CsI(Na) crystal from Hilger Crystals (section 8.2): a) no coupling between the crystal and the E-PMT light-guide and b) crystal coupled to the light-guide with silicon gel. The values for Constant, Mean and Sigma correspond to the parameters obtained for the Gaussian-fit function depicted.

with gel, using equation 3.1 with subtraction of a 74 ADC channel pedestal to the mean value shown in the plots.

Appendix E

Preliminary investigation of a NaI(Tl) WSF prototype

The NaI(Tl) crystal described in section 8.1.1 was used in a preliminary experiment to compare with the performance obtained with the CsI(Na) crystals. The NaI(Tl) crystal is 5 mm thick and it is encapsulated between two 0.8 mm thick glass windows to prevent damage caused by moisture.

The NaI(Tl) crystal is coupled to the E-PMT matrix (figure D.2), centered on E-PMT2. A set of 13 WSFs cut, polished and aluminised following the same procedures as for the CsI(Na) prototypes, was coupled with silicone gel to the top surface of the crystal (i.e., the gamma ray entrance surface). The WSFs are read out with the tube M16-B using the same data acquisition system as for the CsI(Na) experiments. This arrangement provides position information along a single direction, perpendicular to the axis of the WSFs.

The set of 13 WSFs was coupled to the crystal in two different positions as illustrated in figure E.1. Configuration B is used to study the edge effects near the NaI(Tl) boundaries.

Figure E.2 shows the distribution of centroids and the mean number of photoelectrons per WSF obtained when the collimator is above WSF 7 in configuration A. Both distributions are wider than the corresponding ones obtained with the 5 mm thick CsI(Na) (for the Y WSFs, which are on the top surface). This suggests a bigger distance from the average depth of gamma ray interaction inside the crystal to the WSFs for the case of NaI(Tl). Two possible causes are the presence of the 0.8 mm thick glass window and the lower conversion efficiency of NaI(Tl) compared to CsI(Na), increasing the probability of gamma ray interactions deeper inside the crystal.

The spatial resolution obtained is of the order of 6~7 mm FWHM, for several measurements at different collimator positions.

The mean sum of the number of photoelectrons per WSF in a set of 6

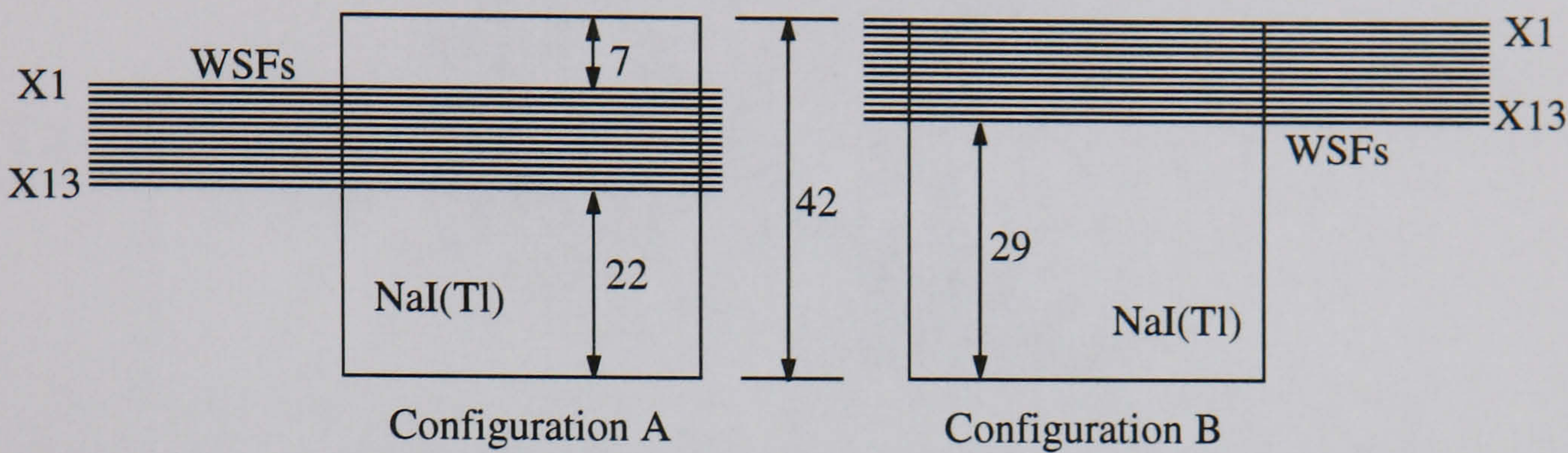


Figure E.1: Two different configurations depending on the relative position of the WSFs and the NaI(Tl) crystal.

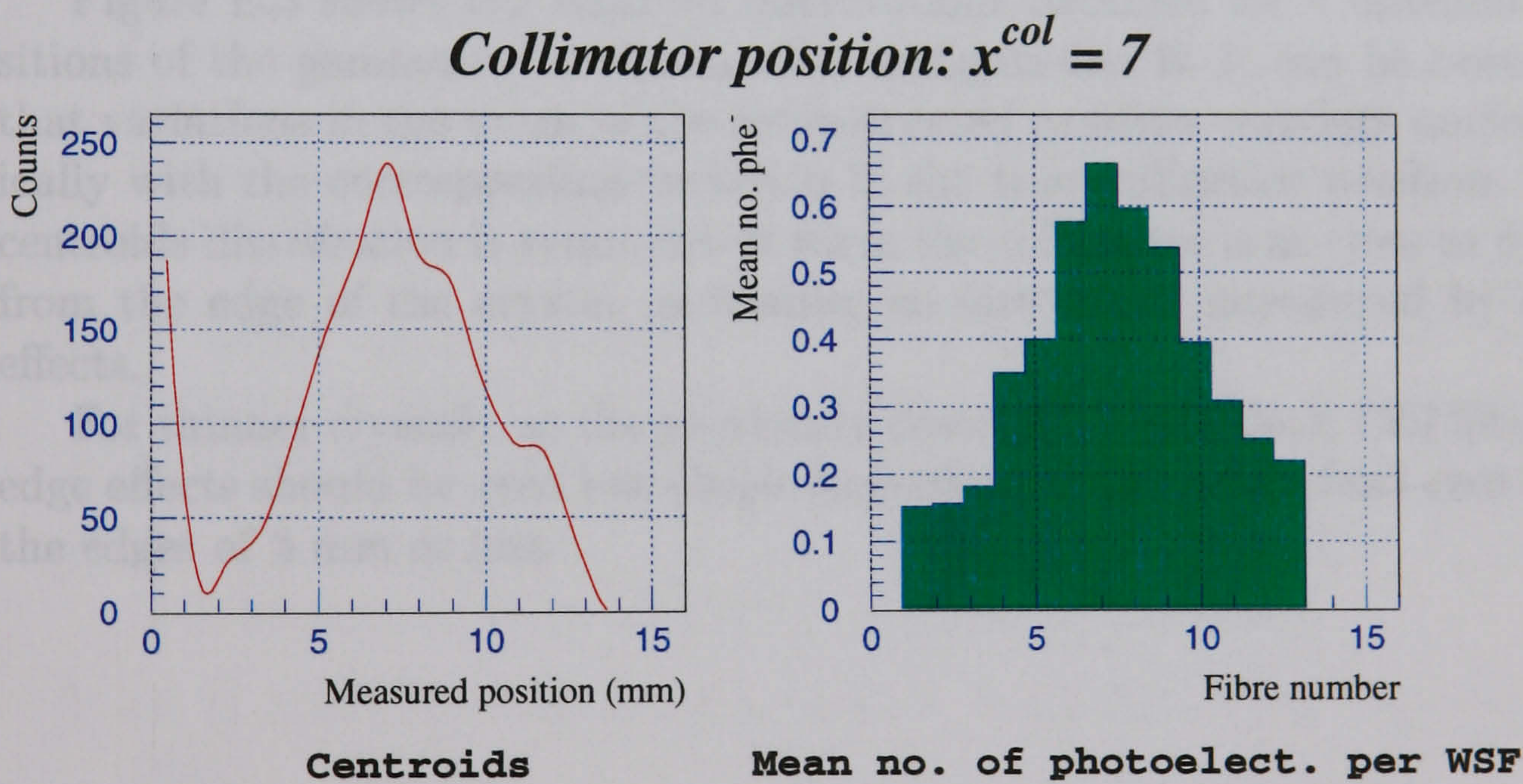


Figure E.2: Distribution of centroids and mean number of photoelectrons per WSF using the NaI(Tl) crystal and configuration A.

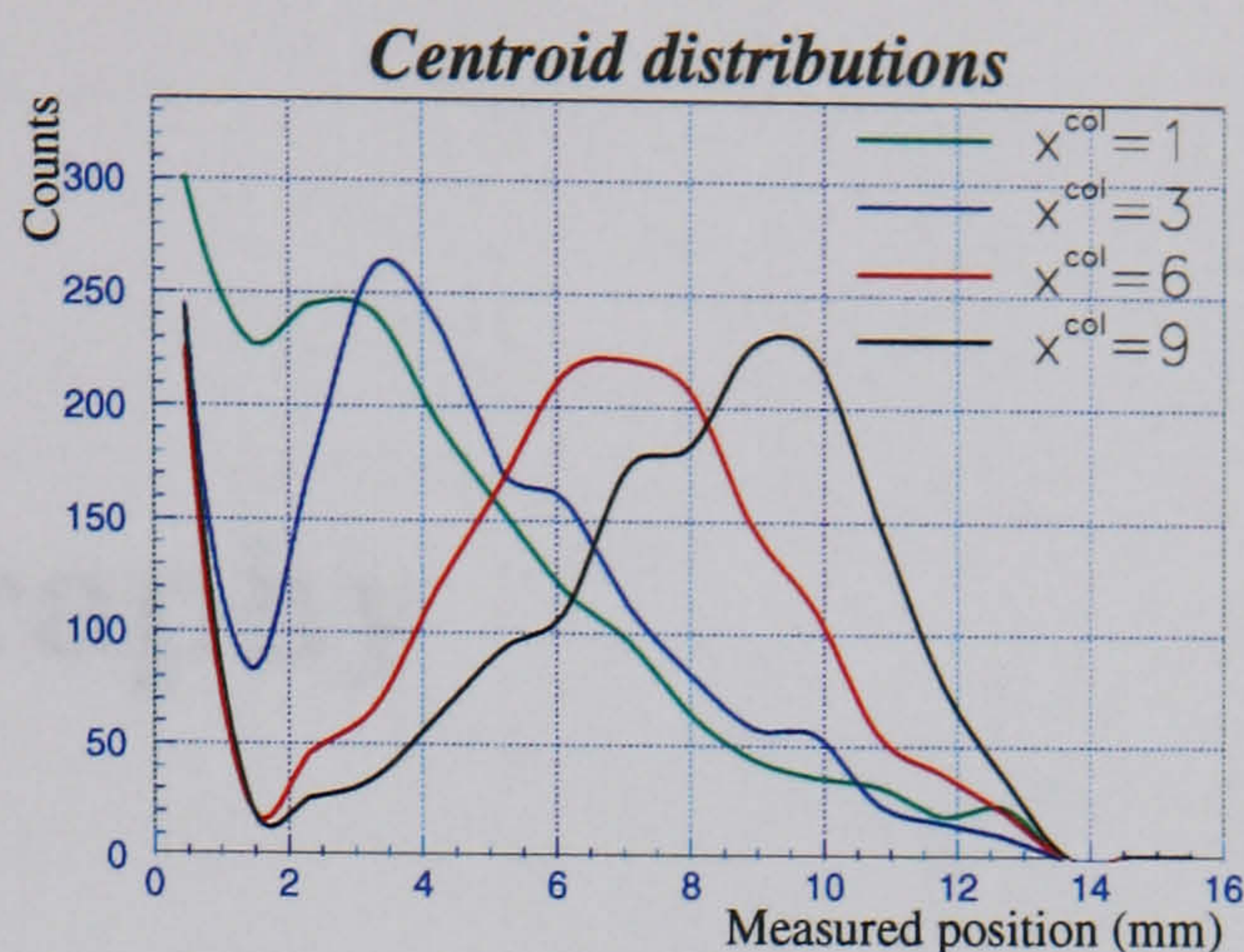


Figure E.3: Distribution of centroids for 4 different positions of the gamma ray collimator, using configuration B.

measurements at different collimator positions is 4.6. This is higher than the previously obtained with the CsI(Na) crystals which is a consequence of the higher light output of NaT(Tl) as shown in table B.1, together with a similar spectral match between the crystal emission and the WSF's absorption for NaI(Tl) and CsI(Na).

Figure E.3 shows the centroid distributions obtained for 4 different positions of the gamma ray collimator for configuration B. It can be observed that variations in the mean of the reconstructed position correlate monotonically with the corresponding variation in the true collimator position. The centroids distribution is symmetrical when the collimator is as close as 6 mm from the edge of the crystal, indicating no distortions introduced by edge effects.

For thinner crystals, as the previously described 3 mm thick CsI(Na), the edge effects should be even less visible suggesting a very small dead area near the edges of 3 mm or less.

Bibliography

- [1] F. Scopinaro, R. Pani, G. De Vincentis, A. Soluri, R. Pellegrini, and L. M. Porfiri. High-resolution scintimammography improves the accuracy of technetium-99m methoxyisobutylisonitrile scintimammography: Use of a new dedicated gamma camera. *Eur.J.Nuc.Med.*, 26(10):1279–1288, 1999.
- [2] M. B. Williams, A. R Goode, V. Galbis-Reig, S. Majewski, A. G. Weisenberger, and R. Wojcik. Performance of a PSPMT based detector for scintimammography. *Phys.Med.Biol.*, 45:781–800, 2000.
- [3] S. Webb, editor. *The Physics of Medical Imaging*. Institute of Physics Publishing, 1998.
- [4] B. Caner, M. Kitapçıl, M. Unlü, G. Erbençi, T. Çalikoğlu, and T. Göğüş. Technetium-99m-MIBI uptake in benign and malignant bone lesions: a comparative study with technetium-99m-MDP. *J.Nucl.Med.*, 33:319–324, 1992.
- [5] K. Yutani et al. Comparison of FDG-PET with MIBI-SPECT in the detection of breast cancer and axillary lymph node metastasis. *Journal of Computer Assisted Tomography*, 24(2):274–280, 2000.
- [6] J. A. Sorenson and M. E. Phelps. *Physics in Nuclear Medicine*. W.B.Saunders Company, 1987.
- [7] M. D. Short. Gamma-camera systems. *Nucl.Instr.Meth.*, 221:142–149, 1984.
- [8] T. G. Turkington, C. M. Laymon, and R. E. Coleman. Imaging properties of a half-inch sodium iodide gamma camera. *IEEE Trans.Nucl.Sci.*, 44(3):1262–1265, 2000.
- [9] H. D. Royal and P. H. Claunh B. C. Brown. Effects of a reduction in crystal thickness on Anger camera performance. *J.Nucl.Med.*, 20(9):977–980, 1979.

- [10] H. H. Barret and W. Swindell. *Radiological Imaging - The theory of image formation, detection and processing*. Academic Press, 1981.
- [11] J. W. Scrimger and R. G. Baker. Investigation of light distribution from scintillators in a gamma camera crystal. *Phys.Med.Biol.*, 12(1):101–103, 1967.
- [12] B. Westerman, R. R. Sharma, and J. F. Fowler. Relative importance of resolution and sensitivity in tumor detection. *J.Nucl.Med.*, 9(12):638–640, 1968.
- [13] A. O. Anger. Sensitivity, resolution, and linearity of the scintillation camera. *IEEE Trans.Nucl.Sci.*, NS-13(3):380–392, 1966.
- [14] B. R. Westerman and H. I. Glass. Physical performance of a gamma camera. *J.Nucl.Med.*, 9(1):24–30, 1968.
- [15] I. Khalkhali et al. Technetium-99m-sestamibi scintimammography of breast lesions: Clinical and pathological follow-up. *J.Nucl.Med.*, 36(10):1784–1789, 1995.
- [16] R. Taillefer, A. Robidoux, R. Lambert, S. Turpin, and J. Laperrière. Technetium-99m-sestamibi prone scintimammography to detect primary breast cancer and axillary lymph node involvement. *J.Nucl.Med.*, 36(10):1758–1765, 1995.
- [17] I. Khalkhali et al. Prone scintimammography in patients with suspicion of carcinoma of the breast. *Journal of the American College of Surgeons*, 178:491–497, 1994.
- [18] D. M. Goldenberg et al. Carcinoembryonic antigen immunoscintigraphy complements mammography in the detection of breast carcinoma. *Cancer*, 89(1):104–115, 2000.
- [19] R. Danielsson, B. Boné, L. Perbeck, and P. Aspelin. Evaluation of planar scintimammography with ^{99m}Tc -MIBI in the detection of axillary lymph node metastasis of breast carcinoma. *Acta Radiologica*, 40:491–495, 1999.
- [20] R. Danielsson, E. Reihner, A. Grabowska, and B. Boné. The role of scintimammography with ^{99m}Tc -sestamibi as a complementary diagnostic technique in the detection of breast cancer. *Acta Radiologica*, 41:441–445, 2000.

- [21] S. Mekhmandarov, J. Sandbank, M. Cohen, S. Ielcuk, and E. Lubin. Technetium-99m-MIBI scintimammography in palpable and nonpalpable breast lesions. *J.Nucl.Med.*, 39(1):86–91, 1998.
- [22] R. Pani, F. Scopinaro, R. Pellegrini, A. Soluri, I. N. Weinberg, and G. De Vincentis. The role of Compton background and breast compression on cancer detection in scintimammography. *Anticancer Research*, 17:1645–1649, 1997.
- [23] G. J. Gruber, W. W. Moses, and S. E. Derenzo. Monte Carlo simulation of breast cancer tumor imaging properties with compact, discrete gamma cameras. submitted to *IEEE Trans. Nucl. Sci.*
- [24] G. F. Knoll. *Radiation detection and measurement*. John Wiley & Sons, 1988.
- [25] M. Miyajima, S. Sasaki, and E. Shibamura. Number of photoelectrons from a photomultiplier cathode coupled with a NaI(Tl) scintillator. *Nucl.Instr.Meth.*, 224:331–334, 1984.
- [26] I. Holl, E. Lorenz, and G. Mageras. A measurement of the light yield of common inorganic scintillators. *IEEE Trans.Nucl.Sci.*, NS-35(1):105–109, 1988.
- [27] E. Sakai. Recent measurements on scintillator-photodetector systems. *IEEE Trans.Nucl.Sci.*, NS-34(1):418–422, 1987.
- [28] M. Moszyński, M. Kapusta, M. Mayhugh, D. Wolski, and S. O. Flyckt. Absolute light output from scintillators. *IEEE Trans.Nucl.Sci.*, NS-44(3):1052–1061, 1997.
- [29] M. Moszyński, M. Kapusta, D. Wolski, W. Klamra, and B. Cederwall. Properties of the YAP:Ce scintillator. *Nucl.Instr.Meth.*, A404:157–165, 1998.
- [30] M. Kapusta, M. Balcerzyk, M. Moszyński, and J. Pawelke. A high-energy resolution observed from a YAP:Ce scintillator. *Nucl.Instr.Meth.*, A421:610–613, 1999.
- [31] S. Baccaro et al. Scintillation properties of YAP:Ce. *Nucl.Instr.Meth.*, 361:209–215, 1995.
- [32] R. Lecomte et al. Investigation of GSO, LSO and YSO scintillators using reverse avalanche photodiodes. *IEEE Trans.Nucl.Sci.*, NS-45(3):478–482, 1998.

- [33] M. Dahlbom et al. Performance of a YSO/LSO detector block for use in a PET/SPECT system. *IEEE Trans.Nucl.Sci.*, 2000.
- [34] C. W. E. van Eijk, J. Andriessen, P. Dorenbos, and R. Visser. Ce³⁺ doped inorganic scintillators. *Nucl.Instr.Meth.*, A348:546–550, 1994.
- [35] C. L. Melcher and J. S. Schewitzer. Cerium-doped lutecium oxyorthosilicate: a fast, efficient new scintillator. *IEEE Trans.Nucl.Sci.*, NS-39(4):502–505, 1992.
- [36] C. L. Melcher and J. S. Schewitzer. A promising new scintillator: Cerium doped lutecium oxyorthosilicate. *Nucl.Instr.Meth.*, A314:212–214, 1992.
- [37] T. Ludziejewski, K. Moszyński, M. Moszyński, and D. Wolski. Advantages and limitations of LSO scintillator in nuclear physics experiments. *IEEE Trans.Nucl.Sci.*, NS-42(4):328–336, 1995.
- [38] K. S. Shah, P. Bennett, and M. R. Squillante. Gamma ray detection properties of lutetium aluminate scintillators. *IEEE Trans.Nucl.Sci.*, NS-43(3):1267–1270, 1996.
- [39] A. Lempicki, M. H. Randles, D. Wisniewski, M. Balcerzyk, C. Brecher, and A. J. Wojtowicz. LuAlO₃:Ce and other aluminate scintillators. *IEEE Trans.Nucl.Sci.*, NS-42(4):280–284, 1995.
- [40] W. W. Moses et al. LuAlO₃:Ce - a high density, high speed scintillator for gamma detection. *IEEE Trans.Nucl.Sci.*, NS-42(4):275–279, 1995.
- [41] C. Dujardin et al. The study of small and large size LuAlO₃:Ce³⁺. *IEEE Trans.Nucl.Sci.*, NS-45(3):467–471, 1998.
- [42] R. Pani et al. Scintillating array gamma camera for clinical use. *Nucl.Instr.Meth.*, 392:295–298, 1997.
- [43] A. G. Weisenberger, E. L. Bradley, S. Majewski, and M. S. Saha. Development of a novel radiation imaging detector system for in vivo gene imaging in small animal studies. *IEEE Trans.Nucl.Sci.*, 45:1743–1749, 1998.
- [44] S. Majewski et al. Development of a gamma radiation imaging detector based on a GSO crystal scintillator and a position sensitive PMT. In *IEEE Nuclear Science Symposium and Medical Imaging Conference Record, Albuquerque, Santa Fe, USA*, 1997.

- [45] S. Surti, J. S. Karp, R. Freifelder, and F. Liu. Optimizing the performance of a PET detector using discrete GSO crystals on a continuous lightguide. *IEEE Trans.Nucl.Sci.*, 47(3):1030–1036, 2000.
- [46] M. Schmand et al. Performance evaluation of a new LSO high resolution research tomograph - HRRT. In *IEEE Nuclear Science Symposium and Medical Imaging Conference*, 1999.
- [47] D. M. Duxbury et al. Preliminary results from the new large-area PETTRA positron camera. In *IEEE Nuclear Science Symposium and Medical Imaging Conference*, 1998.
- [48] J. B. Birks. *The theory and practice of scintillation counting*. Pergamon Press, 1964.
- [49] Hamamatsu Photonics K.K. *Photomultiplier Tube, principle to application*. 1994.
- [50] Philips Photonics. *Photomultiplier tubes, principles & applications*. 1994.
- [51] S. Orito, T. Kobayashi, K. Suzuki, M. Ito, and A. Sawaki. New proximity focusing photomultiplier resistant to high magnetic field. *Nucl.Instr.Meth.*, 216:439–445, 1983.
- [52] L. Lecomte and V. Perez-Mendez. Channel electron multipliers: Properties, development and applications. *IEEE Trans.Nucl.Sci.*, NS-25:964–973, 1978.
- [53] K-i Kuroda and D. Sillou. New type of position sensitive photomultiplier. *Rev.Sci.Instrum.*, 52(3):337–346, 1981.
- [54] A. Sawaki, S. Ohsuka, and T. Hayashi. New phototubes and photomultipliers resistive against high magnetic fields. *IEEE Trans.Nucl.Sci.*, NS-31(1):442–446, 1984.
- [55] S. Suzuki, T. Nakaya, A. Suzuki, H. Suzuki, K. Yoshioka, and Y. Yoshizawa. PMTs of superior time resolution, wide dynamic range, and low cross-talk multi-anode PMTs. *IEEE Trans.Nucl.Sci.*, NS-40(4):431–433, 1993.
- [56] S. Suzuki, T. Suzuki, T. Matsushita, and H. Kume. New mesh PMTs for high magnetic environments. *IEEE Trans.Nucl.Sci.*, NS-33(1):377–380, 1986.

- [57] H. Kichimi, H. Sagawa, Y. Yoshimura, T. Kishida, H. Suzuki, and T. Taguchi. Timing characteristics of a micro-channel plate and fine-mesh photomultiplier tubes in a 1 T field. *Nucl.Instr.Meth.*, A235:451–457, 1993.
- [58] F. Takasaki, K. Ogawa, and K. Tobimatsu. Performance of a photomultiplier tube with transmissive dynodes in a high magnetic field. *Nucl.Instr.Meth.*, 228:369–373, 1985.
- [59] Hamamatsu Photonics K.K. Photomultiplier tubes and assemblies for scintillation counting & high energy physics. www.hamamatsu.com.
- [60] H. Kume, S. Suzuki, J. Takeuchi, and K. Oba. Newly developed photomultiplier tubes with position sensitivity capability. *IEEE Trans.Nucl.Sci.*, NS-32(1):448–452, 1985.
- [61] H. Kume, S. Muramatsu, and M. Iida. Position sensitive photomultiplier tubes for scintillation imaging. *IEEE Trans.Nucl.Sci.*, NS-33(1):359–363, 1986.
- [62] H. Uchida, T. Yamashita, M. Iida, and S. Muramatsu. Design of a mosaic BGO detector system for positron CT. *IEEE Trans.Nucl.Sci.*, NS-33(1):464–467, 1986.
- [63] T. Hayashi. New photomultiplier tubes for medical imaging. *IEEE Trans.Nucl.Sci.*, NS-36(1):1078–1083, 2000.
- [64] T. Yamashita, M. Watanabe, K. Shimizo, and H. Uchida. High resolution block detectors for PET. *IEEE Trans.Nucl.Sci.*, NS-37(2):589–593, 1990.
- [65] N. J. Yasillo, R. N. BECK, and M. Cooper. Design considerations for a single tube gamma-camera. *IEEE Trans.Nucl.Sci.*, 37:609–615, 1990.
- [66] A. J. Bird and D. Ramsden. Images obtained with a compact gamma-camera. *Nucl.Instr.Meth.*, 299:480–483, 1990.
- [67] L. H. Barone et al. Toward a nuclear-medicine with sub-millimeter spatial-resolution. *Nucl.Instr.Meth.*, 360:302–306, 1995.
- [68] M. Salomon, H. Coombes, M. Nissen, and J. G. Rogers. Fibre scintillators coupled to a multianode photomultiplier as a high rate tracking detector. *IEEE Trans.Nucl.Sci.*, NS-34(1):525–527, 1987.

- [69] S. Suzuki, T. Matsushita, T. Suzuki, S. Kimura, and H. Kume. New position sensitive photomultiplier tubes for high energy physics and nuclear medical applications. *IEEE Trans.Nucl.Sci.*, NS-35(1):382–386, 1988.
- [70] C. F. Perdrisat et al. Tests of crossed-wire position-sensitive photomultipliers for scintillating-fiber particle tracking. *Nucl.Instr.Meth.*, 365:378–384, 1995.
- [71] A. J. Bird, H. Zhong, and D. Ramsden. A position-sensitive phoswich. *Nucl.Instr.Meth.*, 310:332–336, 1991.
- [72] A. Truman, M. J. Palmer, P. T. Durrant, A. J. Bird, D. Ramsden, and J. Stadsnes. A PSPMT based auroral x-ray imager. *Nucl.Instr.Meth.*, 368:492–497, 1996.
- [73] Z. He and D. Ramsden. A broad-band position-sensitive phoswich detector for gamma-ray astronomy. *Nucl.Instr.Meth.*, 336:330–335, 1993.
- [74] C. J. Hailey, F. Harrison, J. H. Lupton, and K.-P. Ziock. An inexpensive hard x-ray imaging spectrometer for use in x-ray astronomy and atomic physics. *Nucl.Instr.Meth.*, A276:340–346, 1989.
- [75] J. M. Poulsen, R. Verbeni, and F. Frontera. Position-sensitive scintillation detector for hard x-rays. *Nucl.Instr.Meth.*, 310:398–402, 1991.
- [76] R. A. Kroeger et al. Thin scintillators and position sensitive photomultiplier tubes for hard X-ray imaging in space. *IEEE Trans.Nucl.Sci.*, NS-44(3):881–884, 1997.
- [77] R. Meunier and A. Maurer. Evaluation of a microchannel photomultiplier and small-size phototubes for Čerenkov counters. *IEEE Trans.Nucl.Sci.*, NS-25(1):528–531, 1978.
- [78] K. Oba, M. Sugiyama, and Y. Suzuki. A 400 anode chevron microchannel plate PMT for high energy application. *IEEE Trans.Nucl.Sci.*, NS-26(1):346–355, 1979.
- [79] B. Leskovar and C. C. Lo. Time resolution performance studies of contemporary high speed photomultipliers. *IEEE Trans.Nucl.Sci.*, NS-25(1):582–590, 1978.
- [80] B. Leskovar and T. T. Shimizu. Time resolution performance studies of Hamamatsu R1564U microchannel plate photomultiplier. *IEEE Trans.Nucl.Sci.*, NS-34(1):427–430, 1987.

- [81] W. Baumgartner and U. Zimmermann. A high-gain channel electron multiplier (CEM) array and some of its operational characteristics. *Advances in electronics and electron physics*, 33A:125–131, 1972.
- [82] J. S. Lapington, A. D. Smith, D. W. Walton, and H. E. Schwarz. Microchannel plate pore size limited imaging with ultra-thin wedge and strip anodes. *IEEE Trans.Nucl.Sci.*, NS-34(1):431–433, 2000.
- [83] J. G. Timothy. Electronic readout systems for microchannel plates. *IEEE Trans.Nucl.Sci.*, NS-32(1):427–432, 1985.
- [84] J. D. Mcgee, E. A. Flinn, and H. D. Evans. An electron image multiplier. *Advances in electronics and electron physics*, 12:87–96, 1960.
- [85] J. Burns and M. J. Neumann. The channeled image intensifier. *Advances in electronics and electron physics*, 12:97–111, 1960.
- [86] V. Jareš and M. Dvořák. A flat channel system for imaging purposes. *Advances in electronics and electron physics*, 33A:117–123, 1972.
- [87] D. Washington, A. J. Guest, and A. G. Knapp. A large-area electron image multiplier. *Advances in electronics and electron physics*, 64A:101–110, 1985.
- [88] J. P. Boutot, P. Lavoute, and G. Eschard. Multianode photomultiplier for detection and localization of low light level events. *IEEE Trans.Nucl.Sci.*, NS-34(1):449–452, 1987.
- [89] J. Kavarabayashi, H. Takahashi, T. Iguchi, M. Nakazawa, A. Takahashi, and R. Tokue. New array type electron multiplier as a two dimensional position sensitive detector. *Nucl.Instr.Meth.*, A353:172–175, 1994.
- [90] H. Kyushima et al. Photomultiplier tube of new dynode configuration. *IEEE Trans.Nucl.Sci.*, NS-41(4):725–729, 1994.
- [91] H. E. Schwarz and J. S. Lapington. Optimisation of wedge and strip anodes. *IEEE Trans.Nucl.Sci.*, NS-32(1):433–437, 1985.
- [92] M. Lampton and C. W. Carlson. Low-distortion resistive anodes for two-dimensional position-sensitive MCP systems. *Rev.Sci.Instrum.*, 50(9):1093–1097, 1979.

- [93] S. Nagai, M. Watanabe, H. Shimoi, H. Liu, and Y. Yoshizawa. A new compact position-sensitive PMT for scintillation detectors. *IEEE Trans.Nucl.Sci.*, NS-46(3):354–358, 1999.
- [94] Y. P. Shao, S. R. Cherry, S. Siegel, R. W. Silverman, and S. Majewski. Evaluation of multi-channel pmts for readout of scintillator arrays. *Nucl.Instr.Meth.*, 390:209–218, 1997.
- [95] J. G. Rogers, D. P. Saylor, R. Harrop, X. G. Yao, C. V. M. Leita0, and B. D. Pate. Design of an efficient position sensitive gamma ray detector for nuclear medicine. *Phys.Med.Biol.*, 31(10):1061–1090, 1986.
- [96] R. H. Redus, V. Nagarkar, L. J. Cirignano, W. McGann, and M. R. Squillante. A nuclear survey instrument with imaging capability. *IEEE Trans.Nucl.Sci.*, NS-39(4):948–951, 1992.
- [97] Y. K. Dewaraja et al. A position-sensitive $\beta - \gamma$ coincidence technique for multiplexed gamma spectrometry of many small samples. *Nucl.Instr.Meth.*, A353:588–592, 1994.
- [98] J. N. Aarsvold et al. A miniature gamma-camera. *Annals of the New York Academy of Sciences*, 720:192–205, 1994.
- [99] Z. He, A. J. Bird, D. Ramsden, and Y. Meng. A 5-inch diameter position-sensitive scintillation-counter. *IEEE Trans.Nucl.Sci.*, 40:447–451, 1993.
- [100] N Schramm, A Wirrwar, F Sonnenberg, and H Halling. Compact high resolution detector for small animal SPECT. In *IEEE Nuclear Science Symposium and Medical Imaging Conference Record*, 1999.
- [101] K. Blazek et al. YAP multicrystal gamma-camera prototype. *IEEE Trans.Nucl.Sci.*, 42:1474–1482, 1995.
- [102] L. M. Barone et al. A detector for submillimeter gamma cameras. *Nuclear Physics B*, pages 729–733, 1995.
- [103] F. Vittori, T. Malatesta, and F. de Notaristefani. The YAP camera: An accurate gamma camera particularly suitable for new radiopharmaceuticals research. *IEEE Trans.Nucl.Sci.*, 44:47–53, 1997.
- [104] R. Pani et al. Multicrystal YAP-Ce detector system for position-sensitive measurements. *Nucl.Instr.Meth.*, 348:551–558, 1994.

- [105] A. Truman, A. J. Bird, D. Ramsden, and Z. He. Pixellated CsI(Tl) arrays with position-sensitive PMT readout. *Nucl.Instr.Meth.*, 353:375–378, 1994.
- [106] S. Majewski et al. Development of an application specific scintimammography detector based on a crystal scintillator array and a PSPMT. *Nucl.Instr.Meth.*, 409:520–523, 1998.
- [107] R. Pani et al. Portable gamma camera for clinical use in nuclear medicine. In *IEEE Nuclear Science Symposium and Medical Imaging Conference Record*, 1997.
- [108] C. S. Levin, E. J. Hoffman, M. P. Tornai, and L. R. MacDonald. PSPMT and photodiode designs of a small scintillation camera for imaging malignant breast tumours. *IEEE Trans.Nucl.Sci.*, NS-44(1):1513–1520, 1997.
- [109] A Wirrwar, N Schramm, H Vosberg, and H-W Müller-Gärtner. Influence of crystal geometry and wall reflectivity on scintillation photon yield and energy resolution. In *IEEE Nuclear Science Symposium and Medical Imaging Conference Record*, 1999.
- [110] CTI PET Systems, Inc, Knoxville Tennessee, USA, www.cti-pet.com.
- [111] Siemens Medical Systems, Inc, Iselin, NJ, USA, www.sms.siemens.com/nmg.
- [112] C. J. Thompson, K. Murthy, Y. Picard, I. N. Weinberg, and R. Mako. Positron emission mammography (PEM): a promising technique for detecting breast cancer. *IEEE Trans.Nucl.Sci.*, NS-42(4):1012–1017, 1995.
- [113] A. Del Guerra et al. Use of a YAP:Ce matrix coupled to a position-sensitive photomultiplier for high resolution position emission tomography. *IEEE Trans.Nucl.Sci.*, 43:1958–1962, 1996.
- [114] S. R. Cherry et al. Optical fiber readout of scintillator arrays using a multi-channel PMT: a high resolution PET detector for animal imaging. *IEEE Trans.Nucl.Sci.*, NS-43(3):1932–1937, 1996.
- [115] Y. Shao et al. Development of a PET detector system compatible with MRI/NMR systems. *IEEE Trans.Nucl.Sci.*, NS-44(3):1167–1171, 1997.

- [116] R. L. Clancy, C. J. Thompson, J. L. Robar, and A. M. Bergman. A simple technique to increase the linearity and field-of-view in position sensitive photomultiplier tubes. *IEEE Trans.Nucl.Sci.*, NS-44(3):494–498, 1997.
- [117] S. Siegel, R. W. Silverman, Y. Shao, and S. R. Cherry. Simple charge division readouts for imaging scintillator arrays using a multi-channel PMT. *IEEE Trans.Nucl.Sci.*, NS-43(3):1634–1641, 1996.
- [118] A. J. Soares, I. Cullum, F. Christie, G. J. Royle, R. D. Speller, and D. J. Miller. Assessment of light distribution at the photocathode of 5" and 1" position sensitive photomultiplier tubes. *Proceedings of the SPIE Medical Imaging Conference 1998*, 3336:618–629, 1998.
- [119] D. Steinbach, S. Majewski, M. Williams, B. Kross, A. Weisenberger, and R. Wojcik. Development of a small field of view scintimammography camera based on a YAP crystal array and a position sensitive PMT. In *Proceedings of the 1996 IEEE Nuclear Science Symposium and Medical Imaging Conference, Anaheim, California, USA*, page 1251, 1996.
- [120] A. J. Bird, Z. He, and D. Ramsden. Multichannel readout of crossed-wire anode photomultipliers. *Nucl.Instr.Meth.*, 348:668–672, 1994.
- [121] L. K. van Geest and K. W. J. Stoop. Hybrid phototube with Si target. *Nucl.Instr.Meth.*, A310:261–266, 1991.
- [122] T. Gys, C. D'Ambrosio, H. Leutz, D. Piedigrossi, and D. Puertolas. A new position-sensitive photon detector based on an imaging silicon pixel array (ISPA-tube). *Nucl.Instr.Meth.*, A355:386–389, 1995.
- [123] E. Chesi et al. Performance of a 256 pad hybrid photon detector for ring imaging. *Nucl.Instr.Meth.*, A387:122–130, 1997.
- [124] D. Puertolas et al. An ISPA-camera for gamma rays. *IEEE Trans.Nucl.Sci.*, 42:2221–2228, 1995.
- [125] C. P. Datema, L. J. Meng, and D. Ramsden. Results obtained using a 61-pixel hybrid photodiode scintillation camera. *Nucl.Instr.Meth.*, 422:656–660, 1999.
- [126] C. P. Datema, L. J. Meng, and D. Ramsden. A compact readout system for multi-pixel hybrid photodiodes. In *IEEE Nuclear Science Symposium and Medical Imaging Conference*, 1998.

- [127] H. Grassmann, E. Lorenz, and H.-G. Moser. Properties of CsI(Tl) - renaissance of an old scintillation material. *Nucl.Instr.Meth.*, 228:323–326, 1985.
- [128] N. G. Blamires. Combination of a scintillator and a semiconductor photodiode for nuclear particle detection. *Nucl.Instr.Meth.*, 24:441–444, 1963.
- [129] J. E. Bateman. Some new scintillator-photodiode detectors for high-energy charged particles. *Nucl.Instr.Meth.*, 67:93–102, 1969.
- [130] A. J. Bird, A. J. Dean, K. J. Grant, G. Malaguti, S. D. Mullerworth, and B. M. Swinyard. Design characteristics of a low-energy gamma-ray imager for future space missions. *Nucl.Instr.Meth.*, A310:323–326, 1994.
- [131] J. Gruber, W. W. Moses, S. E. Derenzo, N. W. Wang, E. Beuville, and M. H. Ho. A discrete scintillation camera module using silicon photodiode readout of CsI(Tl) crystals for breast cancer imaging. *IEEE Trans.Nucl.Sci.*, NS-45(3):1063–1068, 1998.
- [132] B. E. Patt, J. S. Iwanczyk, C. Rossington Tull, N. W. Wang, M. P. Tornai, and E. J. Hoffman. High resolution CsI(Tl)/Si-PIN detector development for breast imaging. *IEEE Trans.Nucl.Sci.*, NS-45(4):2126–2131, 1998.
- [133] S. Derenzo. Initial characterization of a BGO-photodiode detector for high-resolution positron emission tomography. *IEEE Trans.Nucl.Sci.*, NS-31(1):620–626, 1984.
- [134] O. Fries et al. A small animal PET prototype based on LSO crystals read out by avalanche photodiodes. *Nucl.Instr.Meth.*, A387:220–224, 1997.
- [135] C. Fiorini, F. Perotti, C. Labanti, A. Longoni, and E. Rossi. Position and energy resolution of a new gamma-ray detector based on a single CsI(Tl) scintillator coupled to a silicon drift chamber array. *IEEE Trans.Nucl.Sci.*, NS-46(4):858–864, 1999.
- [136] C. S. Levin and E. J. Hoffman. Investigation of a new readout scheme for high resolution scintillation crystal arrays using photodiodes. *IEEE Trans.Nucl.Sci.*, 44(3):1208–1213, 1997.

- [137] M. P. Tornai, B. E. Patt, J. S. Iwanczyk, C. S. Levin, and E. J. Hoffman. Discrete scintillator coupled mercuric iodide photodetector arrays for breast imaging. *IEEE Trans.Nucl.Sci.*, NS-44(3):1127–1133, 1997.
- [138] R. J. Evans, I. D. Jupp, F. Lei, and D. Ramsden. Design of a large-area CsI(Tl) photo-diode array for explosives detection by neutron-activation gamma-ray spectroscopy. *Nucl.Instr.Meth.*, 422:900–905, 1999.
- [139] A. J. Tuzzolino, E. L. Hubbard, M. A. Perkins, and C. Y. Fan. Photoeffects in silicon surface-barrier diodes. *Journal of Applied Physics*, 33(1):148–155, 1962.
- [140] C. Y. Fan. Detection of scintillation photons with photodiodes. *Rev.Sci.Instrum.*, 35(2):158–163, 1964.
- [141] G. Keil. Gamma-ray spectrometry with a scintillator-photodiode combination. *Nucl.Instr.Meth.*, 66:167–172, 1968.
- [142] B. E. Patt and J. S. Iwanczyk. Improved energy resolution for scintillator based gamma-ray detectors obtained using a CsI(Tl)/Si-PIN detector. *Rev.Sci.Instrum.*, 68(10):3926–3927, 1997.
- [143] S. E. Holland, N. W. Wang, and W. W. Moses. Development of a low noise, black-side illuminated silicon photodiode arrays. *IEEE Trans.Nucl.Sci.*, NS-44:443–447, 1997.
- [144] W. W. Moses, I. Kipnis, and M. H. Ho. A 16-channel charge sensitive amplifier IC for a PIN photodiode array based PET detector module. *IEEE Trans.Nucl.Sci.*, NS-41(4):1469–1472, 1994.
- [145] W. W. Moses, S. E. Derenzo, R. Nutt, W. M. Digby, C. W. Williams, and M. Andreaco. Performance of a PET detector module utilizing an array of silicon photodiodes to identify the crystal of interaction. *IEEE Trans.Nucl.Sci.*, NS-40(4):1036–1040, 1993.
- [146] S. E. Derenzo. Gamma-ray spectroscopy using small cooled bismuth germanate scintillators and silicon photodiodes. *Nucl.Instr.Meth.*, 219:117–122, 1984.
- [147] N. Hartsough, B. Pi, J. Gormley, and J. Ashburn. Performance characteristics of a compact, quantized gamma camera. *1999 Meeting of the Society of Nuclear Medicine*, 2000.

- [148] E. Gatti and P. Rehak. Semiconductor drift chamber - an application of a novel charge transport scheme. *Nucl.Instr.Meth.*, 225:608–614, 1984.
- [149] P. Lechner et al. Silicon drift detectors for high resolution room temperature X-ray spectroscopy. *Nucl.Instr.Meth.*, A337:346–351, 1996.
- [150] C. Fiorini, A. Longoni, F. Perotti, C. Labanti, P. Lechner, and L. Strüder. Gamma-ray spectroscopy with CsI(Tl) scintillator coupled to silicon drift chamber. *IEEE Trans.Nucl.Sci.*, NS-44(6):2553–2560, 1997.
- [151] E. Gramsch, E. M. Gullikson, W. W. Moses, and R. Avila. Operating characteristics of avalanche photodiodes for PET systems. In *IEEE Nuclear Science Symposium and Medical Imaging Conference Record*, 1996.
- [152] Ochi, Nishi, and Tanimori. Study of a large area avalanche photodiode as a fast photon and a soft x-ray detector. *Nucl.Instr.Meth.*, A378(NO-1-2):267–274, 1996.
- [153] T. Kirn, Y. Musienko, T. Flügel, and D. Renker. Properties of the most recent Hamamatsu avalanche photodiode. *Nucl.Instr.Meth.*, A387:199–201, 1997.
- [154] R. Lecomte, J. Cadorette, A. Jouan, M. Hèon, D. Rouleau, and G. Gauthier. High resolution positron emission tomography with a prototype camera based on solid state scintillation detectors. *IEEE Trans.Nucl.Sci.*, NS-37(2):805–811, 1990.
- [155] M. Moszyński, M. Kapusta, J. Zalispa, and M. Balcerzyk. Low energy γ -rays scintillation detection with large area avalanche photodiodes. *IEEE Trans.Nucl.Sci.*, NS-46(1):880–885, 1999.
- [156] R. Chen et al. Readout of scintillation light with avalanche photodiodes for positron emission tomography. *Nucl.Instr.Meth.*, A433:637–645, 1999.
- [157] M. Moszyński, M. Kapusta, D. Wolski, M. Szawlowski, and W. Klamra. Energy resolution of scintillation detectors readout with large area avalanche photodiodes and photomultipliers. *IEEE Trans.Nucl.Sci.*, NS-45(3):472–477, 1998.
- [158] J. S. Iwanczyk, J. B. Barton, A. J. Dabrowski, J. H. Kusmiss, and W. M. Szymczyk. A novel radiation detector consisting of an HgI₂

- photodetector coupled to a scintillator. *IEEE Trans.Nucl.Sci.*, NS-30(1):363–367, 1983.
- [159] J. B. Barton, E. J. Hoffman, J. S. Iwanczyk, A. J. Dabrowski, and J. H. Kusmiss. A high resolution detection system for positron tomography. *IEEE Trans.Nucl.Sci.*, NS-30(1):671–675, 1983.
 - [160] W. Li, Z. He, G. F. Knoll, D. K. Wehe, and C. M. Stahle. Spatial variation of energy resolution in 3-D position sensitive CZT gamma-ray spectrometers. *IEEE Trans.Nucl.Sci.*, NS-46(3):187–192, 1999.
 - [161] T. E. Schlesinger et al. Large volume imaging arrays for gamma-ray spectroscopy. *Journal of Electronic Materials*, 28(6):864–868, 1999.
 - [162] W. Worstell, S. Doulas, O. Johnson, and C.-J. Lin. Scintillator crystal readout with wavelength-shifting optical fibres. In *IEEE Nuclear Science Symposium Conference Record*, pages 1869–1873, 1994.
 - [163] Franz Kniest, 2000. Bicron, European office, personal communication.
 - [164] R. Wojcik, B. Kross, S. Majewski, A. G. Weisenberger, and C. Zorn. Embedded waveshifting fiber readout of long scintillators. *Nucl.Instr.Meth.*, 342:416–435, 1994.
 - [165] Bicron. Scintillating optical fibres, 1998. 12345 Kinsman Road, Newbury Ohio 44065-9677,USA.
 - [166] Brian Anderson, 2000. Dept. Physics and Astronomy, University College London, personal communication.
 - [167] G. Aguillion and et al. Thin scintillating tiles with high light yield for the OPAL end-caps. *Nucl.Instr.Meth.*, A417:266, 1998.
 - [168] G. Appollinari. Scintillator-strip / WLS-fibre EM shower maximum detectors in the CDF plug upgrade. *IEEE Trans.Nucl.Sci.*, 40(4):484–489, 1993.
 - [169] D. V. H. Bengis and R. M. Sealock. Position sensitive δE detector. *IEEE Trans.Nucl.Sci.*, NS-42(4):374–378, 1995.
 - [170] Ltd Kuraray Co. Scintillation materials, 1999. Methacrylic Resin Division, 8F, Maruzen Building, 3-10, 2-Chome Nihonbashi, Chou-ku, Tokyo, 103-0027, Japan.

- [171] S. Majewski, B. Kross, R. Wojcik, A. Weisenberger, and C. Zorn. Studies of position-sensitive photomultipliers in readout of scintillating and waveshifting fibers. *Nucl.Instr.Meth.*, 323:489–504, 1992.
- [172] D. Grigoriev, O. Johnson, W. Worstell, and V. Zavarzin. Characterization of a new multianode PMT for optical fiber readout at low-level light intensity. *IEEE Trans.Nucl.Sci.*, 44(3):990–993, 1997.
- [173] Y. Bonushkin et al. Tests of a third generation multianode phototube. *Nucl.Instr.Meth.*, 381:349–354, 1996.
- [174] P. Križan et al. Tests of a multianode PMT for the HERA-B RICH. *Nucl.Instr.Meth.*, 394:27–34, 1997.
- [175] G. Comby and R. Meunier. Test of a new 64-channel PMT for imaging. *Nucl.Instr.Meth.*, A269:246–260, 1988.
- [176] S. Siegel, S. R. Cherry, A. R. Ricci, Y. Shao, and M. E. Phelps. Development of continuous detectors for a high resolution animal PET system. *IEEE Trans.Nucl.Sci.*, NS-42(4):1069–1074, 1995.
- [177] Imaging Sensors Photonis. XP1700 multi-channel photomultipliers.
- [178] C. D'Ambrosio, T. Gys, H. Leutz, D. Piedigrossi, D. Puertolas, and S. Tailhardat. Photon counting with a hybrid photomultiplier tube (HPMT). *Nucl.Instr.Meth.*, A338:389–397, 1994.
- [179] C. P. Datema, L. J. Meng, and D. Ramsden. The detection of minimum ionising particles with scintillating fibres using multi-pixel hybrid photodiodes. *IEEE Trans.Nucl.Sci.*, 45:338–342, 1998.
- [180] S. Vasile, P. Gothoskar, R. Farrell, and D. Sdrulla. Photon detection with high gain avalanche photodiode arrays. *IEEE Trans.Nucl.Sci.*, NS-45(3):720–723, 1998.
- [181] S. Vasile, R. J. Wilson, S. Shera, D. Shamo, and M. R. Squillante. High gain avalanche photodiode arrays for DIRC applications. *IEEE Trans.Nucl.Sci.*, NS-46(4):848–852, 1999.
- [182] D. Bisello et al. Silicon avalanche detectors with negative feedback as detectors for high energy physics. *Nucl.Instr.Meth.*, A367:212–214, 1995.

- [183] A. V. Akindinov, A. N. Martemianov, P. A. Polozov, V. M. Golovin, and E. A. Grigoriev. New results on MRS APDs. *Nucl.Instr.Meth.*, A387:231–234, 1997.
- [184] N. Bacchetta et al. MRS detectors with high gain for registration of weak visible and UV light fluxes. *Nucl.Instr.Meth.*, A387:225–230, 1997.
- [185] Dr.Tariq Ali, 1999. Dept Physics, Imperial College London, personal communication.
- [186] M. D. Petroff and M. G. Stapelbroek. Photon-counting solid-state photomultiplier. *IEEE Trans.Nucl.Sci.*, NS-36(1):158–162, 1989.
- [187] D. Adams et al. First large sample study of visible light photon counters (VLPC's). *Nuclear Physics B*, 44:340–348, 1995.
- [188] J. Warchol. Characterization and performance of visible light photons counters (VLPCs) for the upgraded dØ detector at the Fermilab Tevatron, 1999. 5th Position Sensitive Detectors Conference, London.
- [189] B. Baumbaugh et al. Performance of a large scale scintillating fiber tracker using VLPC readout. *IEEE Trans.Nucl.Sci.*, 43(3):1146–1152, 1996.
- [190] B. Baumbaugh et al. Small cryostem for operation of visible light photon counters (VLPC). *IEEE Trans.Nucl.Sci.*, NS-43(3):1741–1745, 1996.
- [191] A. J. Soares, I. Cullum, D. J. Miller, G. J. Royle, and R. D. Speller. Development of a small gamma camera using wavelength-shifting fibres coupled to inorganic scintillation crystals for imaging 140 keV gamma rays. *IEEE Trans.Nucl.Sci.*, 46(3):576–582, 1999.
- [192] W. Worstell, O. Johnson, and V. Zavarzin. Development of a high resolution PET detector using LSO and wavelength-shifting fibers. In *IEEE Nuclear Science Symposium and Medical Imaging Conference, San Francisco, USA*, 1995.
- [193] W. Worstell, O. Johnson, H. Kudrolli, and V. Zavarzin. First results with high-resolution PET detector modules using wavelength-shifting fibers. In *IEEE Nuclear Science Symposium Conference Record*, 1997.

- [194] M. B. Williams, R. M. Sealock, S. Majewski, and A. G. Weisenberger. PET detector using waveshifting optical fibers and microchannel plate PMT with delay line readout. *IEEE Trans.Nucl.Sci.*, 45:195–205, 1998.
- [195] A. Levin and C. Moisan. A more physical approach to model the surface treatment of scintillation counters and its implementation into DETECT. In *IEEE Nuclear Science Symposium and Medical Imaging Conference, Anaheim,,* pages 702–706, 11-2-1996.
- [196] G. F. Knoll, T. F. Knoll, and T. M. Henderson. Light collection in scintillation detector composites for neutron detection. *IEEE Trans.Nucl.Sci.*, 35(1):872–875, 2-1-1998.
- [197] L. Levi. *Applied Optics: A Guide to Optical System Design, vol. 1.* John Wiley & Sons, 1968.
- [198] R. Pani et al. Multi-PSPMT scintillation camera. In *IEEE Nuclear Science Symposium Conference Record*, 1997.
- [199] R. R. Raylman et al. The potential role of positron emission mammography for detection of breast cancer. A phantom study. *Medical Physics*, 27(8):1943–1954, 2000.
- [200] A. Goode et al. A system for dual-modality breast imaging. In *IEEE Nuclear Science Symposium Conference Record*, 1999.
- [201] R. R. Raylman et al. An apparatus for positron emission mammography guided biopsy. In *IEEE Nuclear Science Symposium Conference Record*, 1999.
- [202] Hamamatsu Photonics K.K. Multianode photomultiplier tube assembly, 1997. product specification.
- [203] A. J. Soares, I. Cullum, D. J. Miller, G. J. Royle, R. D. Speller, and J. Thomas. Photon counting with the Hamamatsu H6568 multi-anode photomultiplier. In *presented at the 5th Position Sensitive Detectors conference, London, U.K., and submitted for publication in Nucl. Instrum. Meth. A*, 1999.
- [204] Jenny Thomas, 2000. Dept. Physics and Astronomy, University College London, personal communication.
- [205] A. J. Soares, I. Cullum, D. J. Miller, G. J. Royle, and R. D. Speller. Development of a wavelength-shifting fibre gamma camera. *IEEE Trans.Nucl.Sci.*, NS-47(3):1058–1064, 2000.

- [206] G. H. Narayan and J. R. Prescott. Line-widths in NaI(Tl) scintillation counters for low energy gamma-rays. *IEEE Trans.Nucl.Sci.*, NS-13(3):132–137, 1966.
- [207] J. D. Valentine, B. D. Rooney, and J. Li. The light yield non-proportionality component of scintillator energy resolution. *IEEE Trans.Nucl.Sci.*, NS-45(3):512–517, 1998.
- [208] G. G. Kelley, P. R. Bell, R. C. Davis, and N. H. Lazar. Intrinsic scintillator resolution. *IRE Trans.Nucl.Sci.*, NS-3(4):57–58, 1956.
- [209] P. Dorenbos, J. T. M. de Haas, and C. W. E. van Eijk. Non-proportionality in the scintillation response and the energy resolution obtainable with scintillation crystals. *IEEE Trans.Nucl.Sci.*, NS-42(6):2190–2202, 1995.
- [210] R. Gwin and R. B. Murrey. Scintillation process in CsI(Tl). I. Comparison with activator saturation model. *Physical Review*, 131(2):501–508, 1963.
- [211] D. W. Aitken, B. L. Beron, G. Yenicy, and H. R. Zulliger. The fluorescence response of NaI(Tl), CsI(Tl), CsI(Na) and CaF₂(Eu) to x-rays and low energy gamma-rays. *IEEE Trans.Nucl.Sci.*, NS-14(1):468–477, 1967.
- [212] C. D. Zerby, A. Meyer, and R. B. Murray. Intrinsic line broadening in NaI(Tl) gamma ray spectrometers. *Nucl.Instr.Meth.*, 12:115–123, 1961.
- [213] P. Iredale. The effect of the non-proportional response of NaI(Tl) crystals to electrons upon the energy resolution for γ -rays. *Nucl.Instr.Meth.*, 11:340–346, 1961.
- [214] J. D. Valentine and B. D. Rooney. Design of a Compton spectrometer experiment for studying scintillator non-linearity and intrinsic energy resolution. *Nucl.Instr.Meth.*, A353:37–40, 1994.
- [215] B. D. Rooney and J. D. Valentine. Benchmarking the Compton coincidence technique for measuring electron response non-proportionality in inorganic scintillators. *IEEE Trans.Nucl.Sci.*, NS-43(3):1271–1276, 1996.
- [216] W. Mengesha, T. D. Taulbee, B. D. Rooney, and J. D. Valentine. Light yield nonproportionality of CsI(Tl), CsI(Na) and YAP. *IEEE Trans.Nucl.Sci.*, NS-45(3):456–461, 1998.

- [217] G. H. Narayan and J. R. Prescott. The contribution of the NaI(Tl) crystal to the total linewidth of NaI(Tl) scintillation counters. *IEEE Trans.Nucl.Sci.*, NS-15(3):162–166, 1968.
- [218] J. R. Prescott and G. H. Narayan. Electron responses and intrinsic line-widths in NaI(Tl). *Nucl.Instr.Meth.*, 75:51–55, 1969.

